RESEARCH

Determination of Optimum Time for the Application of Surface Treatments to Asphalt Concrete Pavements - Phase II

LRRB

LOCAL
ROAD RESEARCH
BOARD

Take the steps...

Research...Knowledge...Innovative Solutions!

Transportation Research

Technical Report Documentation Page

1. Report No. MN/RC 2008-16	2.	3. Recipients Accession No.	
4. Title and Subtitle Determination of Optimum Time for the Application of Surface Treatments to Asphalt Concrete Pavements - Phase II		5. Report Date June 2008	
		6.	
7. Author(s) Mihai Marasteanu, Raul Velasquez, William Herb, John Tweet Mugur Turos, Mark Watson, Heinz G. Stefan		8. Performing Organization Report No.	
9. Performing Organization Name and Address Department of Civil Engineering University of Minnesota 500 Pillsbury Dr. SE Minneapolis, Minnesota 55455		10. Project/Task/Work Unit No.	
		11. Contract (C) or Grant (G) No. (c) 81655 (wo) 137	
12. Sponsoring Organization Name and Address Minnesota Department of Transportation 395 John Ireland Boulevard Mail Stop 330 St. Paul, Minnesota 55155		13. Type of Report and Period Covered Final Report	
		14. Sponsoring Agency Code	
15. Supplementary Notes http://www.lrrb.org/PDF/200816.pdf			

16. Abstract (Limit: 200 words)

Significant resources can be saved if reactive type of maintenance activities are replaced by proactive activities that could significantly extend the pavements service lives. Due to the complexity and the multitude of factors affecting the pavement deterioration process, the current guidelines for applying various maintenance treatments are based on empirical observations of the pavement surface condition with time.

This report presents the results of a comprehensive research effort to identify the optimum timing of surface treatment applications by providing a better understanding of the fundamental mechanisms that control the deterioration process of asphalt pavements.

Both traditional and nontraditional pavement material characterization methods were carried out. The nontraditional methods consisted of X-Ray Photoelectron Spectroscopy (XPS) for quantifying aging, while for microcracks detection, electron microprobe imaging test (SEM) and fluorescent dyes for inspection of cracking were investigated. A new promising area, the spectral analysis of asphalt pavements to determine aging, was also presented.

Traditional methods, such as Bending Beam Rheometer (BBR), Direct Tension (DTT), Dynamic Shear Rheometer (DSR) and Fourier Transform Infrared Spectroscopy (FTIR) for asphalt binders and BBR and Semi-Circular Bending (SCB) for mixtures were used to determine the properties of the field samples studied in this effort.

In addition, a substantial analysis of measured pavement temperature data from MnROAD and simulations of pavement temperature using a one-dimensional finite difference heat transfer model were performed.

17. Document Analysis/Descriptors Asphalt binder, SEM, asphalt mixture, XPS, surface treatments, chip seal, low temperature cracking, fracture toughness, fracture energy,	creep compliance, fluorescent dye, spectral analysis, heat transfer, strength	18. Availability Statement No restrictions. Document available from: National Technical Information Services, Springfield, Virginia 22161	
19. Security Class (this report) Unclassified	20. Security Class (this page) Unclassified	21. No. of Pages 287	22. Price

Determination of Optimum Time for the Application of Surface Treatments to Asphalt Concrete Pavements - Phase II

Final Report

Prepared by:

Mihai Marasteanu
Raul Velasquez
William Herb
John Tweet
Mugur Turos
Mark Watson
Heinz G. Stefan

University of Minnesota
Department of Civil Engineering

June 2008

ACKNOWLEDGEMENTS

TABLE OF CONTENTS

LIST OF TABLES

LIST OF FIGURES

EXECUTIVE SUMMARY

Finding the optimum time for applying surface treatments is critical in developing a proactive maintenance program as part of a successful pavement management system. Transportation agencies could save significant resources if reactive type of maintenance activities were replaced by proactive activities that could significantly extend the pavements service lives. Due to the complexity and the multitude of factors affecting the pavement deterioration process, most of the guidelines for application of various maintenance treatments are based on empirical observations of the pavement surface condition with time.

This report presents the results of a comprehensive research effort to identify the optimum timing of surface treatment applications by providing a better understanding of the fundamental mechanisms that control the deterioration process of asphalt pavements.

First, a brief literature search, which included research published as recently as January 2008, was performed. It was found that, similar to earlier research efforts, current guidelines for applying surface treatments are based on empirical macroscopic observations of the pavement surface condition with time, and often times require experienced engineering judgment. In all references, the importance of applying treatments to pavements in relatively good condition was noted. No references relating the suitability for treatment application to the change in mechanical properties of the asphalt materials were found.

Next, a detailed description of the test sections used in this investigation and of the materials collected from the field sites was performed and is included in Chapter 2 and in Appendix A. Additional information, available in an unpublished 2002 MnDOT report and regarding the construction and preliminary evaluation of the test sites, is included in Appendix B. The in depth analysis of the various factors present in the experimental field sites revealed that, for the TH 56 sections, the asphalt mixtures used in 1999 and 1995 sections, respectively, were slightly different: the 1999 sections were built with a PG 58-28 asphalt binder (mix design MVWE35035B); the 1995 sections used a penetration grade 120/150 asphalt binder (mix design 41WEA50055Y). In addition, it was found that the emulsion application rate increased with the age of the pavement being treated.

In Chapter 3, different types of nontraditional pavement materials characterization methods were investigated and some were carried out to evaluate the surface condition of pavements, mainly the presence of microcracks and the presence of oxidative aging products in the surface layer of asphalt pavements. For aging, a method based on X-Ray Photoelectron Spectroscopy (XPS) was briefly described and experimental results are presented. For microcracks detection, electron microprobe imaging test (SEM) and fluorescent dyes for inspection of cracking were presented. A new promising area in remote sensing and detection, the spectral analysis of asphalt pavements to determine aging, was also presented in this chapter. The limited results indicated that the use of the XPS and SEM tests is not warranted for routine pavement maintenance activities. The remote sensing and detection appears to currently lack the level of resolution needed to identify changes in asphalt surface characteristics that would indicate the need for surface treatment application. The application of fluorescent dyes has the potential to reveal the presence of microcracks not detectable by visual observation or current pavement condition surveying methods, and should be further pursued in field experiments.

The mechanical tests performed on the asphalt binder samples, such as the Bending Beam Rheometer (BBR), Direct Tension Test (DTT), and Dynamic Shear Rheometer (DSR), and on the mixture samples, such as the BBR on thin mixture beams and the Semi-Circular Bend Testing (SCB), are presented in Chapter 4. In addition, the Fourier Transform Infrared Spectroscopy (FTIR) test performed on the extracted asphalt binders is presented. At the end of the chapter, the test results from all test methods are tabulated.

Chapter 5 contains extensive statistical analyses of the experimental results presented in Chapter 4, based on ANOVA, correlation matrices and Tukey honest difference tests. The analyses focused on identifying significant asphalt binder and mixture properties that affect the deterioration process of asphalt pavements that could be used as triggers in an effort to determine the optimum time of surface treatment application. Plots of the experimental data are presented as figures in Appendix D. Although the analyses did not identify a clear "winner," they led to a number of important conclusions that clearly indicate the potential use of some of these test methods in improving the timing of surface treatment application and the type of treatment. For the TH 56 sections binder data, the FTIR appeared to be the most sensitive to the age of the material and had a significant positive correlation with pavement age. The DSR, BBR, and DT data analyses were less significant and many times led to contradictory results; note, however, that the emulsion application rate was also adjusted with the age of the pavement, and these results appear to indicate that this is a good practice. The mixture BBR analyses seemed to agree the most with common knowledge. For example, the 1995 pavement had higher creep stiffness, and a lower relaxation rate than the 1999 sections, indicating that older pavements are stiffer and have a lower relaxation rate than newer pavements. The depth below the pavement surface was found to have a very significant effect on the m-value; the relaxation rate of the lower layer was higher than the upper layer, which also agrees with the current knowledge about aging. However, the analyses also indicated that the 1995 and 1999 sections were significantly different, due to either the use of different asphalt mix designs and possibly binders, or to different construction practice. Based on the limited number of tests performed on TH 251 samples, it appears that the surface treatment that prevents aging the best is the chip seal. Samples treated with chip seal had the highest mixture fracture energy, the lowest mixture and binder stiffness and the highest binder relaxation rate. Additionally, the binders extracted from the section treated with chip seal show one of the highest strains at failure.

Chapter 6 contains a substantial analysis of measured pavement temperature data from MnROAD and simulations of pavement temperature using a one-dimensional finite difference heat transfer model. Several methods to extract pavement thermal diffusivity from pavement temperature measurements at two or more depths are also described in this chapter. The analysis clearly indicated that surface temperature gradients can be up to 5°C/cm, which suggest that aging is more significant in the very top few centimeters of the pavement. In addition, the temperature rate of change at the surface can be as high as 40°C/hour during rain events when the pavement surface is hot, which may lead to microcracks formation. It was also found that the daytime maximum pavement temperature greatly exceeds maximum air temperature, with surface temperatures of up to 63°C (145°F) in mid-summer, 5°C above the upper limit of the asphalt binder performance grade (PG) commonly used in Minnesota.

Chapter 7 contains the conclusions and recommendations from the research performed in this study.

CHAPTER 1

INTRODUCTION

This research represents phase II of a research effort that investigates the optimum timing of the application of surface treatments on asphalt pavements. In phase I, a comprehensive literature search was performed on the types of surface treatment applications and on the experimental methods. A number of field sections that had the potential to provide samples for the comprehensive laboratory evaluation of the material properties relevant to the timing of surface treatments applications were identified.

The literature search performed in Phase I has shown that most of the work done in the area of surface treatments focused on the construction practice and on the monitoring of the performance of the treatment over various periods of times. Some of the most recent studies also address the economic issues involved in the selection process and the timing of the application of treatments. To date there are no research studies that investigated the deterioration process of pavements in terms of crack formation and propagation related to traffic and environmental loading as well as environmental deterioration, to better select the appropriate application time for surface treatment. Also, there is very little information with respect to the role played by surface treatments in preventing or delaying the aging process in the treated pavement. These important issues need to be further investigated to better understand and quantify the benefits of applying various types of treatments.

Background

Additional literature review was performed during phase II to include detailed information on the Minnesota experience with surface treatments and recent published research.

Minnesota Experience with Surface Treatments

In Minnesota, seal coats usually comprise of an asphalt emulsion layer that is covered by a layer of aggregate one-stone thick [1] and is commonly referred to as a chip seal. Minnesota Department of Transportation (MnDOT) specifications also require (except in the case of residential streets) a light application of diluted asphalt emulsion, commonly known as a fog seal, over the top of chip seals [1]. The addition of the fog seal is beneficial because it helps to lock in the chips, which prevents vehicle damage, and adds additional life to the pavement by increasing its impermeability to air and water [1]. Furthermore fog seals, can provide better visibility for the centerline and edge striping because they blacken the surface. Chip Seals and Fog Seals are among some of the most popular surface treatment activities reported in the literature for flexible pavements in the US.

In addition to the current condition of the roadway, the design and construction of the chip seal are significant contributing factors to the success of surface treatments. Currently, Minnesota experiences good success with its' chip seal program; however, in the early 1990's, chip seal use around the state reached historically low levels, attributed mainly to poor performance and short life spans of the chip seal treatments [2]. Chip seals designed and applied

improperly can become very expensive since the main strategy to rehabilitate a failed chip seal treatment involves an expensive mill and overlay procedure.

To address the poor performance of Minnesota chip seal surface treatments, Wood and Olson [2] conducted a statewide survey and concluded that the poor performance of the surface treatments was linked to several factors including the design, programming, and construction of chip seals. Based on studies of chip seal programs around the world, Janisch [1] recommended that Minnesota adopt a procedure based on the McLeod method, which was modified to increase the resistance of the treatments to snow plows. Janisch and Gaillard published the Minnesota Seal Coat Handbook [1] which includes a detailed section about the design method, materials and design quantities needed to successfully construct a chip seal.

The results of the design enhancement and the handbook have contributed to the current success with Chip Seal Treatments now experienced by the State [2]; there have been no reports of failed surface treatments in the last five years, and, with the addition of polymer modified asphalt and the use of heavier chips, the average service lives of treatments have improved from 5 – 7 years to 8 – 10 years [2].

Other Studies

Of critical importance in the success or failure of a chips seal surface treatment are the aggregate and emulsion application rates. Lee *et. al.* [3] used the third-scale model mobile loading device to investigate the effects, among other things, of aggregate and emulsion application rates on the performance measures of aggregate retention and bleeding. The researchers noted that often times applying the right amounts of asphalt binder and aggregates is more of an art form than a science because too much aggregate, or not enough asphalt can cause the roller or traffic to grind excess aggregate into the seated aggregate particles and dislodge them [4]. In addition, not enough aggregate or too much asphalt can cause bleeding [3]. The authors developed a method to determine the optimum aggregate and emulsion application rates and found that the McLeod design procedure produced reasonable aggregate and emulsion application rates for granite, but produced drier mixes when lightweight aggregate were used (the McLeod method is based on conventional aggregate, and is not applicable for lightweight aggregate) [3].

Gransberg and Zaman [5] compared a total of 342 chip seal projects constructed in Texas between 1996 and 2001 to determine which type of treatment was the most effective in terms of cost and performance [6]. 165 of the projects used a CRS-2P (Cationic Rapid Set) asphalt emulsion as the binder, and 177 projects used an AC15-5TR asphalt binder. Other significant factors, such as contractor and aggregate type, were almost identical (with the exception of seal coats constructed with conventional asphalt binder used precoated lightweight aggregate) among the 342 projects, and the only difference was the type of binder used. They found that, even though the emulsions were used on roads that were in poorer, condition they still were the most cost effective option and had a higher skid resistance and better ride quality. They found that both the emulsion and the conventional asphalt binder resulted in similar pavement condition scores, even though the emulsions were used on roads that were in poorer condition [5].

In 2002 Wade *et al.* [7] published the results on the use of chip seals on high volume high speed roads in SD (seal coats are typically used on low volume roads because the aggregates can get thrown by vehicle tires and cause vehicle windshield damage). They investigated the use of

different aggregates (quartzite, natural) and design parameters (aggregate gradation, emulsion application rate) on the performance of the surface treatment. The performance of the surface treatment was based on various qualities such as macro-texture, condition survey, aggregate retention and embedment, and was measured both immediately after and three months after construction. They discovered that the polymer modified emulsion provided a very strong bond with both types of aggregates, and they also noted that precoated aggregates improved bonding and seemed to reduce cracking.

In a recent NCHRP Report, Peshkin *et. al.* [8] contacted highway agencies in the U.S. and abroad to identify current methodologies of determining the appropriate time to apply preventive maintenance treatments. They found out that there was little guidance available on timing, and that most agencies made their decisions based on:

- Predetermined treatment schedule
- Elapsed time since a previous treatment was applied
- Maintenance surveys
- Pavement management systems

They further investigated the timing of surface treatments by reviewing more than 200 references. They found only a handful of reports that specifically addressed the timing of treatments; none contained detailed research on change in material properties [8].

As part of this research project, Peshkin *et. al.* [8] developed OPTime, a Microsoft® Excel-based tool that operates based on the well accepted concepts of benefit and cost, to determine the optimal time, and compare various treatment alternatives, including the "do-nothing" alternative. OPTime methodology is based on a Life Cycle Cost Analysis that incorporates agency specific performance and cost data in order to determine the optimal time to apply a treatment. The methodology is based on the premise that treatments applied at different times will produce different levels of benefits, and that there is an "optimal time" at which the maximum benefit can be achieved at the lowest possible cost. Treatments placed either too soon, or too late will provide little to no benefit. OPTime has been applied in numerous places with varying degrees of success as described below.

The Arizona Department of Transportation (ADOT) found that, of the five different application ages under investigation, the most effective option was applying treatment at age 13. Age 13 was the latest of the five application ages; this is to be expected when the same equation is used for all application ages. The results do appear to contradict engineering judgment, but they do highlight the importance of obtaining representative datasets, and compiling separate datasets for different treatment application ages.

The Michigan Department of Transportation (MDOT) performed an analysis using the OPTime software that investigated applying chip seals at 10, 11, and 12 years after initial construction. They chose the appropriate model inputs and conducted their analysis based on data from 17 chip seal projects on HMA sections. The analysis indicated that applying the treatment at age 11 is the most cost effective treatment option, but for all practical purposes they found little difference between applying the treatment at age 11, or age 12.

Gransberg and James [9] identified 38 "best practices" that covered a broad range of categories related to the design, construction, administration and even including practices that involve selecting pavements for treatment. The best practices were found in an extensive

literature review and confirmed through specific survey responses [9]. The best practices relating to pavement selection and timing are listed below.

- Used chip seals as a preventive maintenance tool that will be applied on a regular cycle to reinforce the preservation benefits of the technology

- Chip seals perform best on roads with low underlying surface distresses

- Chip seals can be used on high volume roads before pavement distress becomes severe or the structural integrity of the pavement is breached.

They noted that in North America the most common events that would trigger the application of a surface treatment were evidence of a particular distress and the need to prevent further water infiltration. Internationally, the most common triggers were the loss of skid resistance, and the need to provide a wearing surface [9].

Recently, Li *et. al.* [10] published the results of their investigation into the feasibility of increasing the use of Bituminous Surface Treatments (BST) in the state of Washington considering the life cycle cost and pavement condition. The primary goal was to find the most cost effective combination of BST and HMA OL procedures. The interest in increased use of BST over the traditional HMA overlay was motivated by funding problems; initial construction costs of BST are usually about 1/10 that of the standard 45mm HMA overlay [10]. The investigation utilized The Highway Development and Management System (HDM-4) software as the primary analysis tool because it could integrate economic, material, structural and condition models into a unified analysis [10]. The software can also be used for pavement performance predictions, rehabilitation/maintenance programming, funding estimates, budget allocations, policy impact studies, and a wide range of other applications. Its effectiveness is dependent on the accuracy of its constituent models, which makes data accuracy and proper calibration paramount.

HDM 4 economic analysis and pavement condition predictions were used to predict the max AADT for BST, and the max. loading (ESALS) for which BST would be appropriate, by integrating BST into existing HMA surfaced pavements [10]. In the analysis, a BST was triggered based on percent cracking. Three different approaches were investigated to determine the proper trigger for an HMA overlay including: a pre-timed treatment schedule (assuming BST life of 8 years and a HMA OL life of 12 years); an HMA overlay when trigger rutting reached 10mm; IRI deterioration to a value of 2.8 or 3.5 m/km. The IRI and rutting were chosen as a trigger for the HMA overlay treatment because BST's do not significantly improve roughness, nor do they address rutting.

It was found that the most cost effective pavement preservation strategy for over 70% of the pavements surveyed involved using BST's in combination with traditional HMA overlays triggered at an IRI of 3.5 m/km. The authors noted that the following considerations should be made when using model data from HDM-4:

- Actual performance may differ from predicted

- HDM-4 model assumes that BST can correct, or fully treat cracking, which is not true

In addition, the model showed that increased BST use leads to rougher pavements and increased user costs, and that the costs were not reduced, but rather shifted from the agency to the user.

In summary, it appears that most of the guidelines for applying surface treatments are based on empirical macroscopic observations of the pavement surface condition with time, and

often times require experienced engineering judgment. All researchers cite the importance of applying treatments to a pavement in relatively good condition. Some references address the economic issues related to timing, Life Cycle Cost Analysis and pavement management, but these types of analyses are highly dependant upon performance models and life expectancy of surface treatments. There were no references found that discussed the pavement condition, or suitability for treatment, based on damage that was not associated with a particular distress.

Problem Statement

One of the most critical tasks in today's transportation agencies pavement management program is to select the appropriate preventive or corrective alternative for rehabilitation and maintenance of pavements. Currently, many agencies spend millions of dollars a year to maintain their pavement networks at acceptable conditions. The resources available to the agencies are not enough to satisfactorily maintain the network at their current service levels. Therefore, a better understanding of the fundamental mechanisms controlling the pavement deterioration process and the process by which various maintenance and rehabilitation methods delay pavement deterioration becomes an important priority.

While in the classical pavement design, the deterioration models are well established, the models for various rehabilitation and maintenance methods are less understood. This is due to the fact that pavement design is based on empirical failure criteria associated with the "terminal" condition of the pavement while little attention is given to pavement evolution during service life, and to the lack of performance data for the various rehabilitation and maintenance methods.

Objectives

The objective of this research is to provide a better understanding of the mechanism by which surface treatments protect the existing pavement from further aging and deterioration due to traffic and environmental loadings and to reasonably predict the optimum time for the application of these treatments. This requires a reasonable understanding of the progression of the complex aging mechanism in asphalt materials as well as the effect of aging on their fracture resistance. It is expected that this research will provide preliminary guidelines in terms of type of treatment and timing of the application. Continuous monitoring of field performance for longer periods of time combined with additional laboratory investigations and data analysis will be required to improve the prediction of the optimum times for the application of surface treatments.

Scope

The research methodology involves a mixture of fundamental analyses, laboratory experiments as well as field investigations. The timing of the surface treatment is related to the aging and distresses that develop in asphalt pavements with time. Ideally, a surface treatment should be applied not too soon (too expensive) and not too late (reduced life) to provide a balance between maximum life and minimum cost. The evolution of the asphalt pavement surface condition is mostly related to the aging characteristics of the asphalt binder and to the evolution of the mechanical properties of the binder with aging. Both destructive and nondestructive tests will be

performed to assess the change in the surface condition with time and to evaluate the influence of important environmental factors such as temperature and moisture.

The work done in this project focus on providing reasonable answers to the following two questions:

- When is the best time to apply a treatment based on a comprehensive evaluation of the pavement surface and of the processes that take place in the top surface layer of the pavement?

- Do surface treatments in addition to "sealing the pavement surface" significantly delay the detrimental aging process of the treated pavement and are some treatments better than others?

Research Approach

In order to fulfill the objectives of this research the following approach will be followed:

- Field samples selected in Phase I of this project will be evaluated using Bending Beam Rheometer (BBR), Direct Tension (DTT), Dynamic Shear Rheometer (DSR) and Fourier Transform Infrared Spectroscopy (FTIR) for asphalt binders and BBR and Semi-Circular Bending (SCB) for mixtures.

- Different non-conventional pavement materials characterization methods, such as X-Ray Photoelectron Spectroscopy (XPS) for oxidative aging investigation, and electron microprobe imaging test (SEM) and fluorescent dyes for cracks inspection will be studied in this project to asses the condition of the pavement surface.

- A key component of this study will involve the analyses of the environmental factors that influence the surface condition of pavements. Detailed analysis of measured pavement temperature data from MnROAD and simulations of pavement temperature using heat transfer models will be performed. The feasibility of using pavement thermal diffusivity as an aging indicator will be discussed in this study.

- The analysis of the test results will focus on finding the experimental parameters that best describe the aging and deterioration of the pavement. The analysis performed in this research will also develop useful correlations between different materials parameters obtained from the different test methods.

CHAPTER 2

FIELD SAMPLE COLLECTION

Introduction

Two sites were used to recover the field samples: Trunk Highway 56 near Austin, MN, and Trunk Highway 251 near Clarks Grove, MN. A total of 10 sections were sampled from TH 56 to study the optimum time for the application of the surface treatment and four sections were sampled from TH 251 to investigate the effectiveness of three different types of surface treatments: CSS-1h (seal coat), Reclamite and Chip seal.

TH 56 sections are divided in two groups according to the construction year: 1995 and 1999. As it can be seen in Table 2.1 sections ten through fourteen correspond to 1999 and sections fifteen through 19 correspond to 1995. According to the construction report for the MnDOT Aging Optimization project [11] each section had a seal coat applied first and then a fog seal applied later in the specified year (see Table 2.1). The seal coat and fog seal used in the TH 56 sections were a cationic rapid setting emulsion (CRS-2P) and a cationic slow setting emulsion (CSS-1H), respectively. Application rates for both seal coat and fog seal for each section are presented in Table 2.1.

Table 2.1. TH 56 sections description

Section No.	Seal coat application year	Pavement construction year	Age when treated	Agg. Type	Emulsion rate (gal/yd^2)	Agg. rate (lb/yd^2)	Fog Seal rate (gal/yd^2)
10	Control	1999	N/A	N/A	-	-	-
14	2000	1999	1	NUQ	0.32	16	0.11
15		1995	5	NUQ			
13	2001	1999	2	DTR	0.34	17-18	0.11
16		1995	6	DTR			
12	2002	1999	3	DTR	0.38-0.42	18-22	0.11
17		1995	7	DTR	0.40-0.44	18	0.11
11	2003	1999	4	DTR	0.4	19	0.13
18		1995	8	DTR	0.44	19.5	0.13
19	Control	1995	N/A	N/A	-	-	-

For TH 56 sections there were two different types of aggregates used: New Ulm Quartzite, denoted by NUQ, and Dresser Trap Rock denoted by DTR. Note in Table 2.1 that as the difference between the treatment and construction years increased, the binder application rate increased as well. The highest emulsion application rates were used for the two sections with the largest difference between the treatment and construction year, seven and eight years respectively. However, it is also noticed that sections treated in the same year have roughly the same emulsion application rate, even though there is a four year construction difference between

the 1995 and 1999 sections. The reason, most likely, is the similar surface condition of the two sections prior to the surface treatment application.

Six cores were taken from each section of TH 56 and TH 251, respectively: three cores from the wheel path and three cores from between the wheel paths, to determine if the compaction effort from traffic in the wheel path results in differences in the mechanical response from samples coming from these two locations. Note that the initial request of the research team was for 3 times as many cores to increase the number of replicates in the analysis.

Additionally, to study the influence of aging with depth, specimens for both asphalt binder and asphalt mixture testing, were prepared from the cores extracted from TH 56 sections at two different depths: 1 and 3 inches.

Due to coring location errors during extraction, the cores from control section 19 of TH 56 were discarded and not use for mechanical testing. Towards the end of the project additional construction information revealed that most likely the asphalt mixtures used in 19995 and 1995 sections, respectively, were slightly different: the 1999 sections were built with a PG 58-28 asphalt binder (mix design MVWE35035B); the 1995 sections used a penetration grade 120/150 asphalt binder (mix design 41WEA50055Y). Note that the control section for 1995 had part of it built with a different asphalt binder (41WEA50055X) from which cores were extracted erroneously, as mentioned above.

Chip Seal and Fog Seal Design

To design chip seal surface treatments, Minnesota uses a design procedure based on the method developed by Norman McLeod in the late 1960's [1]. An important modification was made to the design procedure that increased the theoretical chip embedment to 70% in order to better withstand the damage caused by snowplows [1]. Of special consideration in the design of a chip seal is the asphalt emulsion application rate given by equation 1.

$$B = \frac{2.44 \times H \times T \times V + S + A}{R} \qquad (1)$$

where:

        B = binder application rate, gallons/yd^2

        H = average least dimension of aggregate, inches

        T = traffic factor (based on expected vehicles per day)

        V = voids in loose aggregate, in decimal percent

        S = surface condition factor, gallons/yd^2

        A = aggregate absorption factor

        R = residual asphalt content of binder, in percent expressed as a decimal

It can be seen in equation 1 that there are four main components affecting the emulsion application rate: the aggregate properties, the expected traffic, the surface condition of the pavement, and the residual asphalt content of the binder. The ideal chip seal is a thin layer of asphalt emulsion on the pavement's surface that is uniformly covered with a layer of aggregate

chips that are one chip thick. The four main components in equation 1 adjust the amount of asphalt emulsion to ensure that there is a sufficient amount to properly embed the aggregate chips.

The average least dimension (H) is calculated based on the flakiness index and the median particle size; it represents the expected seal coat thickness in the wheel paths where traffic will force the aggregate to lie on their flattest side. The voids in loose aggregate (V) represents the voids present when the chips are dropped from the chip spreader and spread onto the pavement; more binder will be required to hold the chips in place if traffic levels are low. The absorption factor (A) adjusts the binder content to account for the binder that gets absorbed by the aggregate and not the roadway [1].

Traffic volume impacts the amount of binder used in that it affects the orientation of the aggregate particles, which in turn affects their embedment depth. Generally speaking, the higher the traffic volume, the lower the binder application rate; higher traffic volumes will cause the aggregates to orient on their flattest side requiring less binder to meet the 70% embedment requirement [1]. If this is not taken into consideration, it is possible for the wheel paths to bleed [1]. The 70% embedment requirement ensures that the aggregate chips are properly retained on the pavement surface [1]. For roads with lower traffic volumes, there is less action by traffic to orient the aggregate chips on their flattest side. Consequently, the chips are more likely to lay on their taller side and thus require more binder to meet the 70% embedment requirement [1].

Probably, the most relevant factor is the surface condition factor, S. The surface condition factor accounts for the fact that as the pavement becomes more oxidized pocked and porous, it will absorb more asphalt binder, and consequently the binder application rate needs to be increased for older, more oxidized pavements (see Table 2.2). Note that Table 2.2 contains rather subjective qualitative descriptions of pavement texture and oxidation. This table is the result of extensive field experience of MnDOT pavement engineers and underscores the importance of experienced field personnel in the construction of successful chip seals.

Table 2.2. Surface Condition Factor, S

Existing Pavement Texture	Correction, S
	U.S. Customary (gal/yd^2)
Black, flushed asphalt	-0.01 to -0.06
Smooth, non-porous	0.00
Slightly porous & oxidized	+0.03
Slightly pocked, porous & oxidized	+0.06
Badly pocked, porous & oxidized	+0.09

The last factor, residual asphalt content (R) accounts for the fact that the cutter, or the water will evaporate as the binder cures. A typical asphalt emulsion is only composed of 67% asphalt cement, where a cutback has 85% asphalt cement [1]. It should be noted that cutbacks are no longer used in Minnesota because of environmental concerns.

Field Samples

Field samples were recovered during August of 2005 using a core bit of inside diameter 6" and length 12". An experienced coring crew from MnDOT's District 6 materials office performed the sample collection. A traffic control crew from Albert Lea, MN provided protection for the

first day of coring. A traffic control crew from Austin, MN provided protection for the second and third days of coring.

Four sections were sampled from TH 251, and ten sections were sampled from TH 56 for a total of 14 sections sampled. For each section, 3 cores were taken from the wheel path, and three cores were taken from between wheel paths, for a total of 6 cores taken from each section. Figures 2.1-2.3 show diagrams of the locations of the cores within each section. The total number of cores collected was 84. Tables 2.2-2.4 present detailed information on the location and size of each core recovered from TH 56 and TH 251.

Figures 2.1-2.2 show the spatial locations of the cores taken from the sections of TH 56. Section 19 is the furthest north, with each sequential section being located within the mile posts to the south, ending with Section 10 at the southernmost position. The locations are denoted by the form: #+00.###. The first digit before the addition sign indicates the reference point, in miles; the last three digits behind the decimal point indicate the location to the thousandth of a mile. The cardinal directions are indicated by arrows, and apply to each section as shown.
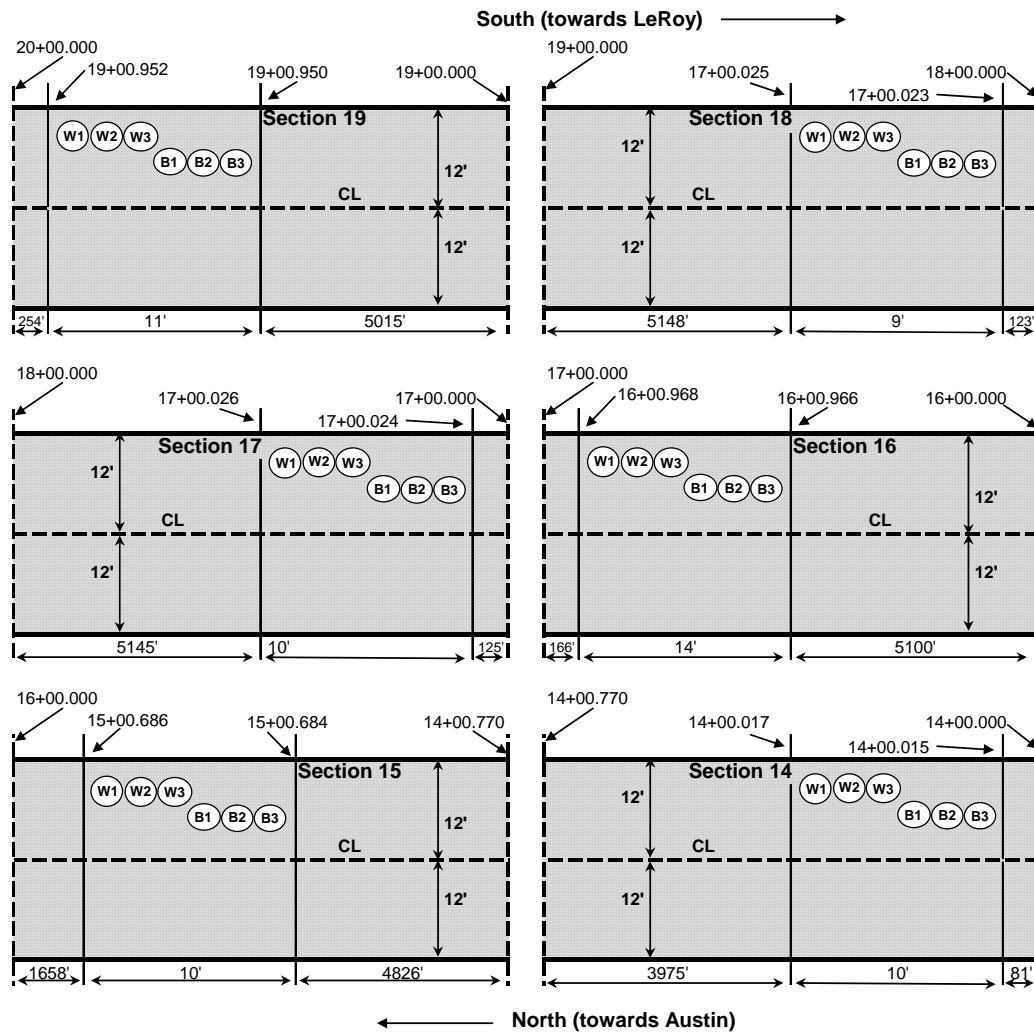
Figure 2.1. Sections 19-14 of TH 56
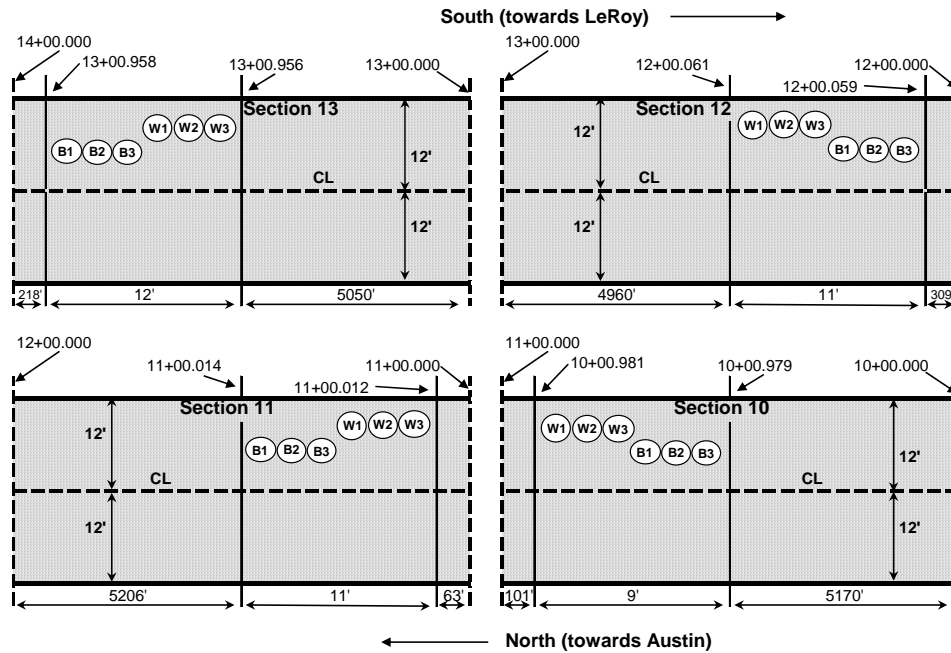
Figure 2.2. Sections 13-10 of TH 56

Figure 2.3 below shows the spatial locations of the cores within the sections of TH 251. Section 2 is the furthest west, and Section 8 is the furthest east. The locations are denoted by the same form of TH 56 sections.
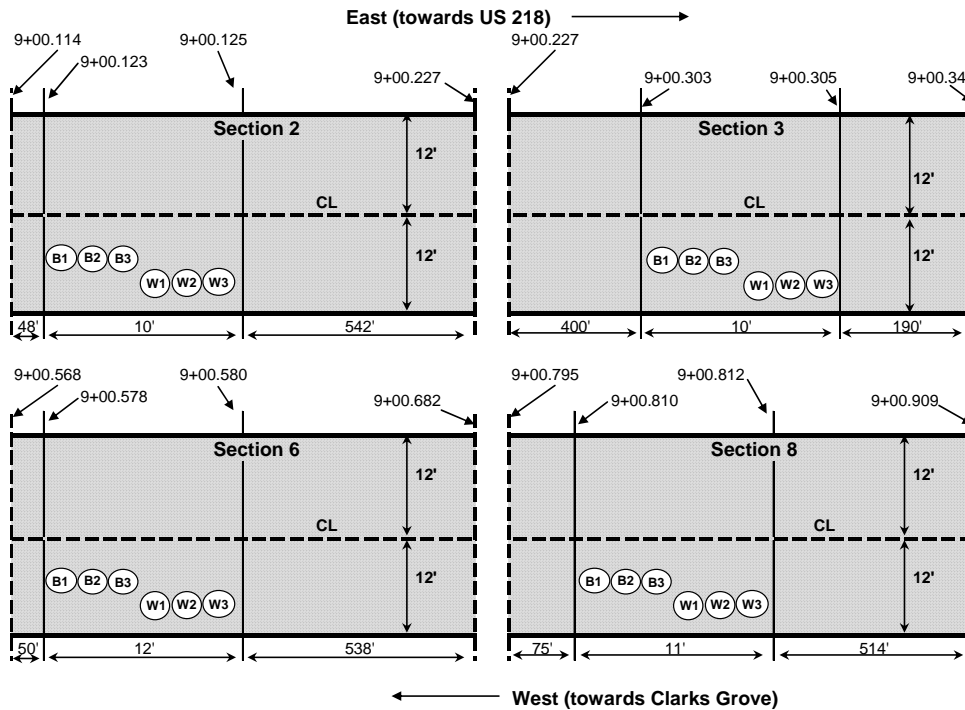
Figure 2.3. Sections from TH 251

11

Tables 2.3 and 2.4 show the location and size of the cores taken from TH 56. The core thickness varies greatly between sections and location in the lane. The maximum thickness of the cores was 11 ¼", the minimum thickness was 4 ¾". The differences between the sections can be attributed to different construction years, coring depths, and deteriorated materials near the bottom of the asphalt layer. The deteriorated asphalt at the bottom of the layer did not have a strong bond with the next lift and frequently separated before the core was removed. The differences across the lane can be attributed to greater traffic compaction in the wheel path.

Table 2.3. TH 56, 1999 Sections.

Year Paved	Treatment	Specimen ID	Thickness (in)	Offset from Centerline	Location
1999	Control	56-10-99-B-1	11	4'-0"	RP 10+00.979
		56-10-99-B-2	11	4'-0"	RP 10+00.979
		56-10-99-B-3	11 1/4	4'-0"	RP 10+00.980
		56-10-99-W-1	11 1/4	8'-0"	RP 10+00.980
		56-10-99-W-2	11 1/4	8'-0"	RP 10+00.981
		56-10-99-W-3	11 1/4	8'-0"	RP 10+00.981
	Seal Coat 2003	56-11-99-B-1	9	6'-0"	RP 11+00.013
		56-11-99-B-2	9	6'-0"	RP 11+00.013
		56-11-99-B-3	8 3/4	6'-0"	RP 11+00.014
		56-11-99-W-1	9	8'-9"	RP 11+00.012
		56-11-99-W-2	8	8'-9"	RP 11+00.012
		56-11-99-W-3	9	8'-9"	RP 11+00.013
	Seal Coat 2002	56-12-99-B-1	7 1/2	6'-3"	RP 12+00.059
		56-12-99-B-2	6 1/2	6'-3"	RP 12+00.059
		56-12-99-B-3	9 1/2	6'-3"	RP 12+00.059
		56-12-99-W-1	4 3/4	8'-9"	RP 12+00.060
		56-12-99-W-2	8 1/4	8'-9"	RP 12+00.060
		56-12-99-W-3	8 1/4	8'-9"	RP 12+00.061
	Seal Coat 2001	56-13-99-B-1	7 1/2	6'-0"	RP 13+00.958
		56-13-99-B-2	7 3/4	6'-0"	RP 13+00.958
		56-13-99-B-3	7	6'-0"	RP 13+00.958
		56-13-99-W-1	8 1/4	9'-2"	RP 13+00.956
		56-13-99-W-2	8	9'-2"	RP 13+00.957
		56-13-99-W-3	6 1/2	9'-2"	RP 13+00.957
	Seal Coat 2000	56-14-99-B-1	8	6'-5"	RP 14+00.015
		56-14-99-B-2	8	6'-5"	RP 14+00.016
		56-14-99-B-3	8	6'-5"	RP 14+00.016
		56-14-99-W-1	7 1/2	8'-9"	RP 14+00.016
		56-14-99-W-2	6 1/2	8'-9"	RP 14+00.017
		56-14-99-W-3	6 1/2	8'-9"	RP 14+00.017

W = Wheelpath, B=between wheelpaths; RP is the reference point, in miles
Shaded cells represent cores taken from between wheel paths

Table 2.4. TH 56, 1995 Sections.

Year Paved	Treatment	Specimen ID	Thickness (in)	Offset from Centerline	Location
1995	Seal Coat 2000	56-15-95-B-1	7 1/2	6'-0"	RP 15+00.684
		56-15-95-B-2	7 1/2	6'-0"	RP 15+00.684
		56-15-95-B-3	7 1/2	6'-0"	RP 15+00.684
		56-15-95-W-1	8	8'-4"	RP 15+00.685
		56-15-95-W-2	8	8'-4"	RP 15+00.685
		56-15-95-W-3	10 1/2	8'-4"	RP 15+00.686
	Seal Coat 2001	56-16-95-B-1	10 1/2	6'-0"	RP 16+00.966
		56-16-95-B-2	10 1/2	6'-0"	RP 16+00.966
		56-16-95-B-3	6 1/8	6'-0"	RP 16+00.967
		56-16-95-W-1	10 1/4	9'-6"	RP 16+00.967
		56-16-95-W-2	10 1/8	9'-6"	RP 16+00.967
		56-16-95-W-3	10	9'-6"	RP 16+00.968
	Seal Coat 2002	56-17-95-B-1	9 1/2	6'-6"	RP 17+00.024
		56-17-95-B-2	6	6'-6"	RP 17+00.024
		56-17-95-B-3	9 1/2	6'-6"	RP 17+00.024
		56-17-95-W-1	9 3/4	9'-0"	RP 17+00.025
		56-17-95-W-2	10 1/2	9'-0"	RP 17+00.025
		56-17-95-W-3	10 1/2	9'-0"	RP 17+00.026
	Seal Coat 2003	56-18-95-B-1	8 3/4	6'-6"	RP 18+00.023
		56-18-95-B-2	8 7/8	6'-6"	RP 18+00.024
		56-18-95-B-3	8 3/4	6'-6"	RP 18+00.024
		56-18-95-W-1	8 1/4	9'-6"	RP 18+00.024
		56-18-95-W-2	8 1/4	9'-6"	RP 18+00.025
		56-18-95-W-3	8	9'-6"	RP 18+00.025
	Control	56-19-95-B-1	8	6'-0"	RP 19+00.950
		56-19-95-B-2	8	6'-0"	RP 19+00.950
		56-19-95-B-3	8	6'-0"	RP 19+00.951
		56-19-95-W-1	7 1/4	9'-0"	RP 19+00.951
		56-19-95-W-2	7 1/8	9'-0"	RP 19+00.951
		56-19-95-W-3	7 1/4	9'-0"	RP 19+00.952

W = Wheelpath, B=between wheelpaths
Shaded cells represent cores taken from between wheel paths
RP is the reference point, in miles

Table 2.5 shows the size and location of the cores taken from TH 251. From the table, it can be seen that the core thickness does vary between sections, and varies to a lesser degree between locations in the lane. The maximum thickness observed for TH 251 was 6 ½", and the minimum thickness was 4 7/8". The differences in thickness can possibly be attributed to compaction of the wheel path due to traffic loading, and construction practices. The maximum difference between the two locations in the lane was only ¼".

Table 2.5. TH 251 Sections.

Treatment	Specimen ID	Thickness (in)	Offset from Centerline	Location
Control	251-2-B-1	6 1/4	6'-6"	RP 9+00.123
	251-2-B-2	6 1/4	6'-6"	RP 9+00.123
	251-2-B-3	6 1/4	6'-6"	RP 9+00.123
	251-2-W-1	6 1/2	9'-0"	RP 9+00.124
	251-2-W-2	6 1/2	9'-0"	RP 9+00.124
	251-2-W-3	6 1/2	9'-0"	RP 9+00.125
CSS-1h 2002	251-3-B-1	6	4'-0"	RP 9+00.304
	251-3-B-2	6	4'-0"	RP 9+00.305
	251-3-B-3	5 3/4	4'-0"	RP 9+00.305
	251-3-W-1	5 3/4	8'-0"	RP 9+00.303
	251-3-W-2	5 3/4	8'-0"	RP 9+00.303
	251-3-W-3	6	8'-0"	RP 9+00.304
Reclamite 2002	251-6-B-1	4 7/8	5'-6"	RP 9+00.578
	251-6-B-2	4 7/8	5'-6"	RP 9+00.578
	251-6-B-3	4 7/8	5'-6"	RP 9+00.578
	251-6-W-1	5	7'-6"	RP 9+00.579
	251-6-W-2	5	7'-6"	RP 9+00.579
	251-6-W-3	5	7'-6"	RP 9+00.580
Chip Seal 2002	251-8-B-1	5 3/8	5'-6"	RP 9+00.810
	251-8-B-2	5 3/8	5'-6"	RP 9+00.810
	251-8-B-3	5 3/8	5'-6"	RP 9+00.810
	251-8-W-1	5 1/8	8'-6"	RP 9+00.811
	251-8-W-2	5 1/8	8'-6"	RP 9+00.811
	251-8-W-3	5 1/4	8'-6"	RP 9+00.812

W = Wheelpath, B = between wheel path
The shaded cells represent cores taken from between wheel paths
RP is the reference point, in miles

Details from the construction records from MnDOT District 6 as well as pictures of the cores taken from the test sections are included in Appendix A. Additional information regarding a preliminary Aging/Optimization study performed in 2002 on TH 56 and I-35 NB that includes the evaluation of three pavement preventive maintenance (PPM) treatments in both the roadway and the shoulders using PSR (ride data), SR (surface ratings), coring and friction numbers is presented in Appendix B. Photos of the TH 56 sections taken in August 2007 are included in Appendix C.

CHAPTER 3

SURFACE CONDITION (AGING AND CRACKING) ASSESSMENT

Introduction

Most of the research investigating surface treatments focuses on the construction practice and on monitoring the performance of the treatment over various periods of times. More recent studies started to address the economic issues involved in the selection process and the timing of the application of treatments. To date there are no research studies that investigated the deterioration process of pavements in terms of crack formation and propagation related to traffic and environmental factors to better select the appropriate application time for surface treatment. Also, there is very little information with respect to the role played by surface treatments in preventing or delaying the aging process in the treated pavement. These important issues need to be further investigated to better understand and quantify the benefits of applying various types of treatments.

In this chapter different types of methods were investigated and some were carried out to evaluate the surface condition of pavements, mainly the presence of microcracks and the aging of the asphalt surface layer of the pavements. These are:

- Investigate the aging of asphalt concrete at the surface of asphalt pavements by means of the X-Ray Photoelectron Spectroscopy (XPS); determine feasibility of XPS technology to asses the condition of the surface of the pavement.

- Evaluate the presence of microcraks in the surface of asphalt pavements using the electron microprobe imaging test (SEM)

- Investigate the feasibility of using fluorescent dyes for inspection of cracking.

- Perform literature review on spectral characteristics of asphalt pavements and determine if this technology can be used to determine the optimum time for the application of surface treatment.

Since most of these methods are not commonly used in pavements research, the next sections describe the instruments and the data obtained in these experimental methods and the feasibility of using them for routine pavement condition investigation is discussed.

Investigation of Aging in the Surface Layers of Asphalt Pavements

Aging in asphalt binders is generally accepted to be the cause of hardening of the asphalt over time. Age hardening has been known from the earliest days of asphalt pavement construction in the United States [12], however, the mechanisms by which aging occurs have been just recently investigated. The primary mechanisms of age hardening were determined to be loss of volatiles, oxidation, and steric hardening [13]. These mechanisms are very complex, and have been discussed in detail elsewhere [14, 15 and 16].

The products of the oxidation process are of interest to this study. The two main oxidation products identified by researchers are benzyl ketone, and sulfoxide [13]. Later research identified ketones as the main contributor of long term age hardening [17]. Ketones are formed when benzylic carbon atom oxidizes to benzylic ketone. The ketone is characterized by a carbon double bonded to oxygen.

There are two stages for the aging of asphalt concrete. The first stage occurs during the mixing of the HMA. The second stage occurs in the field after construction. The two main differences between the stages are the temperature and exposure to oxygen. Research shows that the oxidation of asphalts is highly temperature and oxygen pressure dependent [14]. During the first stage, the asphalt is exposed to high temperatures (up to 163°C) and uniform oxygen pressure. During the second stage, both the temperature and oxygen pressure vary throughout the depth of the pavement. The top surface of the asphalt concrete layer is exposed to the highest temperatures and ambient oxygen pressure. Below the top surface, the temperature decreases with depth (for daytime), and the oxygen pressure is diffusion controlled [15].

The rate of oxidation is different for the two different stages. The first stage has rapid formation of oxidation products, mostly sulfoxides and some ketones. There is also a loss of volatiles during the first stage. During the second stage, the oxidation process produces almost exclusively ketones. Steric hardening also occurs during the second stage as the ambient temperature is low enough to allow for polar molecules to reassociate [14].

Being able to investigate the evolution of aging with time in an asphalt pavement is a top priority in asphalt research. Thus, detecting ketones or any other products of the oxidation by means of a simple experiment is of significant importance in predicting the evolution of aging at the surface of asphalt pavements. The most popular method is based on Fourier Transform Infrared (FTIR) spectral analysis performed on samples of asphalt binder extracted from field mixtures. FTIR method is described in detail in this chapter.

Due to concerns related to the use of chemical solvents in the extraction process that can alter the properties of the binder, there has been an increased interest in developing other techniques that can detect aging products directly on the asphalt mixtures. Most of this work is research in progress performed by the asphalt group at Western Research Institute using NMR and FTIR-ATR methods, and no detailed documentation was available at the time this project was finalized. The only documented method that showed promise was on the use of X-Ray Photoelectron Spectroscopy (XPS) and this method is presented next.

X-Ray Photoelectron Spectroscopy (XPS)

XPS is a surface analytical technique that can provide elemental and molecular information of the specimen's surface. XPS testing offers relatively low operational complexity, it requires minimal specimen pre-treatment and produces low damage to the specimens. Samples tested with this technique can range from complex polymers, to pottery and powders. The XPS machine itself is a combination of a vacuum chamber, x-ray emitter, electron collector, and data recorder [18].

Photo-ionization and energy dispersive analysis are used in x-ray photoelectron spectroscopy (XPS) to determine the electronic state and composition of the specimen's surface [19]. This technique utilizes soft x-ray (*e.g.* 200-2000 eV) radiation to study the surface of the specimen. X-ray photoelectron spectroscopy is based on the following physical process: the

photon emitted by the radiation source is absorbed by an atom leading to ionization and to the emission of an electron. Then, the number of emitted photoelectrons as a function of their kinetic energy can be measured by means of electron energy analyser [19].

It is important to notice that monochromatic sources of radiation are used in this technique in order to have a fixed known energy (*e.g.* energy of a photon given by Einstein relation: $E= hv$, where h is Planck constant and v is the frequency of radiation) coming in at the surface of the sample [19]. Additionally, high vacuum environment is necessary to avoid interference from gas phase collisions. A simplified version of the photoionization process is as follow:

$$B + \boldsymbol{hv} \rightarrow B^+ + e^-$$ (2)

where B is the neutral atom, $\boldsymbol{hv}$ is the photon, B^+ is the ionized atom and e^- is the emitted electron.

Using (2) and conservation of energy then:

$$E(B) + \boldsymbol{hv} = E(B^+) + E(e^-)$$ (3)

Since the energy of the electron is only kinetic then (3) can be rewritten as:

$$KE = \boldsymbol{hv} - (E(B^+) - E(B))$$ (4)

The difference between the energy of the ionized and neutral atoms is called binding energy (BE) of the electron. The latter is a direct measure of the energy required to move the electron from its initial level to the vacuum level [19]. Each element has a characteristic binding energy related to each atomic orbital meaning that every element will have different set of peaks in the photoelectron spectrum at kinetic energies determined by (4) (*e.g.* the kinetic energy is a function of the binding energy and the photon energy).

Thus, the location of peaks at particular energies in the XPS spectrum indicates the presence of a specific element in the surface of the specimen [18]. The binding energy (BE) of an electron is a function of:

- Level where photoemission is occurring
- Local chemical and physical environment
- Oxidation state of the atom

Changes in the local environment and in the oxidation of the atoms under study will change the location of the peaks in the spectrum. This is called chemical shifts [19]. Chemical shifts in XPS can be used to determine the oxidation state of the surface of the specimen. An example of a XPS spectrum and a chemical shift due to oxidation of Titanium is presented in Figure 3.1. From Figure 3.1 it can be observed that atoms of titanium exhibit larger chemical shifts. Titanium dioxide TiO_2 (higher oxidation state) have higher binding energy than the pure metal Ti (*e.g.* the curve of titanium dioxide is shifted to the left).
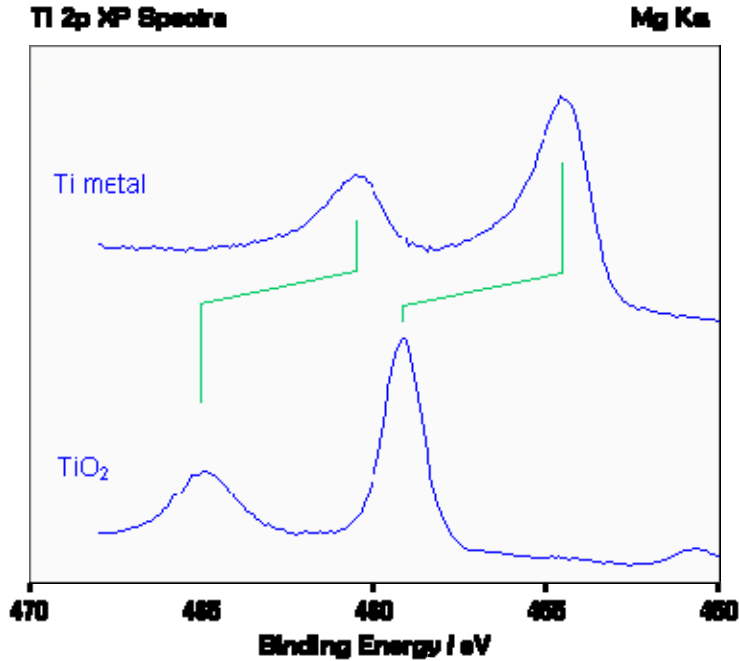
Figure 3.1. Oxidation States of Titanium using XPS taken from [19]

Materials

Asphalt mixture samples collected from the field and asphalt binders aged in laboratory conditions and extracted from the field asphalt mixtures were tested to determine the capability of the XPS technique to detect the level of oxidation of asphalt. Tables 3.1 and 3.2 describe the asphalt mixtures and asphalt binders, respectively, that were tested. Duplicate specimens were available for Cell 35 mixtures ad are identified as 1 and 2 in Table 3.1. Cells 33 and 34 had no replicates. For all asphalt binder samples, two replicates were available and are identified as *a* and *b* in Table 3.2.

Table 3.1. Asphalt Mixture used in XPS testing

ID	Identification	Origin
T-1, T-2	Cell 35, core surface	MnROAD mixture
C-1, C-2	Cell 35, core center	MnROAD mixture
B-1, B-2	Cell 35, core bottom	MnROAD mix
33	Cell 33 – core surface	MnROAD mix
34	Cell 34 – core surface	MnROAD mix
TWM1 a, b	Parking lot mixture	Theodore Wirth Golf Course

18

Table 3.2. Binders used in XPS testing

ID	Identification	Origin
PTW-1 Ua, Ub	Unaged PG58-28 (plain)	Hwy 17, Ontario, Canada
PTW-1 Ra, Rb	RTFOT PG58-28	Hwy 17, Ontario, Canada
PTW-1 Pa, Pb	PAV, PG58-28	Hwy 17, Ontario, Canada
BI-7 Pa	PAV, PG58-28	Binder Inventory Study (used in MnROAD cell 33)
R506 a, b	RTFOT, PG58-28	MnDOT
P506 a, b	PAV, PG58-28	MnDOT
TWB1 a, b	Extracted from mixture	Theodore Wirth Golf Crse PL
BC03-0004 a, b	Extracted from shingles	MnDOT shingles study

Specimen Preparation

The XPS test requires that the specimen can be attached to a small platform, have a smooth surface, and have thickness less than 2 mm. The specimen preparation techniques will have an effect on the results; however, it is still not clear what this effect is. The following specimen preparation procedures were used in this study:

1. Diamond Sawing

    -   Specimen dimensions: 15 mm x 15 mm x 2 mm

    -   Used for preparing samples from mix cores

    -   First cut to semi circular cross-section with large diamond blade, then cut to quarter circle cross section with large diamond blade, finally trimmed 2 mm from top of quarter circle using small diamond blade

    -   Cut to final dimensions by shear machine

    This technique can lead to possible carbon contamination from the diamond saw dust; this may have a strong effect on the amount of oxidized carbon observed, furthermore, small specimen size may not be representative of the asphalt mix. Moreover, large aggregate particles reduce amount of information from the binders.

2. Razor Chip Mining

    -   Use razor or sharp edge to chip out mastic from surface of mix core

    -   Take chips from different locations of the surface in order to obtained representative sample.

    -   Place a double sided piece of tape on the test platform

    -   Place multiple chips on the tape such that there are no gaps between the chips, and the entire area near the center of the platform is covered – assuming the sample would be representative of mix

    In this technique the steel and other contaminants from the blade can affect the results. Moreover, chips are easily contaminated by dust coming from air and crushed aggregate.

3. Flowing binders onto substrate

- Use both silicon and steel substrates
- Place substrate on heater and heat to 160 degrees Celsius
- Scoop a small amount of binder from tin and press against center of substrate
- Allow binder to melt and flow onto substrate – use scooping device to spread binder when necessary
- Remove substrate from heater when binder surface was smooth, no more than 60 seconds after placing binder on substrate

In this case, contamination from scooping device or substrate can influence the results of the XPS. In addition, the binder on substrate is highly susceptible to dust contamination from air. Table 3.3 below lists the specimens tested and the preparation technique used.

Table 3.3. Specimen preparation

ID	Preparation Technique
T-1, T-2	Diamond sawing
C-1, C-2	Diamond sawing
B-1, B-2	Diamond sawing
33	Razor chip mining
34	Razor chip mining
PTW-1 Ua, Ub	Binder flowed onto substrate
PTW-1 Ra, Rb	Binder flowed onto substrate
PTW-1 Pa, Pb	Binder flowed onto substrate
BI-7 Pa	Binder flowed onto substrate
R506 a, b	Binder flowed onto substrate
P506 a, b	Binder flowed onto substrate
TWM1 a, b	Razor chip mining
TWB1 a, b	Binder flowed onto substrate
BC03-0004 a, b	Binder flowed onto substrate

XPS Test Procedure

XPS tests were conducted at the University of Minnesota Characterization Facility. The XPS machine used for the test was manufactured by Physical Electronics Inc. and it uses a conventional MgKα X-Ray source at 250 watts. For surveys, the resolution was between 0.5eV/step to 1.0eV/step. For peaks, the resolution was 0.05eV/step. The following steps were taken for each XPS test:

1. Attach sample to test platform - This step is different for each specimen preparation technique described earlier. If the specimen was prepared using the diamond saw, it can be

attached directly to the platform using screws. If the specimen was prepared by using the chip mining method, the chips must be attached to the platform using double sided tape. If the specimen was prepared by flowing binder onto a substrate, the substrate must be attached to the platform using screws.

2. Load test platform into sample chamber

3. Vacuum pump specimen for approximately 30 minutes - Excess gases must be removed from the surface of the specimen. If volatile gas pressure is too high, or a pocket of gases is released from the specimen, the X-Ray source could be damaged and/or the results will not be useful. The XPS test requires high vacuum inside the test chamber for useful results.

4. Position specimen in test chamber and prepare X-Ray machine - The specimen is next moved into the test center where it is positioned near the X-Ray source. The test chamber pressure should be within operational limits before the machine is activated.

5. Run tests - The XPS tests are run from a computer terminal using the XPS software. Data is collected by the computer and interpreted by the software. Five tests are run for each specimen. The first is a survey; the remainders are peaks for Carbon, Oxygen, Sulfur, and Silicon.

6. Unload specimen from machine - The specimen is removed from the test chamber to the sample chamber. Once the chamber is returned to atmospheric pressure, the specimen is removed from the machine.

XPS Results

The data collection system records the number and energy of the electrons excited from the specimen during testing. Once the test is completed, the system plotted the binding energy of the electrons versus the number of electrons observed. Peak envelopes in the graph represent specific elements. An analysis program was used to fit each peak envelope to a curve. The area beneath each fitted curve was used to determine the total atomic percentage of the specific element contained within the sample. Curves shifted from main peaks are different functional groups. The analysis was performed by the XPS specialist at the University of Minnesota Characterization Facility.

The analysis of the carbon peak yields the functional group makeup of carbon in the sample. As it was mentioned before, one of the main products of oxidation aging in asphalt binders is represented by ketones (characterized by a carbon doubled bonded with oxygen C=O). Thus finding the amount of oxygen double bonded to carbon in the specimens is of great interest in this study.

Figures 3.2 to 3.10 shows the results from XPS testing on the mixes described in Table 3.1.
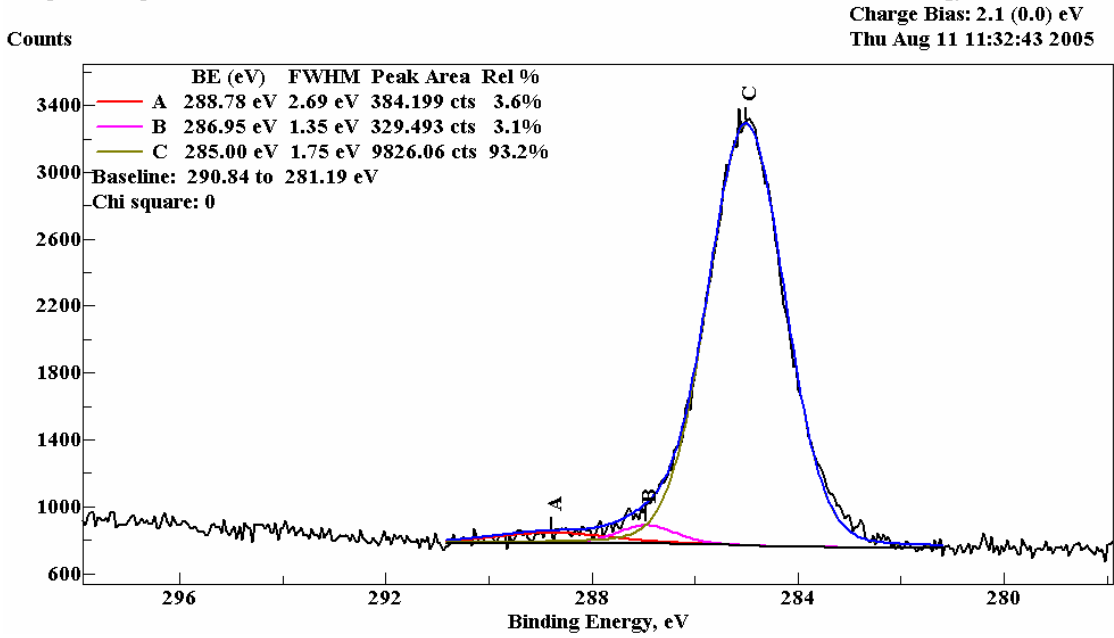
Figure 3.2. XPS testing results for specimen T-1
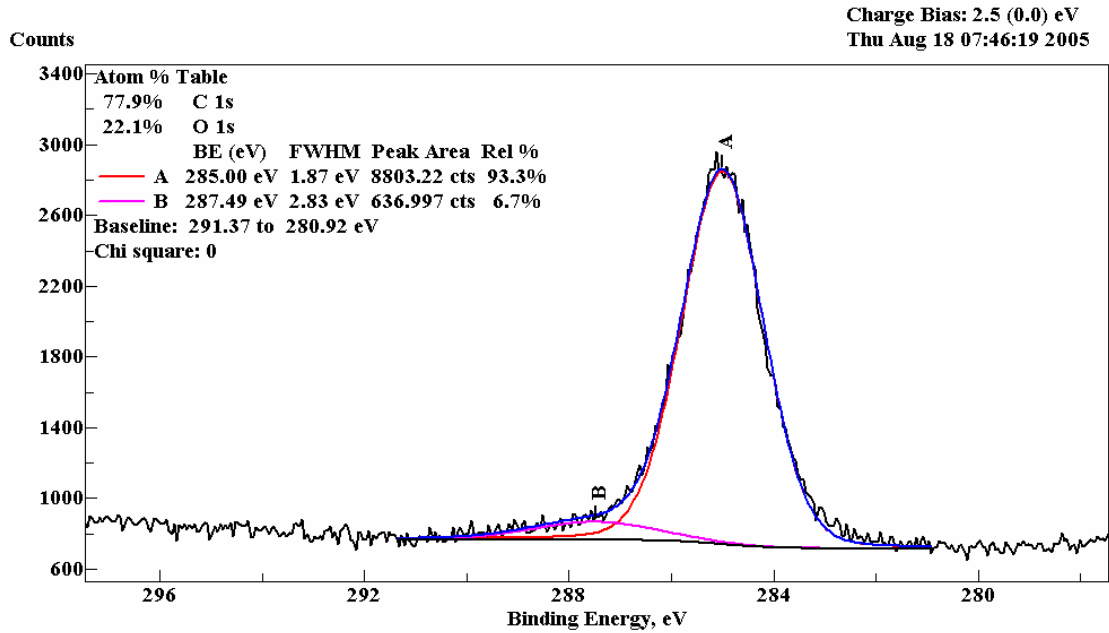
Figure 3.3. XPS testing results for specimen T-2

22
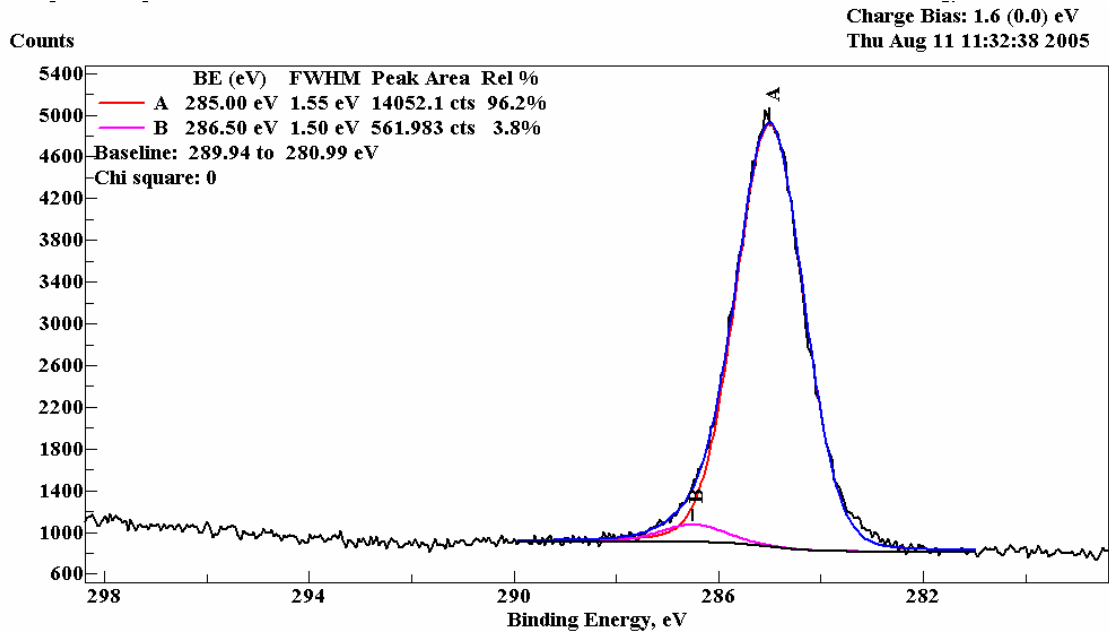
Figure 3.4. XPS testing results for specimen C-1
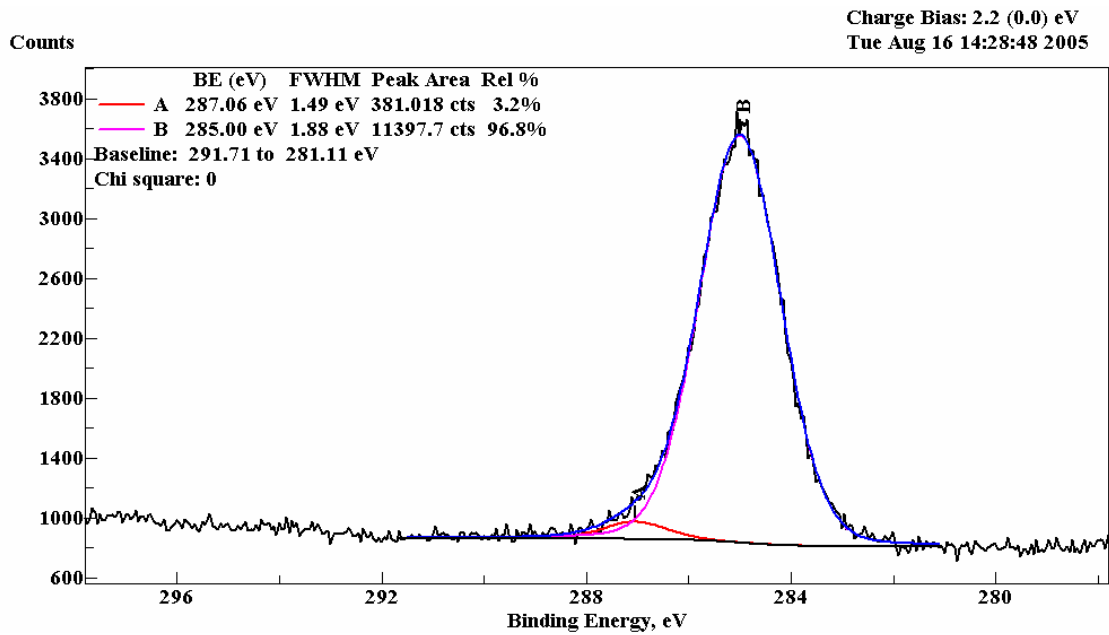
Figure 3.5. XPS testing results for specimen B-1
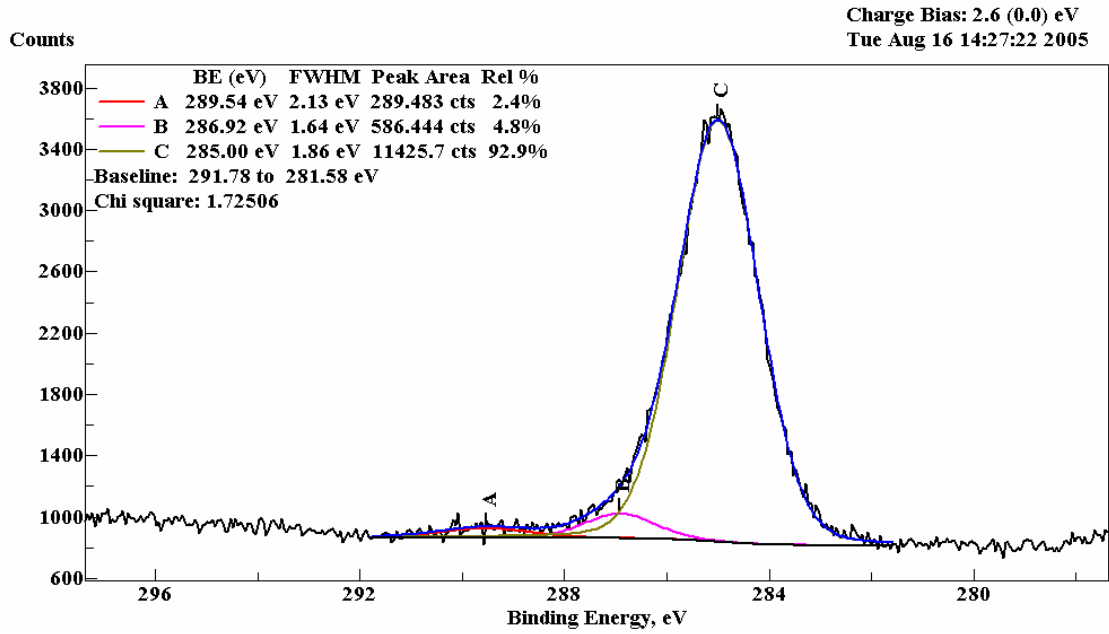
Figure 3.6. XPS testing results for specimen B-2
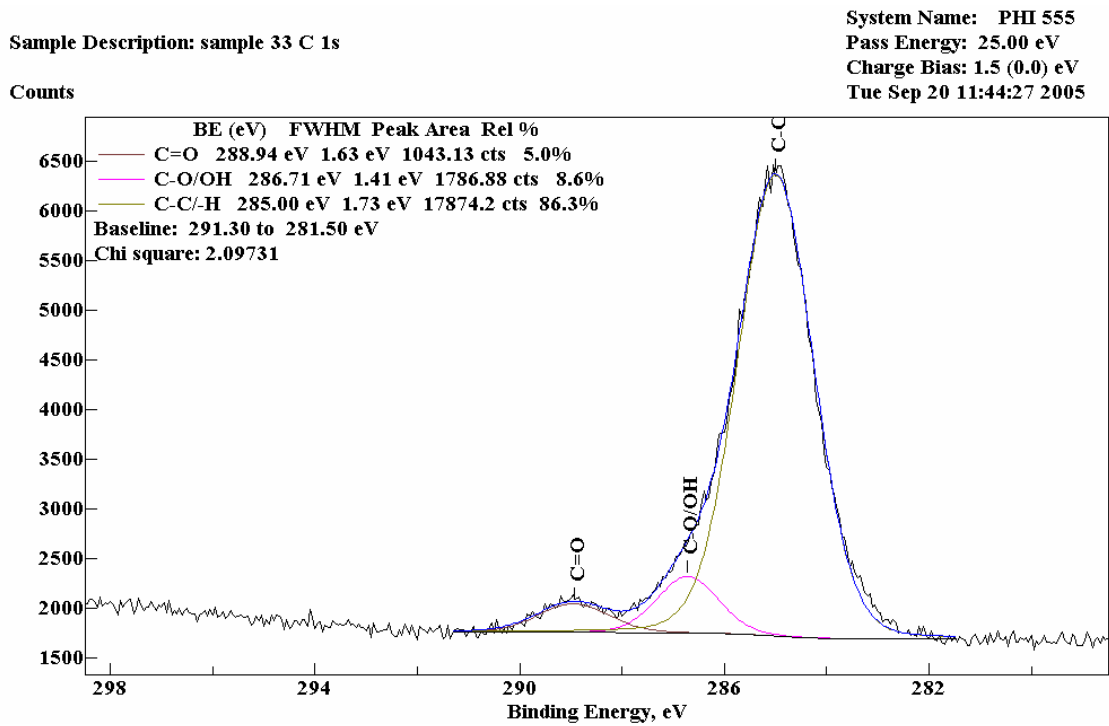
Figure 3.7. XPS testing results for specimen 33

Counts

	BE (eV)	FWHM	Peak Area	Rel %
C-C/C-H	285.00 eV	1.91 eV	14623.2 cts	95.2%
C-O/-OH	287.35 eV	3.13 eV	737 cts	4.8%

Baseline: 291.15 to 281.00 eV
Chi square: 2.20781
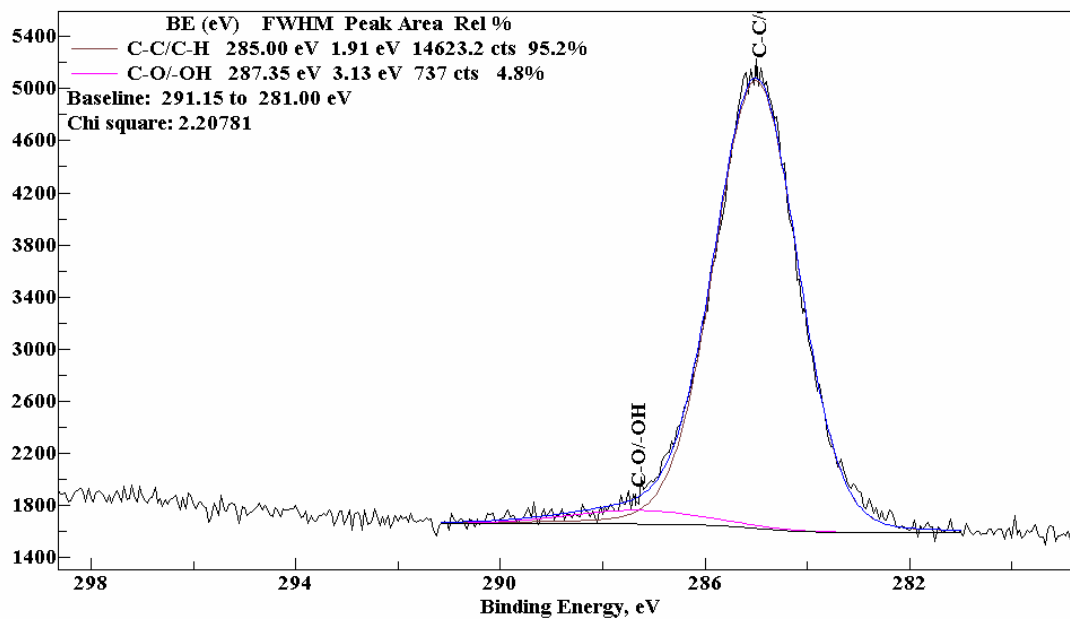
Figure 3.8. XPS testing results for specimen 34

Counts

	BE (eV)	FWHM	Peak Area	Rel %
A	288.32 eV	1.24 eV	962.818 cts	3.4%
B	286.72 eV	1.60 eV	26279.3 cts	93.2%
C	285.01 eV	1.25 eV	969.127 cts	3.4%

Baseline: 292.74 to 282.89 eV
Chi square: 2.41262
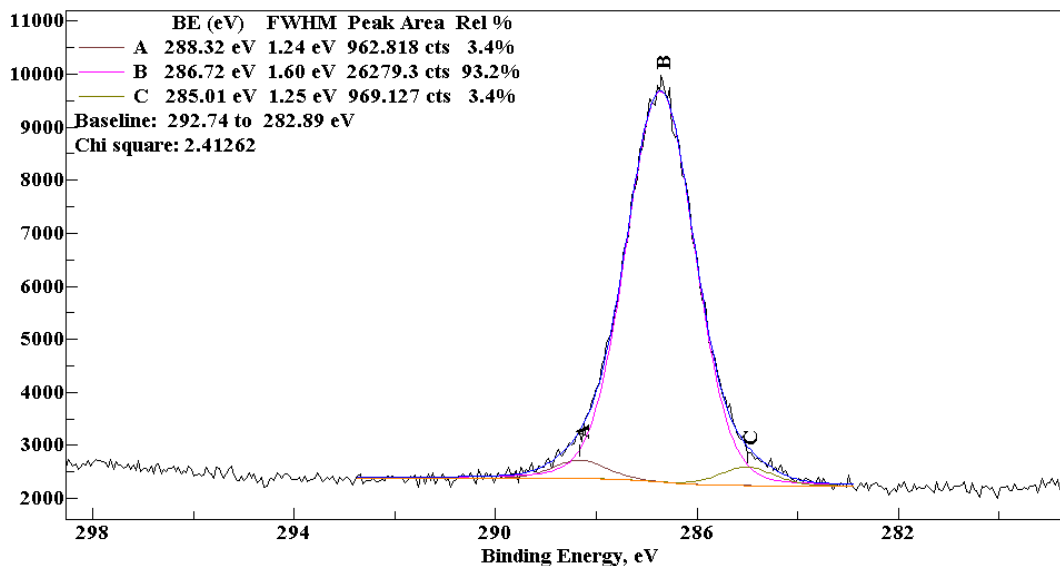
Figure 3.9. XPS testing results for specimen TWM1a

25
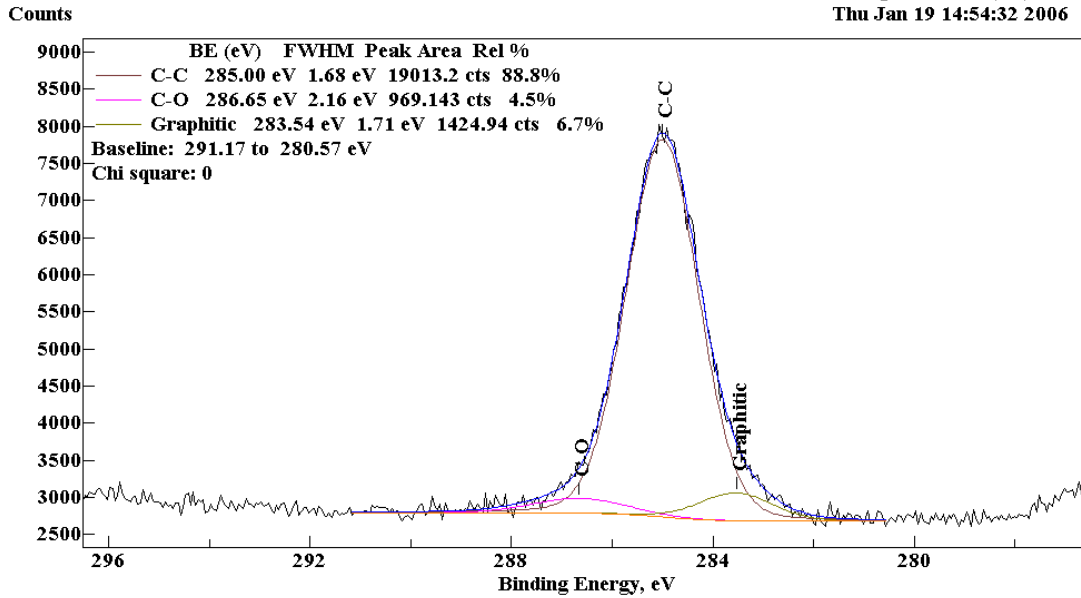
Figure 3.10. XPS testing results for specimen TWM1b

Figures 3.11 to 3.23 shows the XPS testing results for the binders listed on Table 3.2.

Figure 3.11. XPS testing results for specimen PTW-1 Ua

PTW Rb C 1s
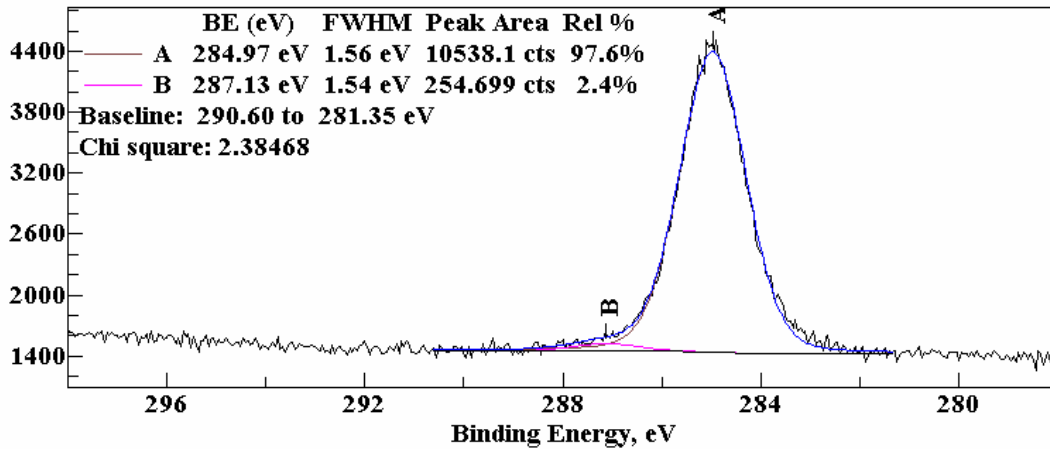
Counts

Figure 3.12. XPS testing results for specimen PTW-1 Rb

Sample Description: PTW-1 Pa C1s
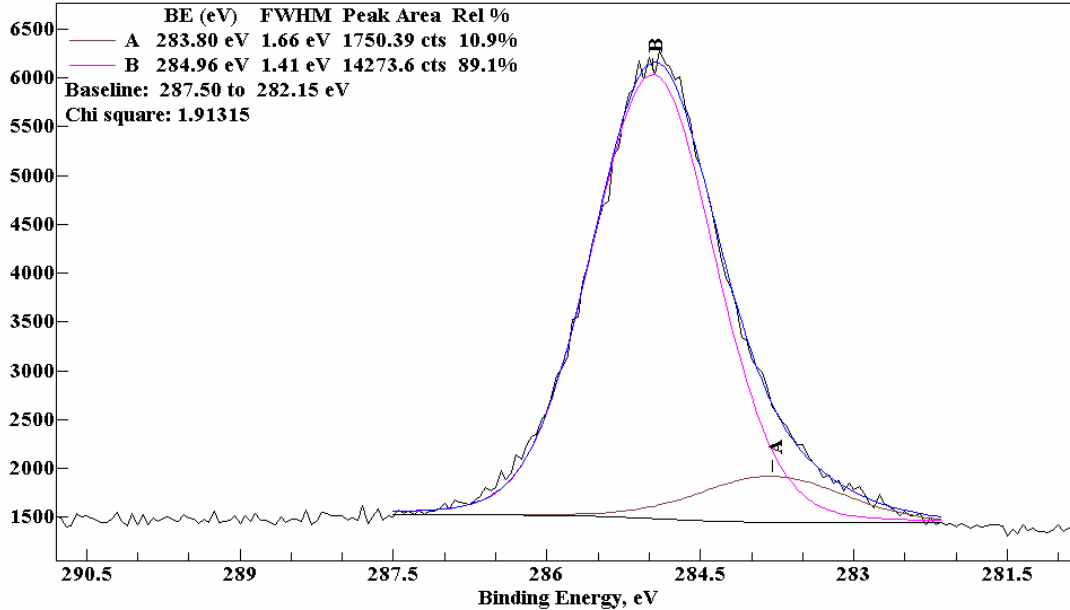
Counts

Figure 3.13. XPS testing results for specimen PTW-1 Pa

27

Counts

```
           BE (eV)   FWHM  Peak Area  Rel %
     A   285.01 eV  1.51 eV  18711.1 cts  96.9%
     B   283.43 eV  0.76 eV  605.05 cts   3.1%
Baseline: 287.85 to 282.10 eV
Chi square: 1.93513
```

Binding Energy, eV
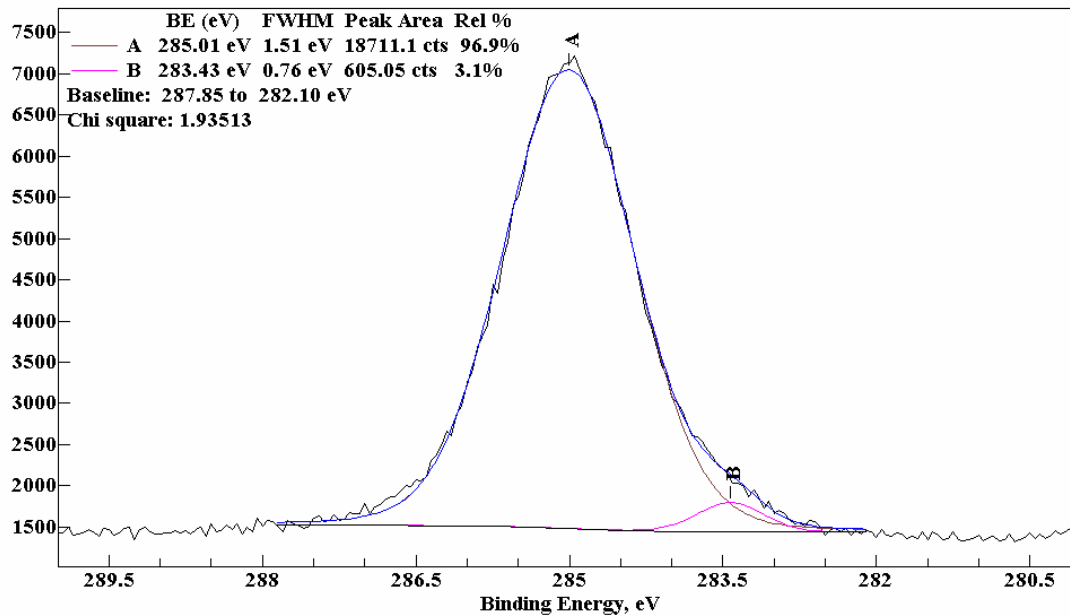
Figure 3.14. XPS testing results for specimen PTW-1 Pb

Counts

```
Atom % Table
  96.5%    C 1s
  2.0%     O 1s
  1.5%     S 2p
           BE (eV)    FWHM  Peak Area  Rel %
   C-C/C-H  285.00 eV  1.50 eV  21607.2 cts  98.8%
   C - O bonds  286.61 eV  0.74 eV  255.995 cts  1.2%
Baseline: 289.05 to 281.55 eV
Chi square: 0
```

Binding Energy, eV
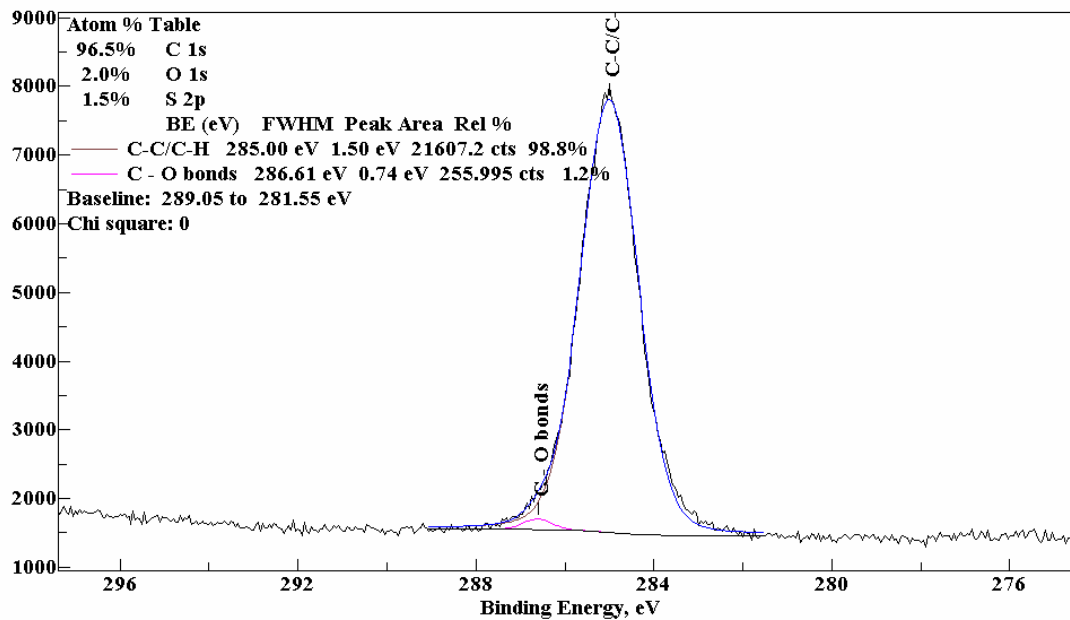
Figure 3.15. XPS testing results for specimen BI-7 Pa

28

Sample Description: R506a HR region C 1s

Counts

BE (eV)   FWHM Peak Area Rel %
—— A   287.27 eV 1.54 eV 48300.5 cts 100.0%
Baseline: 293.30 to 283.25 eV
Chi square: 2.73531

Binding Energy, eV
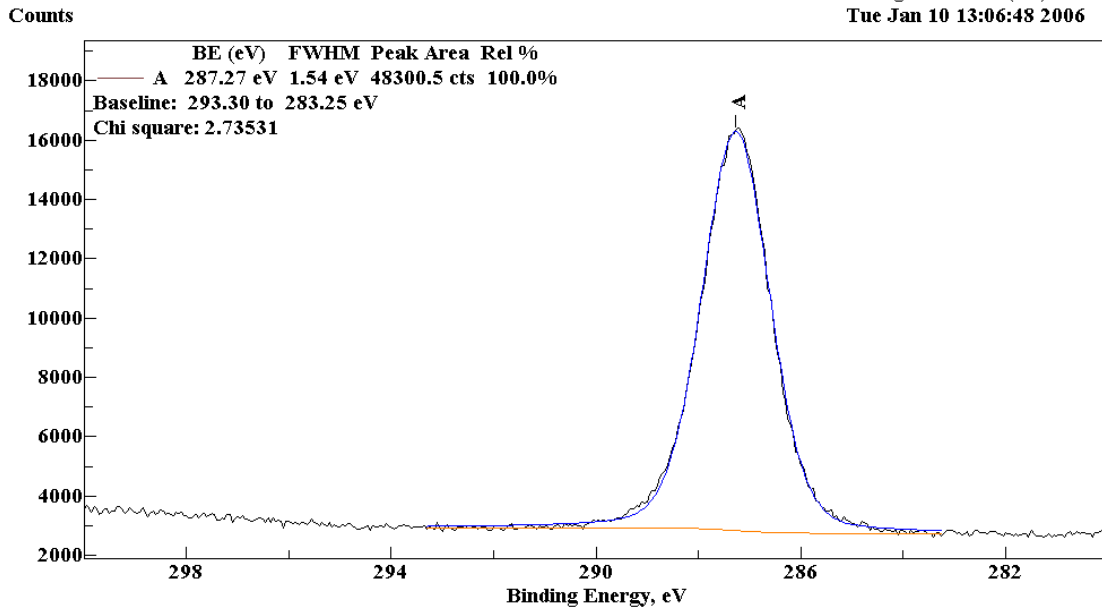
Figure 3.16. XPS testing results for specimen R506a

Sample Description: R506b HR region C 1s

Counts

BE (eV)   FWHM Peak Area Rel %
—— A   285.00 eV 1.56 eV 47483 cts 100.0%
Baseline: 290.36 to 280.76 eV
Chi square: 2.94272

Binding Energy, eV
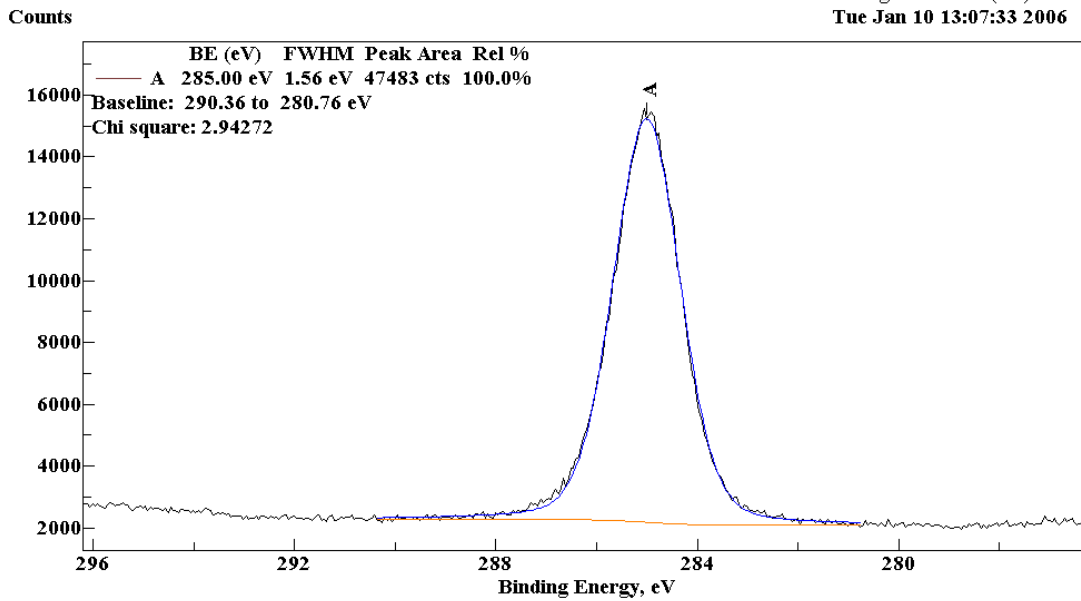
Figure 3.17. XPS testing results for specimen R506b

Counts

	BE (eV)	FWHM	Peak Area	Rel %
A	285.00 eV	1.57 eV	51901.8 cts	96.7%
B	286.84 eV	1.52 eV	1750.84 cts	3.3%

Baseline: 290.63 to 280.88 eV
Chi square: 2.85929

Binding Energy, eV
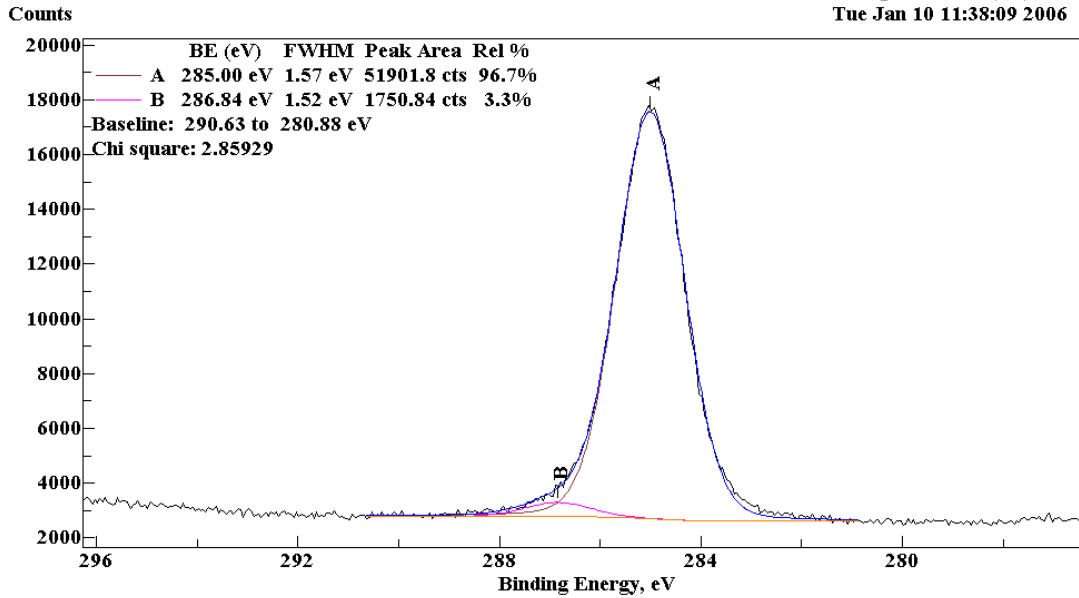
Figure 3.18. XPS testing results for specimen P506a

Counts

	BE (eV)	FWHM	Peak Area	Rel %
A	285.00 eV	1.56 eV	37570 cts	100.0%

Baseline: 291.31 to 280.96 eV
Chi square: 2.99425

Binding Energy, eV
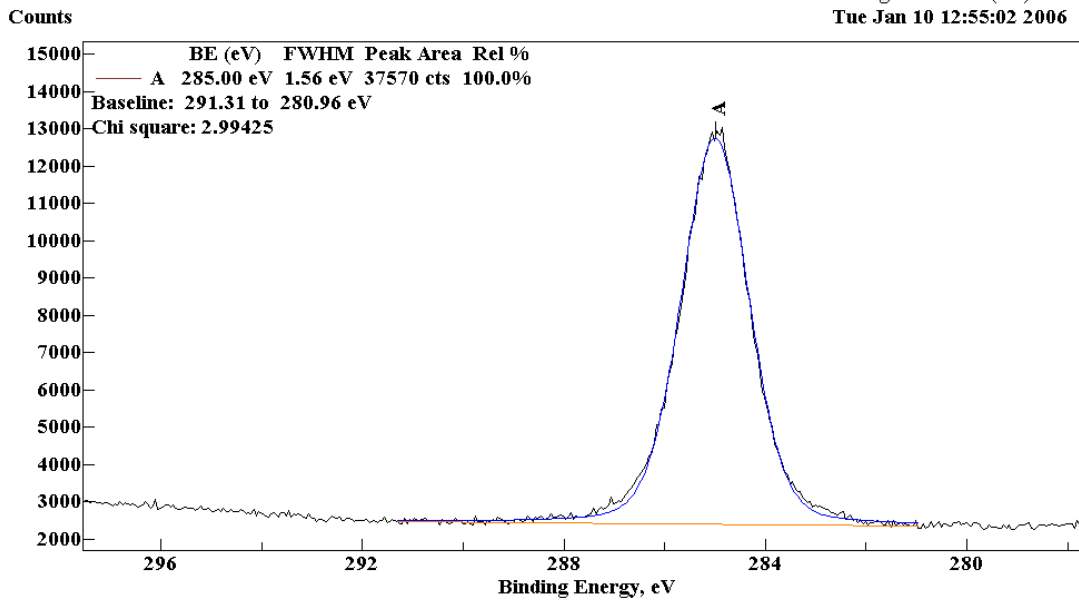
Figure 3.19. XPS testing results for specimen P506b

Min: 0   Max: 10471

Curve Fit Summary
Goodness of Fit: 2.61   Iterations: 10   TWB1a C 1s

#	CommentArea	Area%	Position	Intensity	FWHM	% Gauss
1	16459	90.6%	287.53	10322	1.43	90.00%
2	1166	6.4%	288.93	556	1.88	90.00%
3	541	3.0%	285.91	382	1.27	90.00%

N(E)

Binding Energy (eV)
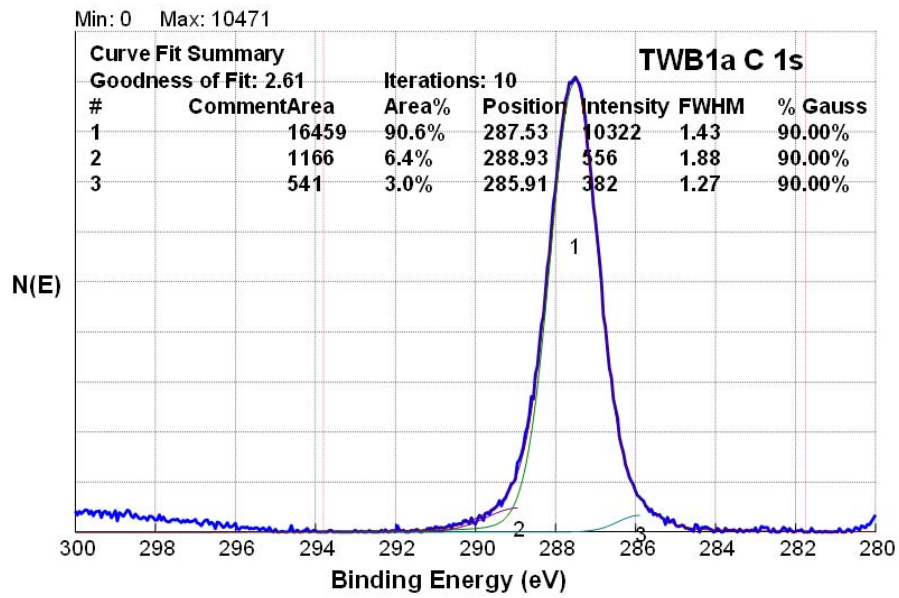
Figure 3.20. XPS testing results for specimen TWB1a

Min: -8   Max: 9790

Curve Fit Summary
Goodness of Fit: 2.74   Iterations: 9   TWB1b C 1s

#	CommentArea	Area%	Position	Intensity	FWHM	% Gauss
1	15998	94.5%	287.68	9694	1.48	90.00%
2	634	3.7%	289.39	256	2.22	90.00%
3	305	1.8%	285.87	244	1.12	90.00%

N(E)

Binding Energy (eV)
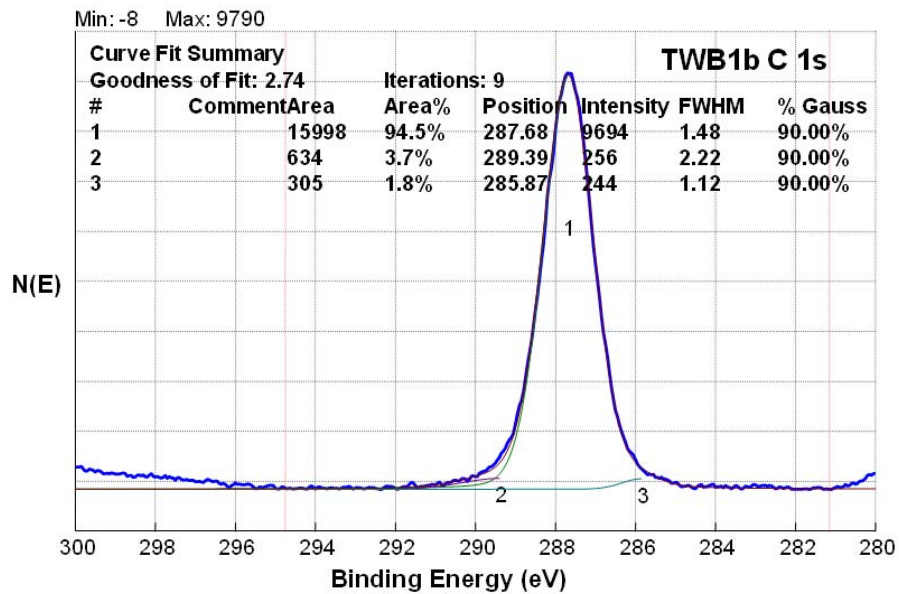
Figure 3.21. XPS testing results for specimen TWB1b

31

Min: 0   Max: 6312

Curve Fit Summary
Goodness of Fit: 2.47   Iterations: 1   BC03-0004a C 1s
Comment Area   Area%   Position   Intensity FWHM   % Gauss
1   10993   100.0%   287.34   6219   1.55   85.00%

N(E)

Binding Energy (eV)
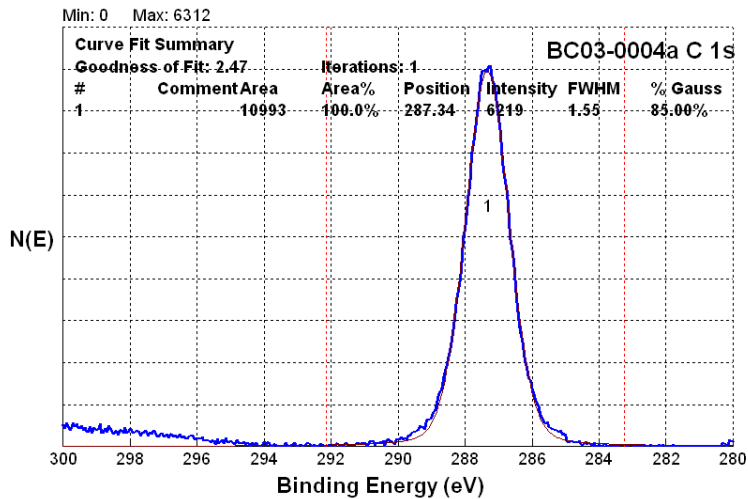
Figure 3.22. XPS testing results for specimen BC03-0004a

Min: 0   Max: 7144

Curve Fit Summary
Goodness of Fit: 2.82   Iterations: 2   BC03-0004b C 1s
Comment Area   Area%   Position Intensity FWHM   % Gauss
1   12004   100.0%   288.81   7063   1.49   85.00%

N(E)

Binding Energy (eV)
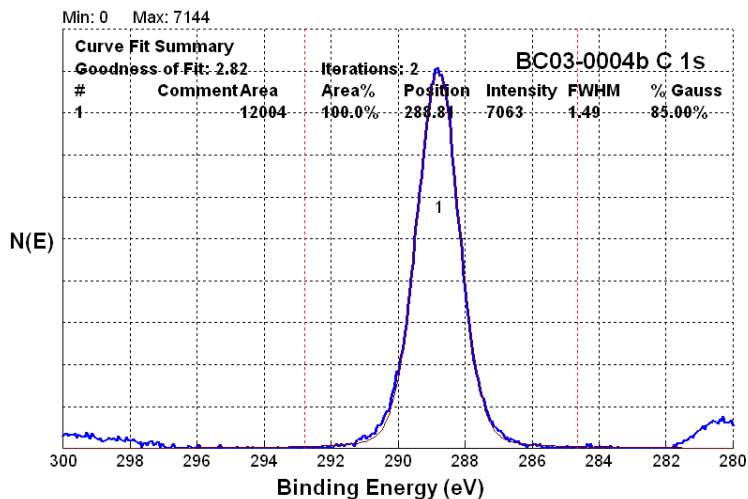
Figure 3.23. XPS testing results for specimen BC03-0004b

The results indicate that the XPS test is capable of detecting the presence of oxidized carbon functional groups. However, very little C=O functional groups (ketones) were detected in both the mixture and the binder samples tested, regardless of the age of the samples. Furthermore, the amounts of ketones varied significantly between the replicates of the same sample, indicating poor repeatability of the test.

Table 3.4 presents a summary of the carbon peak results for all the specimens tested including mixes and binders; according to Petersen *et al.* [15] larger percentages of single and double oxygen bonds suggest the presence of oxidation products.

The results from the MnROAD mixture samples show that very little oxidation was detected from the tests. The surface samples from Cell 35 were expected to have a high percentage of ketones but only one out of the two replicates showed aging. The bottom samples from Cell 35 were also expected to have aging, but again only one out of the two replicates had ketones detected. The mixture samples from the Theodore Wirth golf course parking lot did not show any C=O content, but did show some graphitic functional groups.

None of the binders tested showed any presence of ketones, even though significant amounts were expected, especially in the shingle and parking lot extracted binders. The parking lot binder results are similar to the corresponding mix results. Both replicates showed a small percentage of graphitic functional groups; their presence could not be explained.

Table 3.4. Relative percentage of the functional groups of carbon from XPS testing

Specimen ID	% C-C/C-H Carbon Chain	% C-O Single O bond	% C=O Double O Bond	Relative CO (%) Total of single and double O bonds
T-1	93.2	3.1	3.6	6.7
T-2	93.3	6.7	0	6.7
C-1	96.2	3.8	0	3.8
B-1	96.8	3.2	0	3.2
B-2	92.9	4.8	2.4	7.2
33	86.3	8.6	5.0	13.6
34	95.2	4.8	0	4.8
PTW-1 Ua	100	0	0	0
PTW-1 Ra	97.6	2.4	0	2.4
PTW-1 Pa	89.1*	0*	0*	0*
PTW-1 Pb	96.9*	0*	0*	0*
BI-7 Pa	98.8	1.2	0	1.2
R506a	100	0	0	0
R506b	100	0	0	0
P506a	96.7	3.3	0	0
P506b	100	0	0	0
TWM1a	93.2	3.4	0	3.4
TWM1b	88.8	4.5	0	4.5
TWB1a	90.6	6.4	0	6.4
TWB1b	94.5	3.7	0	3.7
BC03-0004 a	100	0	0	0
BC03-0004b	100	0	0	0

*Samples may have been damaged, therefore results may be inaccurate

The XPS results for both mixes and binders can be summarized as follows:

1. MnROAD mixes:
   - Cell 35 surface T-1 specimen had 3.1% C=O and T-2 specimen had no C=O
   - Cell 35 center C-1 specimen had no C=O
   - Cell 35 bottom B-2 specimen had 2.4% C=O and B-1 specimen had no C=O
   - Cell 33 surface specimen had 5.0% C=O
   - Cell 34 surface specimen had no C=O
2. TWM1 mix:
   - The two replicates showed no C=O
3. Highway 17 binder (PTW-1):
   - The unaged (Ua) specimen showed no C=O
   - The RTFOT (Ra) specimen showed no C=O
   - The PAV specimen appeared to be damaged
4. MnROAD binder (BI-7):
   - The PAV specimen showed no C=O
5. 506 Binders:
   - The R506 specimens showed no C=O
   - The P506 replicates showed no C=O
6. BC03-0004 shingle binder:
   - The two replicates showed no C=O
7. TWB1 binder:
   - The two replicates showed no C=O

These results appear to suggest that the XPS test may not be a useful procedure for investigating aging products in asphalt binders and mixtures, which contradicts the research results presented elsewhere.

Detection of Microcracks in the Surface Layers of Asphalt Pavements

The main objective of this study is to identify factors that can be used to determine the optimum time of surface treatment applications. To date, this time was determined exclusively based on empirical observations and on standard pavement management practice directly related to funding constraints. The two key mechanisms by which the surface treatments protect the surface of the pavement are: protection against further aging of the existing surface (some rejuvenation may take place as well) and sealing the microcracked surface and therefore preventing the evolution of microcracks into visible cracks that can significantly affect ride quality and pavement performance in general. The next sections describe two methods that have the potential to be used to detect microcracks on the pavement surface. However, one should be aware of two specific features of asphalt pavements that significantly increase the level of

difficulty of detecting microcracks: the surface texture and the ability of asphalt pavements to heal at warmer temperature, which may indicate that the best time to detect microcracks is in late fall and winter.

Electron Microprobe

Electron microprobe testing can be used to establish the chemical composition of small areas of specimens. Electron microprobe is one of several particle-beam techniques available in industry. In the electron microprobe analysis, a beam of accelerated electrons are sent to the surface of the specimen. This electron beam is focused on the surface of a specimen by means of a series of electromagnetic lenses. X-rays are produced within a small volume of the specimen due to these energetic electrons. Each element in nature emits a specific set of X-rays. Thus, detection of almost all elements (with the exception of hydrogen, helium, and lithium) with their corresponding concentration is possible by means of the electron microprobe analysis [20]. This technique has high spatial resolution and sensitivity. One test can be run in a reasonably short period of time (one or two minutes). The time consuming part of the test is the specimen preparation as the specimen needs to be polished and carbon coated to provide a conductive surface [21].

The electron microprobe can also work as a scanning electron microscope (SEM) to obtain highly magnified images of the surface of the specimen [21]. This function of the electron microprobe was used in this study to evaluate the microcracks present in the surface of the pavement. The physical process that occurs in the electron microprobe can be summarized as follows: a beam of high energy electrons bombards the specimen to enable electron transitions; then, characteristic X-rays are identified using their unique wavelengths (or energy) to identify the composition of the specimen [21].

Electron microprobes contain an electron optical column (see Figure 3.24) which produces the electron beam and controls its diameter when focused on the specimen [21]. At the top is an electron gun comprised of a tungsten wire bent into a v-shape and heated with an electric current to about 2700 K which frees electrons from the apex of the wire [21]. As the electrons are accelerated by an electrical potential of 5 to 30 kV, a pair of electromagnetic lenses focuses the electrons like a convergent lens focuses light. One lens restricts the number of electrons in the beam current and the other focuses the beam on the sample and controls its diameter (*e.g.* 0.1 microns or less) [21].
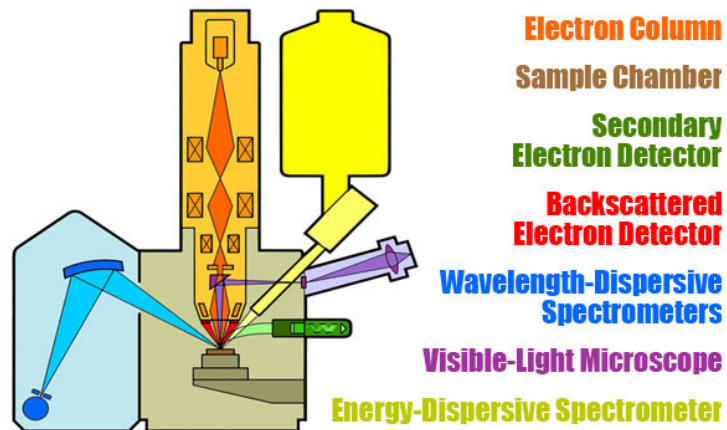
Figure 3.24. Electron microprobe components [21]

Electron microprobe testing is considered as a *spot* analytical technique meaning that compositional information is collected only from a small volume (between one and nine cubic micrometers). Thus, highly localized compositional data is obtained when using this technique [21].

X-rays behave as both particle and wave and thus can be described in terms of their energies or wavelengths. Electron microprobe is equipped with an energy-dispersive (ED) spectrometer (see Figure 3.24) which electronically orders X-rays with respect to their energies [21]. Furthermore, it has several wavelength-dispersive (WD) spectrometers (see Figure 3.24) which use diffraction to sort X-rays with respect to their wavelengths [21]. The X-rays in WD spectrometers are dispersed with respect to their wavelengths by a crystal. This crystal reflects just one wavelength of the incoming X-rays toward the detector [21]. Thus, the WD spectrometer is tuned to a single wavelength at a time which results in more accurate measurements. On the other hand, the ED spectrometer can quickly collect the full spectrum. The major elements and their relative concentrations in the specimen can be obtained with this spectrum. Although, the ED spectrometer works better for simple qualitative analyses, it produces relatively large error [21].

Using electron microprobe as SEM for imaging

There are two methods used in the electron microprobe to acquire images:

- measuring secondary electrons
- measuring backscattered electrons

Secondary electrons are electrons that are liberated from its energy level by a beam electron. They are former orbital electrons that once freed; they leave a vacancy into which other electrons from a higher energy level fall as they radiate a characteristic X-ray. Secondary electrons have low energies and only the ones created within a few nanometers of the specimen surface can escape. Thus, secondary electrons are very sensitive to surface topography and can be used to obtained images of the specimen [21].

Backscattered electrons are beam electrons that have been scattered back toward the surface of the specimen. These electrons are not part of the specimen unlike the secondary electrons. Backscattered electrons have energies greater than secondary electrons making them

less sensitive to topography. The backscattered electrons are influenced by the atomic numbers of the elements in the surface of the specimen [21]. For example, in heavier elements the backscattered electron retains much of its original energy. On the other hand, for lighter elements, the backscattered electron loses more energy before it re-emerges to the detector [21]. This effect is used to produce images called: "*backscattered electron images*". The images obtained using this method exhibit bright area where the mean atomic number is high and dark areas where the mean atomic number is low [21]. It is important to notice that the electron microprobe has detection limits which differ for each element and are generally affected by the overall composition of the specimen and the analytical conditions.

Electron microprobe (SEM) Test Procedure

For this study backscattered electrons imaging was used to investigate microcracks in the surface of the pavement. The following procedure was followed to run one test in the Electron microprobe:

1. Cut a thin (5 mm) asphalt concrete specimen with the following dimensions: 27 mm wide by 46 mm long. The maximum size of the specimen is 100 x 100 x 50 mm but the latter dimensions are recommended.

2. Polish the surface of the specimen down to 1-micron.

3. Carbon-coat the surface to provide a conductive surface.

4. Perform imaging of the surface using both secondary-electron and backscattered-electron mapping.

Electron microprobe (SEM) Results

Three tests were run on one laboratory prepared specimen and two field samples. The laboratory prepared specimen was used as a control sample and to study the distribution of microcracks for a new asphalt concrete pavement. The two field specimens were used to study the differences between samples coming from the wheel path and between the wheel paths. The field specimens were cored from TH 251. Specimen TH 251 6W2 was recovered from the wheel path and specimen TH 251 6B1 from between the wheel paths of a section that received surface treatment in 2002.

The left photo in Figure 3.25 shows the image obtained using SEM for the laboratory prepared specimen. From this figure no visible cracks are observed. When the image is further magnified some microcracks appear (right photo).
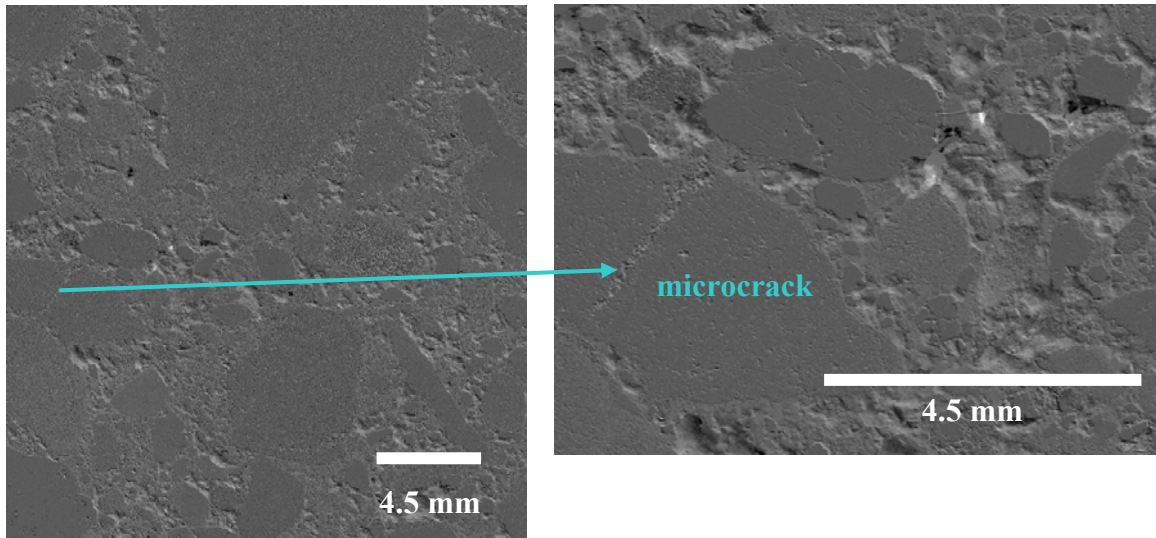
Figure 3.25. Electron microprobe images for laboratory prepared specimen

Figures 3.26 and 3.27 represent images of specimen TH 251 6B1 (between the wheel paths). In Figure 3.26 a macrocrack crossing one of the aggregates can be seen. Further magnification of this image is presented in Figure 3.27 and the presence of some more microcracks becomes visible.
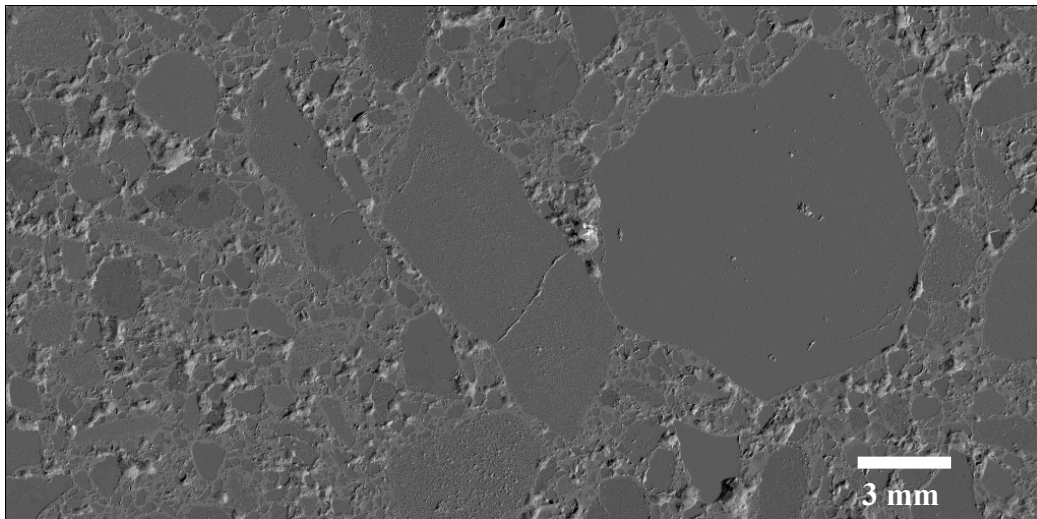
Figure 3.26. Electron microprobe image for TH 251 6B1 sample
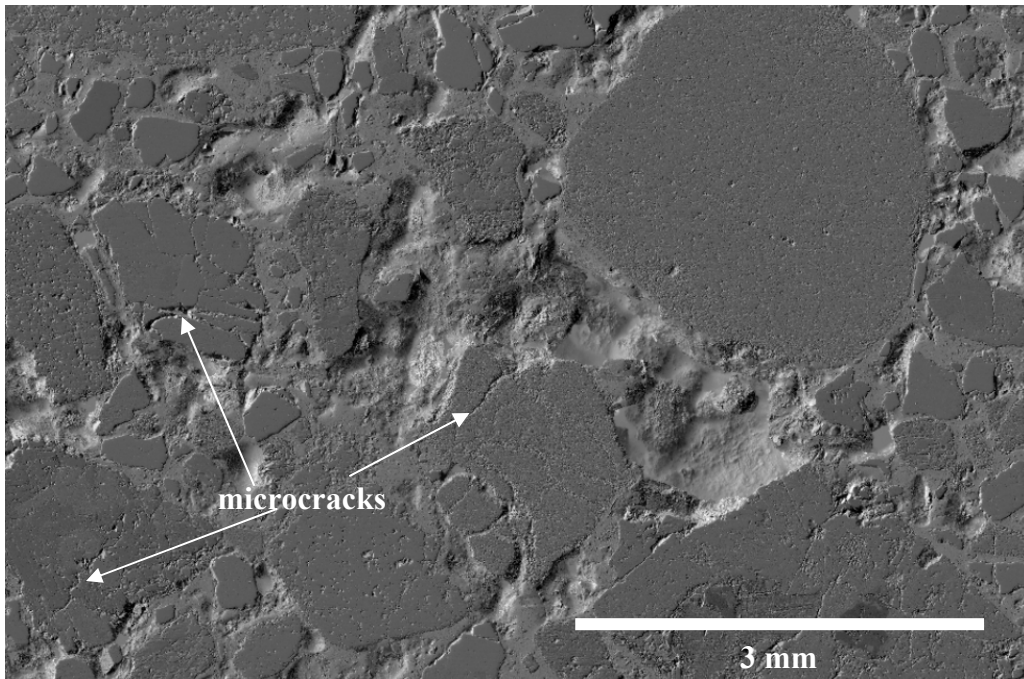
Figure 3.27. Magnified view of the image for TH 251 6B1 sample

Figures 3.28 and 3.29 represent images of sample TH 251 6W2 (in the wheel path). No visible cracks are observed in Figure 3.28; however, if this is further magnified, then some microcraks become visible (Figure 3.29).
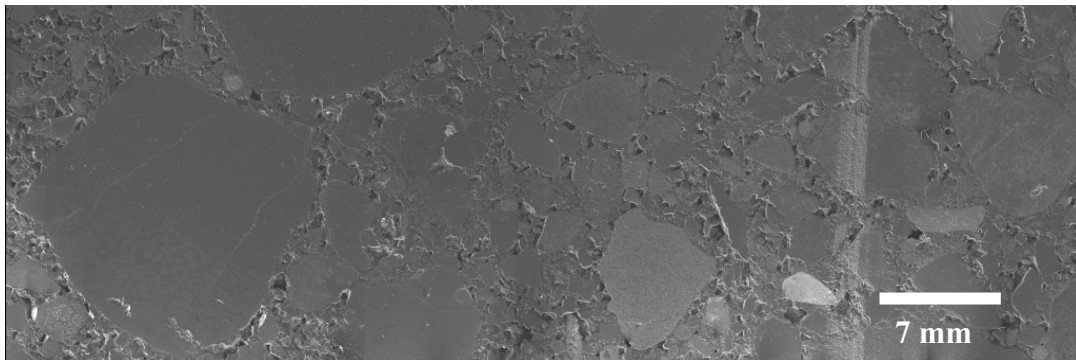
Figure 3.28. Electron microprobe image for TH 251 6W2 sample
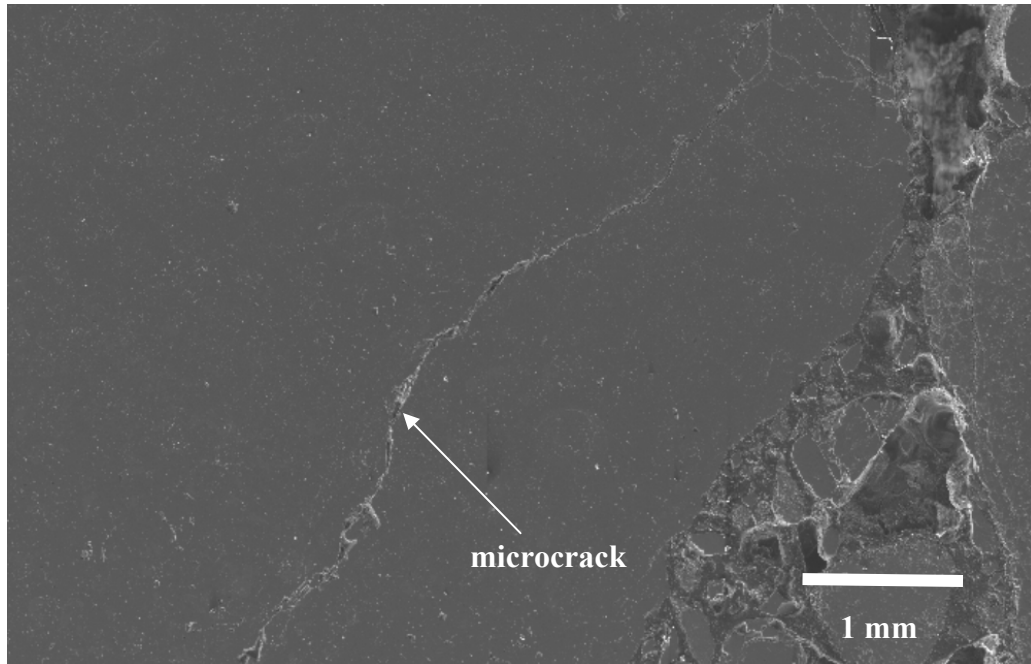
Figure 3.29. Magnified view of the image for TH 251 6W2 sample

No significant differences can be observed between the sample coming from the wheel path and the one from between the wheel path. Although some differences between the field samples (subjected to long term aging and traffic) and the laboratory prepared specimen (subjected to short term aging) can be observed from the SEM images, it is difficult to establish which of the three surfaces are in the best and the worst condition. However, one important similarity is noticed in all scans: the cracks observed are on the aggregate surface and no cracks were observed in the asphalt mastic.

Based on the images presented in Figures 3.25-3.29 it can be conclude that the application of the SEM technology to assess the surface condition of the pavement is difficult due to the localized nature of the test. Specimen preparation can be expensive and time consuming and the specimen tested might not be representative of what is observed in the field. Furthermore, the fact that only cracks on the surface of the aggregates were detected seems to indicate that microcracks are not present at room temperature due to healing. Most likely, there is a much better chance of detecting microcracks in pavements during the very cold season; in this case, specimens cut from the pavement should be stored at low temperatures and immediately tested at the same low temperatures to prevent any microcrack closing due to healing effects.

Another important conclusion is that microcracks exist in the aggregates used in asphalt pavements, most likely due to either the crushing process or the field compaction, which can affect the cracking resistance of the mixtures, in particular at low and intermediate temperatures.

Investigation of microcracks inspection using fluorescent penetrant

The previous method used sophisticated instruments and provided information only at a localized level. Due to the difficulties encountered in performing these tests and to the less than conclusive results, it was decided to pursue a different avenue that could result in a simpler investigative method that could also provide a global characterization of the pavement. Based on discussions with Tom Wood, the TL of the project, and Professor Heinz Stefan, it was decided to perform a preliminary laboratory investigation on the feasibility of using fluorescent dyes to detect cracks.

One of the most common applications of fluorescence is in environmental and hydrology engineering testing, where a water soluble dye is added to the rainwater to help in the location of any water leaks [22]. Fluorescent dyes absorb light at specific wavelengths and in return emit fluorescence energy at a higher wavelength [23]. Each dye has a distinct emission spectrum, which can be used for multicolor analysis. The emitted fluorescence energy of the dye can be detected be means of a UV lamp (also called Blacklights, see Figure 3.30) [23]. UV lamps are used to provide long wave ultraviolet light (wavelength ≈ 360 nm). These lamps are built the same way as conventional fluorescent lamps but the glass tube is coated with a phosphor that converts short wave ultraviolet light within the tube to long wave ultraviolet light rather than to visible light.

Figure 3.30. 4-watt UV-lamp

The method of using a liquid fluorescent penetrant for cracks and defects inspection has been long used in several industries: aerospace, automotive, welding, pipelines, steel mills, etc [23, 24 and 25]. This method presents a number of advantages over other techniques as discussed in [26]. In that study three methods, light-optical microscopy, fluorescent microscopy after penetration with a fluorescent liquid, and scanning electron microscopy (SEM), were evaluated with respect to their efficiency to detect microscopic surface cracks of clinical relevance in dental ceramic materials. It was found that microscopic cracks of critical sizes can be detected using the fluorescent penetrant method, which were not detectable by light-optical microscopy and SEM.

However, the materials tested in these applications were metals or ceramics with smooth non porous surface unlike asphalt concrete pavements. In spite of this less ideal surface of asphalt pavements it was decided to perform preliminary tests on two different asphalt concrete specimens with smooth and rough surface, respectively. A water soluble fluorescent dye was

sprayed to the surface of each specimen. After waiting for few seconds to let the solution flow trough the cracks, the surface of the specimen was cleaned with a towel and inspected with the UV-lamp. Figure 3.31 shows the results for the specimen with the smooth uniform surface with one small crack present
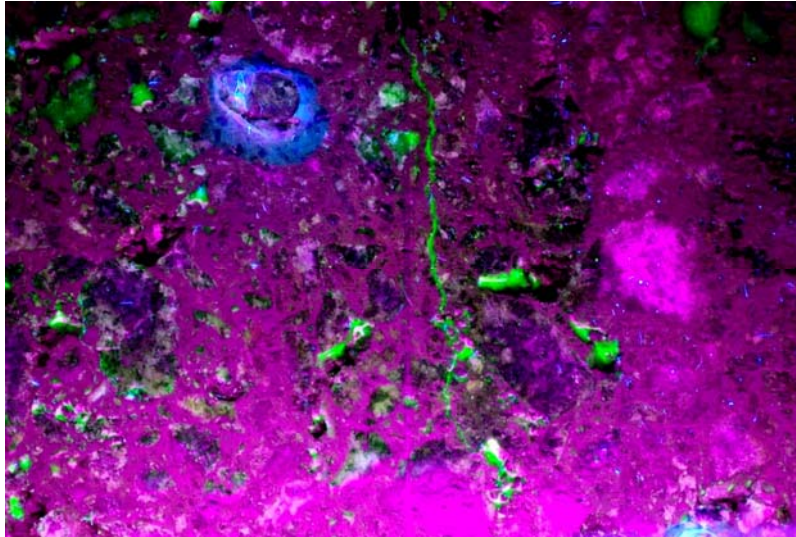
Figure 3.31. Specimen with smooth surface

For the specimen with the porous surface it was very difficult to detect any type of cracks since the microtexture of the surface masked the presence of cracks, as seen in Figure 3.32.
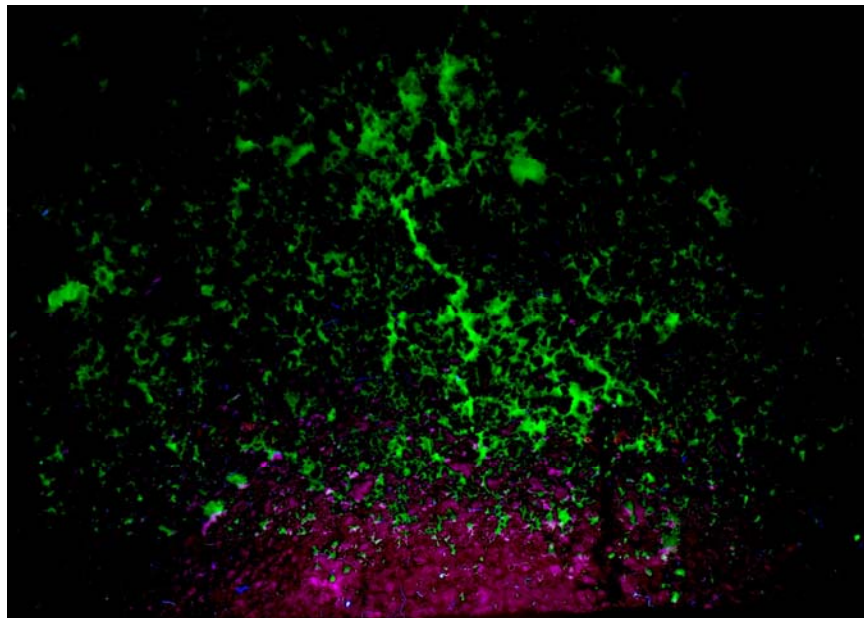
Figure 3.32. Specimen with porous surface

Due to time constraints no further experiments were performed. However, the research team, based also on discussions with Dr. Koichi Takamura from BASF and Dr. Ray Robertson from WRI, suggests that further work needs to performed in this area taking into consideration the following ideas for improvement of the detection capabilities of this method for microcracks present on the surface of asphalt pavements:

- Mix penetrant with a surfactant to enhance its ability to penetrate microcracks. Suggested surfactants range from simply adding about 1% dish washing soap to using a 1% non-ionic surfactant solution of EO (ethylene oxide) > 20 with low critical micelle concentration.

- Use a powerful UV lamp and develop better surface preparation and cleaning techniques

- Perform field tests (MnROAD) at night time; in particular it would be interesting to perform measurements on the exact same area of a pavement at different temperature regimes to determine if the presence of microcracks is affected by the season in which the measurements are performed.

Spectral analysis of asphalt pavement surface

In the past years, advanced detection systems used primarily in atmospheric and environmental applications, have been used as potential investigative tools in other areas, including transportation. Studies performed by several researchers [27, 28, 29 and 30] have shown that the principles of imaging spectrometry can be used to estimate the physical structure and chemical composition of the surface of asphalt pavements. Thus, it may become possible to use spectral characteristics of asphalt pavements to provide useful information regarding aging and deterioration of the road.

Imaging spectrometers measure the electromagnetic radiation reflected or emitted from surfaces (*e.g.* asphalt pavement) or the atmosphere [27]. The intensity of the radiation reflected by the surface at different wavelengths depends on the following factors [27]:

- Source of radiation (*e.g.* the sun)
- Physical structure of the surface
- Chemical constituents in the surface
- How radiance is modified by the atmosphere

These factors can be studied using imaging spectrometers by sampling a large number of wavelengths. Usually, imaging spectrometers measure reflected and emitted radiation with wavelengths ranging from the ultra-violet (UV) region to the Near- Infrared (NIR) region (covering a spectral range from 350 to 2500 nm) [27].

A common way to quantify spectral analysis values is by units of reflectance (%) [27]. Reflectance is defined as the ratio of the measured radiation coming from an object divided by the radiance reflected by a near-perfect reflector (*e.g.* pressed halon) [27]. Thus, by comparing with a reference value, spectral analysis based on reflectance is standard and removes some of the problems that affect the reflected radiation measured by the spectrometers such as illumination geometry, light source and scatter radiation effects [27].

Imaging spectrometry can be divided in two groups based on the measurement scale:

- Ground spectrometry: from ground measurements on the scale of individual materials.
- Hyperspectral remote sensing: from satellite or airplane sensors, on the scale of land cover types.

Both methods sample the earth surface in a large number of narrow spectral bands over a continuous range [27]. These measurements allow for investigations of the chemical and physical properties of the materials studied as well as surface geometry. Distinct chemical and physical characteristics of the material under investigation are reflected in different spectral characteristics [27].

Application of imaging spectrometry to asphalt pavement

Herold *et al* [29] used both ground spectrometry and hyperspectral remote sensing to study aging and deterioration of asphalt pavements. In their study, ground spectra were acquired with an Analytical Spectral Devices (ASD) Full Range spectrometer. The ASD spectrometer samples a spectral range of 350-2500 nm at a sampling interval of about 2 nm. Hyperspectral remote sensing data was obtained from the NASA-JPL's Airborne Visible/Infrared Imaging Spectrometer (AVIRIS). The AVIRIS sensor records 224 spectral bands with a bandwidth of approximately 10 nm. The spectral range for this sensor is from 350 to 2500 nm. It is important to notice that the spatial resolution for the AVIRIS is approximately 4 meters [29]. Based on their measurements, the authors developed a comprehensive database of spectral libraries that consist of nearly 6000 individual reflectance spectra representing almost 147 materials and surface types. The spectral libraries were used to analyze the spectral properties of pavement surfaces of different conditions.

The spectra presented by Herold *et al* [29] show that the reflectance increases towards longer wavelengths with a reflectance peak in the shortwave infrared range (SWIR). Concrete and gravel roads have the highest reflectance and new asphalt pavements including parking lots have the lowest reflectance over the entire spectral range. Different material spectra contain absorption features in the shortwave infrared range (SWIR) that can be related to their mineral composition. An example that shows the spectral signature of different asphalt surface conditions is presented in Figure 3.33 based on ASD measurements.
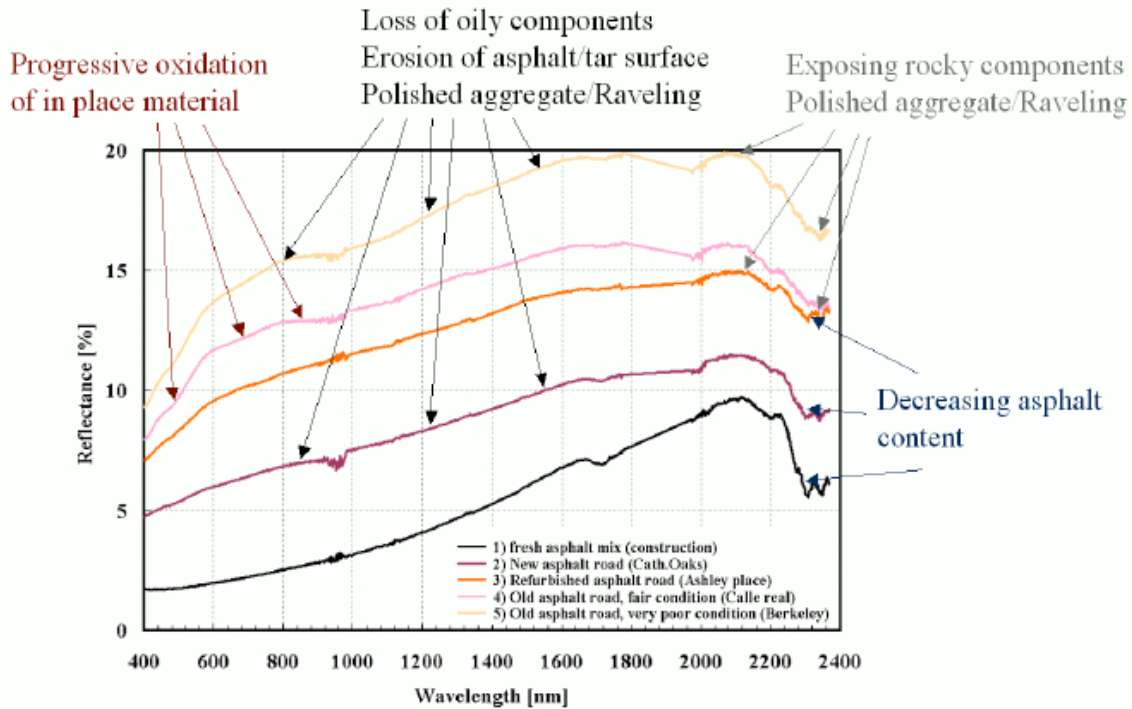
Figure 3.33. Spectra of different asphalt pavements taken from [29].

The following trends can be observed:

- A general increase in brightness when the asphalt pavement is older.
- The development of specific absorption features that relate to the decreasing asphalt content in the aggregate.
- The oxidation of in place material shown as an increase in iron absorption at approximately 520 nm, 670 nm and 870 nm.
- The degradation from polished aggregates and raveling is also detectable.

The authors indicate that using remote sensing data instead of ground measurements usually decreases the spectral detail. Thus, if a detailed study of surface characteristics is required then the ground spectrometry (ASD) is recommended. AVIRIS measurements are generally noisy due to system limitations and atmospheric interference, especially for low reflectance targets like asphalt surfaces [29]. Moreover, using 4 meters as spatial resolution does not provide the information needed to spectrally represent asphalt surfaces. However, the AVIRIS spectra can indicate some distinct differences among pavements with different age and conditions in the visible and short-wave infrared ranges.

The following observations can be made after studying the spectra library and the field observations presented by Herold *et al* [29]:

- An aging pavement surface gets brighter with decreasing hydrocarbon absorptions. As the pavement ages and deteriorates its reflectance increases in all parts of the spectrum.

- Structural distresses like cracking cause less reflectance with increasing hydrocarbon features. This fact indicates limitation in the spectral analysis to asses asphalt pavements conditions.
- The presence of raveling increases the brightness of the surface due to the increasing mineral reflectance and less prominent hydrocarbon absorptions.
- The spectral effects of asphalt aging are more sensitive to short-term aging than long-term aging.
- Asphalt aging and cracking have opposite spectral effects.

More detailed information about the spectral analysis methods and accuracy assessment can be found in [30].

Conclusions and Recommendations

In this chapter a number of methods have been investigated to detect the presence of asphalt aging (oxidation) products directly from asphalt mixtures and to detect the presence of microcracks at the surface of asphalt pavements. Based on the research performed the following conclusions can be drawn:
- The results performed on both asphalt binder and asphalt mixture specimens suggest that the XPS procedure used in this study does not provide useful information with respect to asphalt oxidative aging due to poor repeatability and inconsistencies of the results.
- Scanning electron microscope (SEM) imaging technology has limited application to pavement surface characterization due to the fact that the specimen size is very small and is not representative of large areas of pavement surface. However, the results indicated the presence of microcracks on the surface of the aggregates but not in the asphalt mastic, which may indicate that at room temperature and higher microcracks heal.
- Preliminary evaluation of detecting cracks with fluorescent dyes indicates that there is potential in using this technology to detect microcracks on the surface of asphalt pavements.

The following recommendations are made for future research:
- The results do not warrant further use of normal XPS for aging studies. It is possible that newer versions of XPS type instruments, such as ion guns and Auger, can provide better results.
- The complexity of running SEM tests and the limited value of the results as part of routine asphalt pavement maintenance activities do not warrant the use of SEM.
- It is suggested that the method to detect microcracks using a fluorescent penetrant is further investigated using more powerful UV lamps and surfactants that allow the fluorescent solution to better penetrate into microcracks.
- It is also suggested that the use of Imaging spectrometry, especially ground spectrometry (ASD), to detect aging and deterioration of asphalt pavement surfaces is further investigated.

CHAPTER 4

MECHANICAL CHARACTERIZATION

Introduction

Mechanical characterization of field samples described in Chapter 2 using SCB (Semi-Circular Bending test), BBR (Bending Beam Rheometer) for asphalt mixtures and DSR (Dynamic Shear Rheometer), DTT (Direct Tension Test), BBR and FTIR (Fourier Transform Infrared Spectroscopy) for asphalt binders extracted from the mixtures is presented in the following sections.

Binder Testing

Bending Beam Rheometer (BBR)

The bending beam rheometer (BBR) testing was performed on a Cannon thermoelectric rheometer, according to AASHTO T 313-05 standard [31]. The BBR is used to perform low-temperature creep tests on beams of asphalt binders conditioned at the desired temperature. Based on the correspondence principle and the elastic solution for a simply supported beam, the creep compliance is obtained. Usually, BBR results are reported in the form of a plot of the inverse of the creep compliance (*i.e.* stiffness, *S*) versus time. For this research, the stiffness and the *m*-value (*i.e.* the slope of stiffness vs. time curve in a log-log scale) at 60 seconds are used to study the effect of aging and the surface treatment type on the mechanical response of asphalt binders.

The binders used for BBR testing were extracted from the specimens tested in Semi-Circular Bending (SCB). Specimens were sent to MnDOT chemical laboratory for extraction after theoretical maximum specific gravity (G_{mm}) was determined. All specimens were extracted using toluene according to MnDOT modified AASHTO T164 method.

BBR tests were conducted at -18˚C and -24˚C for all TH 56 and TH 251 sections. Two replicates were tested for each specific condition (*e.g.* -18˚C, wheel path, and 3 in. depth). The average results for the binders from 1999 and 1995 TH 56 sections are given in Tables 4.1-4.2 and for the binders from TH 251 in Table 4.3.

Note that the column "Age before treatment" represents the number of years from the construction of the pavement until the seal coat application date. Typical log-log scale stiffness vs. time curve obtained for each section tested is presented in Figure 4.1.

Table 4.1. BBR creep stiffness @ 60sec for 1999 TH 56

Section #	Application year	Age before treatment	Temperature (°C)	Location *	Depth (in)	S (MPa)	m-value
10	-	-	-24	W	1	525	0.227
			-18			291	0.282
			-24		3	531	0.232
			-18			284	0.286
			-24	B	1	569	0.227
			-18			304	0.278
			-24		3	539	0.232
			-18			286	0.289
11	2003	4	-24	W	1	504	0.243
			-18			270	0.292
			-24		3	528	0.245
			-18			258	0.302
			-24	B	1	474	0.229
			-18			266	0.288
			-24		3	516	0.250
			-18			251	0.284
12	2002	3	-24	W	1	530	0.246
			-18			261	0.302
			-24		3	490	0.254
			-18			248	0.320
			-24	B	1	486	0.249
			-18			268	0.300
			-24		3	523	0.242
			-18			272	0.304
13	2001	2	-24	W	1	509	0.251
			-18			245	0.314
			-24		3	520	0.243
			-18			279	0.308
			-24	B	1	467	0.241
			-18			267	0.299
			-24		3	510	0.244
			-18			273	0.300
14	2000	1	-24	W	1	526	0.255
			-18			258	0.317
			-24		3	556	0.237
			-18			291	0.294
			-24	B	1	519	0.242
			-18			270	0.290
			-24		3	548	0.228
			-18			296	0.281

* W= wheel path, B= between wheel path

Table 4.2. BBR creep stiffness @ 60sec for 1995 TH 56

Section #	Application year	Age before treatment	Temperature (˚C)	Location *	Depth (in)	S (MPa)	m-value
15	2000	5	-24	W	3	556	0.240
			-18			264	0.295
			-24		1	537	0.236
			-18			284	0.294
			-24	B	3	534	0.244
			-18			278	0.307
			-24		1	542	0.232
			-18			294	0.285
16	2001	6	-24	W	3	485	0.261
			-18			281	0.405
			-24		1	505	0.237
			-18			270	0.300
			-24	B	3	534	0.246
			-18			250	0.305
			-24		1	545	0.242
			-18			269	0.292
17	2002	7	-24	W	3	486	0.255
			-18			243	0.322
			-24		1	430	0.256
			-18			223	0.310
			-24	B	3	502	0.246
			-18			263	0.308
			-24		1	465	0.252
			-18			221	0.309
18	2003	8	-24	W	3	460	0.261
			-18			249	0.325
			-24		1	482	0.245
			-18			274	0.292
			-24	B	3	476	0.235
			-18			271	0.305
			-24		1	507	0.240
			-18			269	0.282

* W= wheel path, B= between wheel path

Table 4.3. BBR creep stiffness @ 60sec for TH 251

Surface Treatment	Temperature (˚C)	Location *		S (MPa)	m-value
Control	-18	B		146	0.326
	-24			321	0.260
	-18	W		166	0.321
	-24			346	0.269
CSS-1h	-18	B		156	0.331
	-24			324	0.274
	-18	W		151	0.334
	-24			334	0.272
Reclamite	-18	B		151	0.330
	-24			319	0.286
	-18	W		161	0.328
	-24			318	0.285
Chip Seal	-18	B		146	0.333
	-24			352	0.279
	-18	W		141	0.336
	-24			387	0.274

* W= wheel path, B= between wheel path
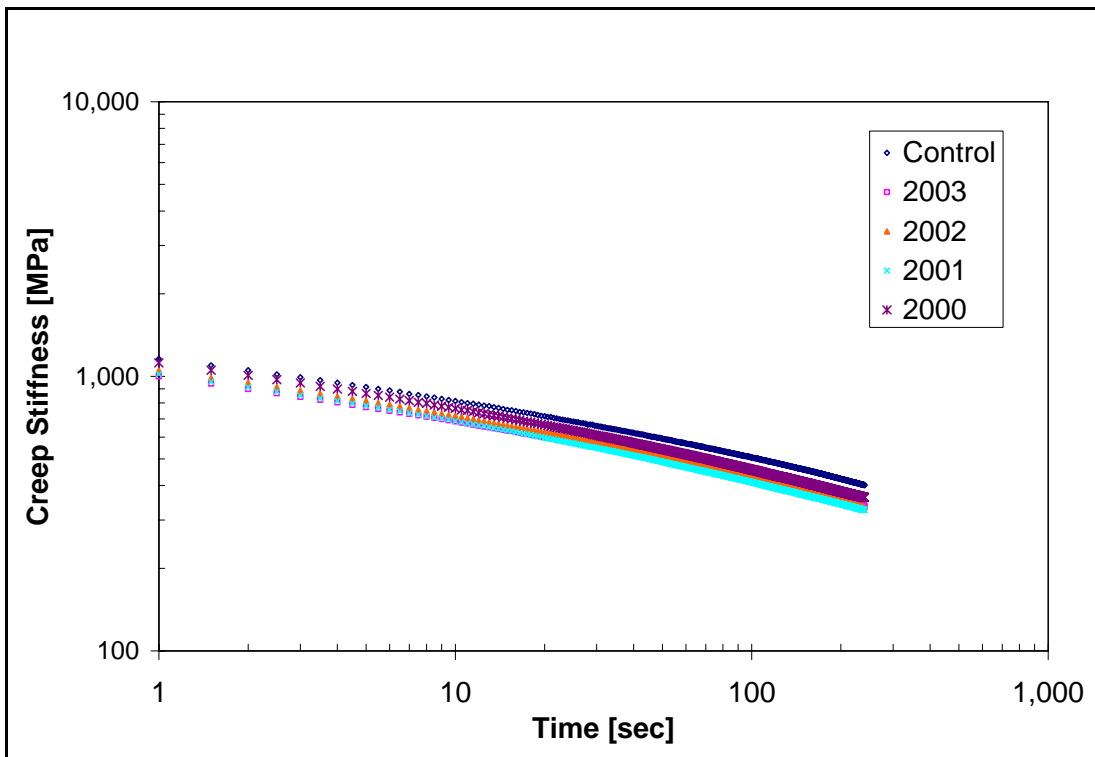
Figure 4.1. Typical plot of BBR creep stiffness vs. time for 1999-TH 56

Direct Tension Test (DTT)

Direct Tension (DT) testing was carried out on a Bohlin Direct Tension with Neslab chilling system, according to AASHTO T 314-02 [32]. The DTT is used to perform uniaxial tension tests at a constant strain rate of 3% per minute on dog-bone shaped specimens of asphalt binders. Typical stress-strain curve from direct tension testing is presented in Figure 4.2.

The asphalt binders used for DTT testing were extracted from the specimens tested in Semi-Circular Bending (SCB) using MnDOT modified AASHTO T164 method.

The average stress and strain at failure at two different temperatures: -18˚C and -24˚C are obtained from four replicates of TH 56 sections and two replicates of TH 251 sections. Tables 4.4-4.5 present the average stress and strain at failure and the coefficient of variation for the binders extracted from the 1995 and 1999 TH 56 sections. Table 4.6 shows the average DTT results for the binders from TH 251.
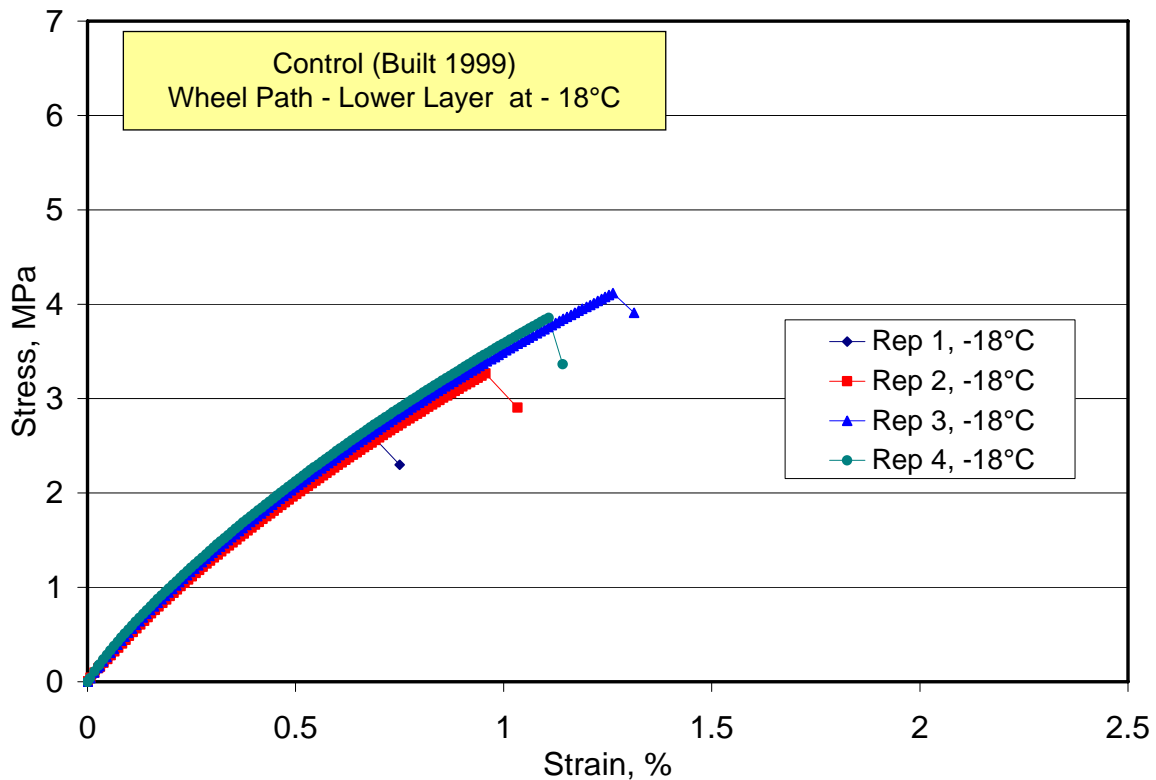
Figure 4.2. Typical plot of direct tension data for 1999-TH 56 section.

Table 4.4. DTT average results for 1995-TH 56

Section #	Application year	Age before treatment	Temp (˚C)	Location *	Depth (in)	σ_f (MPa)	CV (%)	ε_f (%)	CV (%)
15	2000	5	-24	B	1	2.43	51.1	0.38	42.6
			-18			4.12	27.0	1.25	37.9
			-24		3	5.15	32.1	0.99	51.2
			-18			3.08	22.5	0.93	30.4
			-24	W	1	3.10	28.3	0.44	36.6
			-18			3.38	13.2	0.95	17.8
			-24		3	4.62	14.6	0.65	43.0
			-18			3.08	15.4	0.89	32.2
16	2001	6	-24	B	1	2.91	55.7	0.48	63.0
			-18			4.08	27.6	1.32	35.7
			-24		3	3.42	23.8	0.53	31.5
			-18			3.89	29.2	1.29	47.3
			-24	W	1	2.33	42.1	0.32	48.9
			-18			2.71	31.7	0.89	65.7
			-24		3	3.56	29.0	0.64	38.0
			-18			3.56	36.8	1.63	48.3
17	2002	7	-24	B	1	3.86	23.6	0.69	27.8
			-18			2.89	26.2	0.91	39.6
			-24		3	2.44	39.4	0.30	32.6
			-18			3.59	36.5	1.10	48.2
			-24	W	1	3.38	40.1	0.70	37.7
			-18			3.11	8.6	0.96	11.9
			-24		3	3.86	39.3	0.65	46.9
			-18			3.23	45.1	1.11	66.4
18	2003	8	-24	B	1	2.78	42.1	0.43	47.9
			-18			3.38	17.0	1.04	19.6
			-24		3	5.50	6.5	0.98	9.2
			-18			4.43	14.7	1.63	26.0
			-24	W	1	2.37	35.2	0.35	39.3
			-18			2.57	24.9	0.79	42.5
			-24		3	3.69	30.1	0.60	38.5
			-18			2.89	32.2	0.74	12.8

* W= wheel path, B= between wheel path

Table 4.5. DTT average results for 1999-TH 56

Section #	Application year	Age before treatment	Temp (˚C)	Location *	Depth (in)	σ_f (MPa)	CV (%)	ε_f (%)	CV (%)
10	-	-	-24	B	1	5.18	11.8	0.85	13.6
			-18			1.65	48.7	0.37	58.5
			-24		3	2.93	48.3	0.46	59.4
			-18			3.86	10.4	1.16	16.1
			-24	W	1	4.81	39.5	0.96	51.9
			-18			3.43	55.1	1.05	78.7
			-24		3	3.42	58.1	0.57	65.8
			-18			3.61	19.0	1.04	23.8
11	2003	4	-24	B	1	5.51	7.5	1.03	10.1
			-18			2.88	19.8	0.87	30.0
			-24		3	3.56	54.9	0.63	67.6
			-18			3.39	23.4	1.12	31.1
			-24	W	1	1.46	46.7	0.20	52.0
			-18			3.23	38.1	1.02	49.4
			-24		3	3.83	76.8	0.75	84.9
			-18			3.59	16.0	1.29	28.5
12	2002	3	-24	B	1	4.56	14.5	0.77	20.7
			-18			2.02	64.5	0.37	81.2
			-24		3	3.71	63.8	0.64	70.7
			-18			1.14	37.3	0.19	41.0
			-24	W	1	3.83	34.1	0.65	38.7
			-18			1.52	48.7	0.25	49.9
			-24		3	4.09	17.4	0.70	19.5
			-18			1.36	44.2	0.36	87.2
13	2001	2	-24	B	1	2.81	65.9	0.47	73.1
			-18			4.63	11.3	1.74	17.7
			-24		3	2.76	22.0	0.41	22.1
			-18			3.07	57.1	0.97	68.4
			-24	W	1	4.58	42.6	0.90	55.5
			-18			2.02	72.8	0.60	90.7
			-24		3	3.26	45.3	0.53	48.5
			-18			2.43	74.3	0.72	95.9
14	2000	1	-24	B	1	2.96	35.9	0.47	43.3
			-18			3.25	46.5	1.10	60.7
			-24		3	3.64	38.0	0.57	43.9
			-18			3.15	42.1	0.97	58.1
			-24	W	1	5.38	25.9	1.14	35.3
			-18			3.62	25.5	1.14	35.9
			-24		3	4.89	6.1	0.84	10.8
			-18			3.17	49.3	0.87	61.8

* W= wheel path, B= between wheel path

Table 4.6. DTT average results for TH 251

Treatment	Temp (°C)	Location *	σ_f (MPa)	ε_f (%)
Control	-24	B	3.22	0.58
	-18		2.59	1.11
	-24	W	2.81	0.52
	-18		2.63	1.06
CSS-1h	-24	B	5.31	1.20
	-18		2.56	0.97
	-24	W	2.93	0.47
	-18		3.12	1.15
Reclamite	-24	B	3.53	0.64
	-18		3.49	1.63
	-24	W	3.64	0.63
	-18		2.83	1.06
Chip Seal	-24	B	2.74	0.65
	-18		1.67	0.73
	-24	W	2.56	0.63
	-18		2.94	1.95

* W= wheel path, B= between wheel path

Dynamic Shear Rheometer (DSR)

Dynamic shear rheometer (DSR) testing was performed on an AR 2000 rheometer from TA Instruments following the standard test method, AASHTO T 315: "Determining the Rheological Properties of Asphalt Binder using a Dynamic Shear Rheometer (DSR)" [33]. The asphalt binders used for the DSR testing were extracted from SCB specimens using the same methodology described for the BBR samples.

Frequency sweep tests were performed on asphalt binders from both trunk highways at 4°C, 10°C, 16°C, 22°C and 28°C. The tests were run on 8-mm parallel plates with a 2.0 mm gap. The samples were allowed to equilibrate for ten minutes at each temperature prior to testing.

All of the frequency sweep tests were performed from 1 to 100 rad/s. The frequencies increased in log mode with five points per decade. Due to the extensive amount of data obtained after DSR testing, only the values of the norm of the complex modulus $|G^*|$ and the phase angle δ at 10 rad/s are presented. The results for TH 56 are presented in Tables 4.7-4.8 and the results for TH 251 in Table 4.9.

Table 4.7. DSR results for 1995-TH 56 @ 10 rad/sec

Section #	Application year	Age before treatment	Location *	Depth (in)	Temp (°C)	δ (°)	IG*I (MPa)
15	2000	5	B	1	4	28.03	51.96
					10	32.87	29.12
					16	38.47	14.84
					22	44.52	6.95
					28	50.77	2.98
			B	3	4	29.73	53.90
					10	34.74	28.55
					16	40.54	13.64
					22	47.76	5.31
					28	54.23	2.07
			W	1	4	27.78	61.21
					10	32.39	34.23
					16	38.05	16.51
					22	44.17	7.33
					28	50.58	3.05
			W	3	4	28.65	49.36
					10	33.73	27.36
					16	39.44	14.14
					22	45.87	6.46
					28	52.39	2.64
16	2001	6	B	1	4	27.16	63.03
					10	31.71	35.92
					16	37.01	18.59
					22	42.86	8.79
					28	49.62	3.55
			B	3	4	29.11	57.80
					10	34.26	31.11
					16	40.01	14.92
					22	46.19	6.48
					28	52.48	2.66
			W	1	4	27.61	59.31
					10	32.48	32.40
					16	37.93	16.91
					22	43.84	8.19
					28	50.01	3.63
			W	3	4	32.4	38.68
					10	38.09	19.92
					16	44.34	9.26
					22	50.81	3.89
					28	56.94	1.54

Section #	Application year	Age before treatment	Location *	Depth (in)	Temp (˚C)	δ (°)	IG*I (MPa)
17	2002	7	B	1	4	29.5	41.06
					10	34.23	23.03
					16	39.78	11.88
					22	45.72	5.62
					28	51.55	2.54
			B	3	4	29.79	47.07
					10	34.95	24.89
					16	40.86	12.29
					22	47.18	5.60
					28	53.51	2.31
			W	1	4	29.69	47.89
					10	34.38	25.72
					16	39.93	12.65
					22	45.64	5.92
					28	51.55	2.53
			W	3	4	32.13	40.11
					10	37.62	20.64
					16	43.68	9.65
					22	49.84	4.23
					28	55.93	1.72
18	2003	8	B	1	4	26.61	55.34
					10	30.98	30.16
					16	36.06	15.96
					22	41.64	7.65
					28	47.63	3.29
			B	3	4	29.8	45.29
					10	35.19	24.00
					16	41.19	11.85
					22	47.65	5.32
					28	54.04	2.19
			W	1	4	27	66.93
					10	31.58	36.87
					16	36.82	18.89
					22	42.51	9.20
					28	48.53	4.03
			W	3	4	32.26	48.70
					10	37.79	24.43
					16	44.02	11.11
					22	50.49	4.59
					28	56.67	1.81

* W= wheel path, B= between wheel path

Table 4.8. DSR results for 1999-TH 56 @ 10 rad/sec

Section #	Application year	Age before treatment	Location *	Depth (in)	Temp (°C)	δ (°)	IG*I (MPa)
10	-	-	B	1	4	28.24	53.85
					10	33.2	30.32
					16	38.98	15.16
					22	45.22	6.87
					28	51.66	2.80
			B	3	4	28.4	52.86
					10	33.24	29.23
					16	38.87	15.00
					22	45.07	6.93
					28	52.04	2.66
			W	1	4	28.84	46.76
					10	33.73	26.27
					16	39.37	13.35
					22	45.57	6.08
					28	51.93	2.47
			W	3	4	28.83	46.55
					10	33.75	25.70
					16	39.37	13.23
					22	45.55	6.10
					28	51.89	2.50
11	2003	4	B	1	4	29.44	51.85
					10	34.5	27.70
					16	40.27	13.20
					22	46.58	5.66
					28	53.36	2.15
			B	3	4	29.55	45.51
					10	34.53	25.51
					16	40.31	12.43
					22	46.59	5.45
					28	53.01	2.24
			W	1	4	29.68	44.45
					10	34.77	23.88
					16	40.57	11.78
					22	46.84	5.28
					28	53.11	2.14
			W	3	4	30.82	42.04
					10	36.15	22.13
					16	42.17	10.58
					22	48.53	4.68
					28	54.98	1.86

Section #	Application year	Age before treatment	Location *	Depth (in)	Temp (°C)	δ (°)	IG*I (MPa)
12	2002	3	B	1	4	30.12	45.57
					10	35.26	24.53
					16	41.13	12.22
					22	47.5	5.47
					28	53.69	2.20
			B	3	4	29.7	47.55
					10	34.87	25.79
					16	40.87	12.53
					22	47.31	5.58
					28	53.69	2.28
			W	1	4	30.65	42.90
					10	35.71	23.25
					16	41.5	11.39
					22	47.77	5.01
					28	54.15	1.95
			W	3	4	31.7	48.73
					10	37.02	24.96
					16	42.97	11.26
					22	49.23	4.65
					28	55.52	1.78
13	2001	2	B	1	4	30.33	43.27
					10	35.47	22.91
					16	41.32	11.24
					22	47.63	5.01
					28	54.02	2.00
			B	3	4	29.27	55.37
					10	34.27	29.76
					16	40.01	14.45
					22	46.21	6.36
					28	52.65	2.54
			W	1	4	30.46	46.66
					10	35.75	25.28
					16	41.79	11.99
					22	48.22	5.10
					28	54.61	2.01
			W	3	4	29.92	54.86
					10	35.03	29.36
					16	40.87	14.24
					22	47.01	6.29
					28	53.36	2.51

Section #	Application year	Age before treatment	Location *	Depth (in)	Temp (˚C)	δ (°)	IG*I (MPa)
14	2000	1	B	1	4	29.43	55.46
					10	34.5	29.30
					16	40.29	13.96
					22	46.56	5.99
					28	52.9	2.44
			B	3	4	26.4	61.43
					10	30.75	35.46
					16	35.85	18.31
					22	41.63	8.53
					28	48.01	3.66
			W	1	4	30.99	46.09
					10	36.58	23.27
					16	42.74	10.71
					22	50.01	3.98
					28	56.37	1.52
			W	3	4	28.7	54.97
					10	33.78	29.45
					16	39.33	14.39
					22	45.29	6.41
					28	51.47	2.67

* W= wheel path, B= between wheel path

Table 4.9. DSR results for TH 251 @ 10 rad/sec

Treatment	Location *	Temp (°C)	δ (°)	IG*I (MPa)
Control	W	4	31.77	37.12
		10	36.66	19.70
		16	42.06	9.37
		22	47.98	3.88
		28	54.03	1.62
	B	4	32.14	31.77
		10	37.17	16.71
		16	42.74	8.20
		22	48.69	3.65
		28	54.55	1.53
CSS-1h	W	4	28.58	51.79
		10	33.2	29.36
		16	38.46	14.78
		22	44.26	6.77
		28	50.52	2.87
	B	4	29.71	42.43
		10	34.34	24.03
		16	39.67	12.31
		22	45.51	5.71
		28	51.6	2.39
Reclamite	W	4	29.33	46.97
		10	33.99	25.46
		16	39.2	12.97
		22	44.86	5.76
		28	51.02	2.41
	B	4	30.36	41.93
		10	34.58	23.86
		16	39.8	11.42
		22	45.52	4.96
		28	51.55	2.08
Chip Seal	W	4	31.39	37.87
		10	36.31	19.89
		16	41.69	9.47
		22	47.52	4.12
		28	53.54	1.69
	B	4	31.57	33.37
		10	36.39	17.65
		16	42.02	8.62
		22	47.84	3.98
		28	53.74	1.61

* W= wheel path, B= between wheel path

Fourier Transform Infrared Spectroscopy (FTIR)

Infrared spectroscopy is one of the most widespread methods used to identify and quantify amounts of known and unknown materials [34]. In infrared (vibrational) spectroscopy a sample located in the chamber of the spectrometer interrupts the path of an infrared light beam. Then, a detector measures the amount of light absorbed for the wavelengths of infrared light. The outcome of this process is a spectrum [34]. FTIR spectroscopy digitally calculates the spectrum using Fourier transform.

Samples used for FTIR testing were extracted from one of the three cores taken at each location (*e.g.* wheel path and between wheel path) from each section in both TH 56 and TH 251. Ten thin slices, with a thickness of approximately 5 mm each, were cut from the cores. The slices were cut using a saw made by Sawing Systems, model 541OB with a 600 mm blade. Sample A represents the first slice (top of the core) and sample J the last one. In the FTIR results the last three measurements of each section combine the asphalt binder coming from two or three different slices (*e.g.* sample DE combines slices D and E).

Each slice was put in a labeled bag, and delivered to MTE. The following steps were performed to run FTIR:

1. The slices were first crumbled by hand; approximately 25 grams of each thin sample were placed into 50 ml Nalgene centrifuge tubes. Then, 25 ml of THF were added to the crumbled samples and the centrifuge tubes were capped.
2. The centrifuge tubes were shaken for 10 minutes on a laboratory shaker.
3. The samples were then centrifuged at 2400 rpm for 10 minutes.
4. The solvent-binder solution was decanted off into 1oz metal tins and evaporated to dryness (no presence of THF).
5. Using a Thermo Nicolet Nexus 470 FT-IR with Omnic control software a spectrum of each sample was collected and saved in the original condition with no spectral processing. Experiment conditions were as follows:

   a. Single bounce ATR with ZnSe crystal

   b. Automatic water vapor and CO_2 suppression

   c. Background collected before each sample

   Some of the binder was scraped off the inside of the tin and smeared onto the ZnSe crystal. The crystal was cleaned with toluene and then acetone. A couple of minutes were allowed for the solvent to evaporate before collecting the next background and sample spectra.
6. Using TQAnalyist spectral analysis software the area of the carbonyl peak at 1700 (analysis peak) was calculated by rationing against the peak at 1377 (path length peak) to account for sample preparation and path length differences. The following parameters were used in the calculation method:

   a. Path length peak

      i. Baseline points: 1325 to 1400

      ii. Measured area: 1325 to 1400

      iii. Approx. peak location: 1377

   b. Analysis Peak

i. Baseline points: 1640 to 1800

ii. Measure area: 1640 to 1750

iii. Approx. peak location: 1700

7. The calculated areas were recorded. If the areas are negative there is little or no peak present and as a result baseline noise causes the spectra to pass both above and below the baseline used in step 6b. To help in evaluating and graphing the data, the lowest negative number present was set to zero and that amount was added to the rest of the calculated areas.

Path length peak results are shown in Tables 4.10-4.11 for TH 56 samples and Table 4.12 for TH 251 samples, respectively. The analysis peak results are presented in Tables 4.13-4.14 for TH 56 samples and Table 4.15 for TH 251 samples, respectively. The normalized area results are presented in Tables 4.16-4.17 and Table 4.18 for TH 56 and TH 251, respectively.

Table 4.10. FTIR path length peak for TH 56 1995 samples

Sample	Sec. 15, Appl. Year 2000		Sec. 16, Appl. Year 2001		Sec. 17, Appl. Year 2002		Sec. 18, Appl. Year 2003	
	W	B	W	B	W	B	W	B
A	0.3490	0.3906	0.3824	0.5104	0.2830	0.4193	0.4140	0.4895
B	0.4780	0.4887	0.2642	0.5164	0.1273	0.1993	0.4860	0.4880
C	0.4551	0.4290	0.4526	0.4791	0.3206	0.4810	0.4555	0.4121
DE	0.4345	0.4670	0.4690	0.3964	0.4486	0.3751	0.4429	0.3734
FG	0.4989	0.4779	0.4474	0.4222	0.4599	0.2647	0.4951	0.2431
HIJ	0.4076	0.4460	0.4645	0.3264	0.4599	0.4862	0.3214	0.3248

Table 4.11. FTIR path length peak for TH 56 1999 samples

Sample	Sec.10, Control		Sec. 11, Appl. Year 2003		Sec. 12, Appl. Year 2002		Sec. 13, Appl. Year 2001		Sec. 14, Appl. Year 2000	
	W	B	W	B	W	B	W	B	W	B
A	0.3704	0.1301	0.4818	0.3881	0.4197	0.3715	0.4763	0.2950	0.4541	0.4304
B	0.4701	0.4823	0.4617	0.1220	0.4498	0.3321	0.4471	0.4780	0.3297	0.4106
C	0.2378	0.2448	0.4829	0.4329	0.4199	0.4444	0.4719	0.0173	0.2448	0.4191
DE	0.4462	0.1740	0.3813	0.3120	0.4632	0.4713	0.3785	0.3086	0.3932	0.4199
FG	0.3973	0.2249	0.4693	0.4742	0.4883	0.4329	0.3839	0.4870	0.4075	0.2144
HIJ	0.3577	0.4038	0.45500	0.4970	0.4575	0.5035	0.4396	0.3367	0.1523	0.3421

Table 4.12. FTIR path length peak for TH 251 samples

	Control		CSS-1h		Reclamite		Chip Seal	
Sample	W	B	W	B	W	B	W	B
A	-	-	0.4371	0.4512	0.0313	0.2694	0.4872	0.4528
B	0.4619	0.2974	0.4203	0.4241	0.4319	0.4807	0.4824	0.3584
C	0.4938	0.4383	0.4735	0.4820	0.4868	0.3097	0.4974	0.3734
DE	0.3915	0.5142	0.4599	0.2667	0.3957	0.3556	0.4926	0.2663
FG	0.4900	0.3569	0.4572	0.4071	0.4700	0.4747	0.4840	0.4040
HIJ	0.4815	0.3992	0.4649	0.3396	0.4863	0.3545	0.4322	0.3479

Table 4.13. FTIR analysis peak for TH 56 1995 samples

	Sec. 15, Appl. Year 2000		Sec. 16, Appl. Year 2001		Sec. 17, Appl. Year 2002		Sec. 18, Appl. Year 2003	
Sample	W	B	W	B	W	B	W	B
A	0.0895	0.1575	0.1434	0.1421	0.0724	0.2188	0.0638	0.2593
B	0.1091	0.1266	0.1834	0.1265	0.0228	0.0591	0.2521	0.2030
C	0.0814	0.0408	0.1765	0.0117	0.0308	0.1325	0.1010	0.1435
DE	-0.0078	0.0679	0.0899	0.0373	0.0736	0.0885	0.0763	0.1151
FG	0.0629	0.0855	0.0684	0.0701	-0.0302	0.0463	0.0372	0.0613
HIJ	0.0538	0.0442	0.0587	0.0216	0.0333	0.0671	0.0188	0.1034

Table 4.14. FTIR analysis peak for TH 56 1999 samples

Sample	Sec.10, Control		Sec. 11, Appl. Year 2003		Sec. 12, Appl. Year 2002		Sec. 13, Appl. Year 2001		Sec. 14, Appl. Year 2000	
	W	B	W	B	W	B	W	B	W	B
A	0.0952	0.0331	0.1238	0.0631	0.0558	0.0981	0.0835	0.0874	0.0394	0.2651
B	0.0982	0.1501	0.0830	-0.1020	0.0816	0.1318	0.0645	0.0500	-0.1203	0.0341
C	0.0762	0.0432	0.0205	0.0229	-0.1050	0.0625	0.0709	0.0049	0.4220	0.0577
DE	0.0121	0.0280	0.0435	0.0406	0.0067	0.0466	-0.1104	0.0398	-0.1011	0.0130
FG	0.0759	0.0328	0.0402	0.0868	0.0240	0.0559	0.0076	0.0510	0.0623	0.0347
HIJ	0.0181	0.0398	0.0679	0.1840	0.0180	0.1416	0.0377	0.0659	0.0364	0.1260

Table 4.15. FTIR analysis peak for TH 251 samples

Sample	Control		CSS-1h		Reclamite		Chip Seal	
	W	B	W	B	W	B	W	B
A	-	-	0.1585	0.2459	0.0262	0.1238	0.1598	0.1823
B	0.0745	0.1090	0.1083	0.1792	0.0836	0.1420	0.0339	0.0738
C	0.1058	0.1586	0.1534	0.2013	0.1474	0.0874	0.0870	0.0552
DE	0.0744	0.1566	0.1275	0.0675	0.0844	0.0954	0.0868	0.0463
FG	0.1067	0.1231	0.0940	0.0942	0.1210	0.0886	0.0011	-0.0407
HIJ	0.0549	0.1432	0.0882	0.0671	0.1671	0.0459	0.0529	0.0354

Table 4.16. FTIR normalized area for TH 56 1995 samples

Sample	Sec. 15, Appl. Year 2000		Sec. 16, Appl. Year 2001		Sec. 17, Appl. Year 2002		Sec. 18, Appl. Year 2003	
	W	B	W	B	W	B	W	B
A	0.2564	0.4032	0.4577	0.2784	0.2558	0.5218	0.1541	0.5297
B	0.2282	0.2591	0.7641	0.2450	0.1791	0.2965	0.4010	0.4160
C	0.1789	0.0951	0.3900	0.1411	0.0961	0.2755	0.2217	0.3482
DE	0.2004	0.1454	0.1917	0.0941	0.1641	0.2359	0.1723	0.3082
FG	0.1261	0.1789	0.1529	0.1660	-0.0256	0.1749	0.0751	0.2522
HIJ	0.1320	0.0991	0.1264	0.0662	0.0724	0.1380	0.0585	0.3183

Table 4.17. FTIR normalized area for TH 56 1999 samples

Sample	Sec.10, Control		Sec. 11, Appl. Year 2003		Sec. 12, Appl. Year 2002		Sec. 13, Appl. Year 2001		Sec. 14, Appl. Year 2000	
	W	B	W	B	W	B	W	B	W	B
A	0.2570	0.2544	0.2570	0.1626	0.1330	0.2641	0.1753	0.2963	0.0868	0.6159
B	0.2089	0.3112	0.1798	0.0196	0.1814	0.1777	0.1443	0.1210	0.0027	0.0830
C	0.3204	0.1765	0.0425	0.0529	0.1770	0.1406	0.1502	0.1049	0.1769	0.1377
DE	0.0271	0.1609	0.1141	0.1301	0.0145	0.0989	0.0379	0.1290	0.0237	0.0584
FG	0.1910	0.1458	0.0857	0.2091	0.0492	0.1291	0.0198	0.1047	0.1529	0.1307
HIJ	0.0506	0.0986	0.1492	0.1537	0.0393	0.2812	0.1283	0.1957	0.2390	0.3174

Table 4.18. FTIR normalized area for TH 251 samples

Sample	Control		CSS-1h		Reclamite		Chip Seal	
	W	B	W	B	W	B	W	B
A	-	-	0.3626	0.5450	0.6136	0.4595	0.3280	0.4026
B	0.1613	0.3665	0.2577	0.4225	0.1936	0.2954	0.1811	0.2059
C	0.2143	0.3619	0.3240	0.4176	0.3028	0.2822	0.1749	0.1478
DE	0.1900	0.3046	0.2772	0.2531	0.2133	0.2683	0.1762	0.1739
FG	0.2178	0.3449	0.2056	0.2314	0.2574	0.1866	0.0300	0.1943
HIJ	0.1140	0.3587	0.1897	0.1976	0.2551	0.1295	0.1224	0.1018

Mixture Testing

Bending Beam Rheometer (BBR)

Creep tests were performed on asphalt mixture beams following *AASHTO T 313-02* standard with some modifications of the load [36].

The mixture beams were cut from the same cores from which the FTIR binder samples were recovered. The mixture beams were tested at -6˚C,-12˚C and -18˚C for samples coming from the wheel path of TH 56 sections and -12˚C and -18˚C for all the other TH 56 and TH 251 samples. For all cores, a thin slice of 10 mm thickness from the top of the core was cut and discarded to obtain a smooth surface (Please note that this top slice was used in the FTIR analysis). Then, a 16 mm slice was cut to obtain the top BBR specimens (referred to as "1 in."). A 12 mm slice was then cut at a depth of 64 mm and used to obtain the bottom specimens (referred to as "3 in."). These slices were further cut from three sides to obtain 127 mm wide irregular slice [36]. Then, each sample (1 in. and 3 in.) was cut into beams approximately 6.2 mm thick to allow testing in the BBR [36].

Four replicates were tested for each condition (*e.g.* wheel path and 1 in. depth at -18˚C) for specimens coming from both TH 56 and TH 251.

The thickness and width of all beams were measured at three locations along the length of the beam and average values were used with the measured deflections to calculate creep compliance from Bernoulli-Euler beam theory [36].

The magnitude of the loads for BBR mixture testing were established separately for each temperature in order to keep beam deflections between two limiting values: a lower limit imposed by the BBR data acquisition system equal to 30 microns and an upper limit derived from Bernoulli-Euler theory assumptions on small rotations and deflections [36]. The upper limit was chosen to be approximately 5% of the beam thickness that corresponds on average to a deflection of 0.3 mm [36]. After preliminary testing, it was found that larger loads had to be applied for lower temperature levels in order to pass the lower limit deflection [36].

The following tables show the average results for BBR mixture testing. Tables 4.19-4.20 show the stiffness and the *m*-value at 60 seconds for specimens coming from TH 56 sections and Table 4.21 for specimens coming from TH 251.

Table 4.19. BBR creep stiffness @ 60sec for 1995 TH 56

Section #	Application year	Age before treatment	Location *	Depth (in)	Temp (˚C)	S (GPa)	m-value
15	2000	5	W	1	-18	9.19	0.088
					-12	9.38	0.134
					-6	6.64	0.156
			W	3	-18	9.82	0.084
					-12	8.74	0.140
					-6	6.01	0.164
			B	1	-18	8.70	0.082
					-12	8.58	0.132
			B	3	-18	9.89	0.082
					-12	9.33	0.139
16	2001	6	W	1	-18	7.87	0.116
					-12	10.33	0.108
					-6	7.95	0.120
			W	3	-18	10.03	0.081
					-12	9.09	0.160
					-6	5.69	0.194
			B	1	-18	8.89	0.084
					-12	8.56	0.129
			B	3	-18	9.59	0.081
					-12	8.49	0.144
17	2002	7	W	1	-18	9.24	0.072
					-12	9.43	0.111
					-6	7.19	0.137
			W	3	-18	11.10	0.084
					-12	7.72	0.157
					-6	4.95	0.202
			B	1	-18	10.23	0.091
					-12	9.26	0.136
			B	3	-18	9.98	0.082
					-12	8.40	0.139
18	2003	8	W	1	-18	10.25	0.080
					-12	9.13	0.109
					-6	7.55	0.124
			W	3	-18	10.86	0.086
					-12	7.86	0.145
					-6	5.75	0.198
			B	1	-18	10.37	0.077
					-12	8.21	0.128
			B	3	-18	10.52	0.077
					-12	9.23	0.134

* W= wheel path, B= between wheel path

Table 4.20. BBR creep stiffness @ 60sec for 1999 TH 56

Section #	Application year	Age before treatment	Location *	Depth (in)	Temp (°C)	S (GPa)	m-value
10	-	-	W	1	-18	8.92	0.096
					-12	8.13	0.153
					-6	4.89	0.170
			W	3	-18	8.25	0.081
					-12	7.62	0.149
					-6	5.39	0.182
			B	1	-18	9.20	0.086
					-12	7.65	0.161
			B	3	-18	9.86	0.093
					-12	7.77	0.149
11	2003	4	W	1	-18	9.92	0.096
					-12	9.10	0.160
					-6	5.82	0.182
			W	3	-18	9.23	0.095
					-12	8.81	0.165
					-6	4.96	0.189
			B	1	-18	9.18	0.096
					-12	8.38	0.166
			B	3	-18	10.22	0.085
					-12	8.58	0.162
12	2002	3	W	1	-18	10.35	0.080
					-12	8.96	0.161
					-6	6.10	0.189
			W	3	-18	10.30	0.099
					-12	7.56	0.180
					-6	4.86	0.218
			B	1	-18	8.58	0.104
					-12	7.38	0.167
			B	3	-18	9.00	0.103
					-12	8.84	0.180
13	2001	2	W	1	-18	10.75	0.082
					-12	10.11	0.158
					-6	5.94	0.180
			W	3	-18	11.31	0.096
					-12	9.15	0.177
					-6	5.72	0.199
			B	1	-18	10.03	0.098
					-12	8.94	0.168
			B	3	-18	9.03	0.106
					-12	7.74	0.169

Section #	Application year	Age before treatment	Location *	Depth (in)	Temp (˚C)	S (GPa)	m-value
14	2000	1	W	1	-18	10.81	0.085
					-12	9.21	0.167
					-6	6.20	0.182
			W	3	-18	10.11	0.099
					-12	10.09	0.161
					-6	6.27	0.186
			B	1	-18	9.20	0.089
					-12	8.33	0.143
			B	3	-18	8.74	0.106
					-12	8.20	0.172

* W= wheel path, B= between wheel path

Table 4.21. BBR creep stiffness @ 60sec for TH 251

Surface Treatment	Temperature (˚C)	Location *	S (GPa)	m-value
Control	-18	W	10.86	0.088
	-12		9.59	0.131
	-18	B	9.91	0.090
	-12		10.38	0.131
CSS-1h	-18	W	9.50	0.099
	-12		8.66	0.144
	-18	B	10.99	0.086
	-12		10.88	0.133
Reclamite	-18	W	9.73	0.085
	-12		8.39	0.160
	-18	B	10.59	0.082
	-12		9.68	0.122
Chip Seal	-18	W	9.26	0.083
	-12		8.51	0.150
	-18	B	8.88	0.101
	-12		7.87	0.141

* W= wheel path, B= between wheel path

Semi-Circular Bending (SCB)

The semi circular bending (SCB) test was first proposed by Chong and Kurrupu [37] to measure the fracture toughness and fracture energy of rocks and other materials. The SCB specimen is a half disc with a notch that is *a*-mm long. SCB test setup is schematically shown in Figure 4.5.

Semi circular bending (SCB) test method takes advantage of the simple specimen preparation procedure and the simple loading setup shown in Figure 4.5.
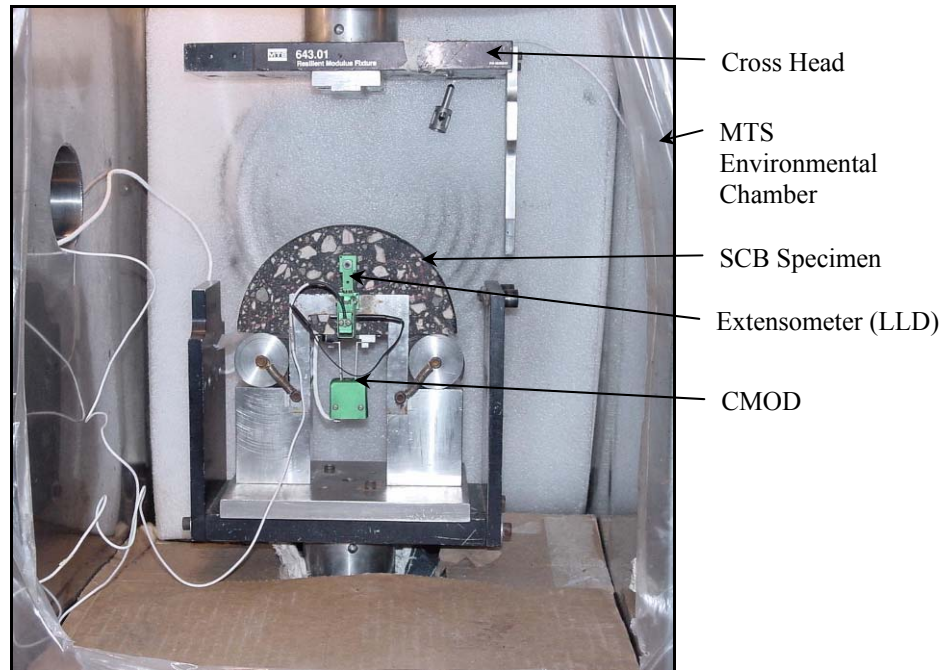
Figure 4.3. SCB test setup [39]

In SCB testing the specimen is loaded from the top and is symmetrically supported from the bottom by two rollers. The span between the rollers was 120 mm. Two displacements are measured during testing: the load line displacement (LLD) by means of a vertical mounted Epsilon extensometer with 38 mm gage length and the crack mouth opening displacement (CMOD) by means of an Epsilon clip gage with 10 mm gage length. The CMOD signal is used to maintain stability of the test in the post-peak region.

Further and detailed description of the SCB test procedure in addition to explanation on how it can be used to measure fracture properties of asphalt mixture can be found in Marasteanu *et. al* [38].

The sample preparation for SCB testing consists in the following steps [39]:

1. In order to analyze the asphalt concrete only and not the surface treatment, 10 mm of the top of each core was removed. In that way, no seal coat and surface irregularities were present in the specimens.

2. The core was then cut into three layers. Each layer was 25 mm in depth. Only the upper and lower layers were saved for the SCB test; the middle layer and remaining material was kept in storage room.

3. Each layer was split into two symmetrical semi-circular specimens. Then a 15 mm notch was cut at the axis of symmetry for each specimen.

4. Specimens were allowed to dry at least 24 hours before further preparation. The bottom thickness surface and the top radius surface were planed parallel to each other with sand paper.

5. Steel buttons were glued to the specimens. Two buttons were glued equidistantly from the notch opening on the bottom of the specimen. These buttons were used for the

CMOD gage. A third button was glued at a set distance from the crack tip. This button was used attached the LLD extensometer.

SCB testing was done at two temperatures: -18°C and -30°C. It is important to mention that the specimens were cooled for 2 hours at the test temperature before testing to remove temperature gradients within the specimen. Two replicates for each condition (*e.g.* wheel path, 1 in. depth at -18°C) were tested for sections in both TH 56 and TH 251.

In addition to SCB testing, Bulk Specific Gravity according to AASHTO T 166-05 standard [40] and Maximum Specific Gravity following AASHTO T209-05 [41] were determined. The maximum specific gravity test was performed on specimens after the completion of the SCB test. The results from these two tests were used to calculate the air void content in the samples.

A typical plot of the loading as a function of the load line displacement (LLD) for each testing temperature is shown in Figure 4.6.
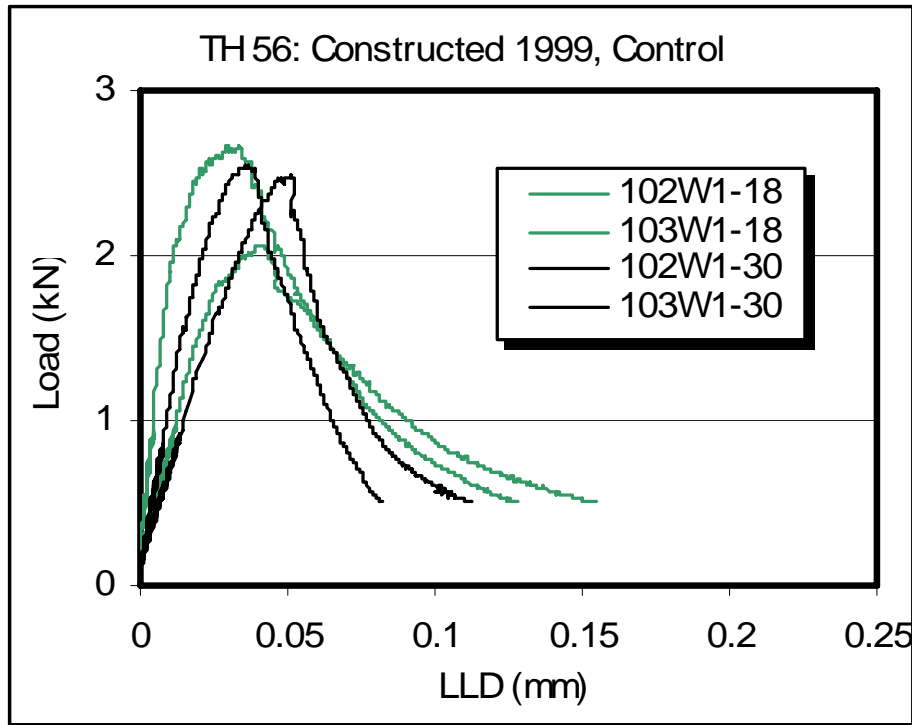
Figure 4.4. Typical plot of load vs. load line displacement from SCB testing [39]

The load and LLD data were used to calculate the fracture toughness and fracture energy. Lim *et. al* [42] show that the stress intensity factor K_I can be reasonably calculated using the following equation:

$$\frac{K_I}{\sigma_0 \sqrt{\pi a}} = Y_I(s_0/r) + \frac{\Delta s_0}{r} B \tag{5}$$

where

K_I = Mode I stress intensity factor;

$$\sigma_0 \quad = P/2rt$$

P = applied load;

r = specimen radius;

t = specimen thickness.

Y_I = the normalized stress intensity factor

$$Y_{I(s_0/r)} = C_1 + C_2(a/r) + C_3 \exp(C_4(a/r)) \tag{6}$$

C_i = constants;

a = notch length;

$$\Delta s_0/r = s_a/r - s_0/r$$

s_a/r = actual span ratio;

s_0/r = nearest span ratio analyzed in the derivation of this equation (0.80, 0.67, 0.61, 0.50)

$$B = 6.55676 + 16.64035(\tfrac{a}{r})^{2.5} + 27.97042(\tfrac{a}{r})^{6.5} + 215.0839(\tfrac{a}{r})^{16} \tag{7}$$

The fracture energy G_f was calculated according to RILEM TC 50-FMC specification [43] that has been extensively used for concrete. The work of fracture is the area under the load-LLD curve. Fracture energy (G_f) is obtained with (8) by dividing the work of fracture by the ligament area, which is the product of the ligament length and the thickness of the specimen.

Fracture energy (G_f), fracture toughness (K_{IC}), bulk specific gravity, maximum specific gravity and air void content are presented in Tables 4.22-4.23 for the specimens coming from TH 56 sections and in Table 4.24 for the specimens coming from TH 251.

Table 4.22. SCB results for TH 56 1995

Section	Location *	Depth (in)	Temperature (°C)	Gmm	Gmb	Voids (%)	K_{IC} (MPa.m$^{0.5}$)	Gf (N/m)
15, Appl. Year 2000, Age:5	B	1	-18	2.48	2.36	4.89	0.65	135.85
				2.50	2.26	9.58	0.59	202.16
		3		2.50	2.29	8.17	0.64	156.28
				2.49	2.29	8.22	0.74	172.13
	W	1		2.42	2.24	7.22	0.70	230.49
				2.48	2.25	9.55	0.71	176.43
		3		2.51	2.27	9.53	0.65	258.03
				2.53	2.27	10.46	0.77	191.42
16, Appl. Year 2001, Age:6	B	1		2.52	2.24	11.17	0.62	179.88
				2.43	2.26	7.30	0.64	181.98
		3		2.50	2.28	8.57	0.61	149.96
				2.50	2.29	8.70	0.71	189.71
	W	1		2.51	2.27	9.25	0.59	203.50
				2.50	2.38	4.87	0.62	151.29
		3		2.55	2.33	8.50	0.71	201.72
				2.52	2.32	8.09	0.64	218.25

17, Appl. Year 2002, Age:7	B	1		2.47	2.26	8.79	0.63	147.65
				2.51	2.25	10.18	0.63	186.28
		3		2.45	2.29	6.46	0.65	198.56
				2.48	2.28	7.92	0.66	183.27
	W	1		2.49	2.27	9.17	0.58	165.49
				2.49	2.28	8.11	0.63	134.23
		3		2.45	2.33	5.12	0.70	194.84
				2.48	2.33	6.24	0.76	201.80
18, Appl. Year 2003, Age:8	B	1		2.49	2.26	9.10	0.69	162.35
				2.48	2.37	4.67	0.70	148.32
		3		2.47	2.30	7.17	0.69	233.00
				2.49	2.29	7.69	0.64	146.29
	W	1		2.47	2.31	6.56	0.54	137.75
				2.49	2.27	8.74	0.56	155.06
		3		2.48	2.34	5.75	0.71	220.88
				2.39	2.34	2.13	0.67	227.47
15, Appl. Year 2000, Age:5	B	1	-30	2.48	2.36	4.89	0.72	135.09
				2.50	2.26	9.58	0.81	144.33
		3		2.50	2.29	8.17	0.80	191.40
				2.49	2.29	8.22	0.73	119.55
	W	1		2.42	2.24	7.22	0.68	207.59
				2.48	2.25	9.55	0.72	103.99
		3		2.51	2.27	9.53	0.62	107.50
				2.53	2.27	10.46	0.80	173.68
16, Appl. Year 2001, Age:6	B	1		2.52	2.24	11.17	0.61	118.66
				2.43	2.26	7.30	0.61	60.89
		3		2.50	2.28	8.57	0.74	166.73
				2.50	2.29	8.70	0.75	165.95
	W	1		2.51	2.27	9.25	0.59	96.16
				2.50	2.38	4.87	0.60	158.04
		3		2.55	2.33	8.50	0.76	142.85
				2.52	2.32	8.09	0.78	224.73
17, Appl. Year 2002, Age:7	B	1	-30	2.47	2.26	8.79	0.60	127.33
				2.51	2.25	10.18	0.66	150.51
		3		2.45	2.29	6.46	0.59	128.93
				2.48	2.28	7.92	0.79	156.94
	W	1		2.49	2.27	9.17	0.61	144.73
				2.49	2.28	8.11	0.65	105.72
		3		2.45	2.33	5.12	0.78	147.75
				2.48	2.33	6.24	0.79	87.40
18, Appl. Year 2003, Age:8	B	1	-30	2.49	2.26	9.10	0.67	120.40
				2.48	2.37	4.67	0.72	183.87
		3		2.47	2.30	7.17	0.68	140.51
				2.49	2.29	7.69	0.60	157.74
	W	1		2.47	2.31	6.56	0.62	90.45
				2.49	2.27	8.74	0.61	102.03
		3		2.48	2.34	5.75	0.77	140.54
				2.39	2.34	2.13	0.70	129.01

* W= wheel path, B= between wheel path

Table 4.23. SCB results for TH 56 1999

Section	Location *	Depth (in)	Temperature (°C)	Gmm	Gmb	Voids (%)	K_{IC} (MPa.m$^{0.5}$)	Gf (N/m)
Control	B	1		2.46	2.27	7.56	0.59	186.78
				2.44	2.28	6.56	0.55	152.00
		3		2.56	2.32	9.43	0.67	221.30
				2.50	2.30	7.89	0.66	271.56
	W	1		2.45	2.25	8.11	0.52	136.34
				2.44	2.26	7.45	0.74	171.50
		3		2.50	2.28	8.72	0.63	281.34
				2.44	2.29	6.16	0.76	251.89
11, Appl. Year 2003, Age:4	B	1	-18	2.48	2.26	9.01	0.64	261.05
				2.46	2.25	8.36	0.65	191.97
		3		2.50	2.27	9.17	0.67	258.17
				2.47	2.27	8.28	0.65	235.71
	W	1		2.46	2.30	6.62	0.55	259.19
				2.46	2.29	7.07	0.57	204.92
		3		2.45	2.28	6.95	0.76	156.57
				2.45	2.26	7.60	0.62	248.68
12, Appl. Year 2002, Age:3	B	1		2.44	2.25	7.87	0.58	182.49
				2.42	2.25	7.10	0.55	223.55
		3		2.47	2.25	9.20	0.65	274.55
				2.45	2.25	7.96	0.68	177.29
	W	1		2.42	2.33	4.02	0.75	246.45
				2.38	2.31	3.08	0.66	189.74
		3		2.48	2.29	7.58	0.72	220.40
				2.46	2.30	6.65	0.64	349.38
13, Appl. Year 2001, Age:2	B	1		2.47	2.28	7.86	0.67	203.93
				2.48	2.25	9.32	0.58	159.71
		3		2.47	2.26	8.52	0.51	112.18
				2.47	2.26	8.32	0.70	123.96
	W	1		2.47	2.34	5.01	0.60	299.88
				2.47	2.35	5.00	0.63	256.39
		3	-18	2.45	2.30	6.13	0.72	217.08
				2.48	2.30	7.23	0.71	270.73
14, Appl. Year 2000, Age:1	B	1		2.45	2.29	6.34	0.63	150.74
				2.48	2.28	7.73	0.67	289.76
		3		2.42	2.24	7.38	0.61	163.57
				2.42	2.26	6.70	0.52	137.39
	W	1		2.49	2.37	4.97	0.67	179.35
				2.43	2.35	3.09	0.69	217.06
		3		2.44	2.29	6.22	0.65	173.48
				2.37	2.27	4.20	0.65	193.54
Control	B	1	-30	2.46	2.27	7.56	0.64	125.60
				2.44	2.28	6.56	0.69	119.07
		3		2.56	2.32	9.43	0.71	154.73
				2.50	2.30	7.89	0.69	185.48
	W	1		2.45	2.25	8.11	0.67	131.90
				2.44	2.26	7.45	0.68	116.79
		3		2.50	2.28	8.72	0.72	139.31
				2.44	2.29	6.16	0.75	133.73

11, Appl. Year 2003, Age:4	B	1		2.48	2.26	9.01	0.62	185.41
				2.46	2.25	8.36	0.64	191.50
		3		2.50	2.27	9.17	0.68	135.45
				2.47	2.27	8.28	0.72	108.51
	W	1		2.46	2.30	6.62	0.69	223.68
				2.46	2.29	7.07	0.64	98.11
		3		2.45	2.28	6.95	0.74	124.29
				2.45	2.26	7.60	0.76	217.26
12, Appl. Year 2002, Age:3	B	1		2.44	2.25	7.87	0.59	129.66
				2.42	2.25	7.10	0.70	151.03
		3		2.47	2.25	9.20	0.63	116.42
				2.45	2.25	7.96	0.67	135.36
	W	1		2.42	2.33	4.02	0.69	165.71
				2.38	2.31	3.08	0.72	202.53
		3		2.48	2.29	7.58	0.70	151.63
				2.46	2.30	6.65	0.75	84.85
13, Appl. Year 2001, Age:2	B	1	-30	2.47	2.28	7.86	0.64	270.01
				2.48	2.25	9.32	0.59	172.12
		3		2.47	2.26	8.52	0.66	200.81
				2.47	2.26	8.32	0.69	181.92
	W	1		2.47	2.34	5.01	0.73	107.09
				2.47	2.35	5.00	0.74	123.48
		3		2.45	2.30	6.13	0.68	223.43
				2.48	2.30	7.23	0.64	168.29
14, Appl. Year 2000, Age:1	B	1		2.45	2.29	6.34	0.66	163.86
				2.48	2.28	7.73	0.63	116.63
		3		2.42	2.24	7.38	0.54	143.09
				2.42	2.26	6.70	0.47	106.95
	W	1		2.49	2.37	4.97	0.71	243.68
				2.43	2.35	3.09	0.79	183.81
		3		2.44	2.29	6.22	0.84	244.78
				2.37	2.27	4.20	0.54	101.77

* W= wheel path, B= between wheel path

Table 4.24. SCB results for TH 251

Surface Treatment	Temperature (°C)	Location *	Gmm	Gmb	Voids (%)	K_{IC} (MPa.m$^{0.5}$)	Gf (N/m)
Control	-18	B	2.40	2.25	6.50	0.63	170.64
			2.40	2.27	5.65	0.89	130.01
	-30		2.40	2.25	6.50	0.78	115.43
			2.40	2.27	5.65	0.75	147.72
	-18	W	2.42	2.30	4.97	0.86	166.18
			2.43	2.31	4.92	0.78	175.49
	-30		2.42	2.30	4.97	0.80	167.49
			2.43	2.31	4.92	0.95	141.70
CSS-1h	-18	B	2.42	2.27	5.86	0.68	132.58
			2.34	2.24	4.03	0.80	125.07
	-30		2.42	2.27	5.86	0.71	120.82
			2.34	2.24	4.03	0.74	137.73
	-18	W	2.42	2.30	5.04	0.75	187.16
			2.43	2.31	5.21	0.75	241.20
	-30		2.42	2.30	5.04	0.89	168.64
			2.43	2.31	5.21	0.80	127.12
Reclamite	-18	B	2.39	2.27	4.89	0.73	68.85
			2.43	2.29	5.92	0.79	168.29
	-30		2.39	2.27	4.89	0.83	50.18
			2.43	2.29	5.92	0.76	50.18
	-18	W	2.41	2.29	4.83	0.74	206.71
			2.42	2.28	5.62	0.68	144.10
	-30		2.41	2.29	4.83	0.82	172.15
			2.42	2.28	5.62	0.81	190.91
Chip Seal	-18	B	2.41	2.23	7.31	0.66	196.47
			2.41	2.23	7.66	0.71	213.24
	-30		2.41	2.23	7.31	0.77	166.17
			2.41	2.23	7.66	0.84	140.80
	-18	W	2.43	2.29	5.78	0.89	163.23
			2.40	2.28	5.00	0.75	246.42
	-30		2.43	2.29	5.78	0.93	158.50
			2.40	2.28	5.00	0.77	81.58

* W= wheel path, B= between wheel path

CHAPTER 5

DATA ANALYSIS

Introduction

Data analysis of the results from the mechanical characterization of the field samples is performed in this chapter. Graphical and statistical analyses are included in this study. The statistical analysis consists of the calculation of the correlation matrix between the parameters for each test and the analysis of variance (ANOVA) assuming a linear relation between the independent and dependent variables. For example, in the ANOVA analysis for the SCB test for TH 56 sections, the independent variables are the fracture toughness (K_{IC}) and the fracture energy (G_f) and the dependent (predictors) variables are the temperature, the age before application of the treatment, location, air voids and depth.

The analysis of the results for each test is divided in two groups: TH 56 sections were used to study the optimum time for the application of the surface treatment; TH 251 sections were used to investigate the effectiveness of three different types of surface treatments: CSS-1h (seal coat), Reclamite and Chip seal. TH 56 analysis is further divided in two groups according to the construction year: 1995 and 1999.

Asphalt Binder Results

As described in chapter 4, the extracted binders from the different sections were experimentally investigated using the BBR, DTT, DSR and FTIR. The analyses of these experimental results are presented in the next sections.

Bending Beam Rheometer (BBR)

TH 56 Sections

An example of BBR test results for TH 56 is presented in Figure 5.1. All the creep stiffness versus time plots are presented in appendix D at the end of this report. Figures D.1-D.2 and D.3-D.4 show the BBR results for sections constructed in 1995 and 1999, respectively. It is observed from these figures that there are not large differences between the creep stiffness functions of the sections treated at different times. Also, it is noticed that generally, the sections treated earlier (*e.g.* 2000, 2001) have higher creep stiffness than the sections treated later (*e.g.* 2002, 2003), which maybe explained by the fact that the emulsion application rate increased as the pavements got older.
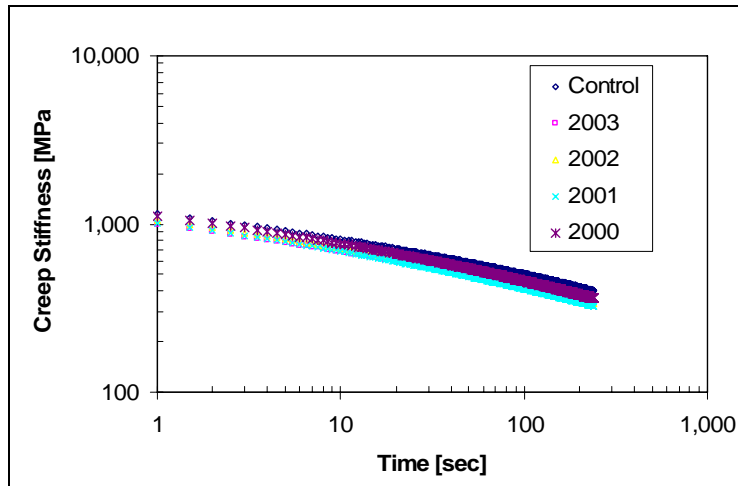
Figure 5.1. Creep stiffness vs. time for between wheel paths, upper layer at -24°C,   TH 56 1999 sections

Bar plots were generated for the PG specification parameters, the stiffness (S) and the *m*–value (slope of the creep stiffness versus time curve in log-log scale) at 60 seconds. Figure 5.2 shows an example of a bar plot for the stiffness at 60 seconds for different treatment application years. Figures D.5-D.6 and D.7-D.8 in the appendix D show S and *m*-value at 60 seconds for the sections constructed in 1995 and 1999, respectively.
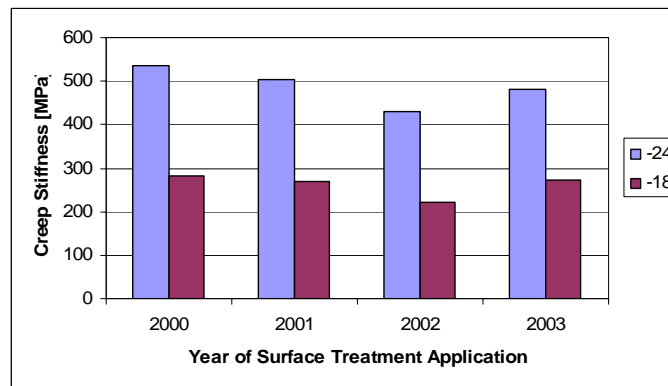
Figure 5.2. Stiffness at 60 sec. for wheel path, upper layer, TH 56 1995 sections

The following is observed in Figures D.5-D.8. Temperature has a drastic effect on both stiffness and *m*-value at 60 seconds and as expected, *S* increases when the temperature decreases and *m*-value increases when the temperature increases. No significant and consistent trend is visually observed for the stiffness and the *m*-value with respect to the year of the surface treatment application.

Statistical Analysis

The correlation factors between the creep stiffness and *m*-value at 60 seconds, age of the pavement in years before treatment, location, temperature, emulsion application rate and depth

were calculated. Correlation factors larger than $2/n^{0.5}$ (rule of thumb), where n is the number of samples, indicates high correlation between the parameters. For the calculation of the correlation matrix, the location parameter was treated as "0" for samples located in the wheel path and "1" for samples located between the wheel paths.

Table 5.1 and 5.2 present the correlation matrix for the sections constructed in 1995 and 1999, respectively. For this case correlation factors larger than 0.353 ($n = 32$) are significant and presented in bold.

Table 5.1. Correlation matrix for binder BBR results of TH 56 1995 sections

Age	1						
Depth	0	1					
Emulsion	0.985	0	1				
Location	0	0	0	1			
M	0.046	0.212	0.018	-0.171	1		
S	-0.137	0.005	-0.137	0.048	**-0.841**	1	
Temperature	0	0	0	0	**0.840**	**-0.973**	1
	Age	**Depth**	**Emulsion**	**Location**	**m**	**S**	**Temperature**

Table 5.2. Correlation matrix for binder BBR results of TH 56 1999 sections

Age	1						
Depth	0	1					
Emulsion	0.990	0	1				
Location	0	0	0	1			
M	-0.007	-0.021	-0.003	-0.161	1		
S	-0.065	0.060	-0.061	-0.017	**-0.950**	1	
Temperature	0	0	0	0	**0.949**	**-0.988**	1
	Age	**Depth**	**Emulsion**	**Location**	**m**	**S**	**Temperature**

In both tables temperature has a positive correlation with m-value meaning that as temperature increases m increases. The correlation between S and temperature is significant and negative. Thus the stiffness increases when the temperature is reduced. There is not a significant correlation between the age before treatment and the parameters obtained in BBR binder testing. In tables 5.1 and 5.2 the rate of emulsion application is included in the calculations to explore the effect of this variable in the experimental results. It was found that the correlation between the emulsion application rate and the age of the pavement before treatment was close to 1 (shaded cells), thus this parameter is not included in the analysis of the following tests because the information provided by this parameter is already included in the age variable. However, this change in application rate makes the analysis more difficult since higher emulsion rates may mask the more pronounced aging in the sections treated later, in particular in the upper layer.

ANOVA analysis was done on the BBR binder data using a linear model and the creep stiffness and m-value at 60 seconds, respectively, as dependent variables and age before treatment, depth, location and temperature as independent variables. The results of this analysis are presented in Table 5.3. Assuming a significance level of 5%, the parameters that are important in the prediction of the dependent variables are presented in bold. Temperature is

significant in the prediction of *S* and *m* for both 1995 and 1999 sections. Age before treatment is important for the prediction of *S* but not for *m*. Based on the p-values, significant differences are observed in *m*-values with respect to depth for 1995 sections, and location for the 1999 sections. Interactions between the predictors (*e.g.* age, depth, location, temperature) generate some significance in the ANOVA that is not observed in the correlation matrix.

Table 5.3. ANOVA of BBR binder results for TH 56 sections

	p-values			
	1995		**1999**	
Coefficient	**S @60 sec**	**m @ 60 sec**	**S @60 sec**	**m @ 60 sec**
Constant	0.000	0.000	0.000	0.000
Age	**0.001**	0.613	**0.012**	0.895
Depth	0.893	**0.026**	**0.021**	0.686
Location	0.174	0.067	0.482	**0.005**
Temperature	**0.000**	**0.000**	**0.000**	**0.000**

TH 251 Sections

An example of BBR test results for TH 251 is shown in Figure 5.3. Creep stiffness versus time plots for all TH 251 sections are presented in Figure D.9. Minor differences are observed in Figure D.9 between the creep stiffness functions of the sections with different surface treatments. It is also noticed that at -18°C, the chip seal section shows slightly lower creep stiffness with respect to time compared to the other treatments. On the other hand, at -24°C, it is observed that the reclamite section has the lowest creep stiffness and the chip seal section has the highest.
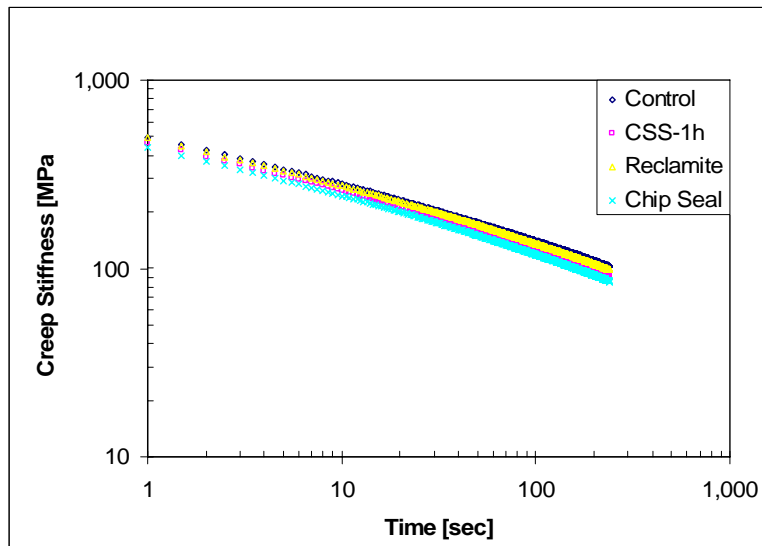
Figure 5.3. Creep stiffness vs. time for wheel path at -18°C, TH 251 sections

Figure 5.4 shows an example of a bar plot for the stiffness at 60 seconds for the different surface treatments applied in TH 251. The bar plots for the creep stiffness and the *m*–value at 60 seconds for all sections are presented in Figure D.10.   Figure D.10 indicates that for a temperature of -18°C there is not a significant difference between the creep stiffness at 60 seconds of the different surface treatments. The *m*-values for both temperatures did not vary significantly with respect to the surface treatment type.
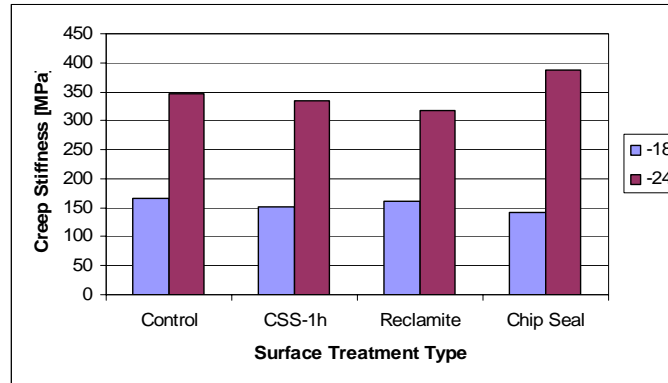
Figure 5.4. Stiffness at 60 sec. for wheel path,   TH 251 sections

Statistical Analysis

The correlation matrix for the creep stiffness and *m*-value at 60 seconds, location and temperature is presented in Table 5.4. Correlation factors more than 0.5 (*n* = 16) are significant and presented in bold. As observed in the correlation matrix of the BBR binder testing of TH 56 sections, temperature has a high positive correlation with *m*-value and a high negative correlation with *S*. There is not a significant correlation between the location of the sample and the creep stiffness and *m*-value at 60 seconds.

Table 5.4. Correlation matrix for binder BBR results of TH 251 sections

Location	1			
m	0.002	1		
S	-0.059	**-0.967**	1	
Temperature	0	**0.974**	**-0.985**	1
	Location	**m**	**S**	**Temperature**

For the ANOVA analysis a linear relation was assumed between independent and dependent variables. The creep stiffness and *m*-value at 60 seconds were selected as dependent variables, respectively, and type of surface treatment, location and temperature as independent variables. The type of surface treatment was treated as a dummy variable with the control section as the reference level. ANOVA results for TH 251 are presented in Table 5.5.

Table 5.5. ANOVA of BBR binder results for TH 251 sections

Coefficient	S@60 sec.		m@ 60 sec.	
	Estimate	p-value	Estimate	p-value
Constant	-398.903	0.000	0.486	0.000
Location	-11.038	0.236	0.000	0.966
Temperature	-30.896	**0.000**	0.009	**0.000**
{F}Treatment[CSS-1H]	-3.299	0.795	0.009	**0.035**
{F}Treatment[RECLAMITE]	-7.224	0.572	0.013	**0.004**
{F}Treatment[CHIP-SEAL]	11.927	0.358	0.012	**0.008**

The parameters that are important, using 5% of significance, in the prediction of the dependent variables are presented in bold. Temperature is significant in the prediction of *S* and *m*. It is observed in Table 5.5 that for the *m* at 60 seconds model, the estimates for all the surface treatments are positive and significant, indicating that the *m*-values in the treated sections are higher than the *m*-values in the control section. The *m*-value is an indicator of the relaxation properties of the asphalt binder; higher values of this parameter indicate that the binder relax stresses faster. This result seems to indicate that the application of surface treatments changes the relaxation properties and does not affect stiffness. This finding supports recent discussions in the asphalt chemistry community that aging not only increases the amount of ketones but also changes the aromaticity of binders, which is related to relaxation properties.

Direct Tension Test (DTT)

TH 56 sections

A typical DTT stress-strain curve from TH 56 is presented in Figure 5.5. Figures D.11-D.14 and D.15-D.18 in the appendix D show direct tension stress-strain curves for sections constructed in 1995 and 1999, respectively. It is observed from these figures that, as expected, at higher temperatures the asphalt binder is more ductile.

Figure 5.6 shows an example of the stress at failure for different treatment application years. The stress and strain at failure from direct tension testing for all sections are presented in appendix D in Figures D.19-D.22. In these figures it is observed that the strain at failure is higher for sections treated in 2000 and 2001 compared to the sections treated in 2003 and 2002. This indicates that as the age before treatment increases, the ductility in the asphalt is reduced. On the other hand, no consistent trend is observed for the stress at failure with respect to the year of the surface treatment application. Please note that in the original SHRP binder specifications, one of the low temperature limits was based on the DTT failure strain and not failure stress.
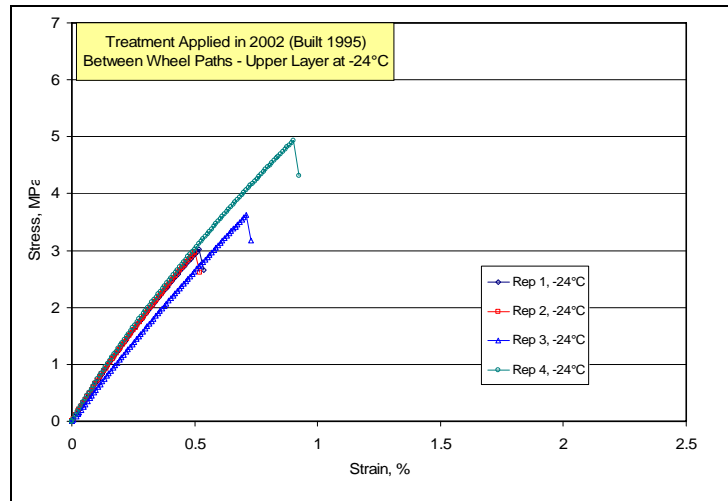
Figure 5.5. DTT stress vs strain curves at -24°C for TH 56 1995 section treated in 2002
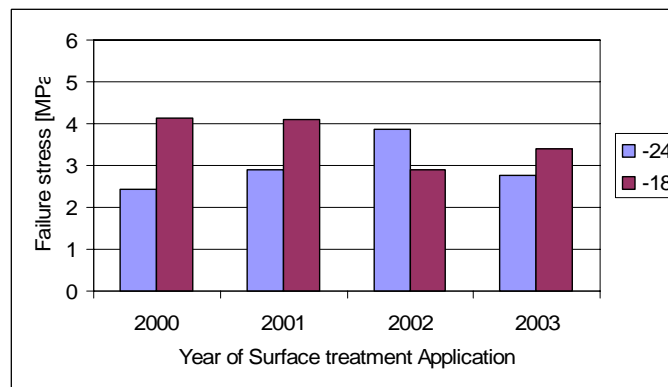
Figure 5.6. Stress at failure from DTT for between wheel paths, upper layer, TH 56 1995 sections

Statistical Analysis

The correlation matrix for the stress and strain at failure, age of the pavement in years before treatment, location, depth, and temperature is presented in Tables 5.6 and 5.7 for the sections constructed in 1995 and 1999, respectively. Correlation factors larger than 0.178 ($n = 125$) are significant and presented in bold.

Table 5.6. Correlation matrix for DTT results of TH 56 1995 sections

Age	1					
Depth	-0.026	1				
Location	0.018	0.008	1			
Strain	0.029	**0.202**	0.119	1		
Stress	0.009	**0.258**	0.137	**0.736**	1	
Temperature	-0.018	-0.008	0.024	**0.553**	-0.007	1
	Age	**Depth**	**Location**	**Strain**	**Stress**	**Temperature**

82

Table 5.7. Correlation matrix for DTT results of TH 56 1999 sections

	Age	Location	Strain	Stress	Temperature	Depth
Age	1					
Location	-0.007	1				
Strain	-0.087	0.031	1			
Stress	-0.098	0.017	**0.799**	1		
Temperature	0	0	**0.198**	**-0.315**	1	
Depth	0.007	0.016	-0.081	-0.066	0	1
	Age	**Location**	**Strain**	**Stress**	**Temperature**	**Depth**

A positive and significant correlation is observed between strain at failure and depth for the samples constructed in 1995. The strain and stress at failure increases with depth according to the results of Table 5.6. As expected, there is a positive correlation between stress and strain at failure and between temperature and strain at failure for the samples constructed in 1995. A negative correlation between the temperature and the stress at failure is observed for the sections constructed in 1999. This negative correlation indicates that when the temperature decreases the stress at failure increases. There are no significant correlations observed between the age before application of the surface treatment and the parameters obtained in the direct tension testing.

ANOVA analysis was done on the direct tension data. Stress and strain at failure are considered as dependent variables and age before application of the surface treatment, depth, location and temperature are considered as independent variables. The results of this analysis are presented in Table 5.8. The parameters that are important in the prediction of the stress and strain at failure are presented in bold. Depth is a significant parameter in the prediction of the stress and strain in the 1995 sections. Temperature is significant for the prediction of strains at failure for sections constructed in 1995 and 1999. As it was observed previously in the correlation matrices, stress at failure depends on the temperature for the samples in sections constructed in 1999 but not in 1995.

Table 5.8. ANOVA of DTT results for TH 56 sections

	p-values			
	1995		1999	
Coefficient	**Stress @ failure**	**Strain@ failure**	**Stress @ failure**	**Strain@ failure**
Constant	0.016	0.000	0.772	0.000
Age	0.879	0.560	0.258	0.331
Location	0.125	0.159	0.837	0.718
Temperature	0.925	**0.000**	**0.000**	**0.027**
Depth	**0.004**	**0.005**	0.444	0.363

TH 251 sections

Figure 5.7 shows a typical DTT stress-strain curve from a TH 251 sample. The complete set of stress-strain curves for TH 251 samples are presented in Figures D.23-D.24 in the appendix D. It can be observed in these figures that the strain at failure increases with temperature increase, while the stress at failure decreases.
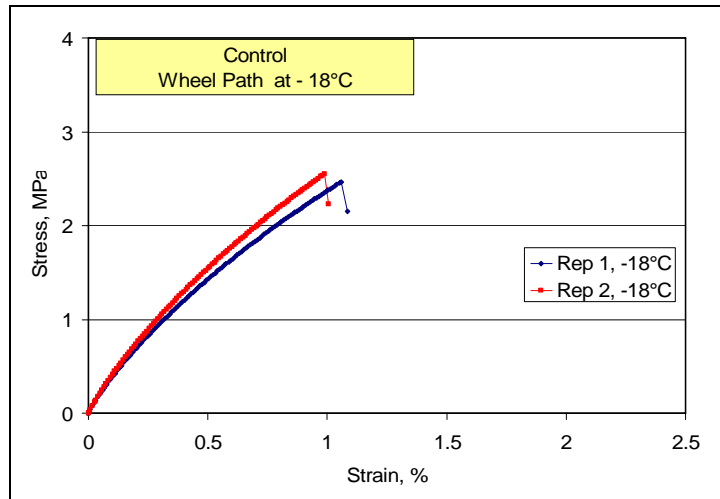
Figure 5.7. DTT stress vs. strain curve at -18°C for control, TH 251

Bar plots with the summary of the stress and strain at failure for TH 251 sections are presented in the appendix D in Figure D.25. An example of the stress at failure for samples located in the wheel path and for different surface treatments is shown in Figure 5.8.
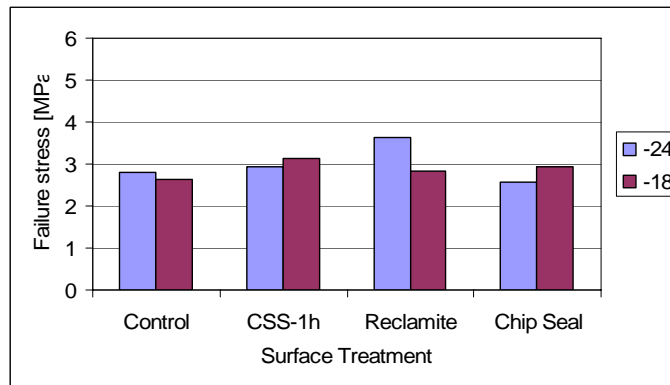
Figure 5.8. Stress at failure from DTT for wheel path, TH 251

It can be seen in Figure D.25 that the samples located in the wheel path, treated with reclamite and tested at -24°C show the highest stress and strain at failure. On the other hand, for samples tested at the same temperature but located in between the wheel paths the higher stress and strain correspond to the CSS-1h treatment. For samples located between the wheel paths, the largest stress and strain at failure at -18°C correspond to the reclamite treatment.

Statistical Analysis

ANOVA analysis was done using the stress and strain at failure as dependent variables, respectively, and the type of surface treatment, location and temperature as independent variables. The type of surface treatment was treated as a dummy variable with the control section as the reference level. The ANOVA results are presented in Table 5.9. The parameters that are important (5% of significance) in the prediction of the stress and strain at failure are presented in

84

bold. Temperature is significant in the prediction of both stress and strain at failure. However, there are no significant differences between the stress and strain at failure of the control section and the sections treated with CSS-1h, reclamite and chip seal.

Table 5.9. ANOVA of DTT results for TH 251 sections

Coefficient	Stress @failure		Strain @failure	
	Estimate	p-value	Estimate	p-value
Constant	0.577	0.551	2.688	**0.000**
{F}Treatment[CSS-1H]	0.669	0.077	0.130	0.514
{F}Treatment[RECLAMITE]	0.552	0.156	0.185	0.371
{F}Treatment[CHIP-SEAL]	-0.335	0.365	0.174	0.384
Temperature	-0.101	**0.028**	0.089	**0.001**
Location	0.211	0.427	-0.003	0.985

Dynamic Shear Rheometer (DSR)

TH 56 sections

The frequency sweep data obtained from DSR testing of TH 56 samples was used to construct frequency master curves. These curves show important information about the behavior of the binders over a range of frequencies. The frequency master curves for the absolute value of the complex modulus |G*| at a reference temperature of 10°C were obtained using the CAM model:

$$\left| G^*(\omega) \right| = G_g \left[1 + \left(\frac{\omega_c}{\omega} \right)^v \right]^{-\frac{w}{v}} \tag{10}$$

where

|G*(ω)| = absolute value of the complex modulus as a function of frequency ω

G_g = glassy modulus

ω_c, v, w = model parameters

Nonlinear regression was used to fit the model parameters to the test data. The shift factors obtained from the master curves for the absolute value of the complex modulus were also applied to the phase angle data to generate the phase angle master curves. Figure 5.9 shows and example of the complex modulus master curves generated for wheel path samples in TH 56 1999 sections at a reference temperature of 10˚C. Figures D.26-D.29 and D.30-D.33 in appendix D show the complex modulus and phase angle master curves for all TH 56 sections.
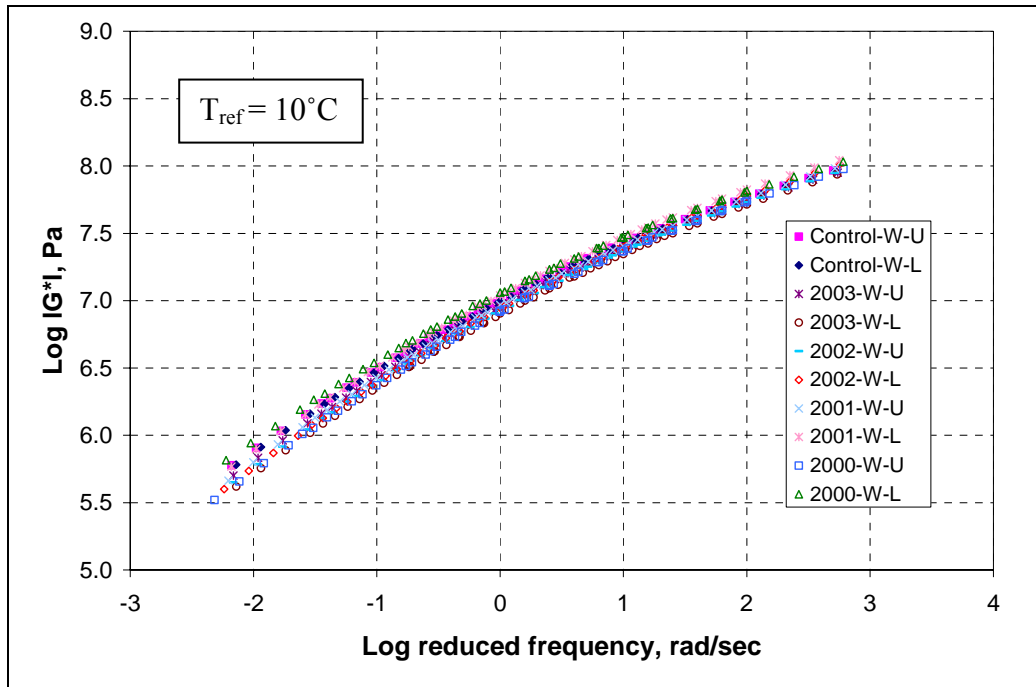
Figure 5.9. Complex modulus master curves for wheel path samples in TH 56 1999 sections.

A number of observations can be made from examining Figures D.26-D.29 for the sections constructed in 1995. For the samples located in the wheel path, the binder extracted from the upper layer of the section treated in 2003 was the stiffest across the entire range of frequencies; this binder also has the lowest phase angle over the range of frequencies. On the other hand, the binder extracted from the lower layer and treated in 2001 has the lowest modulus and the highest phase angle over the range of frequencies. In the case of the samples located between the wheel paths, the binder extracted from the upper layer of the 2001 section has the highest modulus, contrary to the binder extracted from the upper layer of the 2002 section which has the lowest modulus over most of the frequency range.

For the sections constructed in 1999 it is observed in Figures D.30-D.33 that for both samples located in the wheel path and between the wheel paths the |G*| master curves were quite close to each other. Furthermore, for the samples located in the wheel path, the binder with the highest modulus corresponds to the binder extracted from the upper layer of the control section. On the other hand, the lowest modulus over most of the frequency range was observed in the binder extracted from the upper layer of the section treated in 2000. For the samples located in between the wheel paths, the highest and the lowest modulus correspond to the binders from the lower layer of the 2000 section and the upper layer of the 2001 section, respectively.

A clear picture of the temperature susceptibility of the binders is given by plotting the complex modulus vs. temperature at a specific frequency. Figures 5.10 and 5.11 show the |G*| vs. temperature curve at 10 rad/s for the samples extracted from sections constructed in 1995 and 1999, respectively.
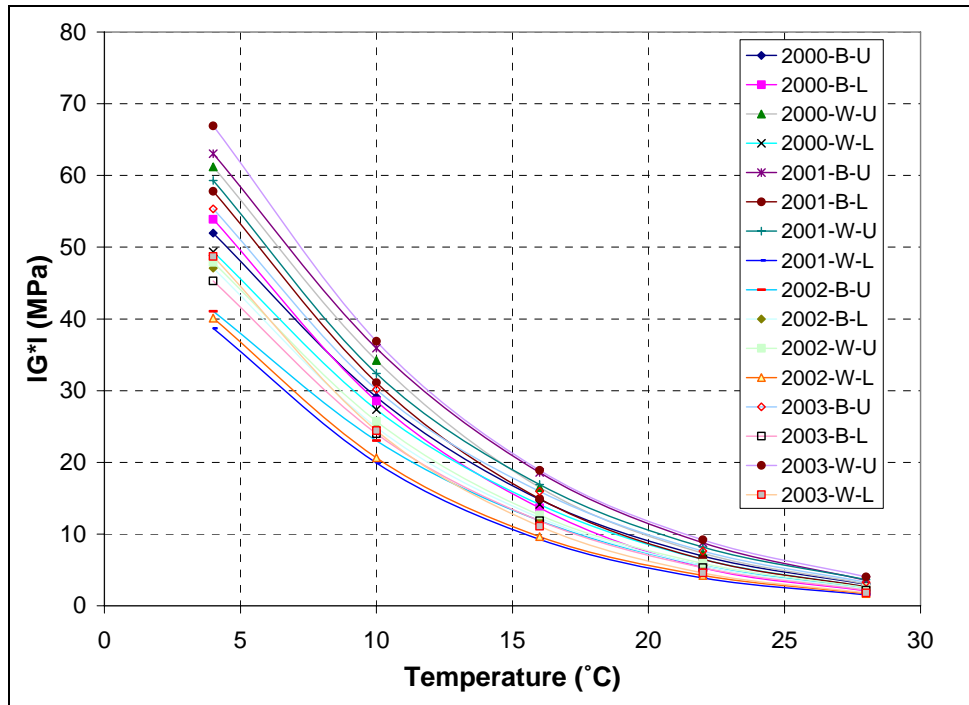
Figure 5.10. |G*| at 10 rad/s vs. temperature for TH 56 1995 sections.
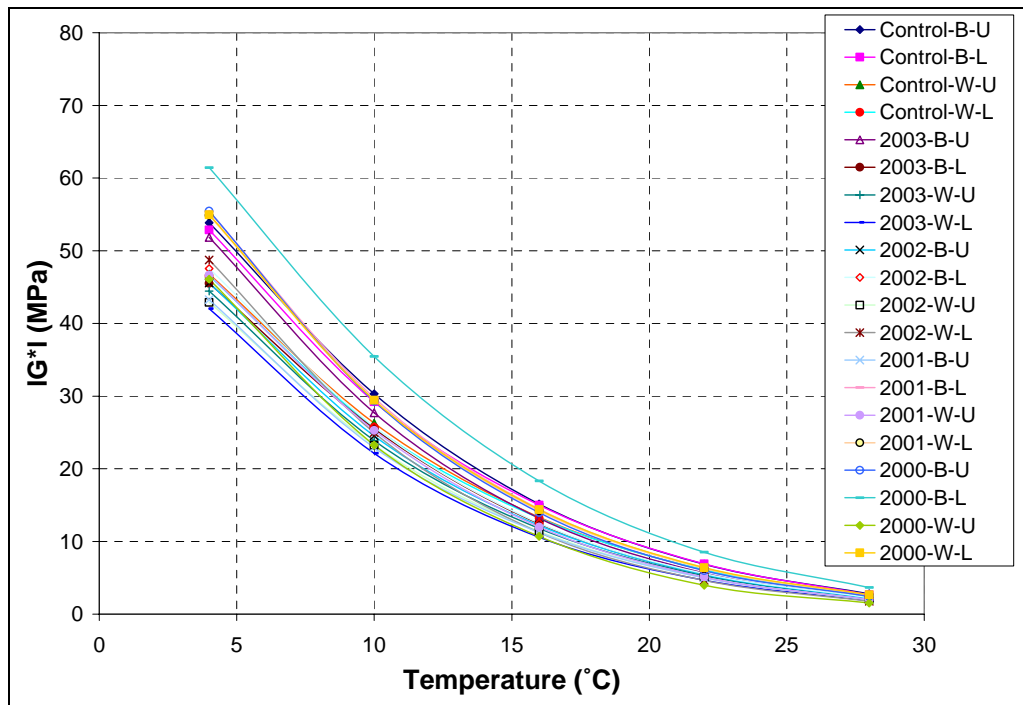
Figure 5.11. |G*| at 10 rad/s vs. temperature for TH 56 1999 sections.

87

In Figure 5.10, the binder with the highest temperature susceptibility corresponds to the asphalt extracted from the upper layer and in the wheel path of the section treated in 2003 and the lowest susceptibility is shown by the binder extracted from the lower layer and in the wheel path of the 2001 section.

The most temperature susceptible of the sections constructed in 1999 corresponds to the binder from the lower layer, between the wheel paths and treated in 2000 (Figure 5.11). The least temperature susceptible is the binder in the wheel path from the section treated in 2003.

Another way to investigate the temperature susceptibility of the binders is by plotting the log of the shift factor (Log a_T) vs. temperature. Figures 5.12 and 5.13 show the Log a_T vs. temperature for the binders extracted from sections constructed in 1995 and 1999, respectively. Larger shift factors mean higher temperature susceptibility. As it can be seen from Figures 5.12 and 5.13, the most and least temperature susceptible binders are from the sections treated in 2000 and 2002, respectively.
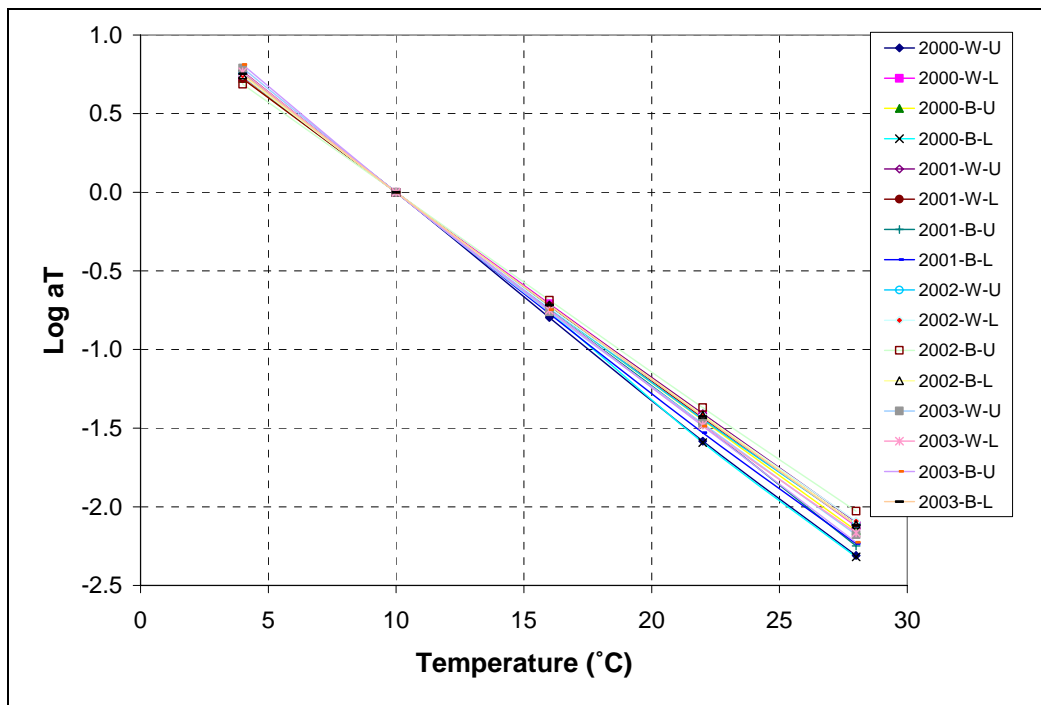
Figure 5.12. Log a_T vs. temperature for TH 56 1995 sections.
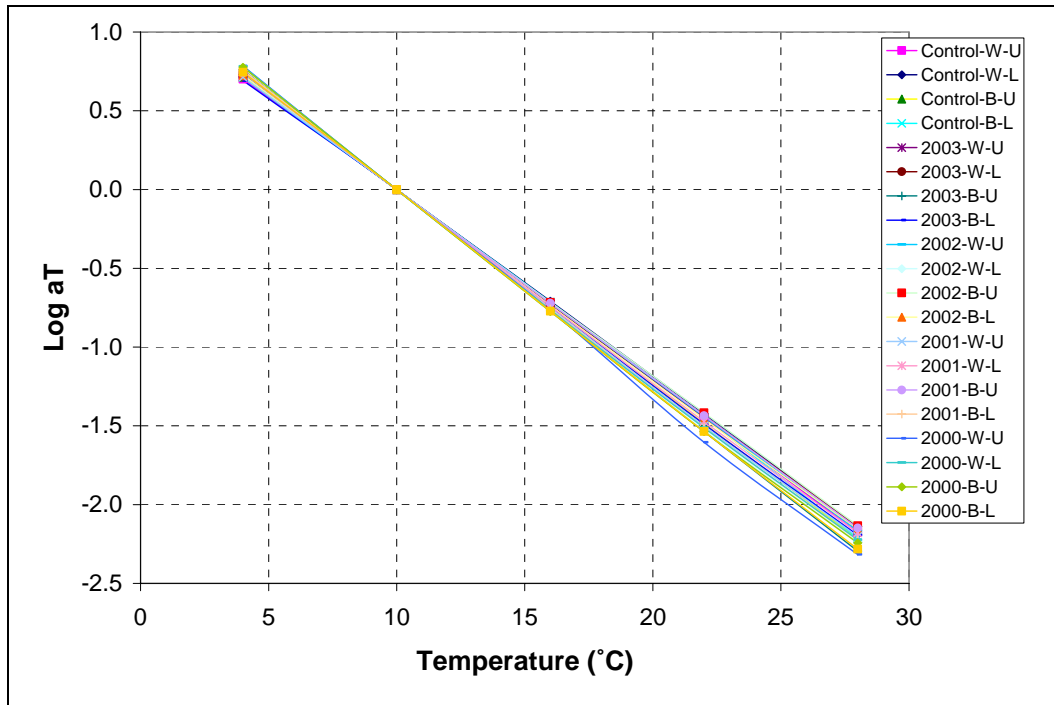
Figure 5.13. Log a_T vs. temperature for TH 56 1999 sections.

Statistical Analysis

The correlation matrix for the absolute value of the complex modulus and phase angle at 10 rad/sec and 4˚C, age of the pavement in years before treatment, location and depth is presented in Tables 5.10 and 5.11 for the sections constructed in 1995 and 1999, respectively. Significant correlation factors are larger than 0.5 ($n = 16$) and presented in bold in the following tables.

Table 5.10. Correlation matrix for DSR results at 10 rad/sec and 4˚C, TH 56 1995 sections

Age	1				
Delta	0.145	1			
Depth	0	**0.714**	1		
IG*I	-0.148	**-0.794**	**-0.502**	1	
Location	0	-0.272	0	0.025	1
	Age	**Delta**	**Depth**	**IG*I**	**Location**

Table 5.11. Correlation matrix for DSR results at 10 rad/sec and 4˚C, TH 56 1999 sections

Age	1				
Delta	0.344	1			
Depth	0	-0.275	1		
IG*I	**-0.592**	**-0.740**	0.385	1	
Location	0	-0.473	0	0.285	1
	Age	**Delta**	**Depth**	**IG*I**	**Location**

As it was expected there is a strong negative correlation between |G*| and the phase angle. For 1995 sections there is a significant positive correlation observed between depth and the phase angle, indicating that as the depth increases, the phase angle increases too. Also, a negative correlation is observed between |G*| and depth, indicating that |G*| decreases with depth.

For the 1999 sections, contrary to what it was expected, there is a significant negative correlation between the age before application of the surface treatment and |G*|; older binders are expected to have higher stiffness. The increase in the emulsion application rate with the age of the pavement before treatment could be one of the reasons why this correlation is observed.

ANOVA analysis was done using |G*| and the phase angle as dependent variables, respectively, and age before application of the treatment, depth and location as the independent variables. The results of this analysis are presented in Table 5.12.

Table 5.12. ANOVA for |G*| and δ at 10 rad/sec and 4°C, TH 56 sections

	p-values			
	1995		**1999**	
Coefficient	**|G*|**	**δ**	**|G*|**	**δ**
Constant	0.000	0.000	0.000	0.000
Depth	0.064	**0.002**	0.062	0.236
Location	0.921	0.161	0.154	0.053
Age	0.560	0.441	**0.008**	0.145

It is observed from Table 5.12 that depth is significant in the prediction of the phase angle for sections constructed in 1995. Age of the pavement before treatment is significant for the prediction of |G*| but as mentioned before, this significance is most likely due to the effect of changing the application rate of the emulsion and not to aging.

TH 251 sections

Figure 5.14 shows the complex modulus master curves generated for the wheel path (W) and between the wheel paths (B) samples from TH 251 sections. It is observed that the binders extracted from the wheel path of the section treated with CSS-1h are the stiffest across the entire range of frequencies. The lowest moduli are observed for the binders from between the wheel paths of the control and chip seal sections.

Master curves for the phase angle of the binders extracted from TH 251 are presented in Figure 5.15. The binder from between the wheel path of the control section has the largest phase angle over the entire frequency range. On the other hand, the lowest phase angle observed is for the binder from the wheel path of the section treated with CSS-1h.
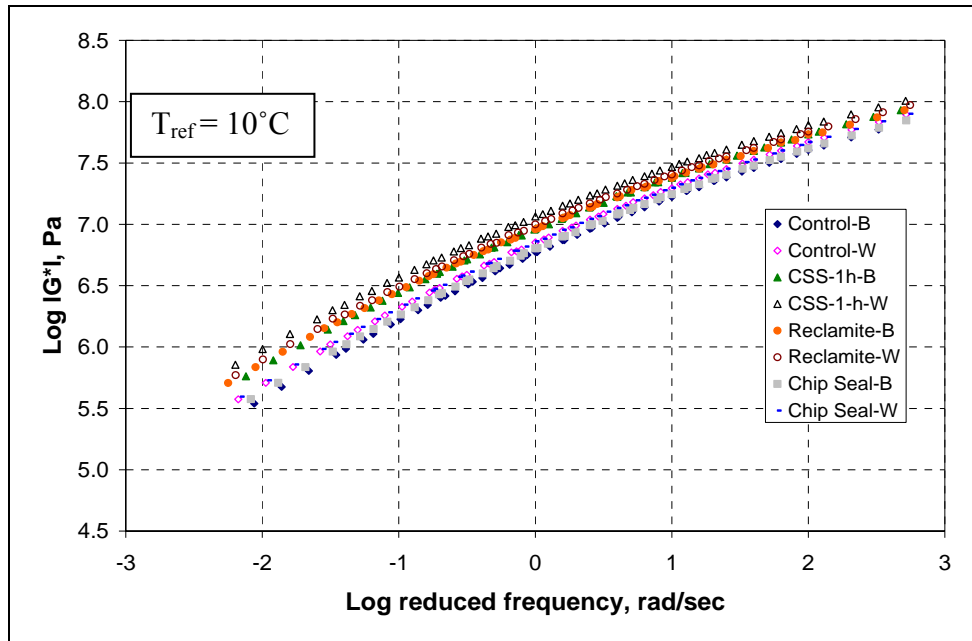
Figure 5.14. Complex modulus master curves for TH 251 sections.
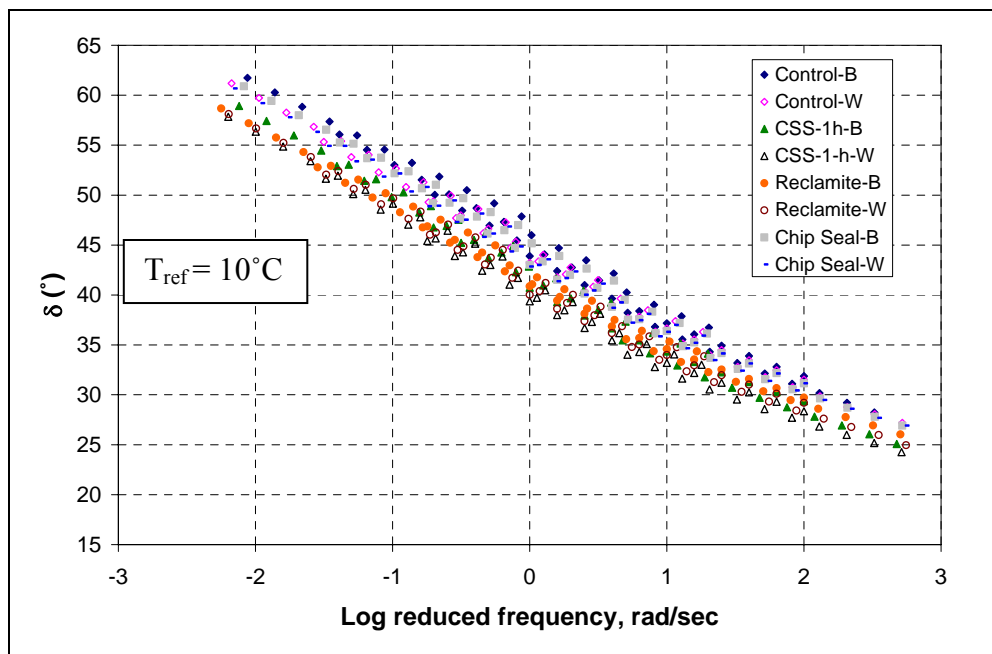
Figure 5.15. Phase angle master curves for TH 251 sections.

Curves of the complex modulus vs. temperature at 10 rad/s are presented in Figure 5.16. The sample with the highest temperature susceptibility is the binder from the wheel path of the section treated with CSS-1h. The lowest susceptibility is observed for the samples from between the wheel paths of the control and chip seal sections.
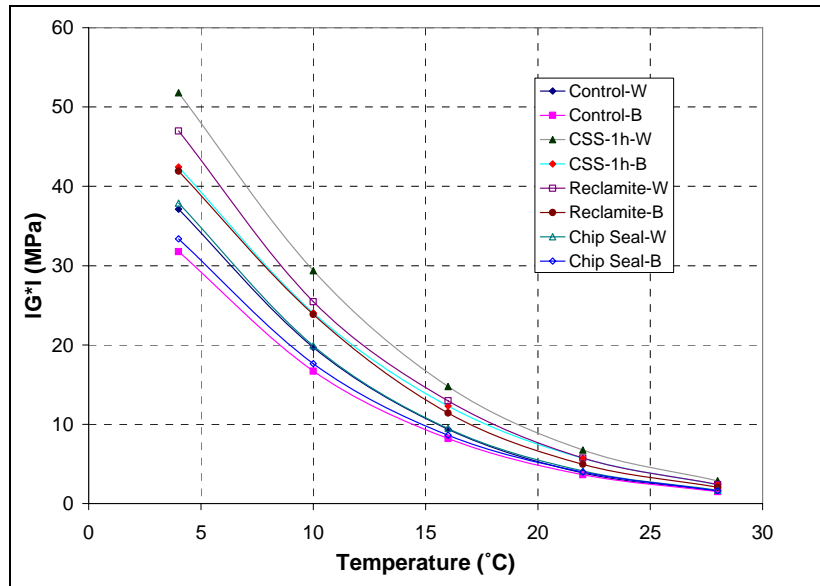
Figure 5.16. |G*| vs. temperature curve at 10 rad/s for TH 251 sections.

Temperature susceptibility of the binders can be also studied by plotting Log a_T vs. temperature as shown in Figure 5.17.
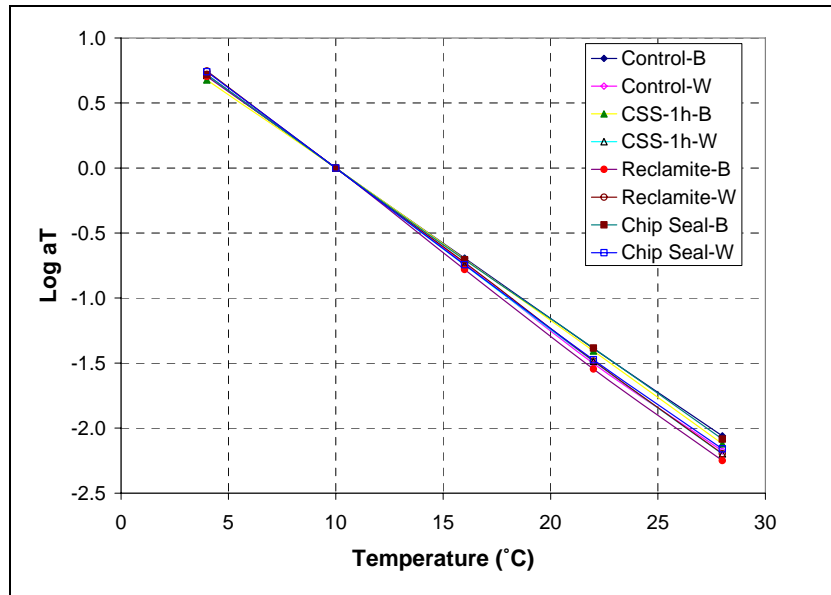
Figure 5.17. Log a_T vs. temperature for TH 251 sections.

Although the shift factors are quite close to each other over most of the temperature range, at the highest temperature some differences are observed. The most and least temperature susceptible binders are from the section treated with reclamite and the control section, respectively.

ANOVA analysis was done assuming linear relation and using |G*| and the phase angle as dependent variables and type of surface treatment and location as the independent variables. The results of this analysis are presented in Table 5.13.

Table 5.13. ANOVA for |G*| and δ at 10 rad/sec and 4°C, TH 251 sections

Coefficient	|G*|		δ	
	Estimate	p-value	Estimate	p-value
Constant	37.477	0.000	31.616	0.000
{F}Treatment[CSS-1-H]	12.667	**0.004**	-2.810	**0.004**
{F}Treatment[RECLAMITE]	10.006	**0.008**	-2.110	**0.008**
{F}Treatment[CHIP-SEAL]	1.178	0.509	-0.475	0.251
Location	-6.066	**0.012**	0.678	0.064

It is observed that |G*| is significantly higher for the sections treated with CSS-1h and reclamite compared to the control section. Location is significant in the prediction of |G*|; the negative sign in the estimate of the location coefficient indicates that the moduli of the samples coming from between the wheel paths are lower than the moduli of samples from the wheel path.

Fourier Transform Infrared Spectroscopy (FTIR)

TH 56 sections

The normalized carbonyl peak area results are presented in Figures 5.18-5.19 for TH 56 1995 sections and Figures 5.20-5.21 for TH 56 1999 sections. Note that control samples were not available for the 1995 sections. Also note that although control samples were available for the 1999 samples it is not known if the sections that were surfaced treated had identical aging characteristics as the section that was not treated due to possible construction practice variability. Ideally, samples from all sections before surface treatments were applied should have been cored and analyzed to determine the base line for aging for all sections.
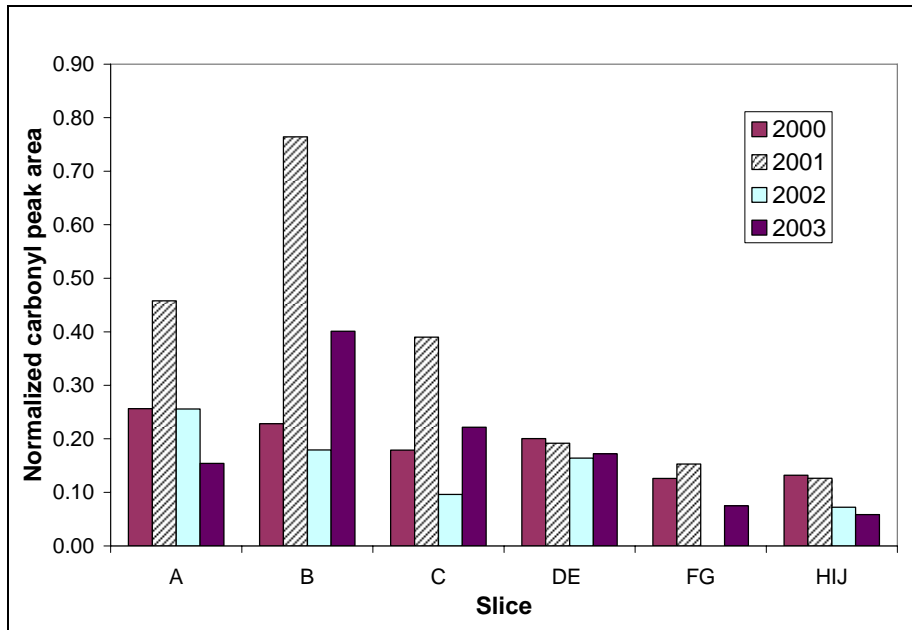
Figure 5.18. FTIR results for wheel path samples from TH 56 1995 sections
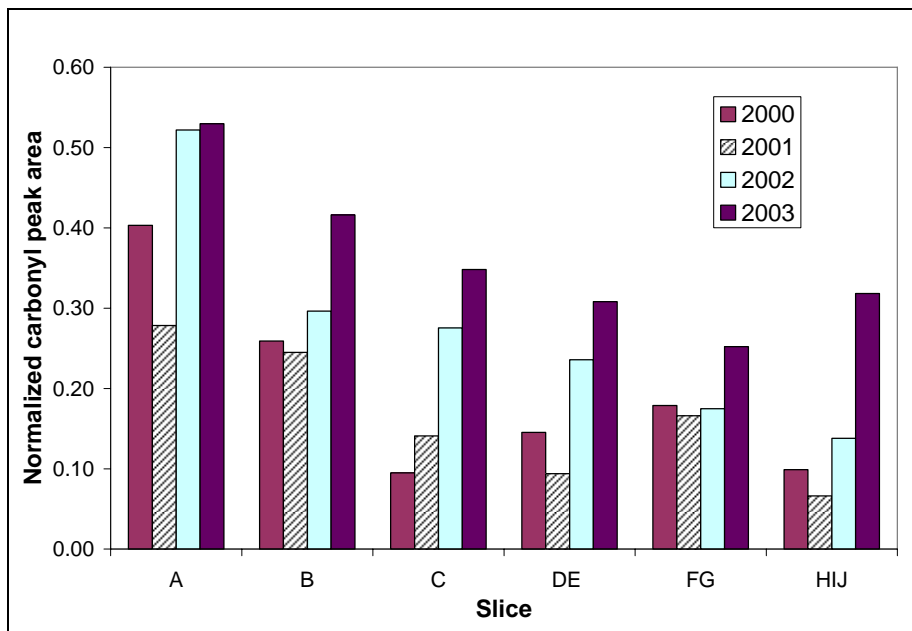
Figure 5.19. FTIR results for between wheel path samples from TH 56 1995 sections
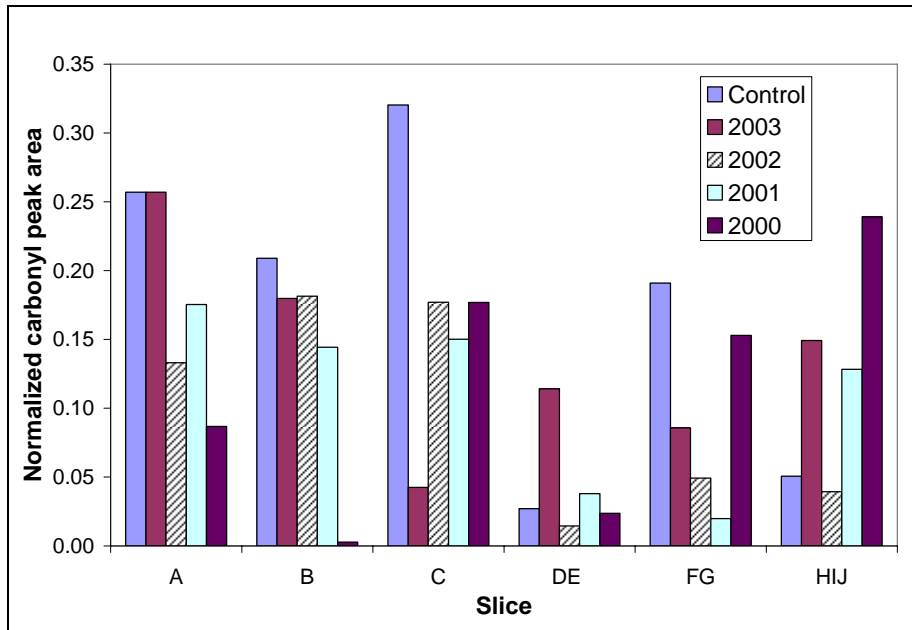
Figure 5.20. FTIR results for wheel path samples from TH 56 1999 sections
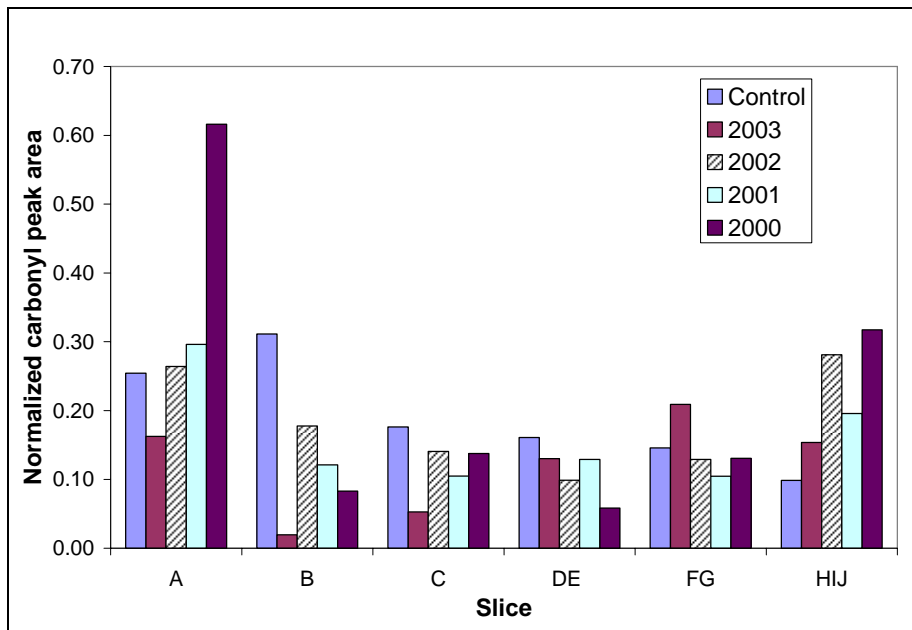
Figure 5.21. FTIR results for between wheel path samples from TH 56 1999 sections

The carbonyl peak area average for the surface samples (A) from the wheel path is smaller than the carbonyl peak area average for the surface samples from between the wheel paths which appears to indicate that higher oxidation is taking place between the wheel paths. The carbonyl peak area average for both locations (wheel path and between the wheel paths) of the surface samples of the 1999 sections are smaller than the carbonyl peak area average for top samples of the 1995 sections. This result was expected since the 1995 TH 56 sections are 4 years older than 1999 TH 56 sections.

The normalized carbonyl peak areas for the top slice of the TH 56 sections are plotted in Figures 5.22 and 5.23. For the 1995 samples located between the wheel paths, the carbonyl content increases, as expected, with the year of treatment application, except for the 2001 treatment (Figure 5.22). However, this trend reverses for the 1999 sections (Figure 5.23). The trends observed for the samples located in the wheel path for 1995 and 1999 sections are the opposite of the trends observed for the samples between the wheel paths; for the 1995 sections the carbonyl content dropped with the year of surface treatment application, except for 2001 treatment, and 1999 sections they increased, except for 2002 treatment.
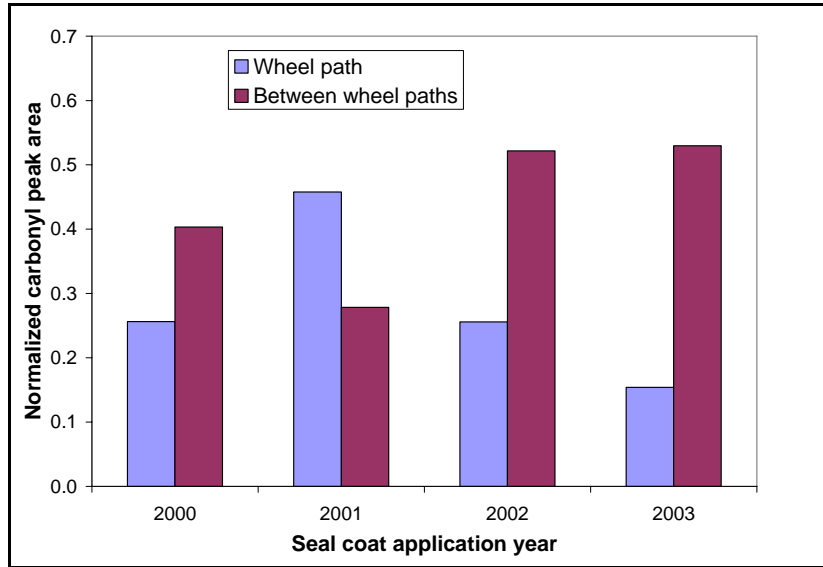
Figure 5.22. Carbonyl peak area for top samples (A) in TH 56 1995 sections
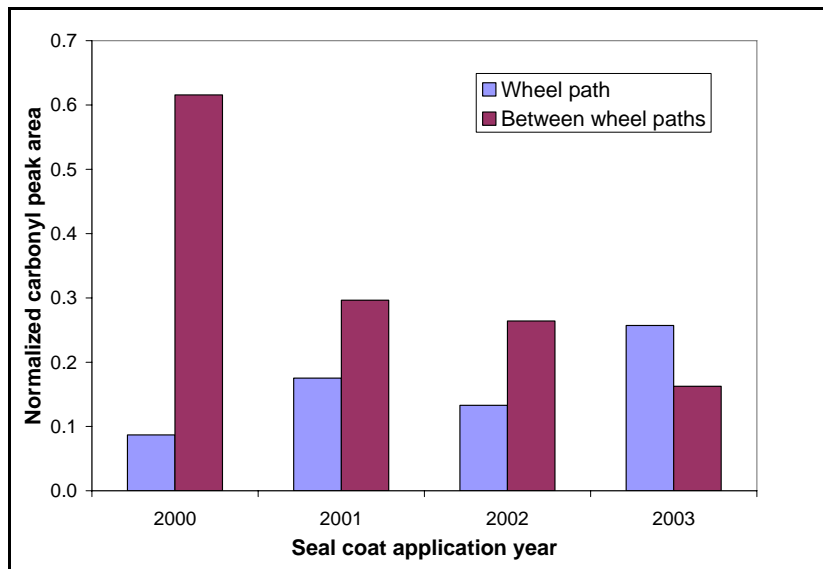
Figure 5.23. Carbonyl peak area for top samples (A) in TH 56 1999 sections

Statistical Analysis

The correlation factors between the normalized carbonyl peak area, age of the pavement in years before treatment, location and depth were calculated. In table 5.14 correlation factors larger than 0.204 (n = 96) are significant and presented in bold. Normalized carbonyl peak area has a positive correlation with age before treatment meaning that as age before treatment increases carbonyl content increases. The correlation between carbonyl area and depth is significant and negative. Thus the asphalt binder in the top of the AC layer ages more than the binder in the bottom.

Table 5.14. Correlation matrix for TH 56 samples

Age	1			
Depth	0	1		
Location	0	0	1	
Carbonyl area	**0.298**	**-0.352**	0.182	1
	Age	**Depth**	**Location**	**Carbonyl area**

ANOVA analysis was done on TH 56 FTIR data using a linear model and the normalized carbonyl area as dependent variable and depth, location and age before treatment as independent variables. Assuming a significance level of 5%, Table 5.15 indicates that all parameters are significant in the prediction of the carbonyl content. The p-value for location is 0.047, close to be not significant; interactions between the location and the other variables generate some significance that is not observed in the correlation matrix.

Table 5.15. ANOVA of FTIR results for TH 56 sections

Predictor	F	p-value
Age	10.87	**0.001**
Depth	15.08	**0.000**
Location	4.02	**0.047**

TH 251 sections

The normalized carbonyl peak area results at different depths are presented in Figures 5.24 and 5.25 for each treatment in TH 251 for samples in the wheel path and between the wheel paths, respectively. Two trends can be clearly observed in these figures: carbonyl content reduces with depth and the samples from the chip seal section have the least amount of carbonyl while the samples from the CSS-1h seal coat section have the largest amount of carbonyl.
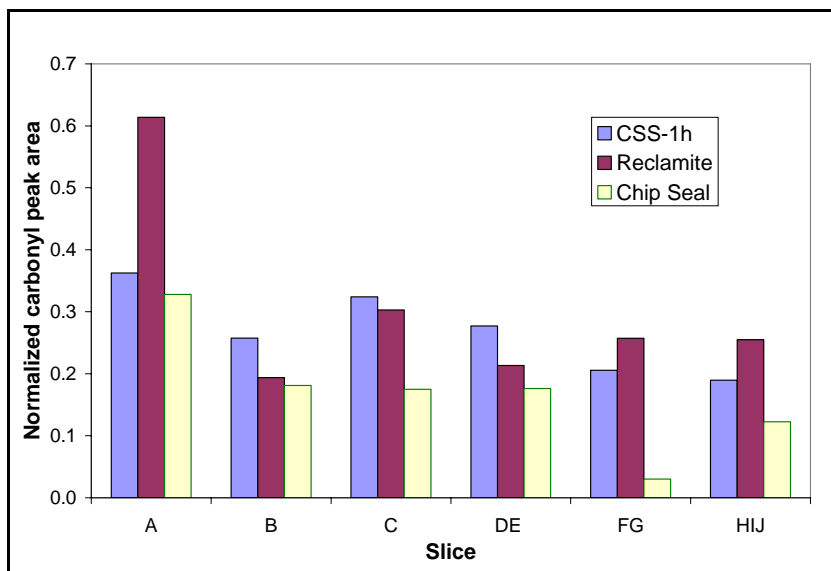
Figure 5.24. Carbonyl peak area for samples located in the wheel path in TH 251
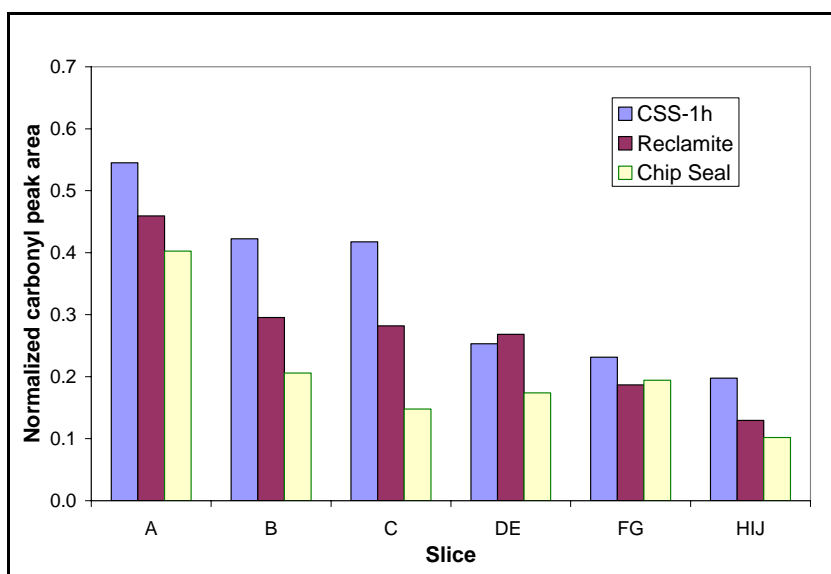
Figure 5.25. Carbonyl peak area for samples located between wheel paths in TH 251

Figure 5.26 presents the amount of carbonyl for the top slice of each surface treatment and for both locations. It is observed that asphalt binders located between the wheel paths oxidized more than the binders located in the wheel path. It also appears that the chip seal sections had the lowest oxidation.
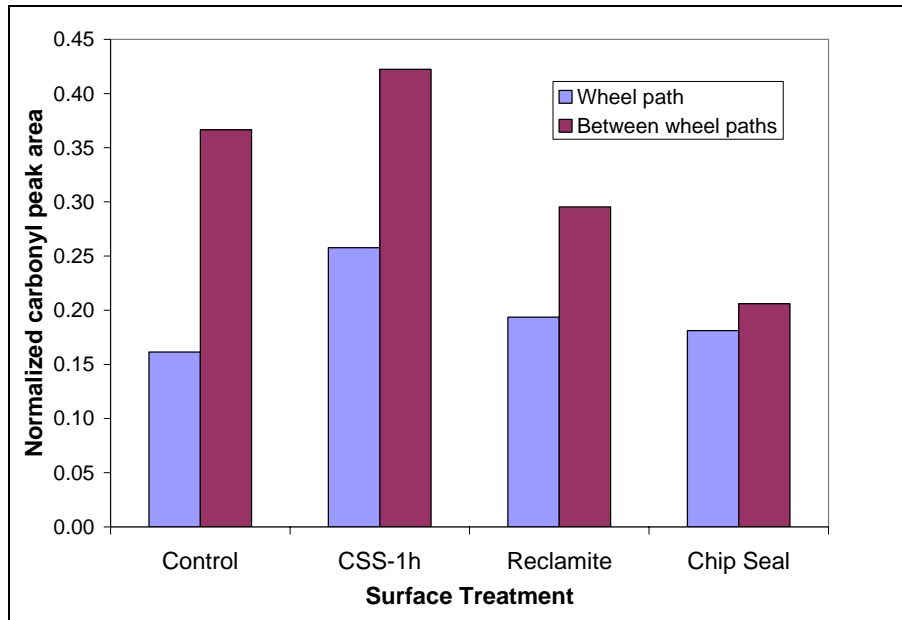
Figure 5.26. Carbonyl peak area for the top layer in TH 251

Due to the limited number of FTIR tests performed on the TH 251 samples, the ANOVA analysis for FTIR results from TH 251 is statistically not significant and thus not performed.

Mixture Results

As described in chapter 4, experimental work was also performed on asphalt mixtures samples cored and cut from the various test sections, which include voids measurements, BBR on thin mixture beams and SCB. The analyses of these experimental results are presented in the next sections.

Air voids

TH 56 sections

Figures 5.27 and 5.28 show the air void content of the samples recovered from the sections constructed in 1995 and 1999, respectively. The air voids were compared with respect to the year the treatment was applied, the location of the sample (wheel path or between the wheel paths) and the depth (upper or lower layer).

Wheel Path **Between wheel paths**
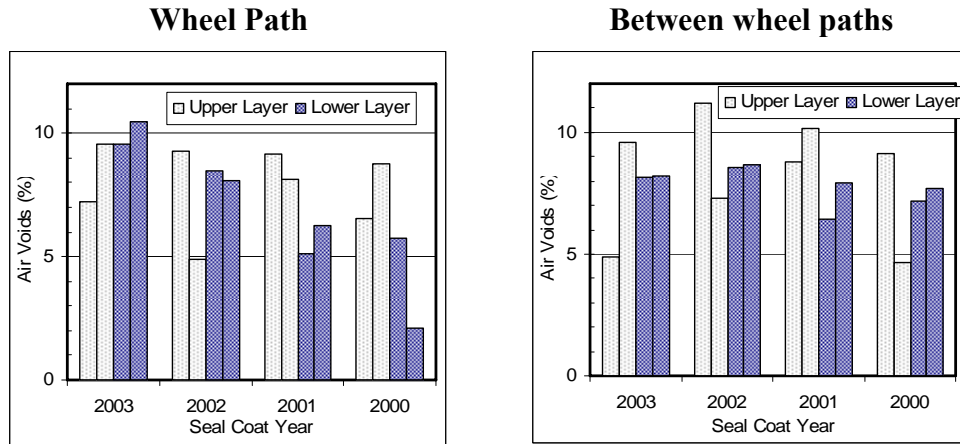
Figure 5.27. Air voids for samples from TH 56 1995 sections

Wheel Path **Between wheel paths**
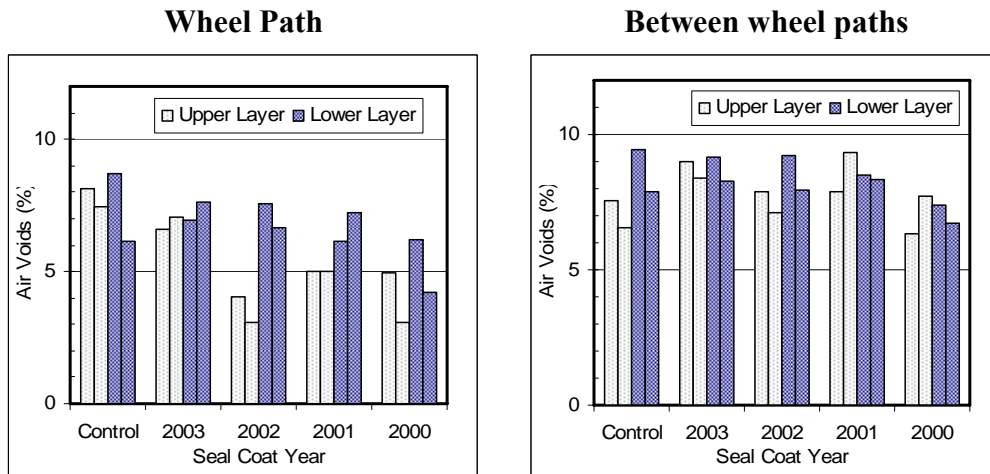
Figure 5.28. Air voids for samples from TH 56 1999 sections

For the 1995 sections it is observed that the air voids in the specimens from the upper layer are slightly higher than the specimens from the lower layer. For the 1999 sections the opposite is observed. It is also noticed that the sections treated earlier have less air voids than the sections treated later, which is more noticeable for the specimens located in the wheel path. The previous figures indicate that the air voids for the specimens taken from the wheel path had lower air voids than from between the wheel paths.

TH 251 sections

Figure 5.29 shows the air void content for the specimens from TH 251. The samples located in the wheel path have less air void content than the samples between the wheel paths. It is also notice that the samples treated with chip seal have slighter higher air void content than the other specimens.
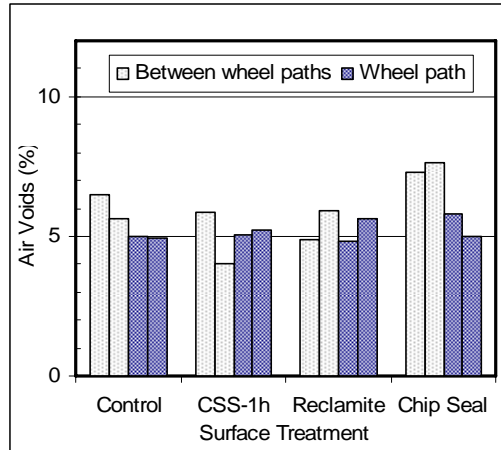
Figure 5.29. Air voids for samples from TH 251 sections

Bending Beam Rheometer (BBR)

TH 56 sections

Figure 5.30 shows an example of mixture BBR results from TH 56. The creep stiffness versus time plots for all sections are presented in Figures D.34 to D.39 in the appendix D.
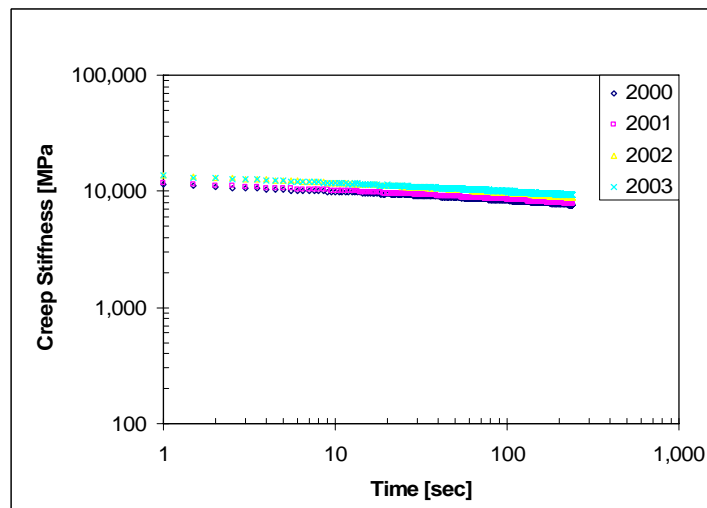
Figure 5.30. Mixture creep stiffness vs. time for between wheel paths, upper layer at -18˚C, TH 56 1995 sections

It can be seen in Figures D.34-D.39 that the creep stiffness curves of the sections treated at different times are similar. However, the values obtained at -18˚C seem to indicate that the mixture samples from the sections treated later in time are stiffer than the samples from the sections treated earlier.

Figure 5.31 shows an example of a bar plot used to investigate how the stiffness of the mixture at 60 seconds changes with respect to the time of application of the treatment.
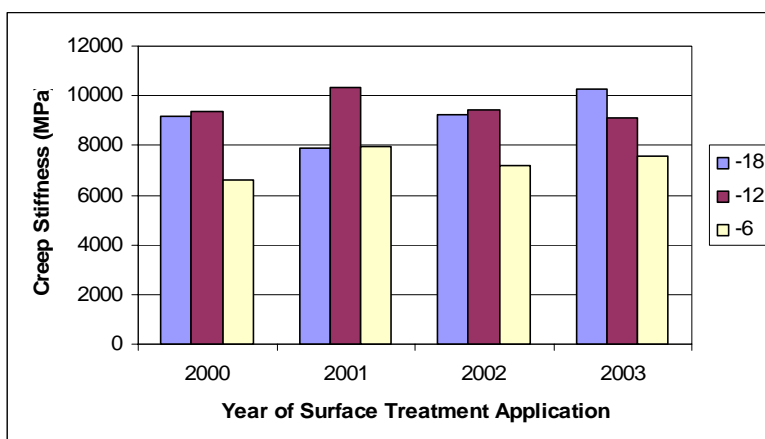
Figure 5.31. Stiffness of the mixture at 60 sec. for wheel path, upper layer, TH 56 1995 sections

Figures D.40-D.41 and D.42-D.43 in the appendix D present the bar plots of the stiffness of the mixture (S_{mix}) and the m–value at 60 seconds for the 1995 and the 1999 sections, respectively. It can be observed in these figures that, at -18°C, the stiffness of the mixtures from the sections constructed in 1995 increases with the age of the pavement before treatment. On the other hand, the opposite is observed for the sections constructed in 1999: the stiffness decreases when the age of the section increases with the exception of the samples from the lower layer and between the wheel paths where the expected trend is observed. No clear trend is observed at other temperatures for S_{mix}. The m_{mix} value did not vary significantly with the time of the treatment application.

Statistical Analysis

The correlation factors between S_{mix}, m_{mix}, age of the pavement before treatment, depth, emulsion application rate, location, temperature and air voids were calculated. The correlation matrix for the BBR mixture results of the sections constructed in 1995 and 1999 are presented in Tables 5.16 and 5.17, respectively. Correlation factors larger than 0.316 ($n = 40$) are significant and presented in bold.

Table 5.16. Correlation matrix for mixture BBR results of TH 56 1995 sections

Age	1						
Depth	0	1					
Location	0	0	1				
m_{mix}	-0.041	0.252	-0.258	1			
S_{mix}	0.088	-0.067	0.290	**-0.837**	1		
Temp	0	0	-0.327	**0.854**	**-0.803**	1	
Voids	**-0.539**	-0.235	0.187	-0.167	0.102	-0.061	1
	Age	**Depth**	**Location**	**m_{mix}**	**S_{mix}**	**Temp**	**Voids**

102

Table 5.17. Correlation matrix for mixture BBR results of TH 56 1999 sections

Age	1						
Depth	0	1					
Location	0	0	1				
m_{mix}	0.016	0.119	-0.207	1			
S_{mix}	-0.106	-0.069	0.110	**-0.773**	1		
Temp	0	0	-0.327	**0.936**	**-0.856**	1	
Voids	**0.388**	**0.368**	**0.705**	-0.077	0.013	-0.231	1
	Age	**Depth**	**Location**	**m_{mix}**	**S_{mix}**	**Temp**	**Voids**

Tables 5.16-5.17 indicate a high negative correlation between S_{mix} and m_{mix} meaning that as the stiffness increases (more brittle mixtures) m_{mix} decreases and the mixture have more problems relaxing the stresses. These two parameters are greatly affected by temperature as it can be observed in these tables. It is also observed from the tables that the air void content decreases as the age of the pavement increases. This trend can be explained by the higher emulsion application rate used the more aged pavements. The high positive correlation factor between location and voids indicates that the samples located between the wheel paths have higher void content compared to samples in the wheel path.

ANOVA analysis was done on the BBR mixture data using the mixture creep stiffness and m-value at 60 seconds as dependent variables, respectively, and age before treatment, depth, location, emulsion application rate, voids and temperature as independent variables. The results of this analysis are presented in Table 5.18. It is observed that temperature is significant in the prediction of S_{mix} and m_{mix} for both 1995 and 1999 sections. According to the p-values, depth is significant for the prediction of the m-value for 1995 samples. In the previous analysis no correlation was observed between these two variables. Interactions between the predictors generate some significance in the ANOVA that is not observed in the correlation matrix.

Table 5.18. ANOVA of BBR mixture results for TH 56 sections

	p-values			
	1995		**1999**	
Coefficient	**S_{mix} @60 sec**	**m_{mix} @ 60 sec**	**S_{mix} @60 sec**	**m_{mix} @ 60 sec**
Constant	0.818	0.053	0.035	0.918
Age	0.705	0.441	0.132	0.199
Depth	0.750	**0.011**	0.944	0.462
Emulsion	0.894	0.837	0.094	0.207
Location	0.969	0.536	0.651	0.908
Temperature	**0.000**	**0.000**	**0.000**	**0.000**
Voids	0.290	0.143	0.401	0.197

TH 251 sections

An example of BBR mixture test results for TH 251 is presented in Figure 5.32. The mixture creep stiffness versus time plots for all TH 251 samples are shown in the appendix D in Figure D.44.
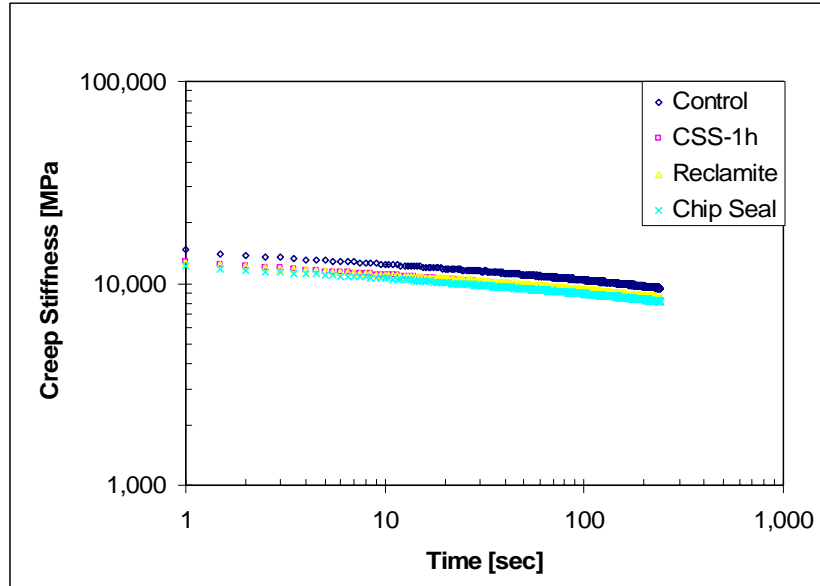
Figure 5.32. Mixture creep stiffness vs. time for wheel path at -18˚C, TH 251 sections

It is observed that at -18˚C the mixture treated with the chip seal shows slightly lower creep stiffness with respect to time compare to the other mixtures. It is also noticed that at -12˚C the mixtures treated with reclamite and chip seal have the lowest creep stiffness.

An example of a bar plot for the stiffness of the mixture at 60 seconds for the different treatments applied to TH 251 is shown in Figure 5.33. The mixture creep stiffness and the *m–* value at 60 seconds for all TH 251 samples are presented in bar plots in the appendix D in Figure D.45.
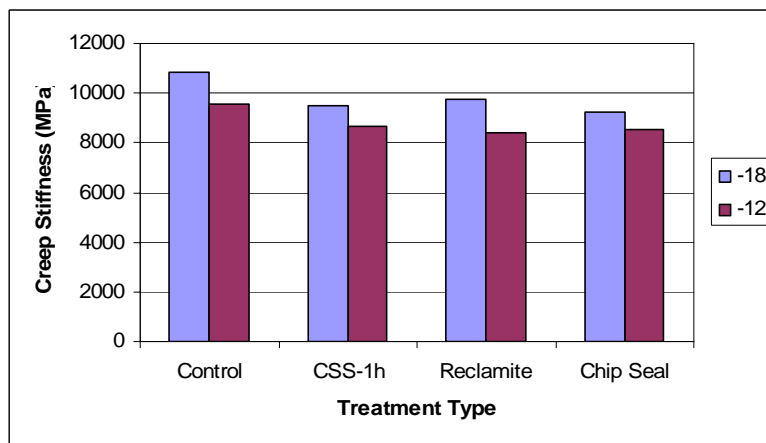
Figure 5.33. S_{mix} at 60 sec. for wheel path, TH 251 sections

The control section samples located in the wheel path have the highest mixture stiffness at both temperatures. On the other hand, the mixtures treated with chip seal have the lowest stiffness and the highest *m*-values. It is also observed that for the samples located between the wheel paths, the highest stiffness corresponds to the mixture treated with CSS-1h.

The correlation matrix for the mixture creep stiffness and *m*-value at 60 seconds, voids, location and temperature is presented in Table 5.19. Correlation factors more than 0.5 (*n* = 16) are significant and presented in bold. Correlation factors similar to the factors for TH 56 are observed for TH 251 sections. A negative and almost significant correlation is observed between void content and the creep stiffness of the mixture, indicating that if the air void content in the mixture increases then its stiffness is reduced.

Table 5.19. Correlation matrix for mixture BBR results of TH 251 sections

Location	1				
m_{mix}	-0.122	1			
S_{mix}	0.312	**-0.560**	1		
Temperature	0	**0.938**	-0.385	1	
Voids	**0.506**	0.071	-0.475	0	1
	Location	m	S_{mix}	Temperature	Voids

For the ANOVA analysis the type of surface treatment was treated as a dummy variable with the control section as the reference level. ANOVA results for the BBR mixture results of TH 251 are presented in Table 5.20.

Table 5.20. ANOVA of BBR mixture results for TH 251 sections

Coefficient	S_{mix}@60 sec.		m_{mix}@ 60 sec.	
	Estimate	p-value	Estimate	p-value
Constant	13275	0.000	0.190	0.000
{F}Treatment[CSS-1H]	-661	0.065	0.010	0.195
{F}Treatment[RECLAMITE]	-788	**0.027**	0.004	0.550
{F}Treatment[CHIP-SEAL]	-614	0.127	0.000	0.971
Location	1404	**0.001**	-0.014	**0.049**
Temperature	-120	**0.007**	0.008	**0.000**
Voids	-1015	**0.002**	0.009	0.102

The parameters that are important in the prediction of the mixture stiffness are location, voids and temperature. Also from the negative coefficient estimate of the reclamite treatment it is observed that the samples treated with reclamite have significantly lower stiffness compared to the control section samples. Although the estimated coefficients from the other two treatments are also negative, they are not significant for the linear model proposed. The only parameters significant in the prediction of the *m*-value of the mixture are temperature and location. The location coefficient estimate for the prediction of S_{mix} is not consistent to what it is expected. The positive sign indicates that the samples located in between the wheel paths have higher stiffness than the samples located in the wheel path.

Semi-Circular Bending (SCB)

TH 56 sections

An example of a typical load–load line displacement (P-u) curve obtained from SCB testing is presented in Figure 5.34. The full set of load-LLD curves for TH 56 samples can be found in appendix D in Figures D.46- D.47 and D.48-D.49 for the sections constructed in 1995 and 1999, respectively. Each plot compares the effect of two testing temperatures (-18˚C and -30˚C) for each combination of location (wheel path or between the wheel path) and depth (upper layer, lower layer).
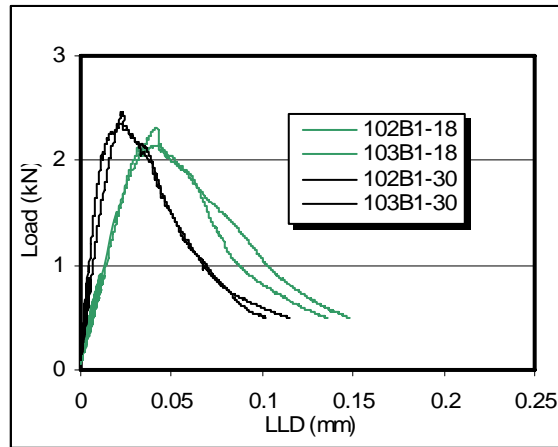
Figure 5.34. Load-LLD curves from SCB testing of control samples at -18˚C and -30˚C, between the wheel paths, TH 56 1999 sections

The following is observed in Figures D.46-D.49. The samples tested at -18°C typically had lower peak load values than the samples tested at -30°C. For the sections constructed in 1999, the specimens from the wheel path had slightly higher peak load values than the specimens from between the wheel paths. For the sections constructed in 1995, on the other hand, there was not a noticeable difference between the peak load values of the samples from the wheel path and between the wheel paths. Samples taken from the lower layer appeared to have a higher peak load value than the samples taken from the upper layer. Note that the data for one of the specimens from between the wheel path and lower layer of the section constructed in 1995 and treated in 2001 is not available due to accidental damage prior to testing.

The fracture properties (G_f, K_{IC}) of the specimens were calculated using the load-LLD curves and plotted to visually analyze the differences between treatment application year, location and depth of the specimens. An example of a bar plot for the fracture energy of samples from sections constructed in 1999 is presented in Figure 5.35. The complete set of bar plots comparing the fracture properties for the 1995 and 1999 sections are shown in appendix D in Figures D.50- D.51 and D.52-D.53, respectively.
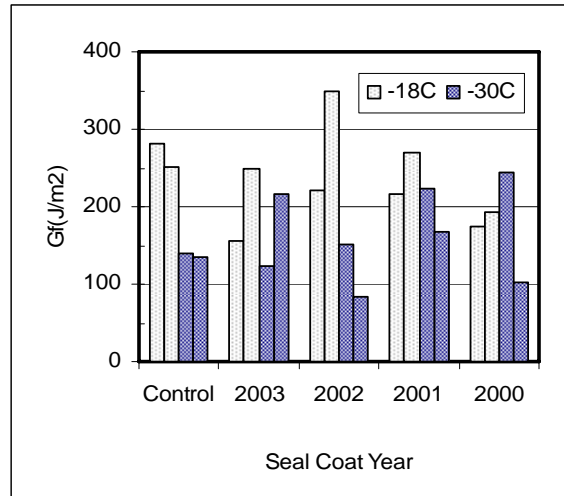
Figure 5.35. Fracture energy for samples in the wheel path, lower layer, TH 56 1999 sections

For the sections constructed in 1995, the samples treated in 2000 and 2001 located in the upper layer and in the wheel path appeared to have lower fracture energy at both temperatures than the samples at the same location but treated in 2002 and 2003. It is also observed in the 1995 sections that the specimens in the wheel path had higher fracture energy than the specimens from between the wheel paths. No significant differences with respect to the year of treatment were observed for the fracture properties of the samples from the lower layer.

For the sections constructed in 1999, the samples located in the upper layer of the treated sections have higher fracture energy at both temperatures than the samples from the control section. Samples located in the lower layer, however, show more variable results: samples from the control section had higher fracture energy than samples from the treated sections.

As seen in Figures D.50-D.53, the differences in fracture toughness with respect to the time of the surface treatment application were not visually significant due to the high variability of the test results.

As a result of visual inspection of Figures D.50-D.53, age at which the pavement is treated appeared to have an effect on the fracture properties of the mixture. For sections constructed in 1999, it seems that earlier treatment is more beneficial for the fracture properties of the mixture, on the other hand, for sections constructed in 1995, later treatment showed better fracture properties. Trends were observed in the samples from the upper layer of the pavement, which suggests that the surface treatment has an important effect on the fracture properties of the upper layer and not in the properties of the lower layer.

Statistical Analysis

The correlation matrix for the fracture toughness, fracture energy, age before treatment, depth, location, temperature and void content was calculated. The correlation matrix for the SCB results of the sections constructed in 1995 and 1999 are presented in Tables 5.21 and 5.22, respectively. Correlation factors larger than 0.25 ($n = 64$) are considered significant and are presented in bold.

Table 5.21. Correlation matrix for SCB results of TH 56 1995 sections

Age	1						
Depth	0	1					
G_f	-0.136	**0.302**	1				
K_{IC}	_-0.223_	**0.483**	0.183	1			
Location	0	0	-0.073	-0.014	1		
Temperature	0	0	**0.550**	**-0.266**	0	1	
Voids	**-0.374**	-0.169	-0.024	-0.106	0.150	0	1
	Age	**Depth**	**G_f**	**K_{IC}**	**Location**	**Temperature**	**Voids**

A significant positive correlation for the fracture toughness and fracture energy with depth is observed, indicating that both fracture parameters increase when the depth increases. Voids content and age before treatment have a negative correlation, when the age of the pavement increases then the void content is reduced. Temperature has a strong effect on both fracture parameters. For the fracture energy and fracture toughness, the correlation is positive and negative, respectively. When the temperature increases the fracture toughness decreases and the fracture energy increases. A negative correlation, close to be significant, between the age before treatment and the fracture toughness (in italic and underline) is also observed. This result may indicate that the toughness of the mixture is reduced when the age of the pavement before treatment increases.

Table 5.22. Correlation matrix for SCB results of TH 56 1999 sections

Age	1						
Depth	0	1					
G_f	0.096	-0.133	1				
K_{IC}	0.116	0.069	0.111	1			
Location	0	0	-0.189	**-0.421**	1		
Temperature	0	0	**0.452**	-0.212	0	1	
Voids	0.375	**0.289**	-0.058	**-0.255**	**0.696**	0	1
	Age	**Depth**	**G_f**	**K_{IC}**	**Location**	**Temperature**	**Voids**

As seen in Table 5.22, there is a positive correlation for the void content with location and depth meaning that as the depth increases the void content increases and that higher void content are found in samples located in between the wheel paths. A negative correlation is observed for the fracture toughness with the location and the void content, indicating that samples located in the wheel path have higher fracture toughness than samples in between the wheel paths. Also, increasing the void content reduces the fracture toughness of the sample.

ANOVA analysis was done on the SCB data using G_f and K_{IC} as dependent variables and age before treatment, depth, location, voids and temperature as independent variables. Table 5.23 presents the results of this analysis.

Table 5.23. ANOVA of SCB results for TH 56 sections

Coefficient	1995		1999	
	G_f	K_{IC}	G_f	K_{IC}
Constant	0.664	0.396	0.925	0.895
Depth	**0.005**	**0.000**	0.124	0.480
Location	0.485	0.980	0.071	0.085
Temperature	**0.000**	**0.013**	**0.000**	0.073
Voids	0.960	0.341	0.287	0.694
Age	0.528	0.186	0.697	0.571

It is observed that temperature is significant in the prediction of G_f and K_{IC} for both 1995 and 1999 sections. Also, depth is significant for the prediction of both fracture parameters for 1995 samples.

TH 251 sections

A typical load-LLD curve obtained from SCB testing of TH 251 specimens is presented in Figure 5.36. All the SCB testing curves for TH 251 samples are shown in appendix D in Figure D.54.
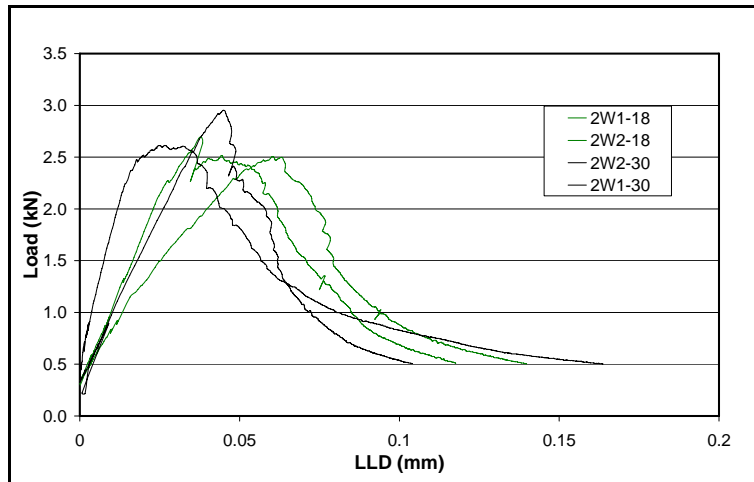
Figure 5.36. Load-LLD curves from SCB testing of control samples at -18˚C and -30˚C, wheel path,   TH 251

From Figure D.54 it is observed that samples tested at -30°C typically had higher peak load values than the samples tested at -18°C. Furthermore, samples tested at -18°C deform more than the samples tested at -30°C. Also, it is observed that specimens from the wheel path had slightly higher peak load values than the specimens from between the wheel paths.

An example of a bar plot for the fracture energy of TH 251 sections is shown in Figure 5.37. Bar plots of G_f and K_{IC} for the different surface treatments are presented in the appendix D in Figure D.55.
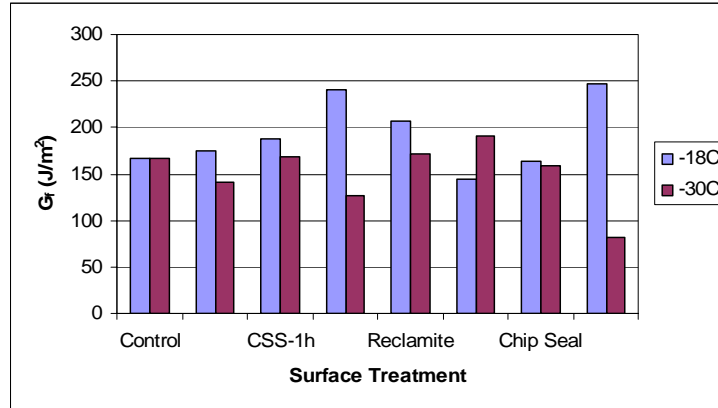
Figure 5.37. Fracture energy for samples in the wheel path, TH 251

It is observed in Figure D.55 that at -18˚C, the highest fracture toughness from between the wheel paths is obtained from the control section. On the other hand, the highest fracture toughness from the wheel path is observed in the section treated with chip seal. The highest fracture energy for both locations at -18˚C is observed in the section treated with chip seal. Also, it is observed that in between the wheel paths and at -30˚C the section treated with chip seal shows the largest fracture energy and fracture toughness. The control and reclamite sections have the highest fracture toughness and fracture energy in the wheel path and at 30˚C, respectively.

Statistical Analysis

The correlation factors between fracture toughness, fracture energy, location, temperature and void content of TH 251 samples were calculated. The correlation matrix for the SCB results of TH 251 is presented in Table 5.24. Correlation factors larger than 0.35 ($n = 32$) are significant and presented in bold.

Table 5.24. Correlation matrix for SCB results of TH 251 sections

G_f	1				
K_{IC}	-0.100	1			
Location	**-0.408**	**-0.386**	1		
Temperature	**0.404**	**-0.357**	0	1	
Voids	0.142	-0.239	**0.440**	0	1
	G_f	K_{IC}	Location	Temperature	Voids

Table 5.24 indicates that as the temperature increases, the fracture energy increases and the fracture toughness decreases. Both fracture properties are lower between the wheel paths.

ANOVA was done using G_f and K_{IC} as dependent variables and type of treatment, location, voids and temperature as independent variables. Table 5.25 presents the results of this analysis.

Table 5.25. ANOVA of SCB results for TH 251 sections

Coefficient	G_f		K_{IC}	
	Estimate	p-value	Estimate	p-value
Constant	135.20	0.034	0.848	0.000
{F}Treatment[CSS-1H]	13.46	0.486	-0.051	0.154
{F}Treatment[RECLAMITE]	-16.19	0.390	-0.040	0.249
{F}Treatment[CHIP-SEAL]	-1.06	0.960	0.009	0.816
Location	-55.21	**0.001**	-0.038	0.187
Temperature	3.12	**0.008**	-0.004	**0.035**
Voids	21.61	**0.046**	-0.024	0.217

It is observed that temperature is significant in the prediction of G_f and K_{IC} for TH 251 sections. Also, void content and location are significant for the prediction of the fracture energy. No significant differences are observed between the fracture energy and fracture toughness of the control section and the sections with surface treatments.

Additional Analysis of TH 56

Asphalt Binder

Additional analysis of variance (ANOVA) was performed on the binder data to include the effects of the design parameters of the seal coat and the emulsion application rate. Previously discussed ANOVA analysis separated the results based upon construction year; this ANOVA considers the construction year as a factor in the model. The factors and interactions of factors, significant at the 5% significance level were further investigated by using a Tukey Honest significant difference multiple comparisons test.

Table 5.26 shows the variables used in the statistical analysis. The variable "Loc" indicates the location, 1 denotes the 1999 built sections and 0 denotes the 1995 built sections. "Loc_year" indicates the year that the surface treatment was applied starting at year 2000 denoted by 1, and increasing in one year intervals until 2003 denoted by 4. The year that the surface treatment was applied is important because it is an indication of certain design parameters of the seal coat, such as the aggregate type, and the emulsion application rate as discussed earlier in chapter 2 (Table 2.1). "Depth" indicates the depth below the pavement surface, with the upper layer denoted by 1, and the lower layer denoted by 0. The variable "WP_BWP" indicates the path that the tested specimen is from, with 1 denoting the wheel path, and 0 denoting between the wheel paths. The sections or cells, which corresponds to the age of the pavement when the treatment was applied, is denoted by the interaction of "Loc" and "Loc_year" or "Loc*Loc_year".

A Box Cox analysis suggested a square root transformation of the creep stiffness data as well as a logarithmic transformation of the *m*-value data in order to make the data behave more normal. After the transformation, the data was used to perform the ANOVA analysis

Table 5.26. Explanation of Variables for ANOVA Binder

Loc	1 = 1999, 0 = 1995
Loc_year	Year of treatment application: 1, 2, 3, 4 denote 2000, 2001, 2002, 2003 respectively
Depth	1 = upper layer, 0 = lower layer
WP_BWP	1 = Wheel path, 0 = Between the wheel paths
Temp	Binder test temperatures: -24°C, -18°C

Table 5.27 and Table 5.28 present the results of the ANOVA analysis for both the transformed binder stiffness and the transformed *m*-value data, respectively. The factors that are statistically significant at the 5% significance level are indicated with bold font. Interactions of factors are denoted with the multiplication operation.

Table 5.27. ANOVA Table for extracted binder $\sqrt{S}$

Source	DF	SS	MS	F	P
Loc	**1**	**1.9573**	**1.9573**	**8.42**	**0.0046**
Loc_year	**3**	**17.324**	**5.77466**	**24.84**	**0**
WP_BWP	1	0.73703	0.73703	3.17	0.078
Depth	1	0.80519	0.80519	3.46	0.0657
Temp	**1**	**1250.13**	**1250.13**	**5377.27**	**0**
Loc*Loc_year	**3**	**3.88801**	**1.296**	**5.57**	**0.0014**
Loc*Depth	**1**	**1.27649**	**1.27649**	**5.49**	**0.0211**
Loc*Temp	1	1.55E-07	1.55E-07	0	0.9994
Loc*WP_BWP	**1**	**1.56989**	**1.56989**	**6.75**	**0.0108**
Loc_year*Depth	**3**	**1.86958**	**0.62319**	**2.68**	**0.0509**
Loc_year*Temp	3	1.3289	0.44297	1.91	0.1336
Loc_year*WP_BWP	3	0.39359	0.1312	0.56	0.6398
Depth*Temp	1	0.41679	0.41679	1.79	0.1836
WP_BWP*Depth	1	0.28969	0.28969	1.25	0.267
WP_BWP*Temp	1	0.26353	0.26353	1.13	0.2896

Table 5.29 compares the significant factors between the two ANOVA asphalt binder models ($\sqrt{S}$ and log[*m*]). The two models are not affected equally by the same factors; some factors that are significant in one model are not significant in the other model. There are five significant factors in the stiffness model, and seven significant factors in the *m*-value model, with four significant factors in common between the two models. All significant factors are denoted with bold font in the table.

Table 5.28. ANOVA Table for extracted binder log[m]

Source	DF	SS	MS	F	P
Loc	**1**	**0.00061**	**0.00061**	**4.79**	**0.031**
Loc_year	**3**	**0.00728**	**0.00243**	**19.01**	**0**
WP_BWP	**1**	**0.00582**	**0.00582**	**45.58**	**0**
Depth	**1**	**0.00154**	**0.00154**	**12.07**	**0.0008**
Temp	**1**	**0.2599**	**0.2599**	**2036.96**	**0**
Loc*Loc_year	3	0.00073	0.00024	1.9	0.1351
Loc*Depth	**1**	**0.00265**	**0.00265**	**20.81**	**0**
Loc*Temp	1	0.00003	0.00003	0.27	0.6018
Loc*WP_BWP	1	0.00007	0.00007	0.51	0.4757
Loc_year*Depth	**3**	**0.00229**	**0.00076**	**5.98**	**0.0009**
Loc_year*Temp	3	0.00038	0.00013	1.01	0.3936
Loc_year*WP_BWP	3	0.0003	0.0001	0.79	0.5035
Depth*Temp	1	0.00027	0.00027	2.11	0.1497
WP_BWP*Depth	1	0.00008	0.00008	0.65	0.4227
WP_BWP*Temp	1	0.0001	0.0001	0.79	0.377

Table 5.29. Binder: Comparison of significant factors of $\sqrt{S}$ and log[m]

	Sqrt[S]		Log[m]	
Source	F	P	F	P
Loc	**8.42**	**0.0046**	**4.79**	**0.031**
Loc_year	**24.84**	**0**	**19.01**	**0**
WP_BWP	3.17	0.078	**45.58**	**0**
Depth	3.46	0.0657	**12.07**	**0.0008**
Temp	**5377.3**	**0**	**2037**	**0**
Loc*Loc_year	**5.57**	**0.0014**	1.9	0.1351
Loc*Depth	**5.49**	**0.0211**	**20.81**	**0**
Loc*Temp	0	0.9994	0.27	0.6018
Loc*WP_BWP	6.75	0.0108	0.51	0.4757
Loc_year*Depth	2.68	0.0509	**5.98**	**0.0009**
Loc_year*Temp	1.91	0.1336	1.01	0.3936
Loc_year*WP_BWP	0.56	0.6398	0.79	0.5035
Depth*Temp	1.79	0.1836	2.11	0.1497
WP_BWP*Depth	1.25	0.267	0.65	0.4227
WP_BWP*Temp	1.13	0.2896	0.79	0.377

Table 5.30 presents the results of the Tukey comparison test for the effect of the construction year (Loc). The mean represents the mean value of the level within the factor, and H Groups denotes homogenous groups which are represented by letters. Levels within a factor that are significantly different from one another are denoted by different letters, where levels within a factor that are indistinguishable from one another share a common letter. The results indicate that the 1995 pavement section has a higher *m*-value and correspondingly lower creep stiffness than the 1999 pavement. However, the difference between the two creep stiffness values is approximately 10MPa, which may not be a practically significant value.

Table 5.30. Tukey HSD Test of asphalt binder $\sqrt{S}$ and log[m] for Construction Year (Loc)

	Loc	Mean	H-Groups
$\sqrt{S}$	1	19.503	A
	0	19.253	B
Log[m]	0	-0.5643	A
	1	-0.5687	B

Table 5.31 presents the results of the Tukey comparison test for the effect of the treatment year on the creep stiffness and the *m*-value. Note that 1 represents the year 2000, when New Ulm Quartzite was used; 2 represents the year 2001 when Dresser Trap Rock was used (Note Dresses Trap Rock was used in 2002 and 2003 as well). Both of these application years had approximately the same emulsion application rates (see Table 2.1). Note that the mean of the square root of the binder stiffness of 1 is significantly higher than 2 and 4; and 2 & 4 are indistinguishable from one another. The *m*-value model confirms these results showing the inverse behavior of the creep stiffness model.

Table 5.31. Tukey HSD Test of asphalt binder $\sqrt{S}$ and log[m] for treatment application year (Loc_year)

	Loc_year	Mean	H-Groups
$\sqrt{S}$	1	19.97	A
	2	19.368	B
	4	19.221	BC
	3	18.954	C
Log[m]	3	-0.5561	A
	2	-0.5628	A
	4	-0.5715	B
	1	-0.5757	B

Table 5.32 presents the results of the Tukey comparison test for the effect of temperature on the creep stiffness and *m*-value. The statistics confirm the previous visual observations made earlier that the stiffness increases with a decrease in temperature, and the *m*-value shows the inverse relationship. Note that the differences between temperatures are both statistically and practically significant.

Table 5.32. Tukey HSD Test of asphalt binder $\sqrt{S}$ and log[m] for Temperature (Temp)

	Temp	Mean	H-Groups
$\sqrt{S}$	-24	22.534	A
	-18	16.223	B
Log[m]	-18	-0.521	A
	-24	-0.612	B

Table 5.33 presents the results of the Tukey comparison test for the effect of the depth and path on the m-value. Note that these factors were not significant in the stiffness model. The results indicate that the lower layer has a statistically significantly higher relaxation rate than the upper layer. The relaxation rate of the wheel path is statistically significantly higher than the relaxation rate between the wheel paths.

Table 5.33. Tukey HSD Test of asphalt binder log[m] for Depth and Path

Variable		Mean	H-Groups
Depth	0	-0.563	A
	1	-0.57	B
WP_BWP	1	-0.5597	A
	0	-0.5733	B

Table 5.34 presents the results of the Tukey comparison test for the effect of the interaction of loc and depth. Note that the bottom layer shows statistically significantly lower relaxation rates for the 1995 section, and the relaxation rates of the remaining loc, depth interactions are indistinguishable from one another. The results of the stiffness model agrees with those of the *m*-value model showing that the lower layer of the 1995 section has the highest stiffness, where the other loc, layer combinations are all indistinguishable from one another. Note that the difference between the two homogenous groups is not large.

Table 5.34. Tukey HSD Test of asphalt binder $\sqrt{S}$ and log[m] for Construction year and depth interaction (Loc*depth)

	Loc	Depth	Mean	H-Groups
$\sqrt{S}$	1	0	19.684	A
	1	1	19.322	B
	0	1	19.274	B
	0	0	19.233	B
Log[m]	0	0	-0.5562	A
	1	1	-0.5676	B
	1	0	-0.5698	B
	0	1	-0.5724	B

Table 5.35 presents the results of the Tukey comparison test for the effect of the surface treatment timing on the creep stiffness. Note that this is the only model that showed treatment year as a significant factor. The section (cell) numbers were added to aid in interpretation.

Table 5.35. Tukey HSD Test of asphalt binder $\sqrt{S}$ for age of pavement construction year and treatment year interaction (Loc*Loc_year)

Cell	Loc	Loc_year	Mean	H-Groups
15	0	1	19.99	A
14	1	1	19.95	A
16	0	2	19.374	B
12	1	3	19.37	B
13	1	2	19.362	B
11	1	4	19.331	B
18	0	4	19.111	B
17	0	3	18.538	C

Table 5.35 shows that sections 14 and 15 are indistinguishable from one another; even though they were four years apart in age, they had the same aggregate type and emulsion application rate for the seal coat. Cells 16, 12, 13, 11, and 18 are all indistinguishable from one another, and all have statistically significantly lower creep stiffness values than cells 15 and 14 by approximately 30 MPa. Cell 17 has the lowest creep stiffness value, approximately 60MPa less than cells 15 and 14, which is difficult to understand because it had the second highest age before treatment was applied. From the analysis, it appears that the optimal application time is 7 years after construction as this cell statistically had the lowest creep stiffness. However this result is not confirmed by the statistical analysis of the *m*-value.

Table 5.36 presents the results of the Tukey comparison test for the effect of the interaction of depth with surface treatment application year (loc_year). Generally speaking, most of the cells are indistinguishable from one another, and the cells that are statistically different do not differ by much. The lower layer of cells treated in 2003 have a statistically significantly higher *m*-value than the upper layer of cells treated the same year; there is no observable difference between the upper and lower layers for the other three treatment years.

Table 5.36. Tukey Test of binder log[m] for treatment year and depth interaction

Loc_year	Depth	Mean	H-Groups
3	0	-0.5539	A
2	0	-0.5575	AB
3	1	-0.5583	AB
4	0	-0.5624	ABC
2	1	-0.5682	BCD
1	1	-0.5731	CDE
1	0	-0.5782	DE
4	1	-0.5806	E

Asphalt Mixtures

A Box Cox analysis suggested no transformation for the creep stiffness data, but recommended a square root transformation of the *m*-value data to avoid violation of the normality assumption. ANOVA was performed in a similar manner as for the extracted binders. Table 5.37 presents the explanation of variables. Note that the asphalt mixture test temperatures are higher than the asphalt binder test temperatures (-18°C is the only common temperature). All other variables and definitions are the same as the binder models.

Table 5.37. Explanation of Variables for ANOVA mixtures

Loc	1 = 1999, 0 = 1995
Loc_year	Year of treatment application: 1, 2, 3, 4 denote 2000, 2001, 2002, 2003 respectively
Depth	1 = upper layer, 0 = lower layer
WP_BWP	1 = Wheel path, 0 = Between the wheel paths
Temp	Mixture test temperatures: -18°C, -12°C, -6°C

Table 5.38 and Table 5.39 present the results of the ANOVA analysis for the creep stiffness and the square root transformed *m*-value data respectively. Factors that are significant at the 5% significance level are indicated by bold font. Interactions between factors are denoted by the multiplication operation. Only two way interactions were investigated because of the difficulty of interpreting three way interactions.

Table 5.38. ANOVA Table for Asphalt Mixture S

Source	DF	SS	MS	F	P
Loc	**1**	**1.33E+07**	**1.33E+07**	**12.4**	**5E-04**
Loc_year	3	3089220	1029740	0.96	0.413
WP_BWP	**1**	**1.72E+07**	**1.72E+07**	**16**	**1E-04**
depth	**1**	**7995910**	**7995910**	**7.44**	**0.007**
temp	**2**	**5.59E+08**	**2.80E+08**	**260**	**0**
Loc*Loc_year	3	6466588	2155529	2.01	0.113
Loc*depth	1	98120.2	98120.2	0.09	0.763
Loc*temp	**2**	**1.05E+07**	**5227259**	**4.86**	**0.008**
Loc*WP_BWP	**1**	**1.15E+07**	**1.15E+07**	**10.7**	**0.001**
Loc_year*depth	3	2788088	929363	0.86	0.46
Loc_year*temp	6	7205858	1200976	1.12	0.352
Loc_year*WP_BWP	**3**	**8573755**	**2857918**	**2.66**	**0.049**
depth*temp	**2**	**1.37E+07**	**6870657**	**6.39**	**0.002**
WP_BWP*depth	1	1398205	1398205	1.3	0.255

Table 5.39. ANOVA Table for Asphalt Mixture $\sqrt{m}$

Source	DF	SS	MS	F	P
Loc	**1**	**0.067**	**0.067**	**163**	**0**
Loc_year	**3**	**0.005**	**0.002**	**4.01**	**0.01**
WP_BWP	1	8E-04	8E-04	1.96	0.16
depth	**1**	**0.025**	**0.025**	**59.8**	**0**
temp	**2**	**0.704**	**0.352**	**853**	**0**
Loc*Loc_year	3	0.002	5E-04	1.28	0.28
Loc*depth	**1**	**0.003**	**0.003**	**6.28**	**0.01**
Loc*temp	**2**	**0.007**	**0.004**	**8.77**	**0**
Loc*WP_BWP	1	2E-04	2E-04	0.45	0.5
Loc_year*depth	3	0.003	0.001	2.5	0.06
Loc_year*temp	6	0.003	5E-04	1.28	0.26
Loc_year*WP_BWP	3	0.002	6E-04	1.56	0.2
depth*temp	**2**	**0.008**	**0.004**	**9.87**	**0**
WP_BWP*depth	**1**	**0.003**	**0.003**	**7.54**	**0.01**

Table 5.40 compares the significant factors between the two ANOVA asphalt mixture models. There are six significant factors in the creep stiffness model, and eight significant factors in the *m*-value model. There are four significant factors that the models have in common, and in all four factors the *m*-value shows much more significance than the creep stiffness model.

Table 5.40. Comparison of significant factors of Asphalt Mixture S and $\sqrt{m}$

	S		sqrt[m]	
Source	F	P	F	P
Loc	**12**	**5E-04**	**162.6**	**0**
Loc_year	1	0.413	**4.01**	**0.01**
WP_BWP	**16**	**1E-04**	1.96	0.16
depth	**7.4**	**0.007**	**59.81**	**0**
temp	**260**	**0**	**853.2**	**0**
Loc*Loc_year	2	0.113	1.28	0.28
Loc*depth	0.1	0.763	**6.28**	**0.01**
Loc*temp	4.9	0.008	**8.77**	**0**
Loc*WP_BWP	11	0.001	0.45	0.5
Loc_year*depth	0.9	0.46	2.5	0.06
Loc_year*temp	1.1	0.352	1.28	0.26
Loc_year*WP_BWP	**2.7**	**0.049**	1.56	0.2
depth*temp	**6.4**	**0.002**	**9.87**	**0**
WP_BWP*depth	1.3	0.255	**7.54**	**0.01**

The effect of construction year on the m-value is the most significant factor in all four models, with the exception of temperature. The construction year has an F ratio of over 160; by comparison the effect of temperature on the creep stiffness properties has an F ratio of 260. There is roughly a 17% difference between the means of the two pavement sections. A fairly strong conclusion can be made that the 1995 pavement has a statistically (and practically) significantly lower m-value than the 1999 section. This could be due to the aging and hardening of the pavement which supports earlier work found in the literature.

Table 5.41 presents the results of the Tukey comparison test for the effect of the construction year (Loc) which shows that the 1995 built section has a significantly higher creep stiffness than the 1999 built section, this contradicts the earlier asphalt binder results which revealed that the 1999 section had the highest creep stiffness. The m-value of the 1999 section is significantly higher than the m-value of the 1995 section which agrees with the results of the stiffness model, and again contradicts the binder results given earlier.

Table 5.41. Tukey HSD Test of Asphalt Mixture S and $\sqrt{m}$ for Construction Year (Loc)

	Loc	Mean	H-Group
S	0	8393.7	A
	1	7932.5	B
$\sqrt{m}$	1	0.3845	A
	0	0.3517	B

Table 5.42 presents the results of the Tukey comparison test for the effect of the depth on the m-value and creep stiffness. The lower layer has a significantly higher relaxation rate than the upper layer. The effect of depth on the relaxation rate is also very significant with an F ratio of 60, the second highest of all four models, excluding temperature. The stiffness model supports observations that show statistically significant higher stiffness at the upper layer, but at a much lower level of significance than the m-value.

Table 5.42. Tukey HSD Test of Asphalt Mixture S and $\sqrt{m}$ for Depth

	depth	Mean	H-Group
S	1	8341.9	A
	0	7984.3	B
$\sqrt{m}$	0	0.3781	A
	1	0.3582	B

Table 5.43 presents the results of the Tukey comparison test for the effect of temperature on the m-value and the creep stiffness. The statistics confirm the previous visual observations that the stiffness increases with decrease in temperature, and the m-value shows the inverse relationship.

Table 5.43. Tukey HSD Test of Asphalt Mixture S and $\sqrt{m}$ for Temperature (Temp)

	temp	Mean	H-Group
	-18	9864.8	A
S	-12	8792.2	B
	-6	5832.4	C
	-6	0.4206	A
$\sqrt{m}$	-12	0.3861	B
	-18	0.2978	C

Table 5.44 presents the results of the Tukey comparison test for the effect of the interaction of depth and temperature. Note that, at the same temperature, the bottom layer consistently shows significantly higher relaxation rates, except at -18°C when the relaxation rates are indistinguishable from one another. Table 5.44 also shows that the relaxation rate of the top layer at -6°C is indistinguishable from the relaxation rate of the bottom layer at -12°C. The creep stiffness values are significantly different only at -6°C, when the upper layer is stiffer than the lower layer by approximately 1000 MPa, this is approximately equal to the decrease in stiffness when the test temperature is raised from -18°C to -12°C.

Table 5.44. Tukey HSD Test of Asphalt Mixture S and $\sqrt{m}$ for depth and temperature interaction (depth*temp)

	depth	temp	Mean	H-Group
	0	-18	9988.6	A
	1	-18	9741	A
	1	-12	8962	B
S	0	-12	8622.3	B
	1	-6	6322.8	C
	0	-6	5342	D
	0	-6	0.4378	A
	1	-6	0.4033	B
$\sqrt{m}$	0	-12	0.3961	B
	1	-12	0.3761	C
	0	-18	0.3002	D
	1	-18	0.2953	D

Table 5.45 presents the results of the Tukey comparison test for the effect of the interaction of path (wheel path, or between the wheel paths) with depth. This factor was only significant for the *m*-value. The *m*-values from the lower layers in either the wheel path, or between the wheel paths are indistinguishable from one another. The *m*-value from the upper layer in between the wheel paths has a higher relaxation rate than the upper layer in the wheel path. The percent difference between the *m*-values from the lower layers in either the wheel path and the upper layer of the wheel path is 14%.

Table 5.45. Tukey HSD Test of Asphalt Mixture $\sqrt{m}$ for path and depth interaction (WP_BWP*depth)

WP_BWP	depth	Mean	H-Group
1	0	0.3798	A
0	0	0.3763	A
0	1	0.3636	B
1	1	0.3528	C

Table 5.46 presents the results of the Tukey comparison test for the effect of the construction year and depth interaction on the *m*-value. The pavement constructed in 1999 has significantly higher *m*-values than the pavement constructed in 1995. The lower layer consistently has a higher relaxation rate than the upper layer. The difference between the upper and lower layers for the 1999 pavement is approximately half of the difference between the upper and lower layers for the 1995 pavement. This may be an indication that the aging process progresses down into the pavement with time.

Table 5.46. Tukey HSD Test of Asphalt Mixture $\sqrt{m}$ for construction year and depth interaction (Loc*depth)

Loc	depth	Mean	H-Group
1	0	0.3915	A
1	1	0.3775	B
0	0	0.3646	C
0	1	0.3389	D

Table 5.47 presents the results of the Tukey comparison test for the effect of the seal coat application year, which is related to certain design parameters, on the *m*-value. Note that 1 corresponds to 2000 when New Ulm Quartzite aggregate was used; 2 corresponds 2001 when Dresser Trap Rock aggregate was used (Dresser Trap Rock was also used in 2002 and 2003). Seal coats applied in these two years had approximately the same emulsion application rates. These results do not confirm the results of the binder analysis which indicated statistical differences between 1 and 2. They do show that the *m*-value of 3 is significantly higher than the *m*-value of 4.

Table 5.47. Tukey HSD Test of Asphalt Mixture $\sqrt{m}$ for Seal Coat Application Year (Loc_year)

Loc_year	Mean	H-Group
3	0.3752	A
2	0.368	AB
1	0.3661	AB
4	0.3632	B

Table 5.48 presents the results of the Tukey comparison test for the effect of the path (wheel path, or between the wheel paths) on the stiffness. The wheel path has a significantly higher stiffness than between the wheel paths by approximately 500MPa.

Table 5.48. Tukey HSD Test of Asphalt Mixture S for path (WP_BWP)

WP_BWP	Mean	H-Group
1	8428.4	A
0	7897.8	B

Table 5.49 presents the results of the Tukey comparison test for the effect of the interaction of path (wheel path, or between the wheel paths) with the pavement construction year, Loc. This interaction was only significant for the stiffness, and not the *m*-value. The stiffness from the lower layer of the 1999 built section is approximately 1000 MPa less than all of the other combinations of path and construction year, which are all indistinguishable from one another.

Table 5.49. Tukey HSD Test of Asphalt Mixture S for path and construction year interaction (WP_BWP*Loc)

Loc	WP_BWP	Mean	H-Group
0	1	8442.2	A
1	1	8414.7	A
0	0	8345.3	A
1	0	7450.3	B

Summary

A summary of the analyses performed previously is presented in Table 5.50. In this table, the red colored cells (darker shadow) contain the parameters that are significant at 5% level; the yellow colored cells (lighter shadow) contain the parameters that are not significant. The positive or negative signs indicate the direction of the relation between the two variables and the cells with "NA" show that the analysis for the two parameters does not apply. The following conclusions can be drawn from Table 5.50:

- Age before treatment of the pavement affects the results of FTIR, BBR binder and DSR. From these three tests, FTIR appears to be the most sensitive to the age of the material. Contrary to what it is expected, BBR and DSR testing indicates that older sections have less stiffness; this trend can be explained by the fact that the emulsion application rate increased with the age of the pavement.

- All the properties obtained from mechanical testing of both mixtures and binders are significantly affected by the temperature. Mixture fracture energy, BBR m_{mix} and m_{binder} at 60 seconds and binder strain at failure increase with temperature increase. On the other hand, mixture fracture toughness, S_{mix} and S_{bin} at 60 seconds and binder failure stress decrease with temperature decrease.

- TH 56 samples located in the wheel path have higher mixture fracture energy and BBR S_{mix} at 60 seconds and larger binder phase angle than samples between the wheel paths. More aging is observed in between the wheel path samples from FTIR testing.

- Mixture fracture energy, fracture toughness, S_{mix}, m_{mix}, S_{bin}, m_{binder}, binder stress and strain at failure and phase angle are overall greater in the lower layer than in the upper layer.

- Higher air void content reduces BBR S_{mix} and increases m_{mix} and mixture fracture energy.

- For TH 251, the pavement sections where surface treatments were applied have less S_{mix} and higher m_{mix} compared to the control section.

The summary of all the correlation matrices calculated before is presented in Table 5.51. The cells in red (darker shadow) indicate high correlation (more than 5% of significance, values larger than $2/n^{0.5}$ where n is the number of samples), the cells in orange (lighter shadow) represent correlation values close to be significant (low correlation), the cells in white (no shadow) represent no correlation between the parameters and cells with "NA" are cases for which the calculations do not apply. Generally, the observations made from the previous table are confirmed. The following additional conclusions can be drawn from Table 5.51:

- Mixture fracture toughness of samples from TH 56 constructed in 1995 decreases with the aging of the pavement. Also, there is negative correlation between the age of the pavement and the phase angle of the binder.

- Air void content negatively affects the fracture toughness of the specimen. As the voids in the sample increases the fracture toughness decreases.

Table 5.50. Summary ANOVA for all test results

Test →	SCB				BBR mix				BBR binder				Direct Tension				DSR				FTIR
	Gf		K_{IC}		S_{mix} @60sec		m_{mix} @60 sec		S @60sec		m @60 sec		σ_f		ε_f		δ @ 4C,10 rad/sec		IG*I @ 4C,10 rad/sec		Carbonyl area
Project →	TH 56		TH 251	TH 56		TH 251	TH 56		TH 251	TH 56		TH 251	TH 56		TH 251	TH 56		TH 251	TH 56		TH 251	TH 56
	95	99		95	99		95	99		95	99		95	99		95	99		95	99		95	99
Age	+		NA			NA			NA	-	-	NA			NA			NA	NA		NA	+	+
Temperature	+	+	+	-		-	-		+	-	+	+	-	-	-	-	+	+	-		-	+	NA
Location		-	-	+		+			-					-			-		-		-	+	+
Depth	+		NA	+		NA	+		NA	+		NA	+		NA	+		NA			NA	-	-
Air voids			+	-	NA		-	NA	NA	NA	NA	NA	NA	NA	NA	NA	NA	NA	NA	NA	+	NA	NA
Treatment	NA	NA		NA	NA		NA	NA		NA	NA		NA	NA		NA	NA		NA	NA		NA	NA

Significant, p-value < 0.05 (red)
Not significant, p-value>0.05 (yellow)

Table 5.51. Summary correlation matrix for all test results

Test →	SCB				BBR mix				BBR binder				Direct Tension				DSR				FTIR
	Gf		K_{IC}		S_{mix} @60sec		m_{mix} @60 sec		S @60sec		m @60 sec		σ_f		ε_f		δ @ 4C,10 rad/sec		IG*I @ 4C,10 rad/sec		Carbonyl area
Project →	TH 56		TH 251	TH 56		TH 251	TH 56		TH 251	TH 56		TH 251	TH 56		TH 251	TH 56		TH 251	TH 56		TH 251	TH 56
	95	99		95	99		95	99		95	99		95	99		95	99		95	99		95	99
Age			NA			NA			NA			NA			NA	+		NA		-	NA	+
Temperature	+	+	+	-	+	+	+	+	+	-	+	+	-	-	+	+	+	NA	-		NA	NA
Location			-	+	-		+		-				+	+			-		NA	+	NA	+
Depth	+		NA			NA			NA			NA	+		NA	+		NA		-	NA	-
Air voids			-			-				NA	NA	NA	NA	NA	NA	NA	NA	NA	NA	NA	NA	NA

High correlation (red)
Low correlation (orange)
No correlation (white)

To isolate interactions between the results from the upper and lower layer the correlation matrices for each test, including each layer separately were calculated. Tables 5.52-5.53 show the summary of the correlation factors for the upper and lower layer, respectively.

Table 5.52. Summary correlation matrix for upper layer

Test →	SCB				BBR mix				BBR binder				Direct Tension				DSR			
	Gf		K_{IC}		S_{mix} @60 sec		m_{mix} @60 sec		S @60sec		m @60 sec		σ_f		ε_f		δ @4C,10 rad/sec		IG*I @4C,10 rad/sec	
Project →	TH 56		TH 56		TH 56		TH 56		TH 56		TH 56		TH 56		TH 56		TH 56		TH 56	
	95	99	95	99	95	99	95	99	95	99	95	99	95	99	95	99	95	99	95	99
Age	-		-	-														-		
Temperature	+	+		-	-	-	+	+	-	-	+	+		-	+	+	NA	NA	NA	NA
Location			+	-																
Air voids				-					NA	NA	NA	NA	NA	NA	NA	NA	NA	NA	NA	NA

- ■ High correlation
- ▨ Low correlation
- □ No correlation

Table 5.53. Summary correlation matrix for lower layer

Test →	SCB				BBR mix				BBR binder				Direct Tension				DSR			
	Gf		K_{IC}		S_{mix} @60sec		m_{mix} @60 sec		S @60sec		m @60 sec		σ_f		ε_f		δ @4C,10 rad/sec		IG*I @4C,10 rad/sec	
Project →	TH 56		TH 56		TH 56		TH 56		TH 56		TH 56		TH 56		TH 56		TH 56		TH 56	
	95	99	95	99	95	99	95	99	95	99	95	99	95	99	95	99	95	99	95	99
Age				+														+		-
Temperature	+	+	-		-	-	+	+	-	-	+	+		-	+	+	NA	NA	NA	NA
Location		-	-	-	+		-										-			
Air voids									NA	NA	NA	NA	NA	NA	NA	NA	NA	NA	NA	NA

- ■ High correlation
- ▨ Low correlation
- □ No correlation

It is observed in Table 5.52 that in the upper layer, age before treatment has a low correlation with both fracture properties and the strain at failure from direct tension. These correlations were not observed previously when all the information of the tests was included. Notice that in Table 5.53 the trend observed for the lower layer between the fracture toughness and age is the opposite than the trend for the upper layer. This observation is not well understood and further testing needs to be performed. The previous negative correlation that was not expected between the age of the pavement and the complex modulus from DSR is observed only in the lower layer and not in the upper layer where most of the aging occurs.

Investigation of the correlation between the different mechanical tests performed in this study was done by calculating the correlation matrix between the results of each test at the only temperature that was common to all tests, -18˚C. Table 5.54 shows the correlations between all the parameters obtained in the mechanical testing at -18˚C.

Table 5.54. Summary correlation matrix for all test results @ -18°C

Test →	SCB				BBR mix				BBR binder				Direct Tension			
	Gf		K_{IC}		S_{mix} @60sec		m_{mix} @60 sec		S @60sec		m @60 sec		σ_f		ε_f	
Project →	TH 56		TH 56		TH 56		TH 56		TH 56		TH 56		TH 56		TH 56	
	95	99	95	99	95	99	95	99	95	99	95	99	95	99	95	99
Age					+				-	-						
Location		-		-		-		+				-	+			
Depth	+		+		+			+			+	+				
Air voids						-		+								
Gf^*	NA	NA	+			+		-			+	+				-
K_{IC}^*	+		NA	NA	+	+		-								
S_{mix}^*		+	+	+	NA	NA	-	-				+				
m_{mix}^*		-		-	-	-	NA	NA				-	-			
S_{binder}^*									NA	NA						
m_{binder}^*	+	+				+		-			NA	NA			+	
σ_f^*		-					-						NA	NA	+	+
ε_f^*											+		+	+	NA	NA

*Correlations calculated based on values corresponding to each test section as indicated in column titles

🟥	High correlation
🟨	Low correlation
⬜	No correlation

In Table 5.54 BBR testing of the mixture shows promising results regarding aging characterization. The stiffness of the mixture increases as it was expected when the age of the pavement increases. BBR mixture results may contain explanatory information to predict SCB, BBR binder and direct tension test parameters. Contrary to the expected trend, the stiffness of the binder at 60 seconds decreases with the aging of the pavement. Calculation of the correlation factors with samples from both the upper and lower layer of the pavement may cause this unexpected correlation. Note that these correlations are based on test results at -18°C which suggests that at lower temperatures (-24°C) the BBR mixture results tend to asymptotic values and less difference is observed.

Additional correlation matrices were calculated for all the test parameters at -18°C for the upper and lower layer, separately. Tables 5.55-5.56 shows the summary results for the upper and lower layer, respectively.

Table 5.55. Summary correlation matrix for upper layer @ -18°C

Test →	SCB				BBR mix				BBR binder				Direct Tension			
	Gf		K_{IC}		S_{mix} @60sec		m_{mix} @60 sec		S @60sec		m @60 sec		σ_f		ε_f	
Project →	TH 56		TH 56		TH 56		TH 56		TH 56		TH 56		TH 56		TH 56	
	95	99	95	99	95	99	95	99	95	99	95	99	95	99	95	99
Age	-				+											
Location						-		+		-			+		+	
Air voids						-		+								
Gf*	NA	NA														
K_{IC} *			NA	NA				-								
S_{mix} *					NA	NA		-								
m_{mix} *				-			NA	NA			-					
S_{binder} *								-	NA	NA	-					
m_{binder} *									-		NA	NA				
σ_f *													NA	NA	+	+
ε_f *													+	+	NA	NA

*Correlations calculated based on values corresponding to each test section as indicated in column titles

■ High correlation
■ Low correlation
□ No correlation

Table 5.56. Summary correlation matrix for lower layer @ -18°C

Test →	SCB				BBR mix				BBR binder				Direct Tension			
	Gf		K_{IC}		S_{mix} @60sec		m_{mix} @60 sec		S @60sec		m @60 sec		σ_f		ε_f	
Project →	TH 56		TH 56		TH 56		TH 56		TH 56		TH 56		TH 56		TH 56	
	95	99	95	99	95	99	95	99	95	99	95	99	95	99	95	99
Age					+			-				+				
Location	-		-	-		-	-									
Air voids					-											
Gf*	NA	NA		+			+					+				
K_{IC} *		+	NA	NA			+					+	-			
S_{mix} *		+		+	NA	NA										
m_{mix} *							NA	NA					-		-	
S_{binder} *									NA	NA	-					
m_{binder} *		+		+					-		NA	NA				
σ_f *			-				-						NA	NA	+	+
ε_f *							-						+	+	NA	NA

*Correlations calculated based on values corresponding to each test section as indicated in column titles

■ High correlation
■ Low correlation
□ No correlation

Tables 5.55 and 5.56 confirm the observations previously stated with the exception of the correlation between age and the stiffness of the binder. It is observed in Table 5.55 that for the upper layer there is no significant correlation between these two parameters. The calculation of

the correlation matrices for the two depths independently seems to remove the unexpected trend observed in Table 5.54. Another conclusion that can be drawn from Table 5.55 is that, in the upper layer of the 1995 TH 56 sections, the fracture energy decreases with the aging of the pavement.

The following observations summarize the additional ANOVA and Tukey HSD Test performed on binder data of TH 56 sections:

- The upper layer of cell 17 had significantly lower creep stiffness values than other cells; however, there was no observable pattern in the creep stiffness values with respect to time.
- The statistical analysis of the m-value did not show cell 17 as being significantly different than other cells.
- The pavement age when treated is not significant in the m-value analysis.
- The statistical analysis did find other instances of statistical significance; but in most cases, the differences between the means were very small. This explains why often times the differences were not observed in the visual analysis.

The following general observations were obtained for the additional ANOVA and Tukey HSD test analysis performed on mixtures of TH 56:

- m-value was much more sensitive to both the pavement construction year and the depth below the pavement surface, as well as the interaction between the two, than was the creep stiffness.
- 1999 sections had significantly higher relaxation rates than the 1995 sections.
- The effect of depth on the m-value, although not as pronounced as the construction year, was significant in the statistical analysis.
- The analysis indicated that the lower layer consistently had a higher m-value than the upper layer, which indicates that the m-value appears to be a good indicator of aging in asphalt pavements.
- The path was also identified as a significant factor in the statistical analysis; the creep stiffness was higher in the wheel path than between the wheel paths. This behavior could be explained by the increased compaction in the wheel paths induced by vehicle loading.

The first attempt in trying to identify the best window of time for the surface treatment application was done by plotting the average fracture properties for each section in TH 56. It is important to notice that the average value presented in the following figures, for both the fracture toughness and fracture energy, includes the results from the samples in the upper and lower layer and in the wheel path and between the wheel paths. Figure 5.38 shows the average fracture toughness against the age of the pavement before treatment for TH 56 sections. There is a window of time between 4 and 6 years were the fracture toughness is higher. However, note that the difference between the maximum and minimum fracture toughness at both temperatures may not be significant given the scale of the y-axis.
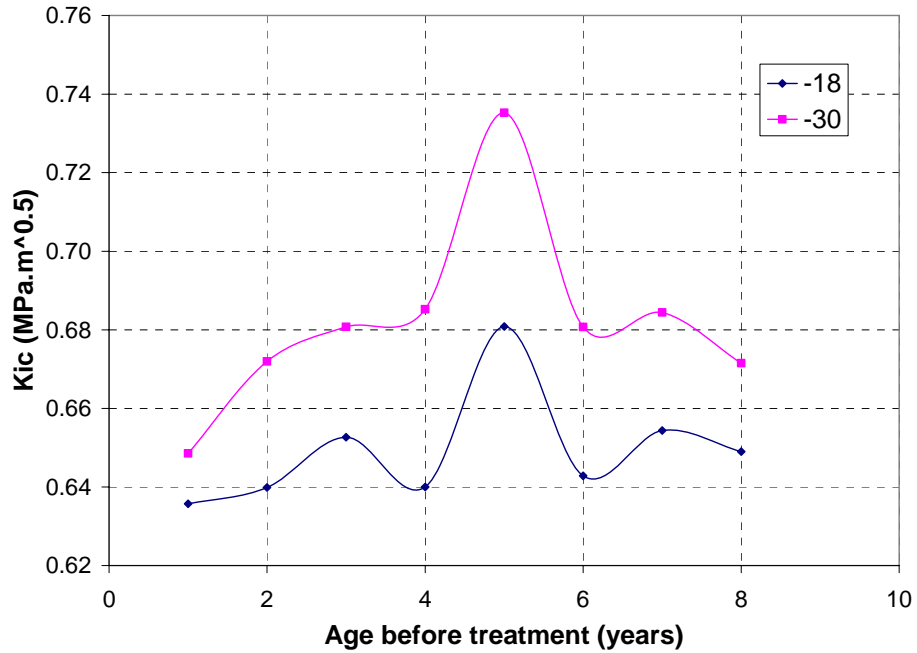
Figure 5.38. Average fracture toughness vs. age for TH 56 sections

Figure 5.39 shows the average fracture energy of all TH 56 sections versus the age of the pavement. In this plot no clear window is observed with respect to when is the best time to apply the surface treatment.
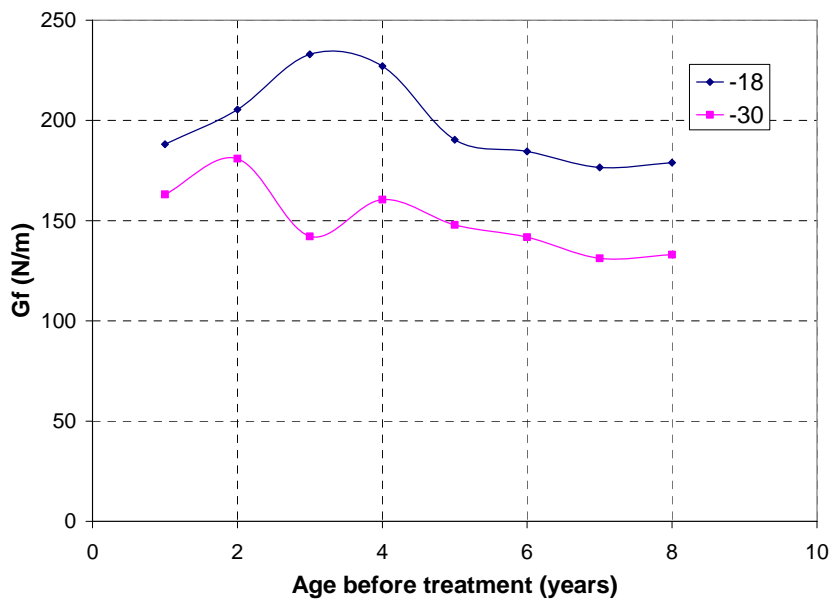
Figure 5.39. Average fracture energy vs. age for TH 56 sections

Finally, Table 5.57 presents a ranking of the three surface treatments used in this project with respect to the parameters obtained at -18˚C in the mechanical testing. In Table 5.57 rank 1

indicates most desired value and rank 4 the least desired value. Note that for low temperature performance higher values are desired for G_f, K_{IC}, m_{mix}, m_{binder}, σ_f and ε_f and lower values are desired for S_{mix} and S_{binder}.

Table 5.57. Ranking of surface treatments @ -18˚C

Rank	G_f	K_{IC}	S_{mix}	m_{mix}	S_{bin}	m_{bin}	σ_f	ε_f
1	Chip Seal	Control	Chip Seal	CSS-1h	Chip Seal	Chip Seal	Reclamite	Reclamite
2	CSS-1h	Chip Seal	Reclamite	Chip Seal	CSS-1h	CSS-1h	CSS-1h	Chip Seal
3	Control	CSS-1h	CSS-1h	Control	Control	Reclamite	Control	Control
4	Reclamite	Reclamite	Control	Reclamite	Reclamite	Control	Chip Seal	CSS-1h

Based on the limited number of tests performed in TH 251 samples it appears that the surface treatment that prevents aging the best is the chip seal. Samples from the section treated with chip seal show the highest fracture energy, the lowest stiffness of the mixture and the binder and the highest *m*-value of the binder. Additionally, the binders extracted from the section treated with chip seal show one of the highest strains at failure.

Some of these conclusions should be interpreted with caution due to the inherent variability of pavement samples and to the fact that not enough replicates were available in this study.

CHAPTER 6

ENVIRONMENTAL FACTORS

Introduction

Pavement temperature, surface heat transfer components, temperature gradients (Figure 6.1) and thermal diffusivity of the pavement are critical factors in quantifying aging effects at the surface of asphalt pavements and in modeling the pavement system response to environmental and traffic loading. Figure 6.1 indicates that during a typical hot summer day large changes of temperature occur within the top 4 cm of the pavement. This large variation of temperature in the top of the pavement has a significant influence on the aging of the asphalt binder.
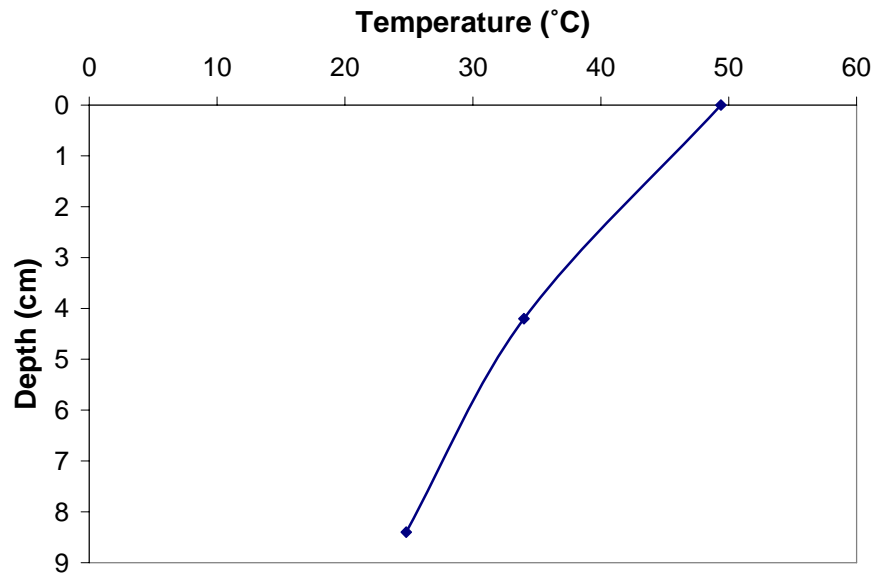
Figure 6.1. Pavement temperature variation with depth in a hot summer day (5/23/2005) MnROAD cell 33.

This chapter presents the analyses of the environmental data that influence the surface condition of asphalt pavements. This chapter includes substantial analysis of measured pavement temperature data from the MnROAD facility and simulations of pavement temperature using a one-dimensional finite difference heat transfer model. The measured pavement temperatures are characterized at diurnal and seasonal time scales, including daily extreme temperatures and temperature gradients, diurnal cycling, and seasonal variations. Temperature simulations provide more detailed information on temperature gradients in the pavement and on the surface heat transfer components than the measurements, and also help to evaluate the quality of the temperature and climate measurement system.

Pavement temperature is determined by heat fluxes at the surface of the pavement and by the thermal properties of the materials. Thus, estimation of the thermal diffusivity of the pavement is necessary in the calculation of temperatures inside an asphalt pavement. Thermal

diffusivity may also be a useful indicator of asphalt pavement aging. The change of thermal diffusivity in time may reflect aging of the pavement due to its dependency to the bonding of material molecules and the presence of microcracks and moisture; all three are expected to change over time in an asphalt pavement. In this chapter, several methods are described to extract pavement thermal diffusivity from pavement temperature measurements at two or more depths.

This chapter is divided in three parts. The first part includes the analyses of pavement temperature data from MnROAD. The second part presents the details of the models used to estimate pavement temperature and comparisons between simulated and measured temperature data. Finally, the third part shows the different methods used to estimate the thermal diffusivity of pavements. Validation of the thermal diffusivity results using MnROAD data is also performed in this study.

Analysis of Temperature Data from MnROAD Cell 33

MnROAD is one of the few research facilities in the world that is instrumented with thermocouples at different depths in the pavement that are constantly monitored for both the main line and the low volume road test cells. The MnROAD database contains extensive temperature information over the last ten years as well as extensive weather information from the weather station at MnROAD.

For this study, the temperature data from cell 33 was selected for in depth analysis. Cell 33 has been also investigated in other research projects and comprehensive mechanical properties are already available for the asphalt mixture used in this cell.

Data Preparation

MnROAD Test cell 33 has seven thermocouples recording temperature at 15 minute intervals at depths of 2.5 (1"), 7.5 (3"), 12.8 (5"), 25.2 (10"), 38.1 (15"), 43.3 (17"), and 60.1 (24") cm, with two thermocouples in the 4" thick asphalt layer (Figure 6.2). 15 minute data were obtained for the period March, 2000 to December, 2005. Small gaps in the data set, *e.g.* 1 hour, where filled using linear interpolation, while longer gaps where left blank. The pavement surface temperature was extrapolated for each time step from the 2.5 and 7.5 cm deep temperature measurements, using equation 11:

$$T_s = T_1 + (T_2 - T_1)\left(\frac{z_1}{z_2 - z_1}\right) + \frac{1}{\alpha}\frac{z_1 z_2}{2}\frac{\partial T_1}{\partial t} \qquad (11)$$

where T_1 and T_2 are the temperatures at depth z_1 (2.5 cm) and z_2 (7.5 cm), respectively, α is the thermal diffusivity of the pavement, and t is time. The first two terms on the right-hand-side of Equation 11 represent a linear extrapolation of the surface temperature, while the last term takes into account the unsteady temperature changes.

132
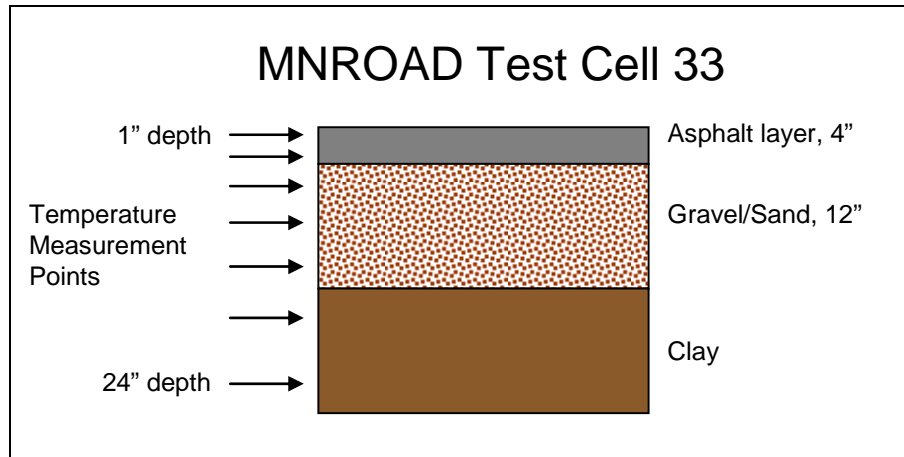
Figure 6.2. Schematic cross section of MnROAD test cell 33.

Pavement Temperature Parameters Related to Thermal Stress and Durability

A number of parameters that characterize pavement temperatures are of interest in the context of pavement durability:

- The **average pavement temperature** affects both the tensile/compressive stress level and the mechanical material properties.

- The **temperature gradient over the pavement thickness** produces bending stresses, which are a concern for rigid pavement (concrete) but of less importance for flexible pavement (asphalt). Nonetheless, it should be recognized that temperature and stress gradients may be higher at or near the surface than over the thickness of the pavement.

- The **diurnal amplitude of pavement temperature** is important for pavement fatigue analysis.

- The **time rate of change of temperature** is of interest because fast temperature changes give the material less time to relax and therefore generates higher stress levels within the material.

Time Series of Pavement Temperature Parameters

A basic analysis of pavement temperatures begins with an examination of the seasonal variation over a full year. The seasonal variation of air temperature and solar radiation is given in Figure 6.3, as these two parameters are the primary forcing parameters of pavement temperature. Figure 6.4 shows the seasonal variation of daily surface temperature and average pavement temperature for cell 33 in 2004. (In all following discussions, surface temperature refers to the extrapolated pavement surface temperature, while pavement temperature refers to the depth averaged temperature over the pavement thickness, i.e. 4 inches for cell 33). The 15 minute data was processed to calculate daily maximum, minimum, and average values of several temperature parameters plotted in Figure 6.4.
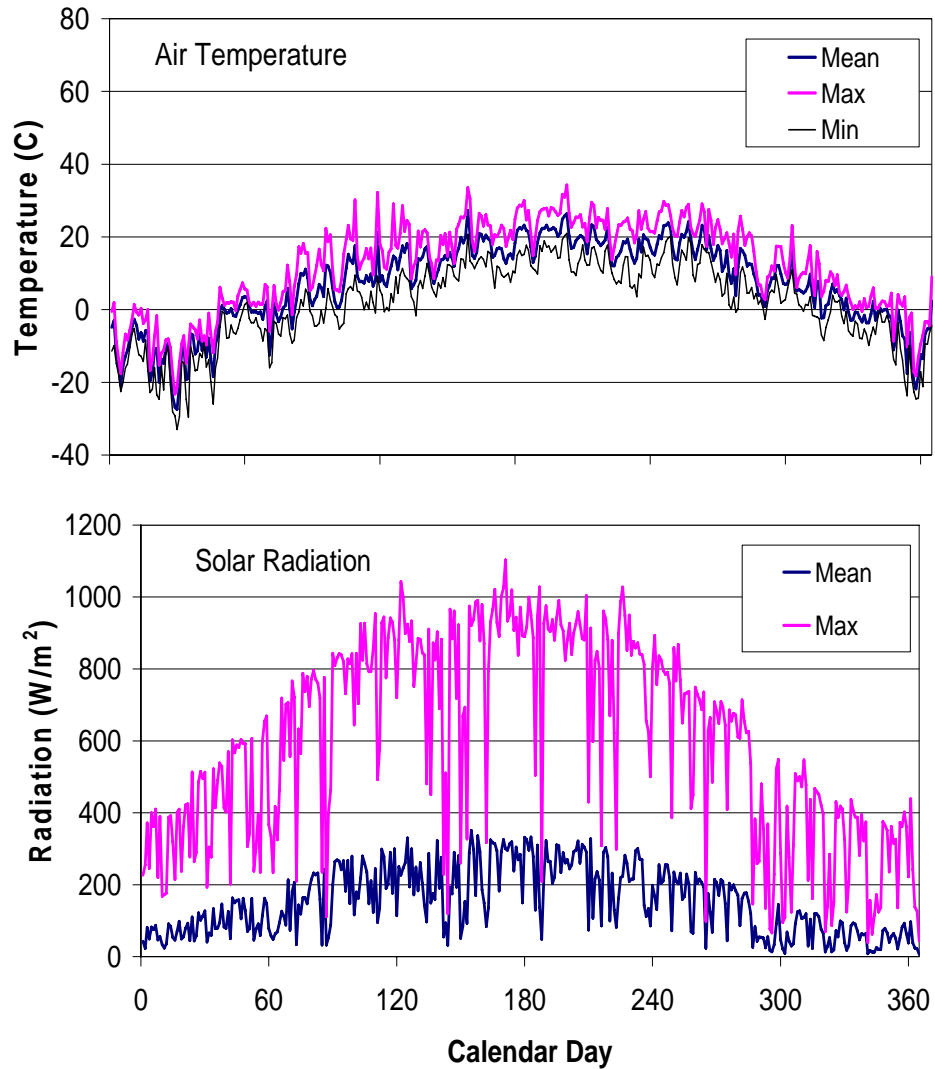
Figure 6.3. Daily mean, maximum, and minimum air temperature and daily mean, and maximum solar radiation, for MnROAD weather station, 2004.
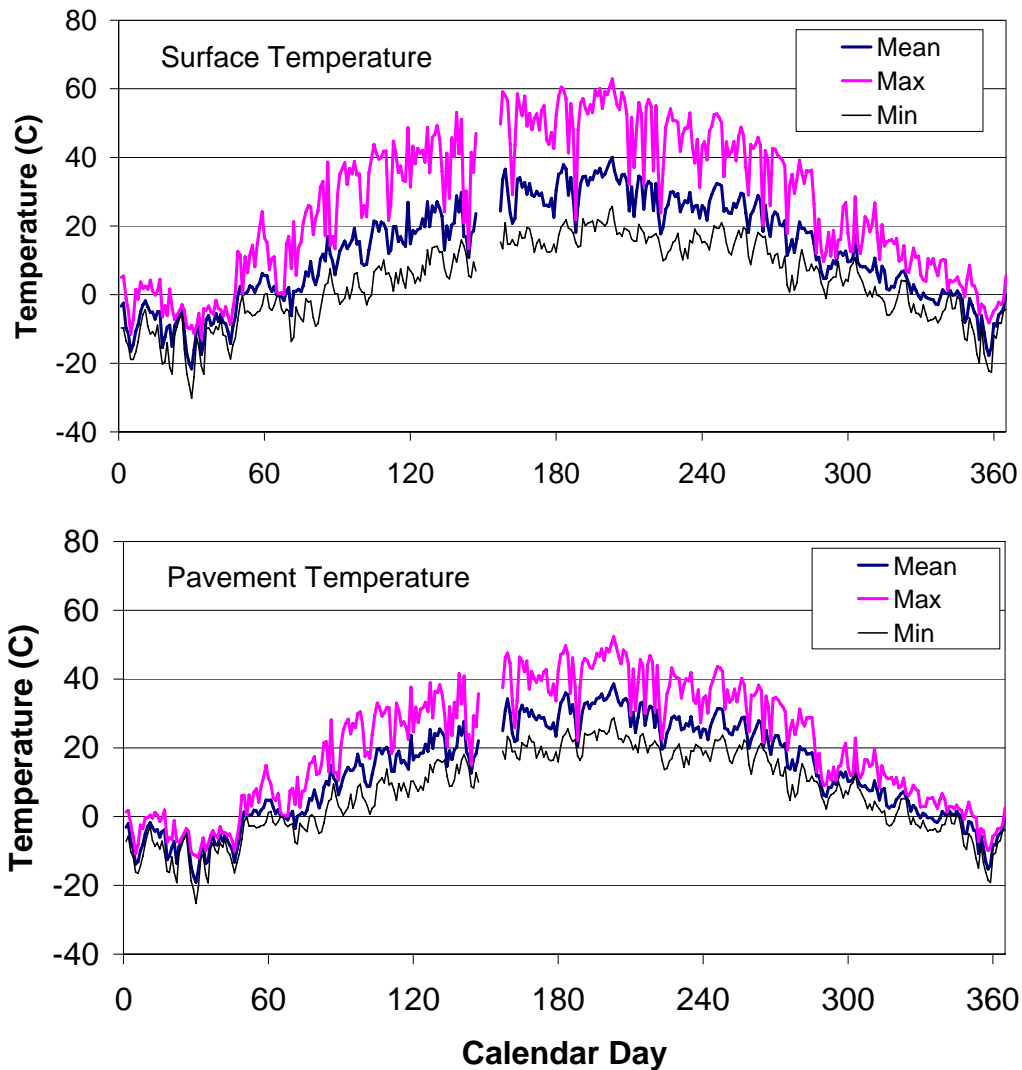
Figure 6.4. Daily mean, maximum, and minimum surface and pavement temperature for test cell 33, 2004.

The daily mean pavement temperature (Figure 6.4) is substantially higher than the daily mean air temperature (Figure 6.3). Surface and pavement temperature go through very similar seasonal variations, with maximum values in July and minimum values in January. Maximum daily surface temperature reaches 63°C, which is 11°C higher than the recorded maximum pavement temperature of 52°C. Diurnal temperature change (daily max – daily min) also exhibits a strong seasonal variation (Figure 6.5), with the highest amplitudes occurring in June. Surface temperature has a significantly higher diurnal change (up to 45°C) compared to pavement temperature (30°C).
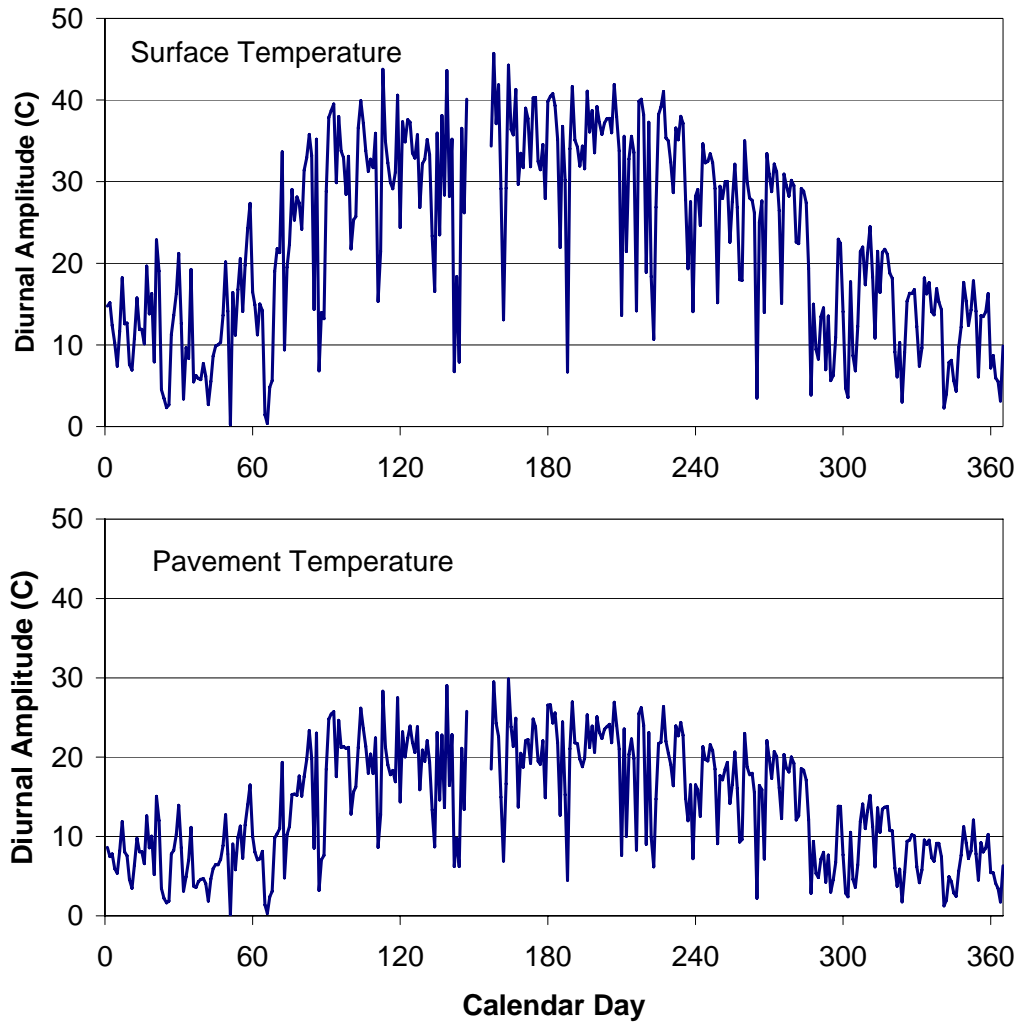
Figure 6.5. Diurnal amplitude of surface and pavement temperature for test cell 33, 2004.

Figure 6.6 shows the seasonal variation of the extreme (maximum and minimum) values of the temperature gradient (dT/dz) and the rate of change (dT/dt). In general, dT/dz and dT/dt follow the trends of the other temperature parameters, with higher values in the summer and lowest values in the winter. The extreme values of dT/dz and dT/dt are negative; they occur when the pavement surface is cooling during the onset of precipitation in spring, summer and fall.
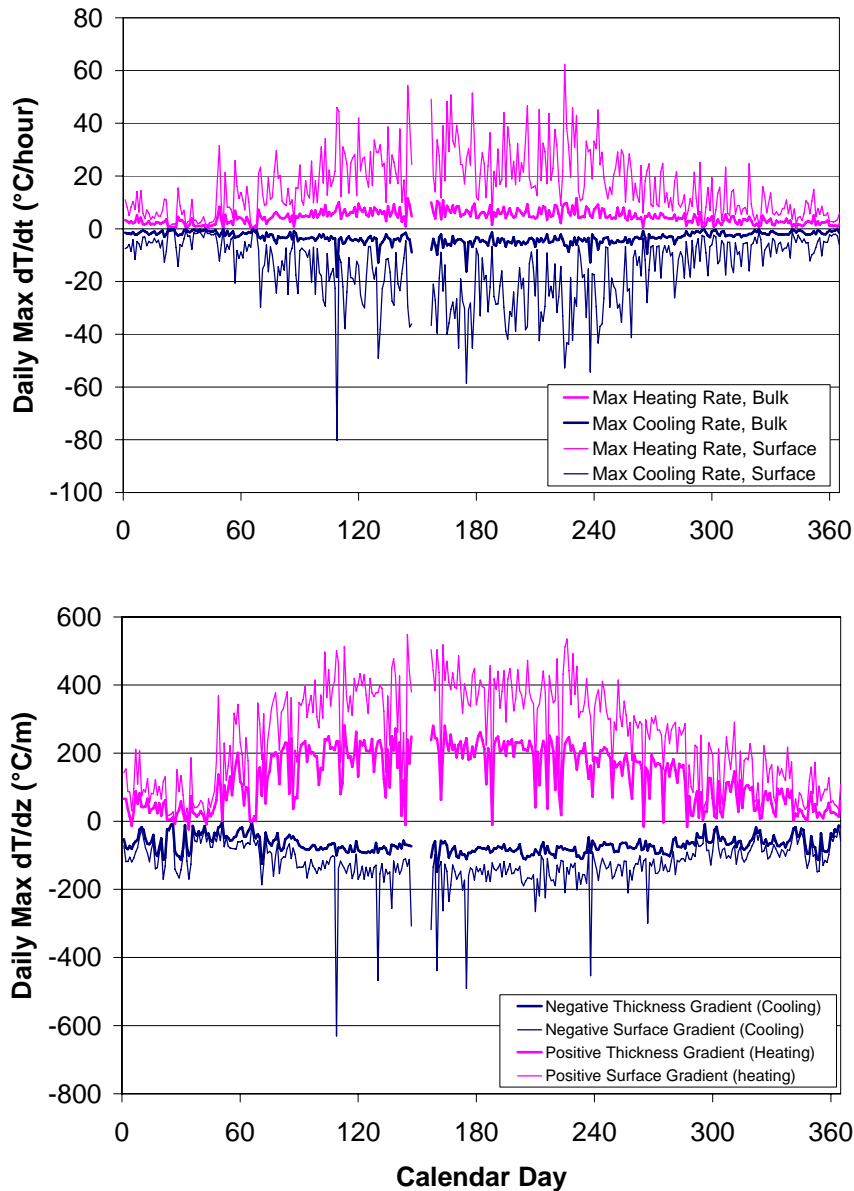
Figure 6.6. Daily extreme temperature gradient (dT/dz) and rate of change of temperature (dT/dt) for test cell 33, 2004.

Examples of measured pavement temperatures and climate conditions for an event with a high cooling rate (4/18/2004, 17:00) and a high heating rate (6/8/2004, 11:45) are given in Figure 6.7. The high cooling rate is caused by precipitation after a warm, sunny day, while the high heating rate is caused by an abrupt transition from heavy cloud cover to high solar radiation.

137
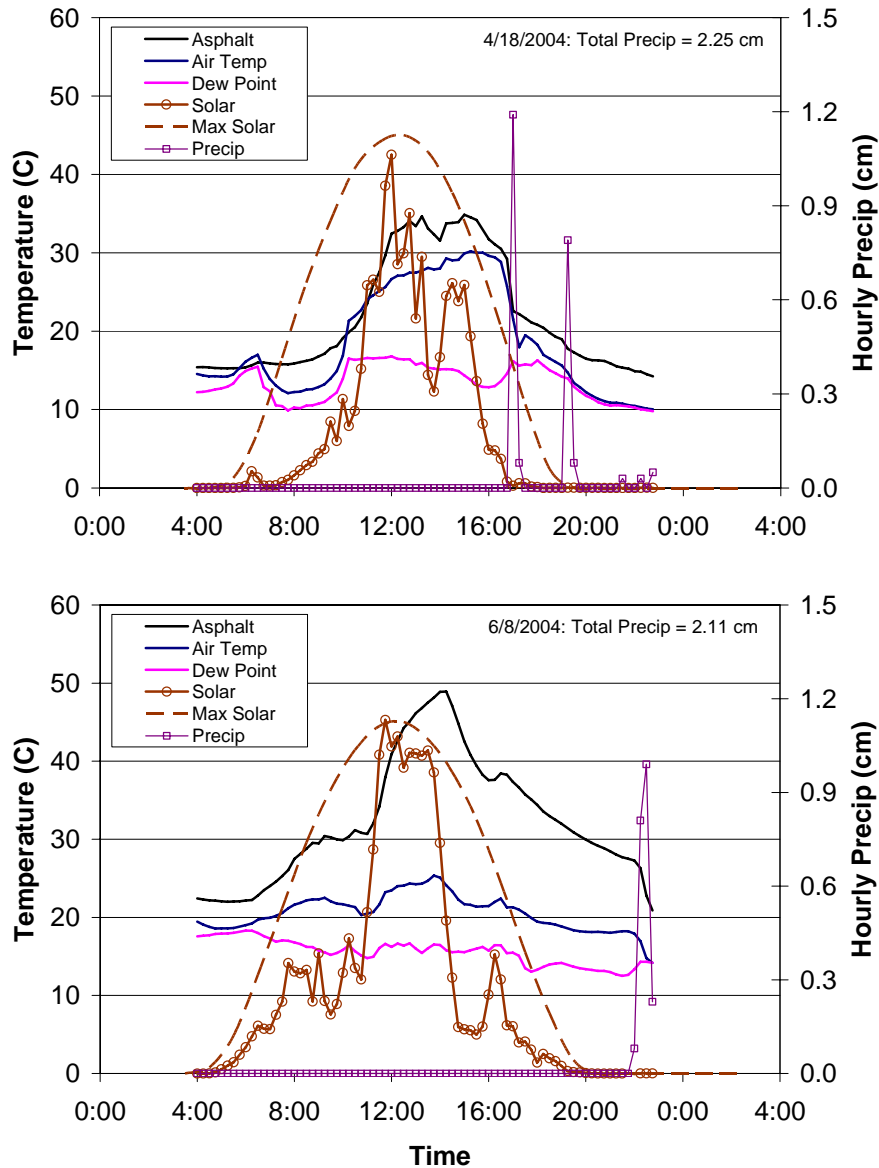
Figure 6.7. Measured pavement temperature and climate conditions for an event with a high cooling rate and a high heating rate

Statistical Distribution of Pavement Temperature Parameters

Time series illustrate the seasonal variation of temperature parameters and extreme values. To give a statistical characterization of the temperature parameters, histograms were created based on temperature data from test cell 33, for the period Jan 1, 2001 to Dec 31, 2005. Monthly temperature summaries are given in Table 6.1, for the period Jan 1, 2001 to Dec 31, 2005.

Table 6.1. Monthly pavement and air temperatures for MnROAD test cell 33 (2001 to 2005). T_a = air temperature, T_p = pavement temperature, T_s = surface temperature

Month	Parameter	Ta (°C)	Ts (°C)	Tp (°C)
Jan	Mean	-7.4	-5.2	-4.9
	Average Maximum	-3.0	2.7	-0.4
	Extreme Maximum	6.0	10.7	5.2
	Mean Diurnal Change	7.9	9.7	13.2
Feb	Mean	-12.0	-8.1	-7.5
	Average Maximum	-7.0	0.7	-2.3
	Extreme Maximum	0.3	19.1	9.6
	Mean Diurnal Change	9.6	11.0	15.3
Mar	Mean	-3.0	4.0	3.6
	Average Maximum	1.5	22.1	13.5
	Extreme Maximum	11.1	33.6	23.2
	Mean Diurnal Change	16.6	9.3	28.5
Apr	Mean	8.5	14.3	13.8
	Average Maximum	13.7	30.3	22.9
	Extreme Maximum	27.9	49.8	39.0
	Mean Diurnal Change	16.4	10.7	26.5
May	Mean	14.9	22.5	22.3
	Average Maximum	19.9	40.3	31.8
	Extreme Maximum	34.9	59.8	47.4
	Mean Diurnal Change	16.9	10.3	28.5
Jun	Mean	19.8	30.2	29.6
	Average Maximum	25.1	50.7	41.3
	Extreme Maximum	34.5	63.7	52.9
	Mean Diurnal Change	20.9	10.7	33.8
Jul	Mean	23.3	35.0	34.6
	Average Maximum	28.9	55.1	46.1
	Extreme Maximum	34.7	63.2	52.8
	Mean Diurnal Change	20.6	11.8	33.7
Aug	Mean	21.6	32.9	32.9
	Average Maximum	27.5	53.3	44.8
	Extreme Maximum	37.5	64.6	54.2
	Mean Diurnal Change	21.0	12.2	33.8
Sep	Mean	14.8	21.8	22.3
	Average Maximum	20.8	37.8	31.2
	Extreme Maximum	29.9	51.9	42.8
	Mean Diurnal Change	15.4	11.3	25.4
Oct	Mean	8.3	11.0	11.8
	Average Maximum	13.8	22.7	18.1
	Extreme Maximum	29.9	39.9	31.4
	Mean Diurnal Change	11.3	11.0	18.8
Nov	Mean	6.0	7.0	7.6
	Average Maximum	11.1	16.5	13.0
	Extreme Maximum	21.7	27.3	21.7
	Mean Diurnal Change	9.2	10.0	15.0
Dec	Mean	-3.6	-2.3	-1.3
	Average Maximum	0.7	4.3	2.3
	Extreme Maximum	14.7	13.0	9.7
	Mean Diurnal Change	6.5	8.7	11.1
All	Mean	7.7	13.4	13.6
	Average Maximum	12.8	27.9	21.7
	Extreme Maximum	37.5	64.6	54.2
	Mean Diurnal Change	14.3	10.6	23.6

Figure 6.8 gives histograms for daily air temperature, surface temperature, and pavement temperature, recorded at test cell 33; each temperature parameter is placed in 10°C bin.
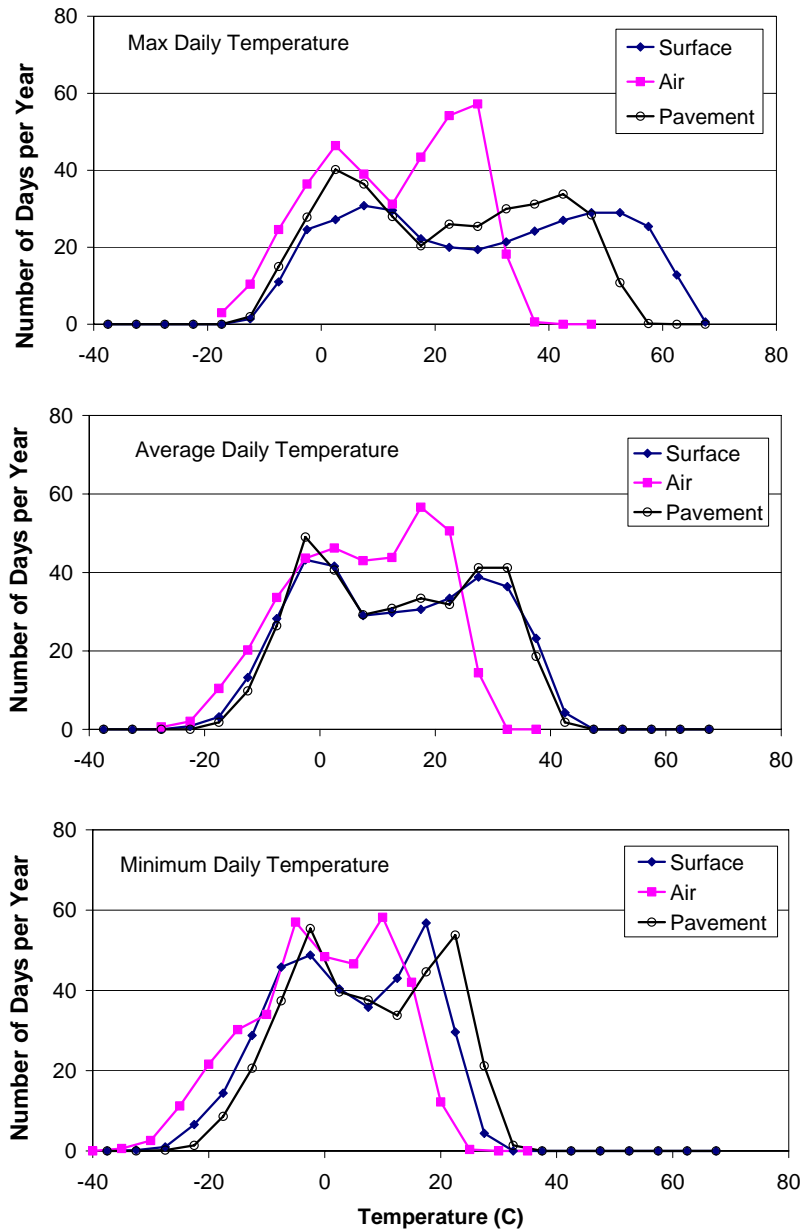
Figure 6.8. Distribution of daily maximum, minimum and average air, surface and pavement temperature for test cell 33, 2001 – 2005.

The histograms have several noteworthy features:

- Maximum daily pavement surface temperature exceeds 60˚C on the 12 hottest days of the year and is then 10˚C higher than maximum pavement temperature and 30˚C higher than maximum daily air temperature. These large differences are attributed to heating by solar radiation.

- Maximum daily pavement surface and pavement temperatures are far more variable throughout the year than minimum daily values.

- Minimum daily pavement surface temperatures reach only 30°C on the hottest days of the year, and are less than 5°C warmer than the daily minimum average pavement temperature, and less than 10°C warmer than daily minimum air temperatures.

- Average daily pavement temperature and average daily surface temperature have very similar distributions; both distributions extend about 10°C higher than average air temperature.

- The distributions in Figure 6.8 show a double peak to some degree. This is attributed to the distribution of the daily maximum solar radiation, given in Figure 6.9.
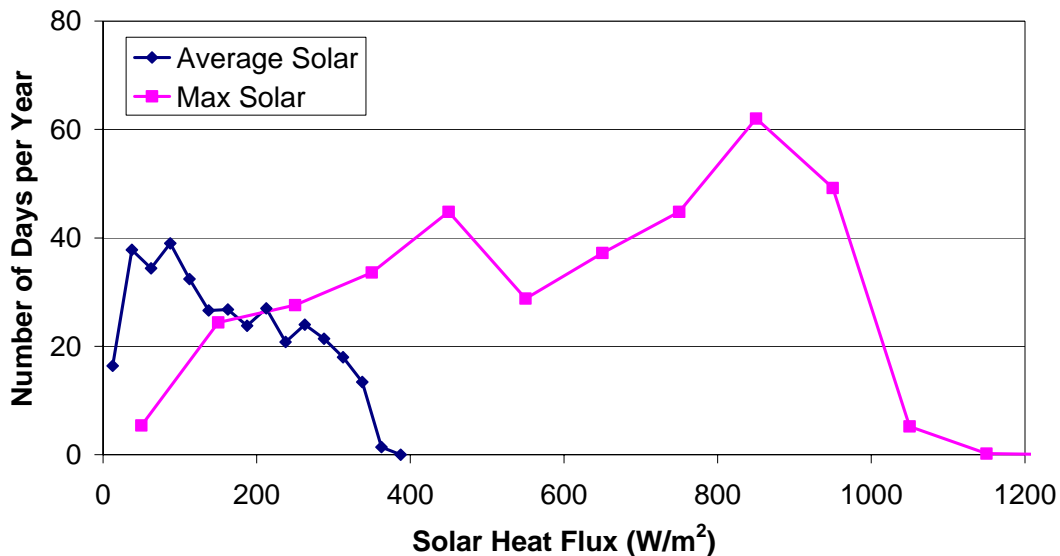
Figure 6.9. Distribution of daily maximum and average solar radiation from the MnROAD weather station, 2001 – 2005.

Figure 6.10 presents the distribution of the diurnal temperature change (daily max – daily min) of the surface, pavement and air temperatures. The asphalt pavement experiences a much greater diurnal temperature change than the air, primarily because of the absorption of solar radiation.
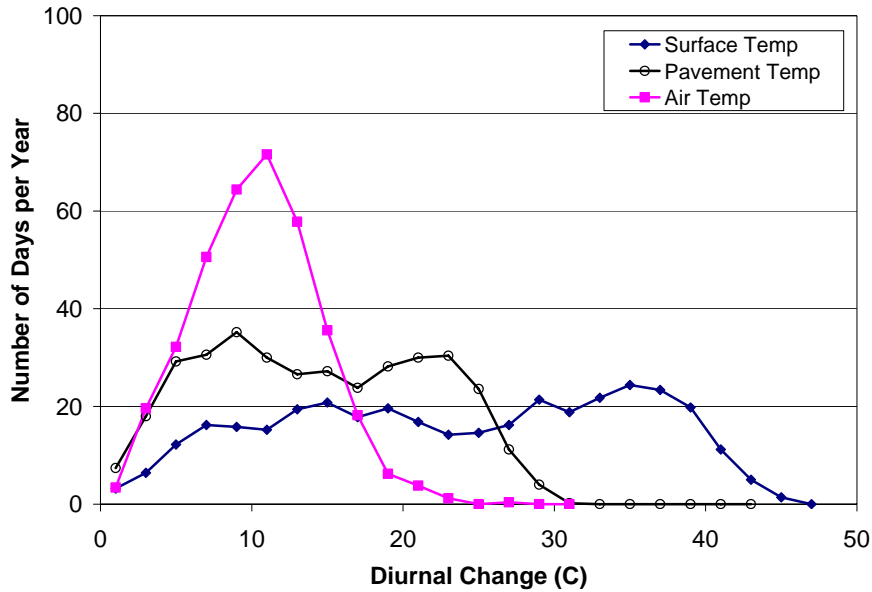
Figure 6.10. Distribution of daily diurnal temperature change (max-min) of the surface and pavement temperature for test cell 33, 2001 – 2005. Each point represents an average yearly 2.5˚C bin count for the five year period

Figure 6.11 gives the histogram of the daily extreme temperature gradient (dT/dz) and of the rate of change (dT/dt). While dT/dt is distributed rather symmetrically about zero, dT/dz has a broader distribution of positive values than negative values.
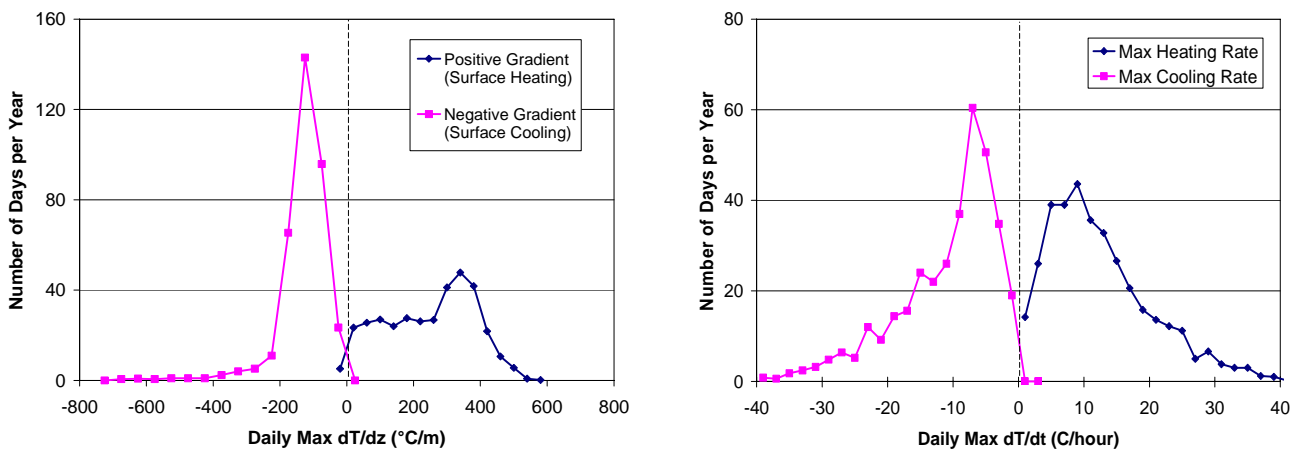
Figure 6.11. Distribution of daily extreme surface temperature gradient (dT/dz) and surface temperature rate of change (dT/dt) for test cell 33, 2001 – 2005. Each point represents an average yearly 2°C bin count for the five year period.

142

The distributions of the temperature gradient with depth and rate of temperature change are further examined using Equation 12, which gives the basic heat balance on a volume of pavement near the surface (Figure 6.12).

$$\rho C_p \Delta z \frac{dT_s}{dt} + K \frac{dT}{dz} - H_s = 0 \tag{12}$$
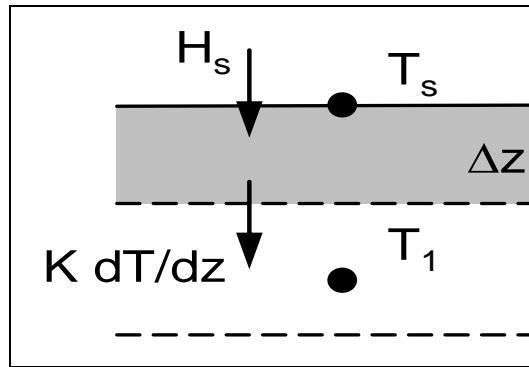
Figure 6.12. Schematic of surface heat transfer components

The surface heat flux, Hs, enters through the pavement surface, while heat is conducted away at the lower boundary with magnitude K dT/dz. Using Equation 12 and measured pavement temperatures, the surface heat flux, Hs, can be estimated. The distribution of the calculated surface heat flux (Figure 6.13) has a distribution similar to the surface temperature gradient (Figure 6.11).
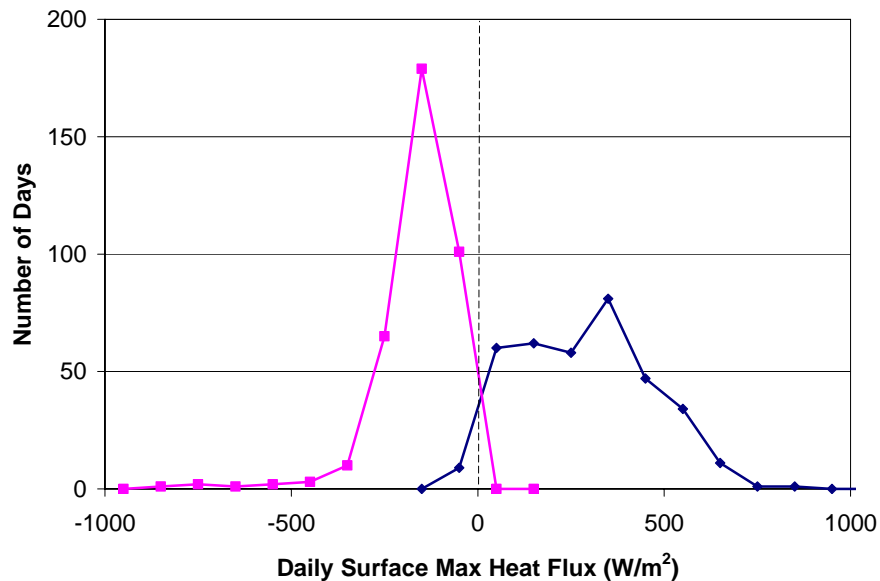
Figure 6.13. Distribution of daily surface heat flux (Hs) for test cell 33, Jan 1 to Dec 31, 2004.

143

Typical values of these heat budget components for a sunny summer day are plotted in Figure 6.14, where the temperatures and heat budget components are taken from a finite difference simulation. Figure 6.14 shows that most of the surface heat transfer is conducted down (K dT/dz), while a smaller fraction produces a change in surface temperature (dT$_s$/dt).
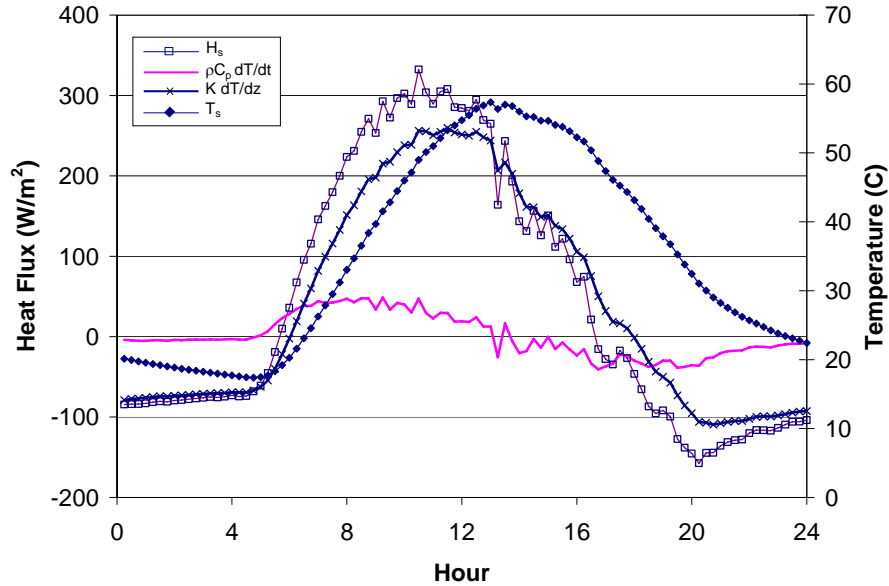
Figure 6.14. Variation of simulated surface temperature (Ts), surface heat flux (Hs), unsteady temperature change (ρC$_p$dT$_s$/dt), and vertical heat flux (KdT/dz) over 1 day (June 29, 2004).

Relationships between Pavement Temperature Parameters

The impact of temperature variation on pavement durability may be dependent on combinations of parameters, rather than the independent variation of single parameters. For example, the combination of low mean temperature and high rate of change of temperature may cause high pavement stress. In this section the interdependency of several important temperature parameters is explored via scatter plots and histograms.

In Figure 6.15 the daily diurnal amplitude of both the surface temperature and the pavement temperature is plotted against daily mean pavement temperature. There is a general trend of increasing diurnal amplitude with increasing mean temperature. Yet the lowest amplitudes occur near the freezing point (0°C) and significant amplitudes exist (20°C) at the lowest mean temperatures (-20°C). Moderate values of diurnal amplitude occur over a broad range of mean temperatures, *e.g.* days with 30°C surface temperature diurnal amplitude occur over the range of -10 to 35°C mean temperature.
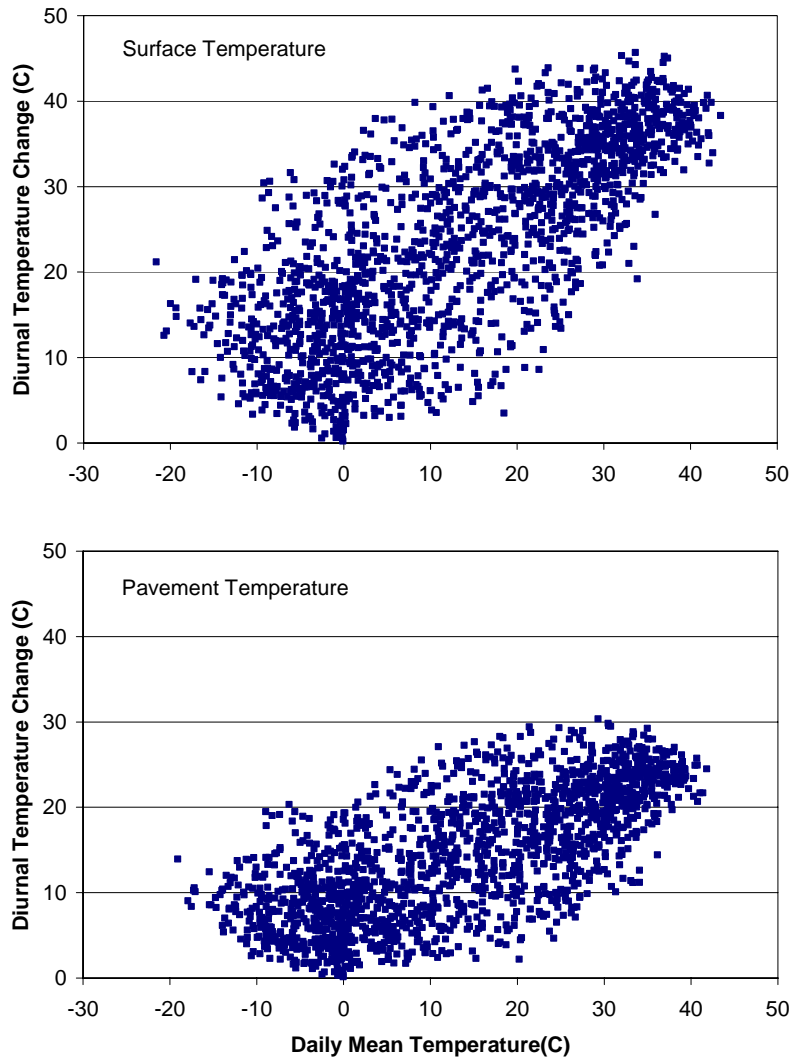
Figure 6.15. Diurnal change (daily max – daily in) versus daily mean temperature for surface temperature and pavement temperature, test cell 33, Jan 1, 2001 – Dec 31, 2005.

Spatial and temporal gradients also tend to increase with increasing pavement temperature. The rate of change of temperature for both heating and cooling events increase with increasing surface temperature, with heating and cooling events having similar distributions (Figure 6.16, upper panel). Daily peak values of the vertical temperature gradient (dT/dz) also increase with increasing surface temperature; positive values correspond to surface heating and negative values correspond to surface cooling.
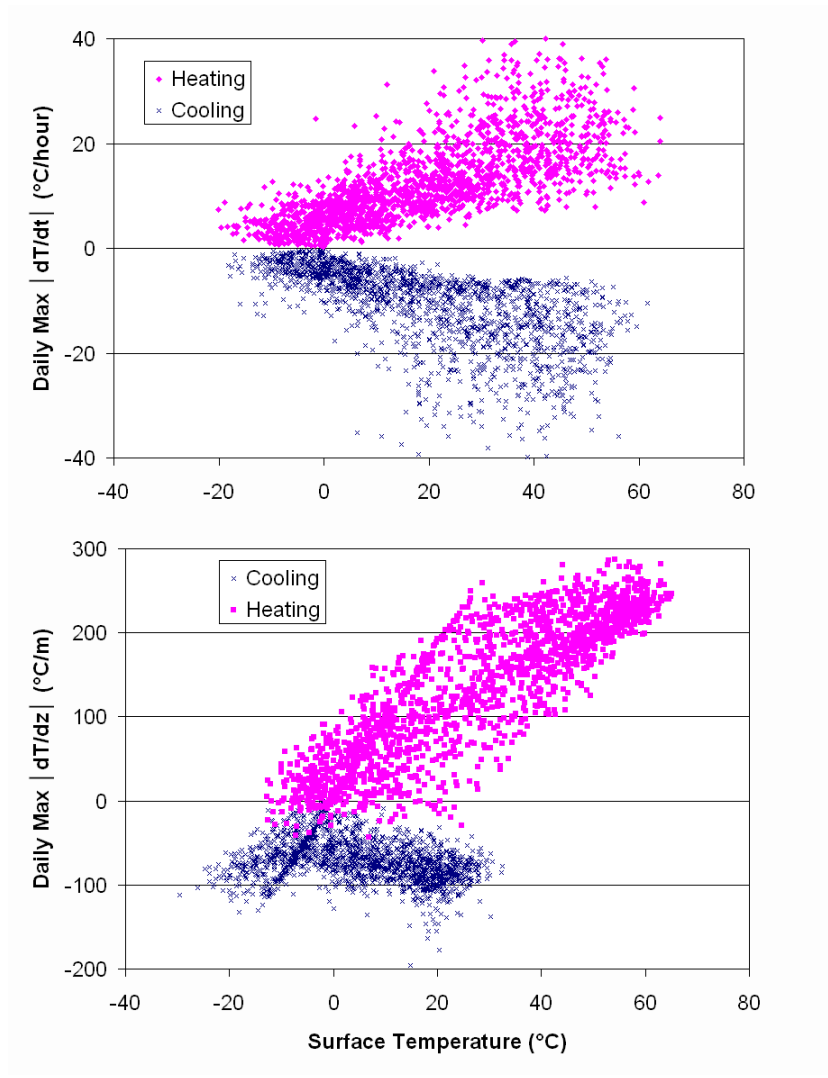
Figure 6.16. Daily extreme temperature gradient (dT/dz) and rate of change (dT/dt) surface temperature for test cell 33, Jan 1, 2001 – Dec 31, 2005.

Pavement Temperature Simulation

While the measured pavement temperatures provide a wealth of information on the dynamics of pavement temperature, computer simulations can provide additional information on the underlying mechanisms of temperature dynamics, including information on the components of heat transfer between the pavement and the atmosphere, detailed temperature profiles in the pavement and base layers, and the relationship of material properties to temperature dynamics. A pavement temperature model was developed at the University of Minnesota St. Anthony Falls Lab (SAFL). The SAFL pavement temperature model is similar to previous models described by Bigl and Berg [44] and Hermanson [45], but is applied for both very long time series (6 month continuous simulations) and for very short duration temperature changes (15 minutes).

146

Model Description

Model Summary

The heat transfer model is one dimensional; temperature is modeled vs. depth, assuming horizontal uniformity. Surface heat transfer is modeled using measured weather parameters (Figure 6.17): air temperature and humidity, solar radiation, precipitation, and wind speed. Conduction of heat into the pavement, base, and soil is modeled using finite difference, with separate material properties for each layer. The model output is temperature vs. depth and time, stored in a text file. The time step of the simulation is largely dependent on the available weather data (a 15 minute time step was used for the simulations). The simulation can be started at any time of year with an initial temperature profile. A more detailed description of the model is given in SAFL Project Report 478 [46].
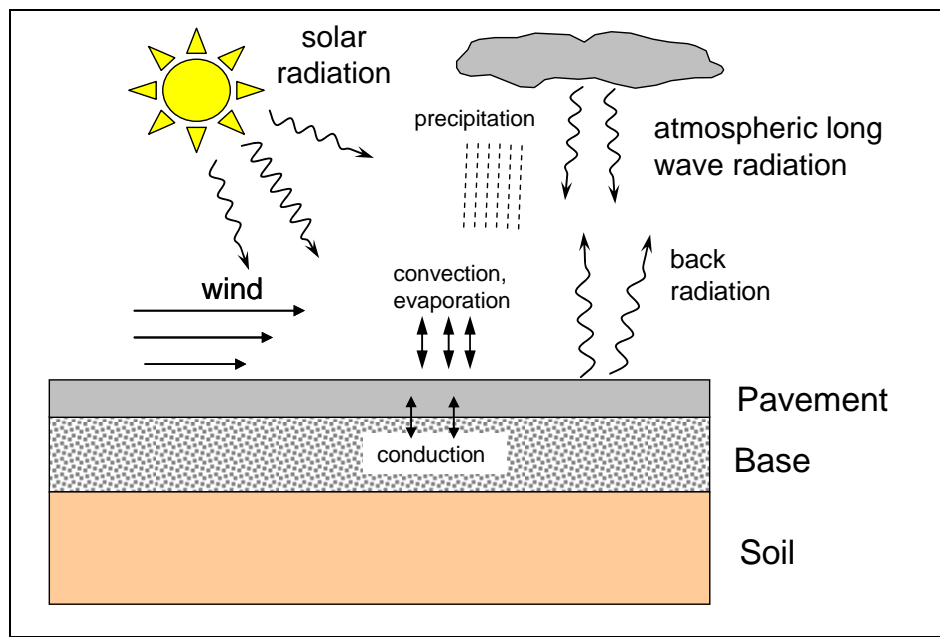
Figure 6.17. Schematic diagram of the processes considered in the pavement temperature model.

Model Inputs

Required inputs to the pavement temperature model include:

1. Climate data: Air temperature (°C), relative humidity (%), wind speed (m/s), and solar radiation (W/m^2). For dry weather periods, it is sufficient to specify climate data at one hour time intervals to simulate surface temperatures. To accurately capture the dynamics of surface temperature prior to storm events, climate data at 10 to 15 minute interval are preferable. Latitude, longitude, and elevation for the site to be simulated are also required for the algorithm to estimate cloud cover.
2. Surface data: albedo, emissivity, and aerodynamic roughness.

3. Pavement/soil data: Thermal diffusivity and specific heat of the pavement layer; thermal diffusivity of the subgrade and base layers. Infiltration is assumed to be zero and the soil and pavement moisture properties are not considered.

4. Initial conditions: An initial vertical pavement/soil temperature profile is specified for an arbitrary number of points, which are then interpolated to the node locations of the model.

Model Formulation

Heat Conduction Model

The heat conduction model uses an implicit finite difference formulation to solve the unsteady heat conduction equation for the vertical pavement/soil profile. The model uses thinner layers for the pavement or the near surface subgrade layers, *e.g.* 2 cm, and thicker layers towards the lower boundary, *e.g.* 1 m. As a result, good simulation results are possible with, *e.g.* 15-20 layers. The model does not presently include moisture dependent thermal properties.

Surface Heat Transfer Formulation

The net vertical heat transfer at the pavement surface includes components due to long wave radiation, short wave (solar) radiation, evaporation, convection, and runoff. The heat transfer formulations used in this study are based on those given by Edinger [47] for lake and reservoirs surfaces, but are applied to pavement and soil by adjusting parameters appropriately.

Model Calibration

The surface temperature model was run using 15 minute climate data from the MnROAD facility. The model was calibrated and verified using measured pavement temperature data for concrete and asphalt test sections from MnROAD. Seven years of 15 minute climate data was available for model implementation (1999-2005), six years of asphalt temperature data (cell 33) and one year of concrete temperature data (cell 38, 2004). Precipitation received in each time step is assumed to completely run off the pavement, so that no standing water is carried over to the next time step, and infiltration is assumed to be zero. The simulations were run using a total soil depth of 10 m and either a 15 minute or 60 minute time step for the time period April 1 to September 30 for each year.

The parameter values in Table 6.2 were obtained by minimizing the root-mean-square error (RMSE) of the simulated and measured pavement temperature values. Surface heat transfer parameters such as albedo and emissivity were calibrated to minimize the simulation error compared to the upper thermocouple node (2.5 cm below the surface). Measured temperatures at other depths were used to calibrate the pavement and soil thermal diffusivity values.

Table 6.2. Calibrated parameter values for the period April 1– September 30, 2004

Parameter	Value
solar albedo	0.14 (calibrated)
surface heat/moisture transfer coefficient for forced convection	0.0015 (calibrated)
coefficient for natural convection	0.0015
wind sheltering coefficient	1.0
pavement emissivity	0.94
(density · specific heat) pavement	2.0e06 J/m^3/°C
pavement thermal diffusivity	3.0e-07 m^2/s (asphalt) (calibrated) 7.0e-07 m^2/s (concrete) (calibrated)
soil thermal diffusivity	1.0e-06 m^2/s (calibrated)

Model Sensitivity

The sensitivity of the simulated temperatures to several key input parameters are given in Table 6.3. Overall, the emissivity of the pavement had the most influence on surface temperature. An increase in emissivity causes a rather uniform decrease in surface temperature, i.e. both the daytime and nighttime temperatures decrease. The simulated temperatures were relatively insensitive to the soil parameters. The sensitivity to the wind sheltering coefficient is notable, indicating that unquantified wind sheltering from trees, buildings, and surface topography introduces uncertainty into temperature simulations.

Table 6.3. Average surface temperature (°C) increase for a 10% increase in the parameter value listed in the first column. Temperatures for the asphalt test section were simulated from Jan 1 to Dec 31, 2004.

Parameter	Overall Average	Average Daily Max	Average Daily Min	Average Amplitude
pavement emissivity	-0.42	-0.54	-0.37	-0.17
coefficient for natural convection	-0.17	-0.32	-0.10	-0.22
wind sheltering coefficient	-0.17	-0.34	-0.09	-0.24
surface heat/moisture transfer coefficient for forced convection	-0.16	-0.32	-0.08	-0.24
solar albedo	-0.12	-0.29	-0.04	-0.25
pavement (density · specific heat)	0.05	-0.56	0.36	-0.92
pavement thermal diffusivity	0.03	-0.28	0.19	-0.48
soil thermal diffusivity	0.00	0.00	0.03	-0.02

Comparison of Simulated and Measured Pavement Temperatures (Snowless Season)

Excellent agreement between simulated and measured asphalt and concrete pavement temperature was obtained for all essentially snow-free months (April-September) using either 15 minute or 60 minute time steps. For 2004, the overall RMSE is 1.5°C for asphalt and 1.2°C for concrete. Time series of simulated and measured surface temperature for asphalt and concrete for June/July (Figure 6.18) and August/September (Figure 6.19) illustrate a high level of agreement.
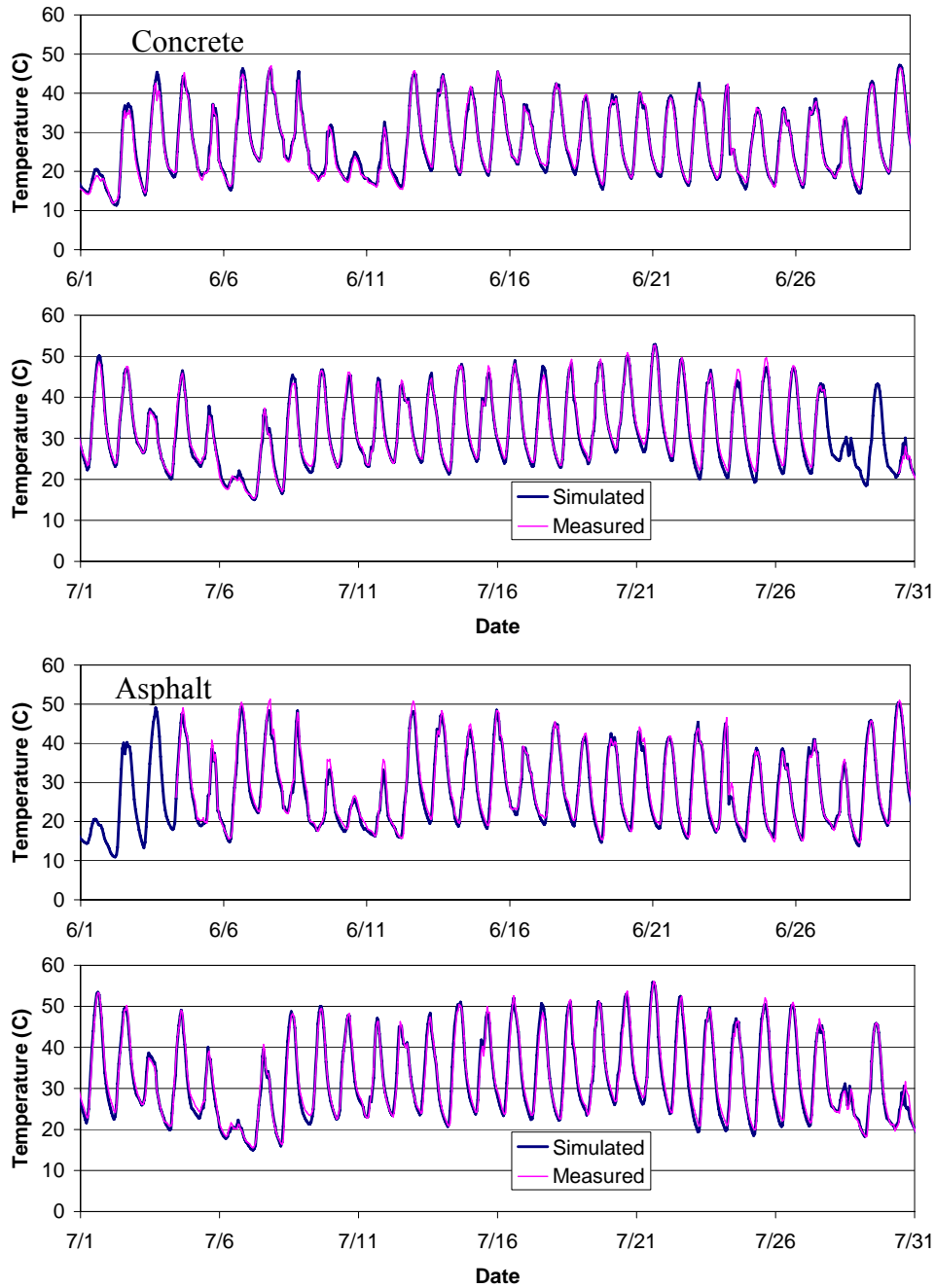
Figure 6.18. Simulated and measured pavement temperature (2.5 cm depth) for June and July, 2004, MnROAD test cells 33 (asphalt) and 38 (concrete), 1 hour time step.

150
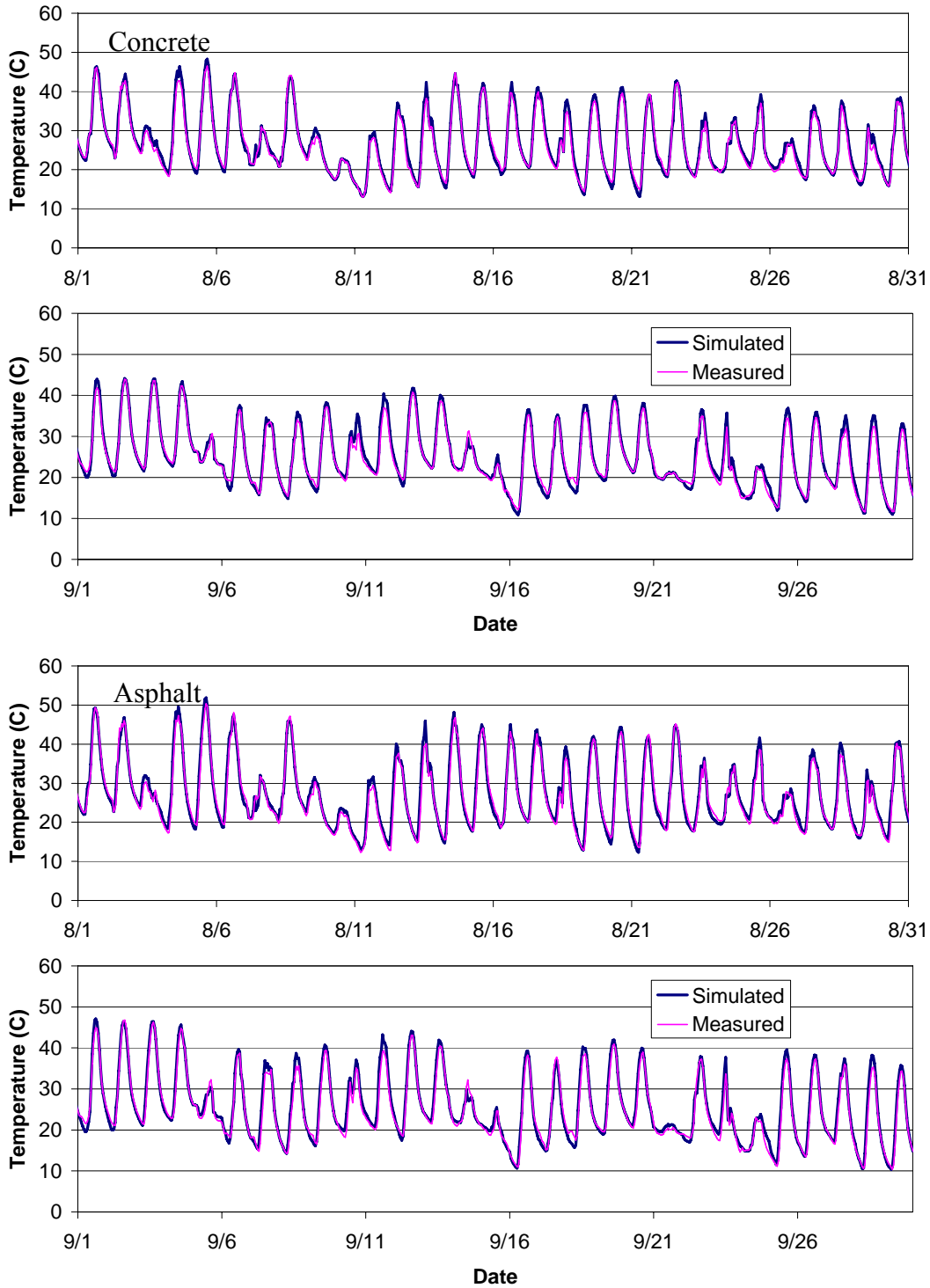
Figure 6.19. Simulated and measured pavement temperature (2.5 cm depth) for August and September, 2004, MnROAD test cells 33 (asphalt) and 38 (concrete), 1 hour time step.

Figure 6.20 gives a direct comparison of simulated hourly surface temperatures versus hourly averaged measured temperatures. The slope of the relationship between measured and simulated surface temperature is very close to 1:1 and the intercept is less than 1°C.
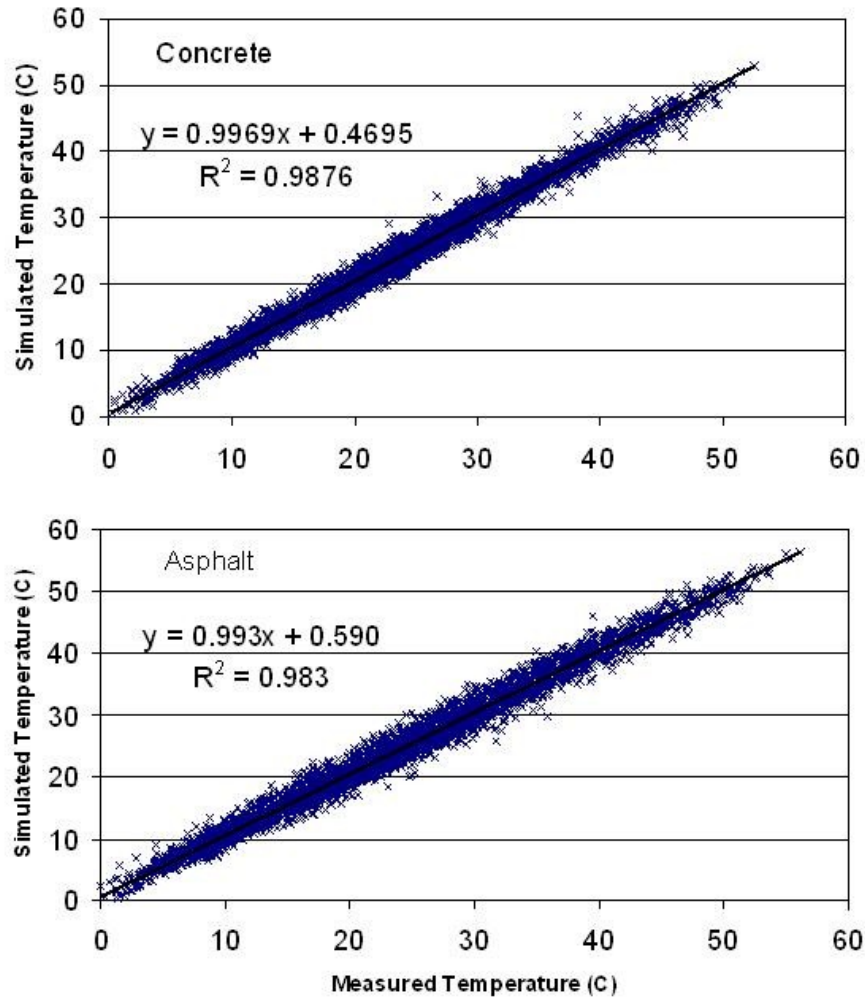
Figure 6.20. Hourly simulated versus measured pavement temperature (2.5 cm depth) for April - September, 2004, MnROAD Test cells 33 (asphalt) and 38 (concrete).

Tables 6.4, 6.5 and 6.6 summarize the accuracy of the temperature simulations (r^2, RMSE) on a monthly basis and for the entire simulation period. The model was calibrated using 2004 data, but works quite well for the other five years of measured asphalt pavement temperatures (Table 6.6).

Table 6.4. Summary of simulation accuracy for the MnROAD asphalt cell 33, for April – October, 2004, 1 hour time step.

	r^2	RMSE (°C)				
	overall	overall	daily max	daily min	daily mean	daily ampl.
April	0.983	1.47	1.42	1.09	1.13	1.30
May	0.973	1.45	1.43	1.13	0.96	1.58
June	0.976	1.50	1.23	0.67	0.58	1.55
July	0.979	1.51	1.08	0.77	0.59	1.42
August	0.975	1.59	2.02	0.81	0.93	1.97
September	0.978	1.50	1.94	0.89	0.94	2.19
All	0.982	1.51	1.57	0.90	0.88	1.70

Table 6.5. Summary of simulation accuracy for the MnROAD concrete cell 38, for April – October, 2004, 1 hour time step.

	r^2	RMSE (°C)				
	overall	overall	daily max	daily min	daily mean	daily ampl.
April	0.975	1.43	1.14	0.91	0.99	1.22
May	0.980	1.13	1.23	0.91	0.76	1.15
June	0.988	0.96	1.02	0.85	0.51	1.39
July	0.987	1.05	1.29	1.14	0.67	1.56
August	0.982	1.17	1.71	0.82	0.76	1.84
September	0.982	1.19	1.91	0.93	0.72	2.28
All	0.986	1.17	1.42	0.93	0.75	1.62

Table 6.6. Summary of simulation accuracy for the MnROAD asphalt cell 33 for six years of simulations (2000-2005), April 1 to October 31, 15 minute time step.

	r^2	RMSE (°C)		
	hourly	hourly	daily max	daily min
2000	0.982	1.60	1.85	1.31
2001	0.981	1.58	2.52	1.43
2002	0.970	1.85	2.28	1.57
2003	0.980	1.44	2.13	1.51
2004	0.981	1.38	2.07	1.32
2005	0.962	1.73	1.90	1.27

Full Year Simulations of Pavement Temperature

Winter conditions can be particularly damaging to asphalt pavements. Numerical simulation of pavement temperature for the winter is more difficult than for other seasons because surface properties change as snow and ice layers form on the pavement surface. Snow layers reduce surface heat transfer by increasing albedo and decreasing emissivity, and freeze/thaw cycles in the presence of moisture complicate heat conduction through the subgrade and soil layers. In

this study, wintertime pavement temperature simulations were performed with the previously described model, but allowing seasonal variation of surface parameters (albedo, emissivity). A snow/ice layer was not added to the model, since snow/ice cover is usually not persistent on traveled roads, and the depth and the period of snow/ice cover are not easy to predict with reliability because of localized variations of snowfall intensity, wind drift, plowing schedules and traffic densities.

Simulations of test cell 33 temperatures for the entire year of 2004 with fixed parameters shows significant variation in simulation errors with season (Figure 6.21, upper panel). The introduction of a seasonally varying albedo significantly improved the simulated pavement temperatures, such that the RMSE was less than 1.8°C for the entire year (Figure 6.21, lower panel). The calibrated, seasonally varying albedo is given in Figure 6.22. The seasonal variation is attributed to the variations in sun angle and pavement surface properties from moisture.
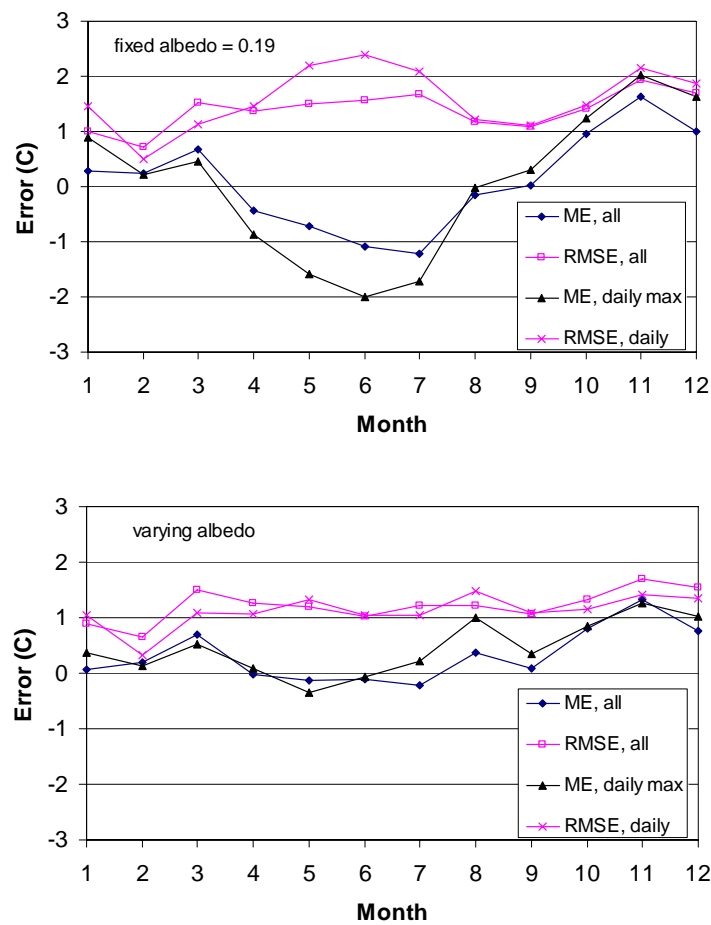
Figure 6.21. Error in pavement temperature (2.5 cm depth) simulation by month for MnROAD test cell 33, 2004 for fixed and varying surface albedo. RMSE is root-mean-square error, ME is mean error.
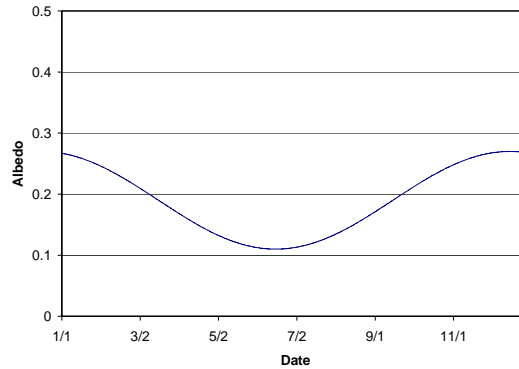
Figure 6.22. Calibrated seasonal variation of surface albedo for test cell 33, 2004. albedo = 0.19+0.08*Cos(2π (cd+15)/365), where cd is the calendar day.

A fresh snow cover insulates any surface including pavements and reflects much more short wave (solar) radiation than most bare surfaces [48]. During periods of snow cover at MnROAD, simulated pavement temperatures temporarily diverge from actual temperatures, but recover quickly when the snow cover is removed (Figure 6.23). A snow/ice cover introduces smaller errors to the simulated temperatures at greater depth below the pavement surface, but the errors may persist for several weeks (Figure 6.23, right panel).
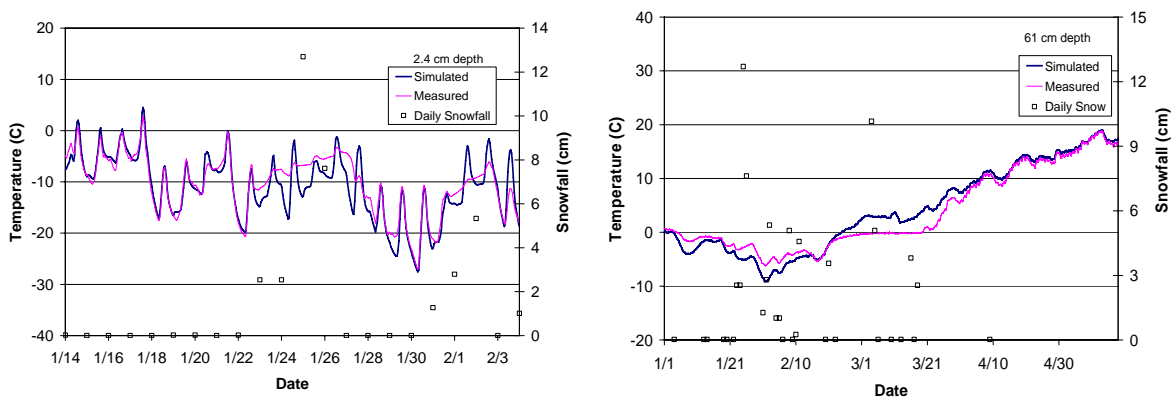
Figure 6.23. Simulated and measured temperature vs. time for 2.5 cm depth (left panel) and 60 cm depth (right panel). Daily new snow fall is measured at the Maple Lake airport.

Pavement Temperature Simulation for a RWIS

The MnDOT roadside weather information stations (RWIS) provide an additional opportunity to evaluate the pavement temperature model. The RWIS station chosen for this study is located on Highway 10 at mile marker 161.3, near St. Cloud (RWIS station Benton 64). This station is relatively well instrumented, including sensors for air temperature, humidity, wind speed and direction, rainfall, solar radiation, pavement surface temperature, and subsurface temperature.

All data are recorded at 10 minute intervals. Data for 2004 were downloaded from the MnDOT/UMD RWIS website [49].

A two week (July 1 to July 15, 2004) time series of the climate parameters and pavement temperatures was assembled for this study. The solar radiation and wind speed values obtained from the RWIS station were clearly erroneous. Solar radiation values reported in units of J/m^2 for each 10 minute time period were therefore corrected to actual units of kJ/m^2, based on comparisons of the RWIS data to solar radiation data from the MnROAD site for the same time period. Wind speed values reported in units of m/s were corrected to actual units of tenths of m/s, based on information on the raw data format. Subsurface temperatures are also measured at the RWIS site, but the actual depths of the two temperature sensors were not available. Information on the website of the sensor manufacturer (SSI) suggests that the upper sensor is typically buried at a depth of 17 inches (43 cm).

A simulation of pavement temperature for the RWIS site was performed using the 2 weeks of climate data from the RWIS station (July 1 to July 15, 2004). Pavement and soil temperatures for the MnROAD cell 33 for July 1, 2004 were used as an initial condition for the simulation. All model parameters were kept at the same value as those used for cell 33 (Table 6.2). The simulated pavement and soil temperatures are compared to the temperatures obtained from the RWIS station in Figures 6.24 and 6.25. The simulated mid-day surface temperature exceeds the measured surface temperature by up to 5°C, and the overall RMSE is 2.4°C. The measured surface temperature agrees more closely with the simulated pavement temperature at 1 cm depth (RMSE=2.0°C), as shown in the lower panel of Figure 6.24. This modest discrepancy in surface temperature may be due to inaccuracies in the climate data, or the model parameters, or the temperature sensing method used at the RWIS station. The measured sub-surface temperature is in reasonable agreement with the simulated temperature at 43 cm (Figure 6.25).
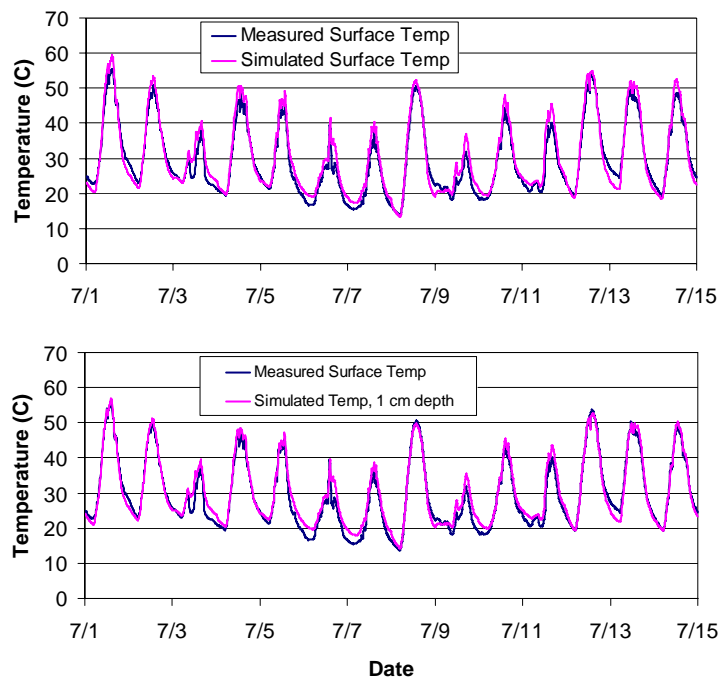
Figure 6.24. Measured and simulated pavement temperature for Highway 10 at mile marker 161.3, near St. Cloud (RWIS station Benton 64) for July 1 to July 15, 2004.
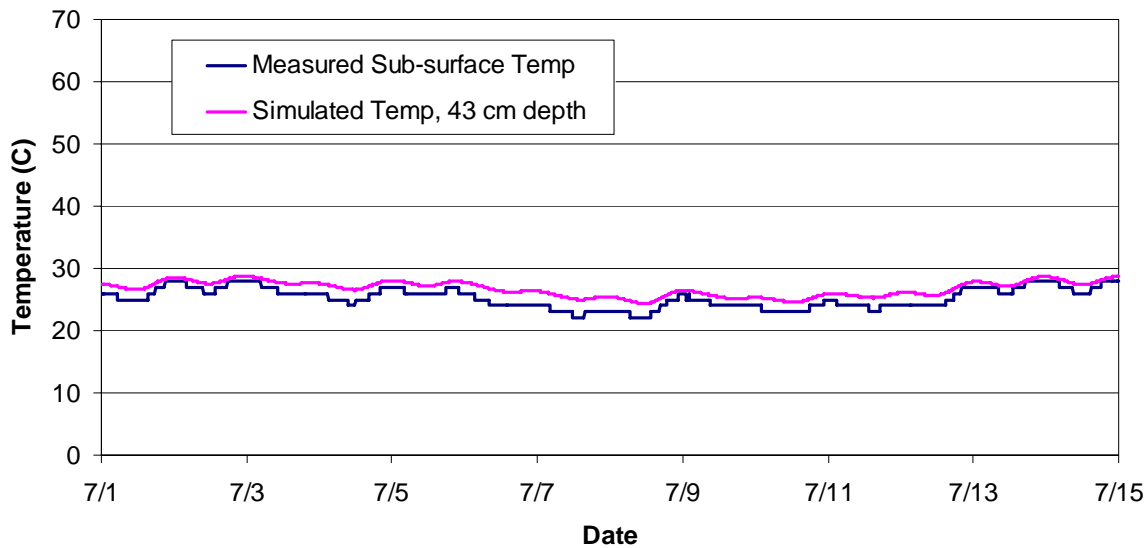
Figure 6.25. Measured and simulated subsurface (43 cm) temperature for Highway 10 at mile marker 161.3, near St. Cloud (RWIS station Benton 64) for July 1 to July 15, 2004.

Comparison of Infrared Measured and Simulated Surface Pavement Temperature

The work proposed for this project included performing measurements of the surface temperature using infrared temperature measuring devices. During discussions with MnROAD staff, it was found out that historical surface temperatures data from MnROAD cells was already available. Tim Clyne, MnROAD forensic engineer provided to the research team pavement surface temperature for MnROAD cell 33, 34, 35 (asphalt) and cell 12 (concrete). These temperatures were measured during FWD testing at specific times between 1998 and 2005 using a Raytek infrared thermometer. The device was mounted on the front of the trailer approximately 1.5-2' above the surface of the pavement. No records on the calibration of this device were available at the time of this report.

Figures 6.26-6.29 show the measured and simulated surface temperature for four MnROAD cells for the years 1998 to 2005.
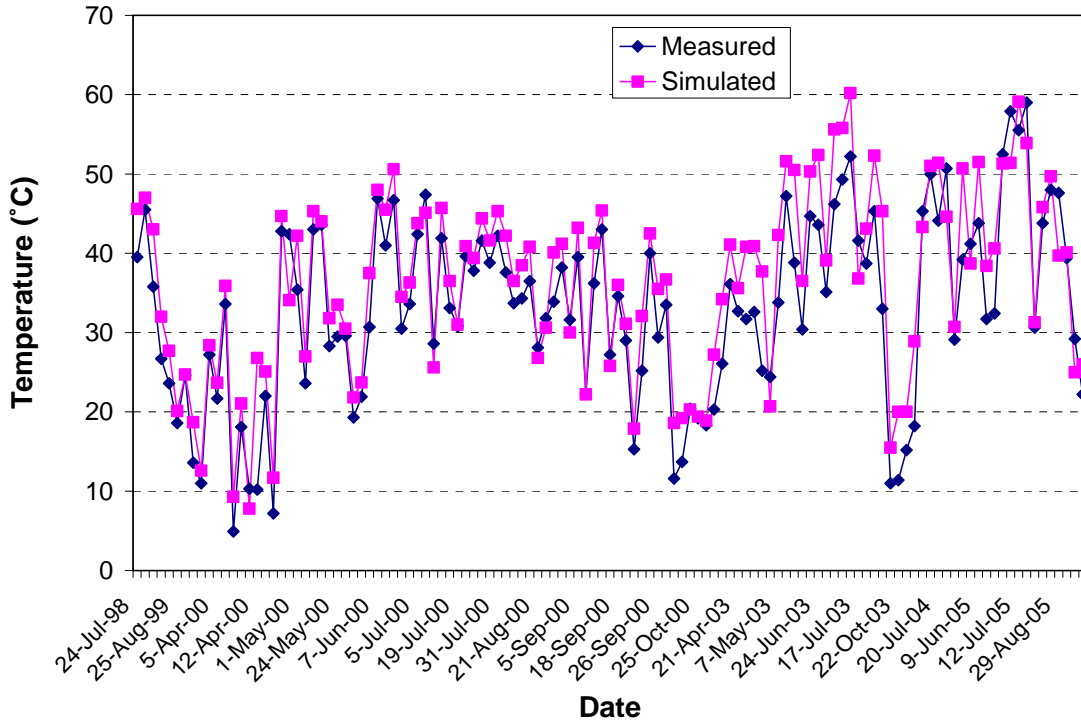
Figure 6.26. Infrared measured and simulated pavement surface temperature for MnROAD test cell 33, 1998-2005.
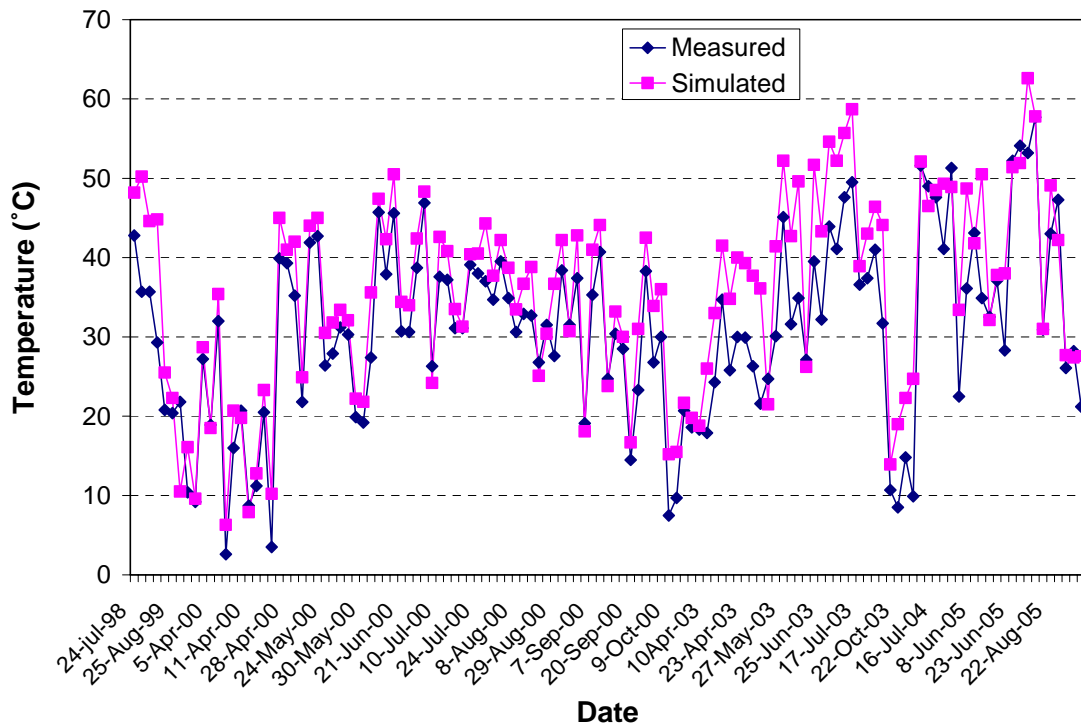
Figure 6.27. Infrared measured and simulated pavement surface temperature for MnROAD test cell 34, 1998-2005.

158
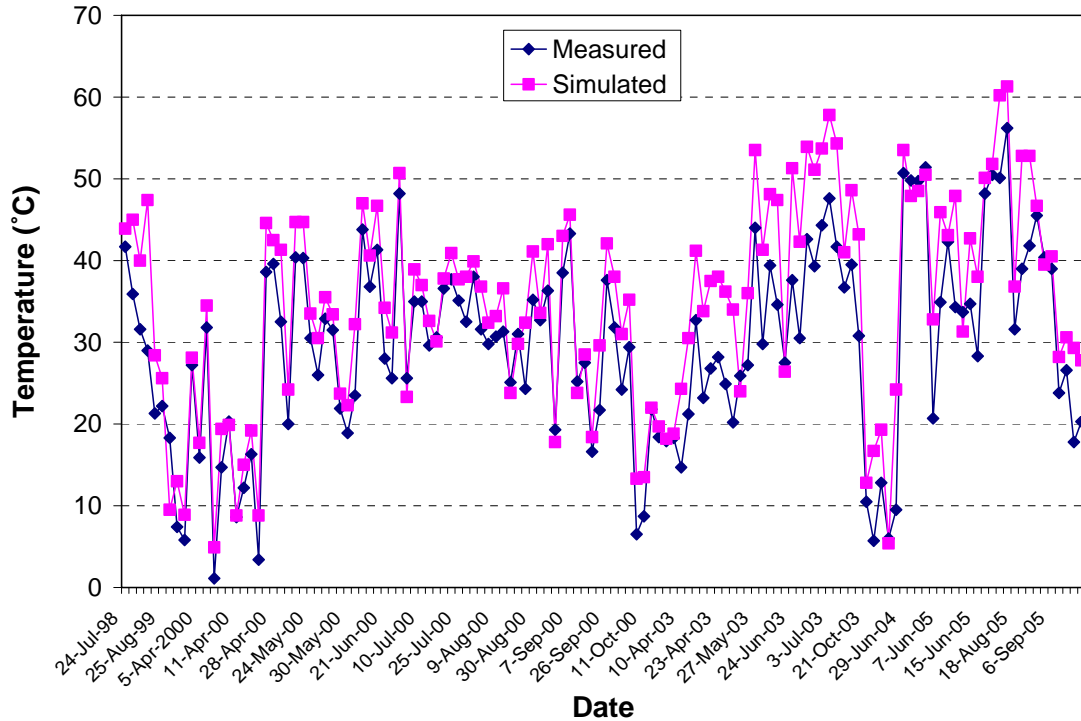
Figure 6.28. Infrared measured and simulated pavement surface temperature for MnROAD test cell 35, 1998-2005.
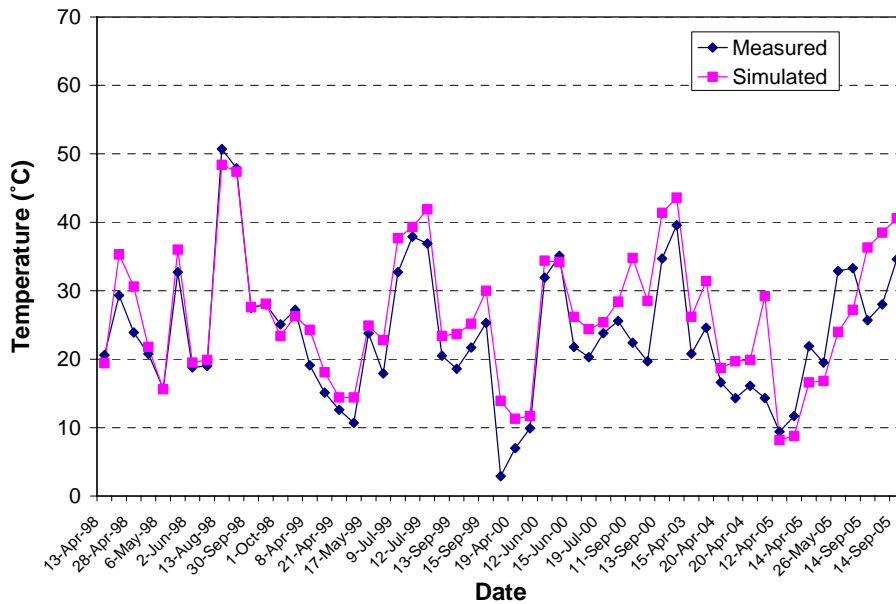
Figure 6.29. Infrared measured and simulated pavement surface temperature for MnROAD test cell 12 (concrete) 1998-2005.

It can be seen from Figures 6.26-6.29 that the simulated surface temperatures are in reasonable agreement with the measured temperatures for both, asphalt and concrete pavements. It is also observed in these figures that the simulated temperature is slightly higher than the measured surface temperature.

This trend can be better observed in Figures 6.30 to 6.33. The scatter plots are slightly above the 1:1 line meaning that the predicted values were higher than the measured ones.
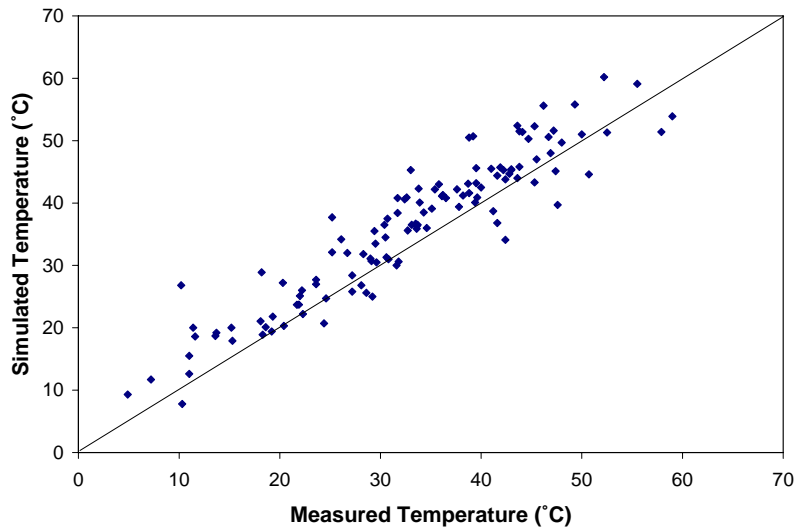
Figure 6.30. Measured vs. simulated pavement surface temperature for MnROAD test cell 33.
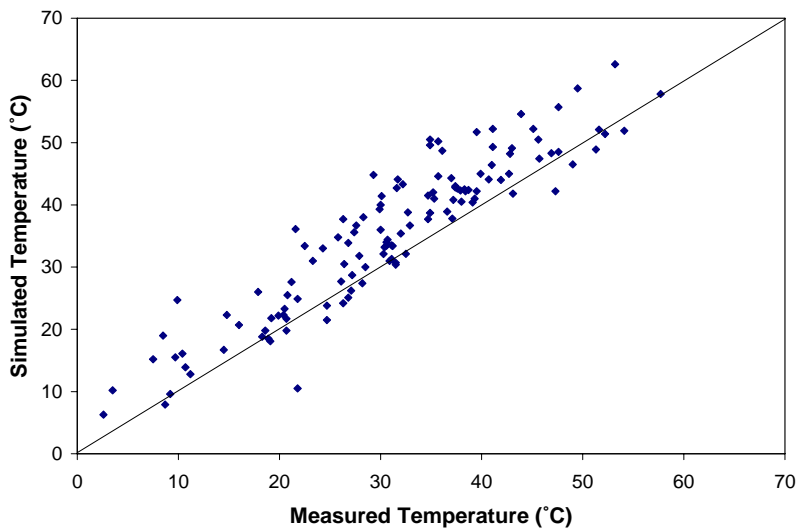
Figure 6.31. Measured vs. simulated pavement surface temperature for MnROAD test cell 34.
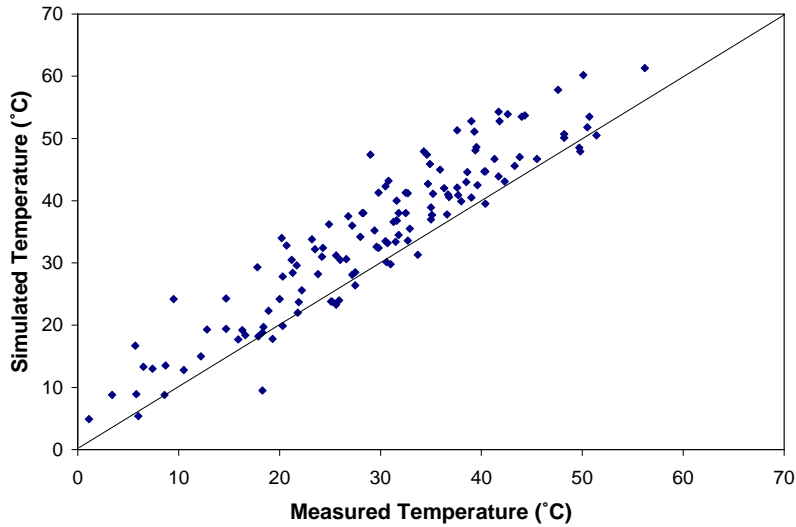
Figure 6.32. Measured vs. simulated pavement surface temperature for MnROAD test cell 35.
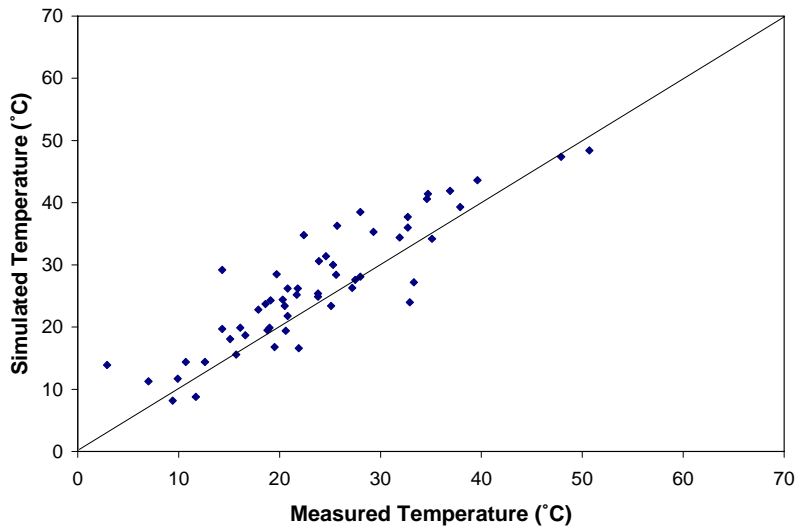
Figure 6.33. Measured vs. simulated pavement surface temperature for MnROAD test cell 12 (concrete).

The agreement between the predicted and measured temperatures appears to be better in certain years, as shown in Figure 6.34 for cell 35, which may indicate the possibility of measuring errors or change in the conditions in which the measurement was performed.
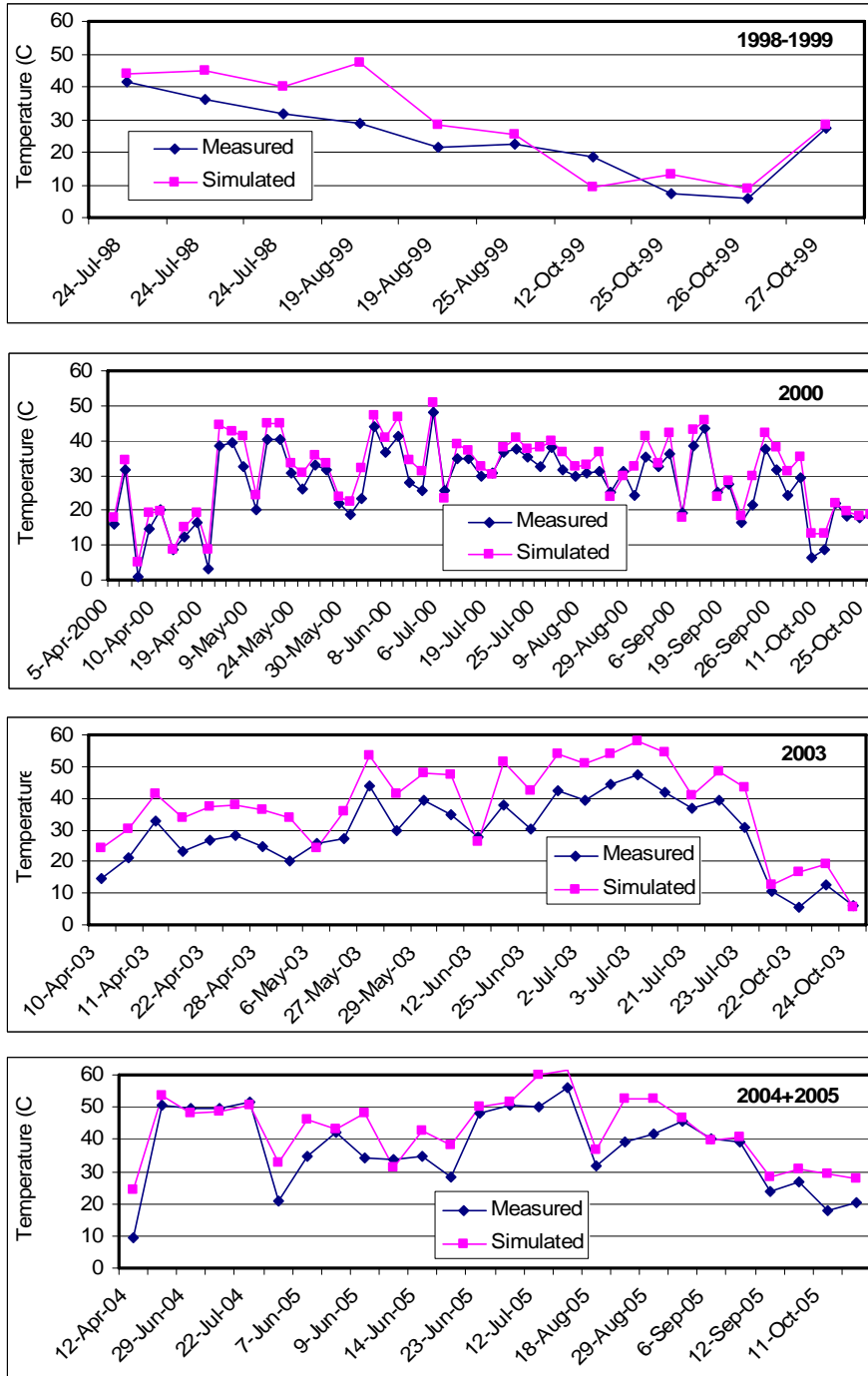
Figure 6.34. Measured vs. simulated pavement surface temperature for MnROAD test cell 35.

Extraction of Pavement Thermal Diffusivities from Measured Temperature Times Series

It is possible that thermal diffusivity is not only useful and necessary to calculate temperatures inside an asphalt pavement; it may also be an indicator of asphalt pavement aging. The change of

thermal diffusivity in time may be related with changes of the bonding of material molecules and the presence of microcracks. Thus, calculation of the pavement thermal diffusivity with time may be use as a tool for aging estimation.

Three methods to extract pavement thermal diffusivity from measured pavement temperature time series at two or more depths are described in the following sections. Two methods use the analytical solutions for heat transfer into a semi- infinite solid and relate the attenuation and the phase shift of diurnal temperature change with depth to thermal diffusivity. The first approach considers the surface temperature forcing to be a simple sinusoidal function with a period of one day. The second method considers the surface temperature as a general time series signal that can be decomposed into periodic functions with a Fourier series. The accuracy of these two methods is limited by the non-homogeneous nature of the pavement/subgrade/soil system. The third method uses a one-dimensional unsteady finite difference heat transfer model (described previously) to extract thermal diffusivities from measured temperatures. This method requires more computational effort, but can take into account the variation in thermal diffusivity between the pavement and underlying subgrade.

In all cases, the analysis was applied to 15-minute temperature data from the MnROAD test cell 33, with an asphalt thickness of 10.1 cm (4 inches). The test section includes two temperature sensors in the pavement and at five other depths in the subgrade and base layers (Figure 6.2).Variations in the thermal diffusivities with season and over a period of years is also determined in the following sections.

Method 1: Extraction of thermal diffusivity by application of an analytical solution for a sinusoidal temperature variation with depth to recorded temperature time series

Analytical Background

For a semi-infinite, uniform slab with no internal heat generation and a specified periodic surface temperature or surface heat flux, an analytical solution exists for the amplitude and the phase of the temperature profile in the slab [50]. For a surface temperature in the form of a simple sinusoid, $T(t) = T_o Cos(2\pi t/\tau)$, the temperature as a function of depth and time is given by:

$$T(z,t) = T_o \, Exp\left(-\sqrt{\frac{\pi}{\alpha\tau}}\, z\right) Cos\left(\frac{2\pi t}{\tau} - \sqrt{\frac{\pi}{\alpha\tau}}\, z\right) \tag{13}$$

where T is temperature, T_o is the surface temperature amplitude, t is time, z is depth normal from the surface, α is thermal diffusivity, and τ is the period. The exponential term is sometimes referred to as the damping factor δ, and the second term under the cosine function is the phase shift ϕ.

Thermal diffusivity α and depth z determine the decrease in amplitude with depth and the phase shift with respect to the surface temperature. If the measured pavement temperature time series at two depths show a periodic variation, the thermal diffusivity can be extracted from the measured variation of amplitude and phase with depth. Method 1 assumes that the surface or near-surface temperature of the pavement can be represented as a pure sinusoid with a period of one day.

Using method 1, temperature time series from MnROAD cell 33 were analyzed as follows:

- The diurnal variation was separated (detrended) from temperature variations at longer time scales by subtracting the 24 hour running average from the raw temperature data for each depth (Figure 6.35).
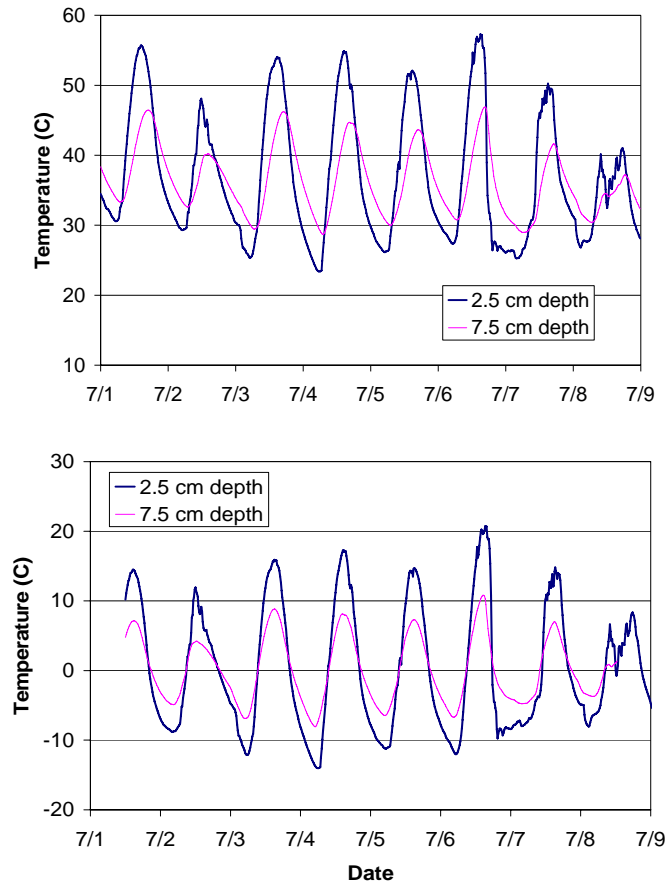
Figure 6.35. Time series of measured temperature in MnROAD cell 33, July 1 – July 8, 2002.

The upper panel in Figure 6.35 gives the raw 15-minute temperature data, while the lower panel gives the "detrended" data after the 24-hour running average has been subtracted from each raw data set, and a phase shift of 2.25 hours (lag) has been applied to the 7.6 cm depth data.

- The phase relationship between the diurnal variation at 2.4 cm and 7.6 cm was then examined by calculating the correlation coefficient between the two time series for varying phase shifts (Figure 6.36). The phase shift values given were applied to the 7.6 cm depth temperature data. The optimum phase shift, ϕ_o, coincided with the highest correlation coefficient.

164
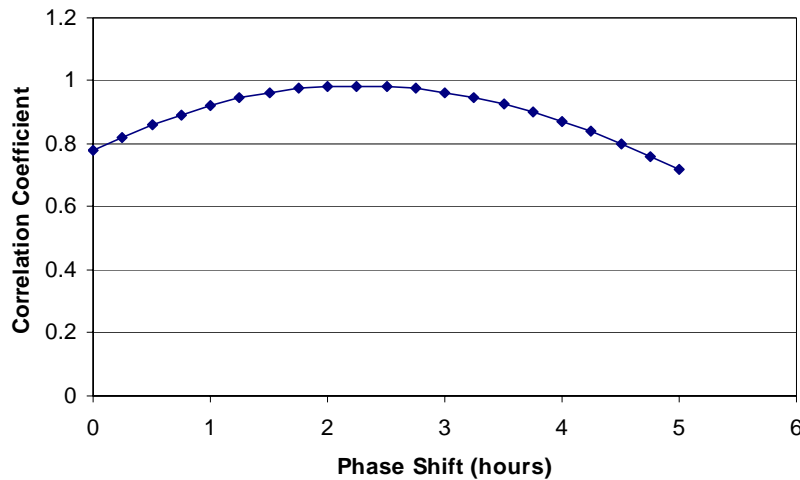
Figure 6.36. Correlation coefficient versus time phase shift for measured temperature at 2.4 and 7.6 cm depth in MnROAD cell 33, July 1 – July 8, 2002.

- The optimum phase shift, ϕ_o (2.25 hours) was then applied to the temperature data at 7.6 cm depth, and the detrended, phase-shifted temperature at 7.6 cm was plotted against the detrended 2.4 cm data (Figure 6.37).
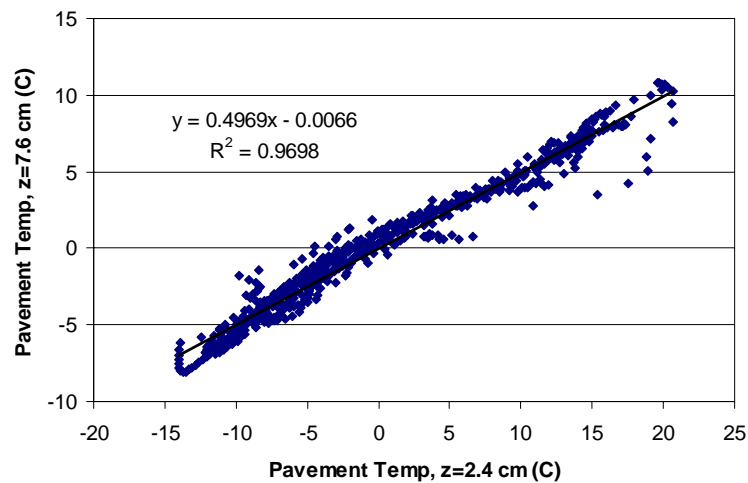
Figure 6.37. Measured temperature at 7.6 cm depth versus 2.4 cm depth in MnROAD cell 33, July 1 – July 8, 2002.

The slope of the relationship, S, gives the decrease in diurnal temperature amplitude from 2.4 cm to 7.6 cm depth, and the thermal diffusivity α_1 was calculated as:

$$\alpha_1 = \frac{\pi}{\tau}\left(\frac{\Delta z}{-\ln(S)}\right)^2 \tag{14}$$

where Δz is the vertical distance between the two measurements.

- The optimum phase angle, ϕ_o, was then used to calculate a second value of the pavement thermal diffusivity α_2:

$$\alpha_2 = \frac{\tau}{\pi}\left(\frac{\Delta z}{2\phi_o}\right)^2 \tag{15}$$

Numerical Results

The above procedure was performed on segments of temperature data varying from 1 to 14 days. Segment lengths of 7 to 10 days gave the best relationships, i.e. the highest r^2 in determining the slope S (Figure 6.37). A full year of data (Jan 1 – Dec 31, 2002) from cell 33 was used to calculate α_1 (diurnal temperature amplitude) and α_2 (optimum phase shift) using non-overlapping 7 day segments, giving 52 separate values of α_1 and α_2 for the year (Figure 6.38). The r^2 for the amplitude relationship (Figure 6.37) is also given.
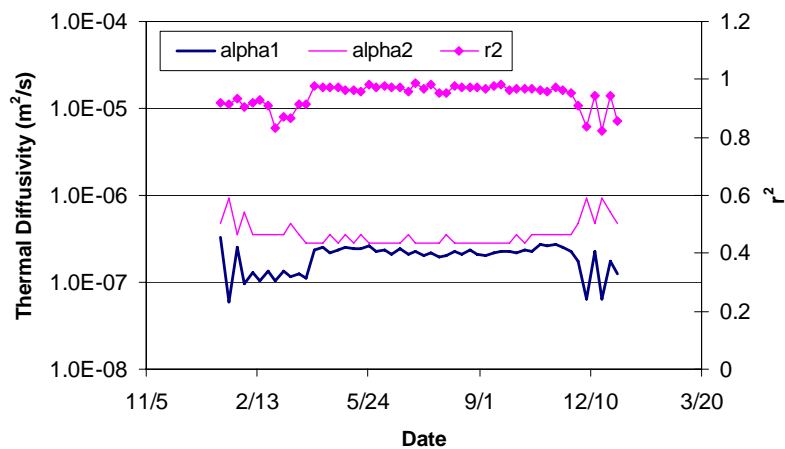
Figure 6.38. Thermal diffusivity (α_1 or α_2) from 7-day running samples of 15-minute data, January 1 – December 31, 2002, MnROAD cell 33

The weekly values of diffusivity are reasonably constant from May through September, although α_2 is consistently about 30% higher than α_1. Much more variation in weekly diffusivity for both α_1 and α_2 is shown in the cold months (Figure 6.38), including up to an order of magnitude disagreement between α_1 and α_2, and lower r^2 in the relationship between the two temperatures.

Figure 6.39 shows the variation in diffusivity over one year, where the values of α_1 and α_2 were calculated using 2-day segments of temperature data instead of 7-day segments. In Figure 6.39, the r^2 for the amplitude relationship is also presented. The results are very similar to those obtained using 7-day segments (Figure 6.38), but with a slightly lower overall r^2 (0.92 for 2-day segments versus 0.94 for 7-day segments).
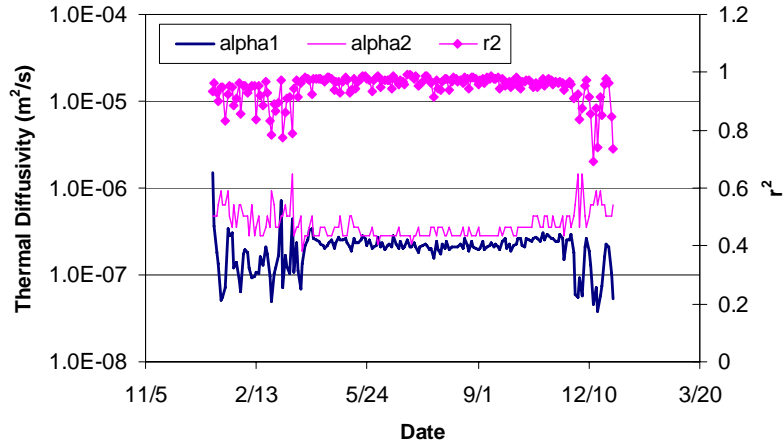
Figure 6.39. Thermal diffusivity from 2-day samples of 15-minute data, January 1 – December 31, 2002, MnROAD cell 33

The same procedure was used to extract the thermal diffusivity of the cell 33 sand/gravel base layer using temperature measurements at 13 and 38 cm below the surface, and for the underlying clay layer using temperature measurements at 43 and 61 cm below the surface. The resulting thermal diffusivity values are given in Figure 6.40.
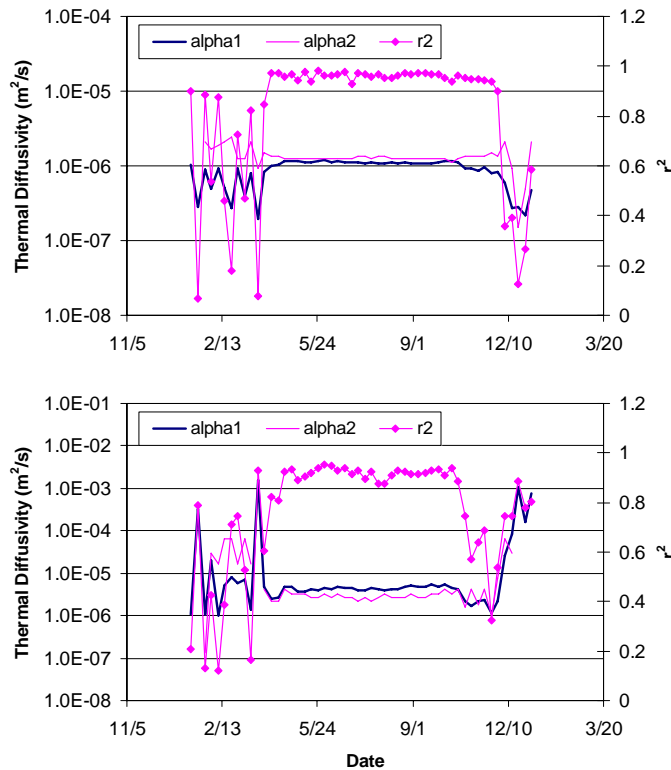
Figure 6.40. Thermal diffusivity in a sand/gravel subgrade layer (upper panel) and a clay base layer (lower panel), MnROAD cell 33

It is apparent that there is more error in the calculated cold month (October-April) values of thermal diffusivity than the warm month (May-September) values. It can be speculated that moisture content and sub-freezing conditions (freeze/thaw cycles) may be the cause of the error, because phase change (latent heat) is not included in the model. Compared to the pavement, there is more uncertainty in the extracted diffusivity for the base layers due to smaller diurnal temperature variations.

As with the asphalt layer, there is no evidence of a systematic variation in diffusivity with season. Table 6.7 gives the average and standard deviation of the diffusivity value for each layer, for the period May 1 to September 1, 2002.

Table 6.7. Mean and standard deviation of thermal diffusivities α_1 or α_2 for asphalt, sand/gravel, and clay layers (MnROAD cell 33), May 1 to September 1, 2002.

Material	α_1 (m²/sec) (n=18)		α_2 (m²/sec) (n=18)	
	Mean	STD	Mean	STD
Asphalt (4" thick)	2.25E-7	0.19E-7	3.00E-7	0.32E-7
Sand/Gravel (12" thick)	11.10E-7	0.31E-7	12.60E-7	0.54E-7
Clay	43.10E-7	3.93E-7	28.20E-7	3.69E-7

While the standard deviation is similarly small for diffusivity extracted from amplitude or phase, the diffusivity values (α_2) extracted from the phase shift (ϕ_o) are higher than diffusivity values (α_1) obtained from amplitude damping (S). It is also noteworthy that the average values of 2.25E-7 and 3.0E-7 m²/s for α_1 and α_2, respectively, are considerably lower than values of asphalt thermal diffusivities summarized by Luca and Mrawira [51], ranging from 3.5E-07 to 14.4E-07 m²/s.

An advantage of using in-situ temperature data to extract material properties is the ability to examine long term trends, *e.g.* aging effects. Table 6.8 gives the extracted diffusivity for the asphalt test section for six years, 2000 – 2005. Both α_1 and α_2 exhibit slight trends over six years, but in opposite direction (Figure 6.41), so that no meaningful trends are extracted from this analysis.

Table 6.8. Mean and standard deviation (STD) of thermal diffusivities α_1 or α_2 for asphalt pavement (MnROAD cell 33), May 1 to September 1, 2000-2005.

Year	α_1 (m²/sec)		α_2 (m²/sec)	
	Mean	STD	Mean	STD
2000	2.29E-7	1.47E-8	2.77E-7	1.74E-8
2001	2.17E-7	1.36E-8	2.93E-7	3.28E-8
2002	2.25E-7	1.94E-8	3.00E-7	3.22E-8
2003	2.23E-7	1.15E-8	2.92E-7	2.43E-8
2004	2.10E-7	0.61E-8	2.97E-7	2.96E-8
2005	2.09E-7	0.84E-8	3.17E-7	3.85E-8
Average	2.19E-7	1.23E-8	2.96E-7	2.91E-8
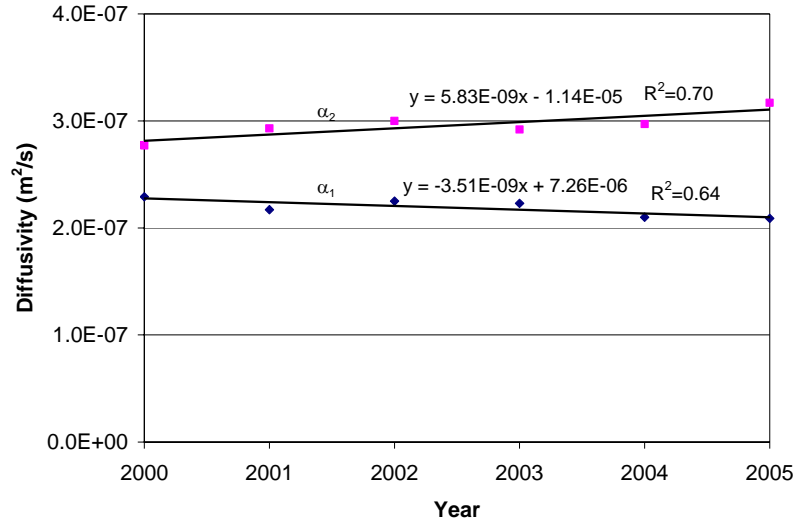
Figure 6.41. Thermal diffusivity (annual average) for MnROAD cell 33

Method 2: Extraction of thermal diffusivity by FFT (Fast Fourier Transform) of measured temperature time series with multiple frequency components

Analytical Background

The diurnal variation in pavement temperature is not an exact single frequency sinusoid, even for cloudless days. This is readily apparent from the plots in Figure 6.35. The sinusoidal nature of the recorded diurnal temperature signal is due to solar radiation. However, solar irradiance does not follow an exact sinusoid during a day and atmospheric conditions are not stationary. Fortunately, any non-sinusoidal signal can be decomposed into the sum of sinusoidal functions using a Fourier series, *e.g* as illustrated by Equation 16:

$$T(t) = a_0 + a_1 \cos(\omega t) + a_2 \cos(2\omega t) + ... \qquad (16)$$

where ω is frequency, t is time, and the coefficients a_i are complex numbers that represent both a magnitude and a phase shift for each frequency component.

For a time variable surface temperature composed of multiple frequency components, each component will decay with depth with a distinct decay rate and phase shift, as given by Equation 13. For a linear heat conduction problem, i.e. constant thermal properties, the temperature variation at some depth can be found as the sum of the response to each frequency component of the surface temperature. This method was applied to the MnROAD cell 33 temperatures using Matlab, as follows:

1) A Fourier transform was applied to a temperature time series at 2.5 cm depth to find the complex Fourier coefficients, a_i.

2) For each frequency component, the attenuation coefficient and phase shift was calculated as in Equation 13, based on a starting value of the thermal diffusivity.

3) The attenuation and phase shift was applied to each complex Fourier coefficient, a_i, and the corresponding time series was calculated with an inverse Fourier transform.

4) The calculated and measured time series at 7.5 cm depth were then compared, and the root-mean-square (RMSE) error was calculated

169

5) Steps 2–5 were repeated for different values of thermal diffusivity, and an optimum value of thermal diffusivity was found by minimizing the RMSE error.

Numerical Results

Method 2 was applied to measured temperature time series from MnROAD test cell 33 in one week time increments. Figure 6.42 gives an example of a Fourier transform of a temperature time series from cell 33.
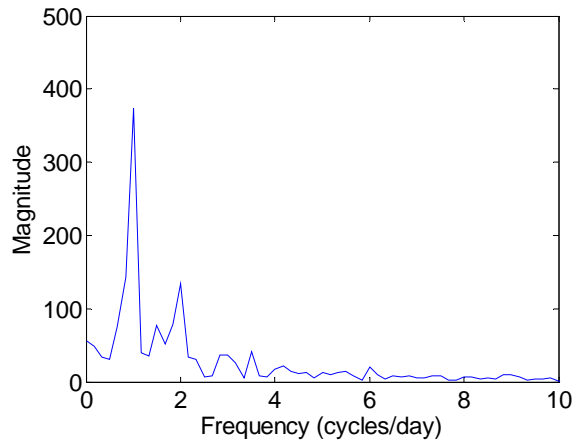
Figure 6.42. Fourier transform magnitude (spectral density) versus frequency for 7-day 15-minute pavement temperature time series (June, 2004) at 2.5 cm depth.

The dominant frequencies are 1 cycle/day and 2 cycles/day, with smaller peaks at higher harmonics. An example of a temperature time series at 7.5 cm depth synthesized from the inverse-FFT according to step 3 in the procedure is presented in Figure 6.43. The temperature shown is the detrended (fluctuating) temperature, i.e. measured temperature minus the mean for the time period.
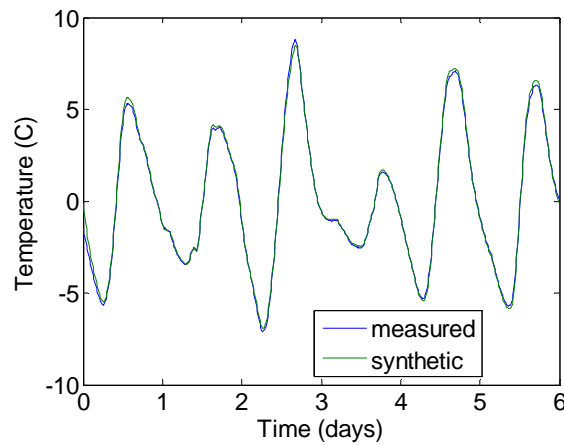
Figure 6.43. Example of measured temperature and synthesized temperature time series at 7.5 cm depth.

170

The synthesized time series matches the measured temperature very closely when an optimized thermal diffusivity value of α = 2.1E-07 m^2/sec is used (the RMSE of the synthetic time series is 0.04 °C).

Weekly thermal diffusivities were determined by minimizing the RMSE between synthesized and measured temperatures for each week of the year. Thermal diffusivity shown in Figure 6.44 was extracted from measured temperatures at 2.4 cm and 7.6 cm depth using the Fourier transform method in 7-day segments of 15-minute data.
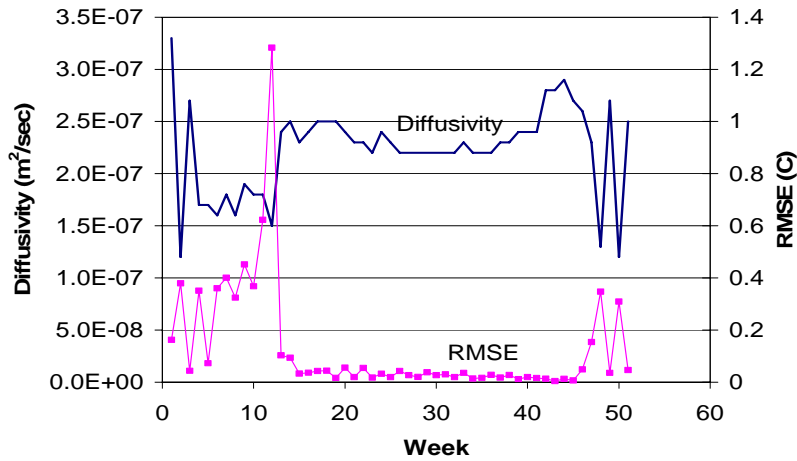
Figure 6.44. Thermal diffusivity and RMSE of fitted temperature versus week number for MnROAD cell 33, 2002.

In Figure 6.44, the diffusivity value is in the range of 2.2E-7 to 2.5E-7 m^2/sec for May through September, with an RMSE less than 0.05°C. There is a modest variation in diffusivity over the year, with lower values in the mid-year. Figure 6.45 shows a weak dependence of thermal diffusivity on mean weekly temperature. The data are for April through October of 2000-2005.

y = -1.11E-09x + 2.57E-07
R^2=0.659
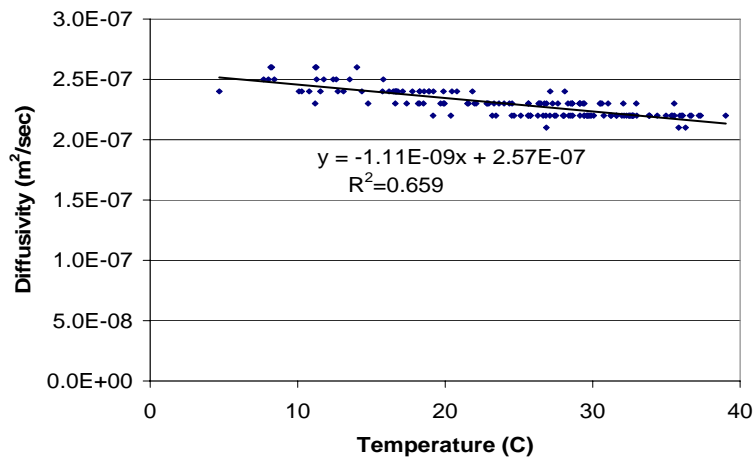
Figure 6.45. Thermal diffusivity versus weekly mean pavement temperature for MnROAD cell 33, week 11 through week 41, 2000-2005.

171

The same analysis was performed on all of the temperature data from MnROAD cell 33 for the years 2000 to 2005, with very similar results (Figure 6.46).
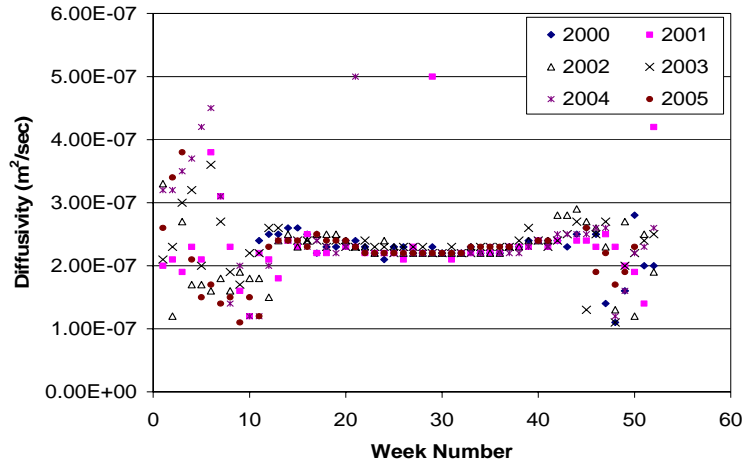
Figure 6.46. Thermal diffusivity versus week for MnROAD cell 33.

As was already seen in the results obtained by method 1, the RMSE of the synthetic temperature fit is much greater, and the thermal diffusivity varies much more in the cold season (October-April) compared to the warmer season (May-September). This variation is likely due to freeze/thaw processes in the pavement, base and subgrade layers, which introduce non-linear thermal behavior to the linear heat conduction problem.

Method 3: Extraction of thermal diffusivity by calibration/optimization of a finite difference model for heat conduction

Analytical Background

The third method to extract thermal diffusivity from temperature measurements uses a one-dimensional finite difference model for heat conduction in the pavement, subgrade and soil layers. The model was described previously in the pavement temperature simulation section of this chapter. The model was formulated to simulate time variable pavement and soil temperature profiles based on heat transfer at the pavement surface. In the model application described below the surface boundary condition was replaced by the measured pavement temperature at 2.4 cm depth. The model was used to simulate sub-surface temperature profiles in hourly time steps. The thermal diffusivity values of the pavement, subgrade and soil were adjusted to find the best match of simulated and measured temperatures at depths of 7.6 cm, 13 cm, 25 cm, 38 cm, 43 cm and 61 cm.

Numerical Results

Optimization results using the finite difference model are given in Figure 6.47. Two cases were examined:

- Case 1: Independent values of pavement, subgrade and soil diffusivity, setting the subgrade thermal diffusivity equal to a constant, 1.0E-06 m^2/s (see Table 6.7); the

optimum pavement thermal diffusivity was found to be 3.0 E-07 m^2/s based on minimizing the RMSE of the simulated pavement temperature from May to September, 2002.

- Case 2: Constant diffusivity for all layers, setting the sub-grade and soil thermal diffusivity equal to that of the pavement, the optimum pavement thermal diffusivity was significantly lower, 2.25 E-07 m^2/s. This is close to the values of diffusivity obtained in methods 1 and 2, which also assume uniform thermal properties.
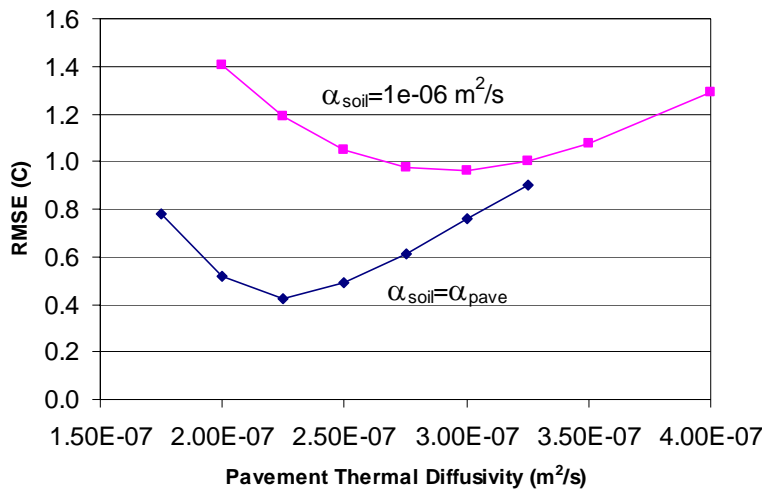
Figure 6.47. RMSE of simulated pavement temperature versus pavement thermal diffusivity for a fixed and a variable value of subgrade/soil diffusivity (α_{soil}).

In summary, thermal diffusivities for MnROAD cell 33 were calculated from the 15-minute temperature data recorded from 2000 to 2005. Three different methods, making different assumptions, were used. The results obtained by all three methods are shown in the Table 6.9. The calculated mean annual thermal diffusivity of the asphalt pavement layer in the warm months given in Table 6.9 ranges from 2.09 to 3.17E-7 m^2/s for the six years of data.

Table 6.9. Summary of thermal diffusivities of asphalt pavement layer (MnROAD cell 33)

Year	Method 1 Single Frequency, Amplitude	Method 1 Single Frequency, Phase	Method 2 Multiple Frequency	Method 3 Finite Difference
2000	2.29E-07	2.77E-07	2.27E-07	
2001	2.17E-07	2.93E-07	2.25E-07	
2002	2.25E-07	3.00E-07	2.29E-07	3.0E-07
2003	2.23E-07	2.92E-07	2.30E-07	
2004	2.10E-07	2.97E-07	2.25E-07	
2005	2.09E-07	3.17E-07	2.27E-07	
Average	2.19E-07	2.96E-07	2.27E-07	

Summary and Conclusions

A number of important conclusions can be drawn from the pavement temperature data analysis:

- Daytime maximum pavement temperature greatly exceeds maximum air temperature, with surface temperatures of up to 63°C (145°F) in mid-summer. Note that the typical asphalt binder grade for this climate is PG 58.

- In general, temperature gradients due to heating are larger than those due to cooling, and surface temperature gradients are higher than the gradient across the thickness of the pavement.

- Surface temperature gradients can be up to 5°C/cm, and temperature rate of change can be up to 40°C/hour. The effect of such a large temperature rate of change needs to be further investigated in relation to the relaxation properties of asphalt binders.

- The highest negative temperature gradients occur during precipitation events, which may lead to tensile surface stress.

- Diurnal amplitude tends to increase with increasing mean temperature, but significant amplitudes exist at cold temperature.

- Daily max, min, and average pavement temperature and diurnal amplitude are not smoothly distributed, but have two peaks that appear to be driven by the distribution of solar radiation.

In addition, the pavement temperature simulations performed in this study have shown that the pavement temperature model developed at SAFL is able to simulate asphalt temperature to within 1 to 2°C RMSE. The pavement temperature model seems suitable to model pavement and subgrade temperatures at RWIS sites and therefore, can provide a tool to check the consistency of the pavement temperature data measured at RWIS sites by predicting expected pavement temperature time series from the measured climate data at the RWIS sites with the model calibrated against the much more detailed data from the MnROAD site. Substantial differences between predicted and measured pavement temperatures at an individual RWIS would be indicative of a need for quality control of the instrumentation, while widespread differences could indicate regional differences in pavement responses to weather.

The pavement temperature simulations are also useful to identify the processes and weather conditions that produce the extreme changes in pavement temperature parameters that lead to pavement degradation, for example, rapid decreases in surface temperature due to the evaporation of precipitation from a warm pavement.

Based on the calculation of the thermal diffusivities of the asphalt pavement and the subgrade the following conclusion can be drawn:

- Temperature data from the cold months give substantial errors in the calculated thermal diffusivity, because freeze/thaw processes introduce non-linear behavior to the heat conduction equation. Thermal diffusivities calculated for each week of the warm months (May to September) showed substantially less variation than those in the colder months (see Figures 6.37, 6.38, 6.39, 6.43 and 6.45).

- There is evidence of a systematic although weak dependence of the thermal diffusivity on temperature at a seasonal timescale.

174

- The thermal diffusivities of the subgrade and the soil (clay) were approximately 4 to 5 times and 10 to 20 times, respectively, larger than the thermal diffusivity of the asphalt pavement (Table 6.7).

- The single frequency thermal diffusivity extraction method (method 1) works best for clear days, i.e. large, smoothly periodic temperature variations. Days with cloud cover and/or snow cover give a non-sinusoidal variation in temperature so that equations (13)–(15) do not accurately capture the variation in temperature with depth and time. The variation in thermal properties between asphalt, subgrade, and base layers also introduces errors in the extracted diffusivity. The best values were obtained for the near surface data, *e.g.* in the asphalt layer, while measurements in the base layers gave less certain diffusivity values.

- The multiple frequency method (method 2) addresses the problem of non-sinusoidal temperature functions and produced more consistent results than the single frequency analysis for days with varying cloud cover, etc. The multiple frequency method is still susceptible to freeze thaw cycles and to non-constant material properties over depth. Overall, method 2 gave more consistent results than method 1 (Table 6.9). The mean thermal diffusivity for the warm season calculated by method 2 varied by less than 2% from year to year (Table 6.9).

- Extracting thermal diffusivities with a finite difference model allows for both non-sinusoidal temperature forcing and non-uniform material properties over depth, and likely results in the most representative values for thermal diffusivity calculated by the three methods. With further work, the effect of freeze-thaw cycles can be included in the finite difference model. The difference in thermal diffusivity between case 1 and case 2 in method 3 may be considered to be the error associated with the assumption of a uniform slab. In methods 1 and 2 the heat transfer equations derived for a uniform structure are applied to a non-uniform series of layers (pavement, subgrade and soil).

- No clear evidence of a systematic variation of thermal diffusivity with asphalt pavement age was found for the 5-year period investigated, and data from one test cell.

- By extending the analysis proposed over periods longer than 5 years, asphalt pavement aging may be detectable in thermal diffusivities results. In the current study aging was not detected, but only data over a 5-year span and from one field site (MnROAD test cell 33) were analyzed.

It is important to note that the pavement temperature analysis can be expanded to determine moisture content in the pavements and subgrade from temperature signals during freeze-thaw cycles. When pavement temperatures cross the freezing point (0°C or 32°F), measured temperature signals in the pavement and subgrade are delayed by latent heat of freezing or thawing. The amount of latent heat depends on moisture content of the pavement and subgrade. By including latent heat of freezing in the heat conduction equation during freeze/thaw cycles one can arrive at moisture estimates from measured temperature time series in spring and fall. Since thermal diffusivity can and has been determined from temperature time series for the warm months, moisture content in the pavement and subgrade can be calculated from temperature time series for the cold months.

The freeze/thaw/moisture model can be combined with measured temperature and moisture time series to characterize the time and length scales over which freeze-thaw cycles occur, from seasonal freezing of the soil to depths of meters to daily freeze thaw cycles in the

upper few centimeters of the pavement. In addition, the freeze/thaw analysis may be able to detect long term changes in the moisture content of pavement due to aging.

CHAPTER 7

CONCLUSIONS AND RECOMMENDATIONS

Conclusions

A number of important conclusions can be drawn from the research performed in this study. The experiments and analyses performed to assess the presence of oxidative aging and of microcracks indicated that:

- The XPS procedure is capable of detecting the presence of oxidized carbon functional groups. However, very little ketones were detected in both the mixture and the binder samples tested, regardless of the age of the samples. The amounts of ketones varied significantly between the replicates of the same sample, indicating poor repeatability of the test.

- Assessing pavement surface condition based on images obtained from SEM testing is impractical due to the localized nature of the test. Specimen preparation is expensive and time consuming and the specimen tested may not be representative of what is observed in the field. The fact that only cracks on the surface of the aggregates were detected seems to indicate that microcracks are not present at room temperature due to healing and that aggregate particles may contain microcracks due to aggregate crushing and mixture compaction and test specimen sawing.

- The microcracks observed in the aggregates of the asphalt pavement SEM images are most likely due to either the crushing process or the field compaction, which can affect the cracking resistance of the mixtures, in particular at low and intermediate temperatures.

- Preliminary evaluation of fluorescent dyes for microcracks detection indicates that there is potential in using this technology on the surface of asphalt pavements but further testing needs to be performed for complete evaluation.

The following conclusions can be drawn from the analysis of the mechanical testing of both asphalt binders and mixtures:

- Pavement age before surface treatment application affects the results of FTIR, BBR binder and DSR. From these three tests, FTIR appears to be the most sensitive to the age of the material. Contrary to what it is expected, DSR and BBR testing indicates that older sections have less stiffness; this trend can be explained by the fact that the emulsion application rate increases with the age of the pavement.

- The properties obtained for both mixtures and binders are significantly affected by the temperature. Mixture fracture energy, BBR m_{mix} and m_{binder} at 60 seconds and binder strain at failure increase with temperature increase. On the other hand, mixture fracture toughness, S_{mix} and S_{bin} at 60 seconds and binder failure stress decrease with temperature decrease.

- For TH 56 sections, the samples located in the wheel path have higher mixture fracture energy, BBR S_{mix} at 60 seconds and larger binder phase angle than samples between the

wheel paths. More aging is observed in between the wheel path samples from FTIR testing.

- Mixture fracture energy, mixture fracture toughness, S_{mix}, m_{mix}, S_{bin}, m_{binder}, binder stress and strain at failure and binder phase angle are overall greater in the lower layer than in the upper layer.

- Higher air void content reduces BBR S_{mix} and increases m_{mix} and mixture fracture energy.

- For TH 251, the pavement sections where surface treatments were applied have less S_{mix} and higher m_{mix} compared to the control section.

- Mixture fracture toughness of samples from TH 56 constructed in 1995 decreases with the aging of the pavement. Negative correlation between the age of the pavement and the phase angle of the binder is observed.

- Air void content negatively affects the mixture fracture toughness. As the voids in the sample increases the mixture fracture toughness decreases.

- It is observed from the correlation matrices calculated independently for each layer that age before treatment has a low correlation with both fracture properties and the binder strain at failure. These correlations were not observed previously when all the information of the tests was included. The previous negative correlation that was not expected between the age of the pavement and the complex modulus from DSR is observed only in the lower layer and not in the upper layer where most of the aging occurs.

- BBR mixture testing shows promising results regarding aging characterization. The stiffness of the mixture increases as it was expected when the age of the pavement increases. BBR mixture results may contain explanatory information to predict SCB, BBR binder and direct tension test parameters.

- Calculation of the correlation matrices for the two depths independently seems to remove unexpected trends observed in the analysis.

- Factors such as pavement construction year, depth, path, and seal coat application year studied in the statistical analysis have statistically significant impact on the low temperature properties, especially on the m-value. However, due to the high degrees of freedom of the models used in the analysis, many of the statistical differences were too small to be of a practical significance.

- The extracted binder analysis indicated that the 1999 sections had higher creep stiffness and a lower relaxation rate than the 1995 sections; the mixture analysis indicated that the 1995 pavement had higher creep stiffness, and a lower relaxation rate than the 1999 sections. The results of the ANOVA of mixtures agree with common knowledge that older pavements are stiffer and have a lower relaxation rate than newer pavements.

- The depth below the pavement surface was identified by the mixture ANOVA as having a very significant effect on the m-value; the relaxation rate of the lower layer was higher than the upper layer which agrees with the current knowledge about aging.

- The effect of the aggregate type used in the chip seal was not discernable because it was confounded with the surface treatment timing factor (age of the pavement when treated). The statistical analysis show conflicting results between the binder and the mixture.

- The first attempt in trying to identify the best window of time for the surface treatment application based on fracture toughness is between 4 and 6 years. However, note that the difference between the maximum and minimum mixture fracture toughness at both temperatures may not be significant.

- Statistical and visual analysis results could not conclusively identify an optimal treatment time. Testing of extracted asphalt binder revealed that cell 17, which corresponds to age 7, had a significantly lower creep stiffness value than other cells. However these results were not confirmed by the *m*-value analysis and by the asphalt mixture results. In general, there was no observable trend of the low temperature properties with respect to surface treatment application time. Most likely, two factors are responsible for this result. The construction process and the asphalt mixtures of the 1995 and the 1999 sections were different. In addition, the variability within a pavement structure is high enough to warrant a high number of replicate samples, which is not possible for practical considerations. In this research only a limited number of samples were available.

- Based on the limited number of tests performed on TH 251 samples it appears that the surface treatment that prevents aging the best is the chip seal. Samples treated with chip seal show the highest mixture fracture energy, the lowest S_{mix} and S_{binder} and the highest m_{binder}. Additionally, the binders extracted from the section treated with chip seal show one of the highest strains at failure.

The pavement temperature data analysis indicated that:
- Surface temperature gradients can be up to 5°C/cm, and temperature rate of change can be up to 40°C/hour. The effect of such a large temperature rate of change needs to be further investigated in relation to the aging effects at the surface and through the asphalt layer depth.

- Daytime maximum pavement temperature greatly exceeds maximum air temperature, with surface temperatures of up to 63°C (145°F) in mid-summer. Note that the typical asphalt binder grade for this climate is PG 58.

- In general, temperature gradients due to heating are larger than those due to cooling, and surface temperature gradients are higher than the gradient across the thickness of the pavement.

- The highest negative temperature gradients occur during precipitation events, which may lead to tensile surface stress.

- Diurnal amplitude tends to increase with increasing mean temperature, but significant amplitudes exist at cold temperature.

- Daily max, min, and average pavement temperature and diurnal amplitude are not smoothly distributed, but have two peaks that appear to be driven by the distribution of solar radiation.

- The pavement temperature simulations performed in this study have shown that the pavement temperature model developed is able to simulate asphalt temperature to within 1 to 2°C RMSE. The pavement temperature model seems suitable to model pavement and subgrade temperatures at RWIS sites and therefore, can provide a tool to check the consistency of the pavement temperature data measured at RWIS sites.

179

- The pavement temperature simulations are also useful to identify the processes and weather conditions that produce the extreme changes in pavement temperature parameters that lead to pavement degradation, for example, rapid decreases in surface temperature due to the evaporation of precipitation from a warm pavement.

- The simulated surface temperatures are in reasonable agreement with the measured temperatures for both, asphalt and concrete pavements. Simulated temperatures are slightly higher than the measured surface temperatures.

- The agreement between the predicted and measured temperatures appears to be better in certain years which may indicate the possibility of measuring errors.

- Temperature data from the cold months give substantial errors in the calculated thermal diffusivity, because freeze/thaw processes introduce non-linear behavior to the heat conduction equation. Thermal diffusivities calculated for each week of the warm months (May to September) showed substantially less variation than those in the colder months

- There is evidence of a systematic although weak dependence of the thermal diffusivity on temperature at a seasonal timescale.

- The thermal diffusivities of the subgrade and the soil (clay) were approximately 4 to 5 times and 10 to 20 times, respectively, larger than the thermal diffusivity of the asphalt pavement.

- The single frequency thermal diffusivity extraction method works best for clear days, i.e. large, smoothly periodic temperature variations. Days with cloud cover and/or snow cover give a non-sinusoidal variation in temperature so that the equations in the model do not accurately capture the variation in temperature with depth and time. The variation in thermal properties between asphalt, subgrade, and base layers also introduces errors in the extracted diffusivity.

- The multiple frequency method for thermal diffusivity extraction addresses the problem of non-sinusoidal temperature functions and produced more consistent results than the single frequency analysis for days with varying cloud cover, etc. The multiple frequency method is still susceptible to freeze thaw cycles and to non-constant material properties over depth. Overall, this method shows more consistent results than the single frequency method.

- Extracting thermal diffusivities with a finite difference model allows for both non-sinusoidal temperature forcing and non-uniform material properties over depth. The result obtained with this method is the closest to the real thermal diffusivity in comparison to the other two methods.

- No clear evidence of a systematic variation of thermal diffusivity with asphalt pavement age was found for the 5-year period investigated.

- By extending the analysis proposed over periods longer than 5 years, asphalt pavement aging may be detectable in thermal diffusivities results. In the current study aging was not detected, but only data over a 5-year span and from one field site were analyzed.

Some of these conclusions should be interpreted with caution due to the inherent variability of pavement samples and to the fact that not enough replicates were available in this study, which is typical in pavement field studies for practical reasons.

Recommendations for future research

The findings of this study represent a promising start in understanding the role played by surface treatments in protecting pavements against aging and cracking deterioration. However, further research needs to be done to determine the optimum time for the application of surface treatments. The following recommendations are made for future research:

- The mechanical tests performed on asphalt binders and mixtures samples in this study can be used to detect changes in properties related to performance. In particular, the BBR test on thin mixture beams appears to be a promising tool in evaluating the properties of thin layers of mixture within the constructed asphalt layers. However, future work has to be carefully planned based on a rigorous statistical design that takes into account the strong effect of construction practice and design, such as using different emulsion application rates to counteract the aging effects.

- The results do not warrant further use of normal XPS for aging studies. It is possible that newer versions of XPS type instruments, such as ion guns and Auger, can provide better results.

- The complexity of running SEM tests and the limited value of the results as part of routine asphalt pavement maintenance activities do not warrant the use of SEM.

- The method to detect microcracks using a fluorescent penetrant should be further investigated using more powerful UV lamps and surfactants that allow the fluorescent solution to better penetrate into microcracks.

- It is suggested that the use of Imaging spectrometry, especially ground spectrometry, to detect aging and deterioration of asphalt pavement surfaces, should be further investigated.

- Pavement temperature analysis can be expanded to determine moisture content in the pavements and subgrade from temperature signals during freeze-thaw cycles. By including latent heat of freezing in the heat conduction equation during freeze/thaw cycles one can arrive at moisture estimates from measured temperature time series in spring and fall.

- The freeze/thaw/moisture model can be combined with measured temperature and moisture time series to characterize the time and length scales over which freeze-thaw cycles occur, from seasonal freezing of the soil to depths of meters to daily freeze thaw cycles in the upper few centimeters of the pavement. In addition, the freeze/thaw analysis may be able to detect long term changes in the moisture content of pavement due to aging.

REFERENCES

(1). *Minnesota Seal Coat Handbook*, sponsored by Minnesota Local Road Research Board, Minnesota Department of Transportation, St. Paul, MN, 1998.

(2). Wood, T. J., and Olson, R. C. "Rebirth of Chip Sealing in Minnesota". *Transportation Research Record* 1989, Vol. 1, TRB, National Research Council, Washington D.C., 2007.

(3). Lee, J., and Kim, R., and McGraw, E. O. "Performance Evaluations of Bituminous Surface Treatment Using Third-Scale Model Mobile Loading Simulator". *Transportation Research Record* 1958, TRB, National Research Council, Washington D.C., 2006, pp. 59-70.

(4). *Asphalt Surface Treatment Procedural Training Manual.* North Carolina Division of Highways, State Road Maintenance Unit, Raleigh, NC, 2000.

(5). Gransberg, D. D., Zaman, M., *Comparing the Performance of Emulsion versus Hot Asphalt Chip Seal Projects in the Texas Department of Transportation's Atlanta District.* Asphalt Emulsion Producers Association report, Annapolis, MD, August 2002.

(6). *Texas Chip Seal Study*, AEMA, April 2003.

(7). Wade, M.J., Ormesher, D., and Peshkin, D.G. "Evaluation of Chip Seals on High-Speed Roadways". *Transportation Research Board,* Washington D.C., 2002.

(8). Peshkin D.G., Hoerner T.E., and Zimmerman K.A. "Optimal Timing of Pavement Preventive Maintenance Treatment Applications" *NCHRP Report 523.* Transportation Research Board, Washington, D.C. 2004.

(9). Gransberg, D., and James, D. M. B. "Chip Seal Best Practices, A Synthesis of Highway Practice". *NCHRP Synthesis 342.* Transportation Research Board, Washington, D.C. 2005.

(10). Li, J., Mahoney, J. P., Muench, S. T., and Pierce, L. M. "Bituminous Surface Treatment Protocol for Washington State Department of Transportation". *TRB 87th Annual Meeting Compendium of Papers DVD*, Washington D.C., 2008.

(11). Cochran, C. *Aging/Optimization Study: Final Construction Report and Early Results.* Unpublished Report, Minnesota Department of Transportation, St. Paul, Minnesota, May 6, 2005.

(12). Bell, C.A., Wieder, A.J., and Fellin, M.J. *Laboratory Aging of Asphalt-Aggregate Mixtures: Field Validation.* SHRP-A-390, Strategic Highway Research Program, National Research Council, Washington D.C., 1994.

(13). Petersen, J.C. "Chemical Composition of Asphalt as Related to Asphalt Durability: State of the Art". *Transportation Research Record 999*, TRB, National Research Council, Washington, D.C., 1984. pp 13-30

(14). Harnsberger, P.M., Ensley, E.K., Duvall, J.J., and Branthaver, J.F. "Aging Studies of Asphalt", *SHRP-A-368: Binder Characterization and Evaluation, Vol. 2: Chemistry.* Strategic Highway Research Program, National Research Council, Washington D.C., 1993. pp. 189-285

(15). Petersen, J.C., and Harnsberger, P.M. *Asphalt Aging: A Dual Oxidation Mechanism and its Interrelationship with Asphalt Composition and Oxidative Age Hardening.* Transportation Research Board 77th Annual Meeting, Washington, D.C., 1998

(16). Branthaver, J.F., and Plancher, H. "Molecular Structuring Studies", *SHRP-A-368: Binder Characterization and Evaluation, Vol. 2: Chemistry*. Strategic Highway Research Program, National Research Council, Washington D.C., 1993. pp. 149-156

(17). Petersen, J.C., Branthaver, J.F., Roberstson, R.E., Harnsbergr, P.M., Duvall, J.J., and Ensley, E.K. "Effects of Physicochemical Factors on Asphalt Oxidation Kinetics". *Transportation Research Record 1391*, TRB, National Research Council, Washington, D.C., 1993. pp 1-10

(18). Losito, I., Sabbatini, L., and Gardella, J., "Electrón, Ion, and Mass Spectrometry". *Comprehensive Desk Reference of Polymer Characterization and Analysis*. Oxford University Press, New York, NY, 2003. pp 375-393

(19). Queen Mary, University of London. Internet. *Surface Analytical Techniques* Retrieved June 14, 2007, http://www.chem.qmul.ac.uk/surfaces/scc/scat5_3.htm

(20). Reed, S.J.B., *Electron Microprobe Analysis*. Cambridge University Press, Cambridge, UK, 2nd edition .1993.

(21). Electron Microprobe Laboratory, University of Minnesota. *Electron Microprobe*. Internet. Retrieved June 15, 2007, http://probelab.geo.umn.edu/electron_microprobe.html

(22). Tarcan, G., and Koca, M. Y., "Hydrogeological and geotechnical assessments of the Kadifekale landslide area, Izmir, Turkey". *Environmental Geology*. Vol. 40, No. 3, January, 2001.

(23). Raj, B., Jayakumar, T., and Thavasimuthu, M., *Practical Non-destructive Testing*, Alpha Science International Ltd, ASM International, second edition, Oxford, UK, 2002. pp 8-16.

(24). Adair, T., and Kindrew, M., *Automated Fluorescent Penetrant Inspection (FPI) System Is Triple A*. 15th World Conference on Nondestructive Testing. Rome, Italy, 15-21 October 2000.

(25). Vasquez, I., "Fluorescent penetrant inspection system performance test using known defect standards". *Materials Evaluation* (USA). Vol. 55, no. 12, pp. 1319-1322. Dec. 1997.

(26). Fischer, H., Karaca, F., and Marx, R., "Detection of microscopic cracks in dental ceramic materials by fluorescent penetrant method", *J Biomed Mater Res* 61: 153–158, 2002.

(27). Roberts, D. A., and M. Herold. "Imaging spectrometry of urban materials", in King, P., Ramsey, M.S. and G. Swayze, (eds.), *Infrared Spectroscopy in Geochemistry, Exploration and Remote Sensing, Mineral Association of Canada, Short Course Series Volume 33*, London, Ontario, 2004. pp 155-181.

(28). Goetz, A.F.H., and Vane, G., "Solomon, J.E., and Rock, B.N. Imaging Spectrometry for Earth Remote Sensing", *Science*, 1985, 228 (4704): 1147-1153.

(29). Herold, M., Gardner, M., Noronha, V., and Roberts, D. "Spectrometry and Hyperspectral Remote Sensing of Urban Road Infrastructure", Online *Journal of Space Communications*, 3, 2003. Internet. Retrieved June 16, 2007, URL: http://satjournal.tcom.ohiou.edu/issue03/applications.html.

(30). Herold, M., Gardner, M. E., and Roberts, D. A. "Spectral resolution requirements for mapping urban areas", *IEEE Transactions on Geoscience and Remote Sensing*, 2003, Vol. 41, Issue 9, Part 1.

(31). American Association of State Highway and Transportation Officials (AASHTO) "Standard T 313-05, Standard Method of Test for Determining the Flexural Creep Stiffness

of Asphalt Binder Using the Bending Beam Rheometer (BBR) ", *Standard Specifications for Transportation Materials and Methods of Sampling and Testing*, Washington, D.C., 25th Edition, 2005.

(32). American Association of State Highway and Transportation Officials (AASHTO) Designation T 314-02, "Standard Method of Test for Determining the Fracture Properties of Asphalt Binder in Direct Tension (DT) ", *Standard Specifications for Transportation Materials and Methods of Sampling and Testing, Part 2B: Tests*, Washington, D.C., 22nd Edition, 2002.

(33). American Association of State Highway and Transportation Officials (AASHTO) Standard AASHTO T 315-02: "Determining the Rheological Properties of Asphalt Binder using a Dynamic Shear Rheometer (DSR) ". *Standard Specifications for Transportation Materials and Methods of Sampling and Testing, Part 2B: Tests*, Washington, D.C., 22nd Edition, 2002.

(34). Ball, D., "Vibrational Spectroscopy". *Comprehensive Desk Reference of Polymer Characterization and Analysis*. Oxford University Press, New York, NY, Ch. 10, pp. 220-247, 2003.

(35). Marasteanu, M., Zofka, A., Turos, M., Li, X., Velásquez, R., Li, X., Buttlar, W., Paulino, G., Braham, A., Dave, E., Ojo, J., Bahia, H., Williams, C., Bausano, J., Gallistel, A., and McGraw, J*., Investigation of Low Temperature Cracking in Asphalt Pavements. National Pooled Fund Study 776*, University of Minnesota, final report, St. Paul, MN, July 2007.

(36). Zofka, A., *Investigation of Asphalt Concrete Creep Behavior Using 3-Point Bending Test*. PhD Thesis. University of Minnesota. Minneapolis, MN, July 2007.

(37). Chong, K.P., and Kuruppu, M.D. "New Specimen for Fracture Toughness Determination for Rock and Other Materials". *International Journal of Fracture*, Vol. 26, R59-R62, 1984.

(38). Marasteanu, M.O., Li, Xue, Clyne, T.R., Voller, V.R., Timm, D.H., and Newcomb, D.E. "*Low Temperature Cracking of Asphalt Concrete Pavements*". LRRB #200423, Minnesota Department of Transportation. St. Paul, MN, March 2004.

(39). Tweet, J., *Effect of Surface Treatment Timing on Fracture Properties of Asphalt Mixtures at Low Temperatures*. Master of Science Thesis. University of Minnesota. Minneapolis, MN, December 2006.

(40). American Association of State Highway and Transportation Officials (AASHTO) Designation T166-05: "Bulk Specific Gravity of Compacted Asphalt Mixtures Using Saturated Surface-Dry Specimens". *Standard Specifications for Transportation Materials and Methods of Sampling and Testing, 26th Edition*, Washington D.C., 2006.

(41). American Association of State Highway and Transportation Officials (AASHTO) Designation T209-05: "Theoretical Maximum Specific Gravity and Density of Bituminous Paving Mixtures". *Standard Specifications for Transportation Materials and Methods of Sampling and Testing, 26th Edition*, Washington, D.C., 2006.

(42). Lim, I. L., Johnston, I. W., and Choi, S.K. "Stress Intensity factors for Semi-Circular Specimens Under Three-Point Bending." *Engineering Fracture Mechanics*, Vol.44, No.3, 363-382. 1993.

(43). RILEM Technical Committee 50-FMC. "Determination of the Fracture Energy of Mortar and Concrete by Means of Three-point Bend Tests on Notched Beams". *Materials and Structures*, Vol. 18, No. 106, pp 285-290. 1985.

(44). Bigl, S.R., and R.L. Berg., *Modeling of Mn/ROAD Test Sections with the CRREL Mechanistic Pavement Design Procedure*. Special Report 96-21, US Army Corps of Engineers, Cold Regions Research & Engineering Laboratory. St. Paul, MN, 1996.

(45). Hermanson, A., "Mathematical model for calculation of pavement temperatures: Comparison of calculated and measured temperatures". *Transportation Research Record*, 1764: 180-188. 2001.

(46). Herb, W.R, B. Janke, O. Mohseni, and H.G. Stefan., *All-Weather Ground Surface Temperature Simulation*. Project Report No. 478, St. Anthony Falls Laboratory, University of Minnesota, Minneapolis, MN, September 2006, 51 pp.

(47). Edinger, J.E., D.K. Brady, and J.C. Geyer. "Heat Exchange and Transport in the Environment". *Report 14: Cooling Water Studies for the Electric Power Research Institute*, The Johns Hopkins University, RP-49, Palo Alto, CA, 1974.

(48). Henneman, H., and H.G. Stefan. "Albedo models for snow and ice on a freshwater lake". *Cold Regions Science and Technology* 29:31-48. 1999.

(49). MnDOT Statewide R/WIS Archive Download Page. Internet. Retrieved August 23, 2007, www.d.umn.edu/~tkwon/RWISarchive/RWISarchive.html

(50). Eckert, E.R.G., and Drake, R.M., Jr. *Analysis of Heat and Mass Transfer*. McGraw-Hill, New York, NY. 1972.

(51). Luca, J., and Mrawira, D., "New Measurement of Thermal Properties of Superpave Asphalt Concrete", *ASCE Journal of Materials in Civil Engineering*, 17(1):72-79. 2005.

APPENDIX A

Construction history of TH 56 specimens
From 2002 Roadway History for District 6, Mn/DOT pg 1125
Note that shoulder construction is not included

And

Construction history of TH 251 specimens
From 2002 Roadway History for District 6, Mn/DOT pg 1454
Note that shoulder construction is not included

| Work Item	Material ID	Date	Depth(in)	Width(ft)	Mode
Bituminous overlay	50	9/9/1999	1.5	24	In place
Bituminous overlay	50	9/9/1999	2	24	In place
Bituminous overlay	31	8/18/1981	3.5	24	In place
Spot overlay	31	6/4/1980	1	NA	In place
Bituminous overlay	31	10/15/1968	1.5	24	New
Agg. Seal coat	F1	7/8/1964	NA	NA	In place
Bituminous layer	31	10/18/1957	2	24	New
Agg. Base	**	10/18/1957	4	26	New
Spot overlay	**	8/18/1955	1	NA	In place
Spot overlay	**	8/13/1954	1	NA	In place
Agg. Seal coat	**	9/29/1952	NA	NA	In place
Agg. Seal coat	**	9/29/1952	NA	NA	In place
Spot overlay	**	9/29/1952	1	NA	In place
Spot overlay	**	9/29/1952	1	NA	In place
Spot overlay	**	9/6/1951	1	NA	In place
Agg. Seal coat	**	10/15/1942	NA	NA	In place
Bituminous overlay	**	10/15/1941	1	26	In place
Gravel Surface	**	9/15/1940	16	36	New

Figure A.1. Sections 10, 11 and 12, TH 56

Figure A.2. Specimens from sections 10, 11 and 12, TH 56

| Work Item	Material ID	Date	Depth(in)	Width(ft)	Mode
Bituminous overlay	50	9/9/1999	1.5	24	In place
Bituminous overlay	50	9/9/1999	2	24	In place
Bituminous overlay	31	8/18/1981	3.5	24	In place
Spot overlay	31	6/4/1980	1	NA	In place
Bituminous overlay	31	10/15/1968	1.5	24	New
Agg. Seal coat	F1	6/29/1966	NA	NA	In place
Agg. Seal coat	F1	7/8/1964	NA	NA	In place
Bituminous layer	31	10/18/1957	2	24	New
Agg. Base	**	10/18/1957	4	26	New
Spot overlay	**	8/18/1955	1	NA	In place
Spot overlay	**	8/13/1954	1	NA	In place
Agg. Seal coat	**	9/29/1952	NA	NA	In place
Agg. Seal coat	**	9/29/1952	NA	NA	In place
Spot overlay	**	9/29/1952	1	NA	In place
Spot overlay	**	9/29/1952	1	NA	In place
Spot overlay	**	9/6/1951	1	NA	In place
Agg. Seal coat	**	10/15/1942	NA	NA	In place
Bituminous overlay	**	10/15/1941	1	26	In place
Gravel Surface	**	9/15/1940	16	36	New

Figure A.3. Sections 13 and 14, TH 56

Figure A.4. Specimens from sections 10, 11 and 12, TH 56

Work Item	Material ID	Date	Depth(in)	Width(ft)	Mode
Bituminous Overlay	41	7/1/1995	4	24	In place
Mill Bituminous		7/1/1995	-1.5	24	In place
Spot Overlay	31	6/4/1980	1	NA	In place
Bituminous Overlay	31	10/6/1970	1.5	25	In place
Bituminous Overlay	41	10/6/1970	3	24	In place
Agg. Seal Coat	F1	6/29/1966	NA	NA	In place
Spot Overlay	**	8/18/1955	1	NA	In place
Agg. Seal Coat	**	9/29/1952	NA	NA	In place
Agg. Seal Coat	**	9/29/1952	NA	NA	In place
Agg. Seal Coat	**	7/29/1950	NA	NA	In place
Bituminous Layer	31	7/29/1950	1.5	24	New
Bituminous Layer	31	7/29/1950	1	26	New
Agg. Base Layer	**	7/29/1950	6	32	New
Gravel Surface	**	7/29/1950	6	34	New

Figure A.5. Specimens from section 15, TH 56

| Work Item	Material ID	Date	Depth(in)	Width(ft)	Mode
Bituminous Overlay	41	7/1/1995	4	24	In place
Mill Bituminous		7/1/1995	-1.5	24	In place
Spot Overlay	31	6/4/1980	1	NA	In place
Bituminous Overlay	31	10/6/1970	1.5	25	In place
Bituminous Overlay	41	10/6/1970	3	24	In place
Agg. Seal Coat	F1	6/29/1966	NA	NA	In place
Spot Overlay	**	9/17/1959	1	NA	In place
Spot Overlay	**	8/18/1955	1	NA	In place
Agg. Seal Coat	**	9/29/1952	NA	NA	In place
Agg. Seal Coat	**	9/29/1952	NA	NA	In place
Agg. Seal Coat	**	7/29/1950	NA	NA	In place
Bituminous Layer	31	7/29/1950	1.5	24	New
Bituminous Layer	31	7/29/1950	1	26	New
Agg. Base Layer	**	7/29/1950	1.5	42	New
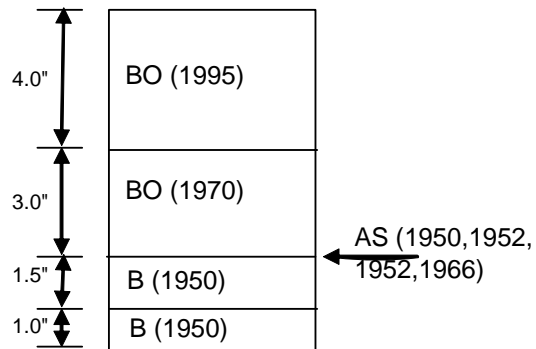
Figure A.6. Sections 16 and 17, TH 56

Figure A.7. Specimens from sections 16 and 17, TH 56

Work Item	Material ID	Date	Depth(in)	Width(ft)	Mode
Bituminous Overlay	41	7/1/1995	4	24	In place
Mill Bituminous		7/1/1995	-1.5	24	In place
Spot Overlay	31	6/4/1980	1	NA	In place
Bituminous Overlay	31	10/6/1970	1.5	25	In place
Bituminous Overlay	41	10/6/1970	3	24	In place
Agg. Seal Coat	F1	6/29/1966	NA	NA	In place
Spot Overlay	**	9/17/1959	1	NA	In place
Spot Overlay	**	8/18/1955	1	NA	In place
Agg. Seal Coat	**	9/29/1952	NA	NA	In place
Agg. Seal Coat	**	9/29/1952	NA	NA	In place
Agg. Seal Coat	**	7/29/1950	NA	NA	In place
Bituminous Layer	31	7/29/1950	1.5	24	New
Bituminous Layer	31	7/29/1950	1	26	New
Agg. Base Layer	**	7/29/1950	6	32	New
Gravel Surface	**	7/29/1950	6	34	New

Figure A.8. Specimens from section 18, TH 56

Work Item	Material ID	Date	Depth(in)	Width(ft)	Mode
Bituminous Overlay	41	7/1/1995	3	24	In place
Bituminous Layer	47	7/1/1995	4.5	24	In place
Spot Overlay	**	6/23/1983	1.5	NA	In place
Spot Overlay	31	5/11/1981	1.5	25	In place
Bituminous Overlay	31	10/6/1970	1.5	25	In place
Bituminous Overlay	41	10/6/1970	3	24	In place
Bituminous Overlay	**	7/8/1964	3	24	In place
Agg. Seal Coat	F1	8/4/1961	NA	NA	In place
Spot Overlay	**	9/17/1959	1	NA	In place
Spot Overlay	**	5/16/1957	0.75	NA	In place
Spot Overlay	**	8/18/1955	1	NA	In place
Agg. Seal Coat	**	9/29/1952	NA	NA	In place
Agg. Seal Coat	**	9/29/1952	NA	NA	In place
Agg. Seal Coat	**	7/29/1950	NA	NA	In place
Bituminous Overlay	31	7/29/1950	1.5	24	New
Bituminous Overlay	31	7/29/1950	1	26	New
Gravel Surface	**	7/29/1950	12	32	New
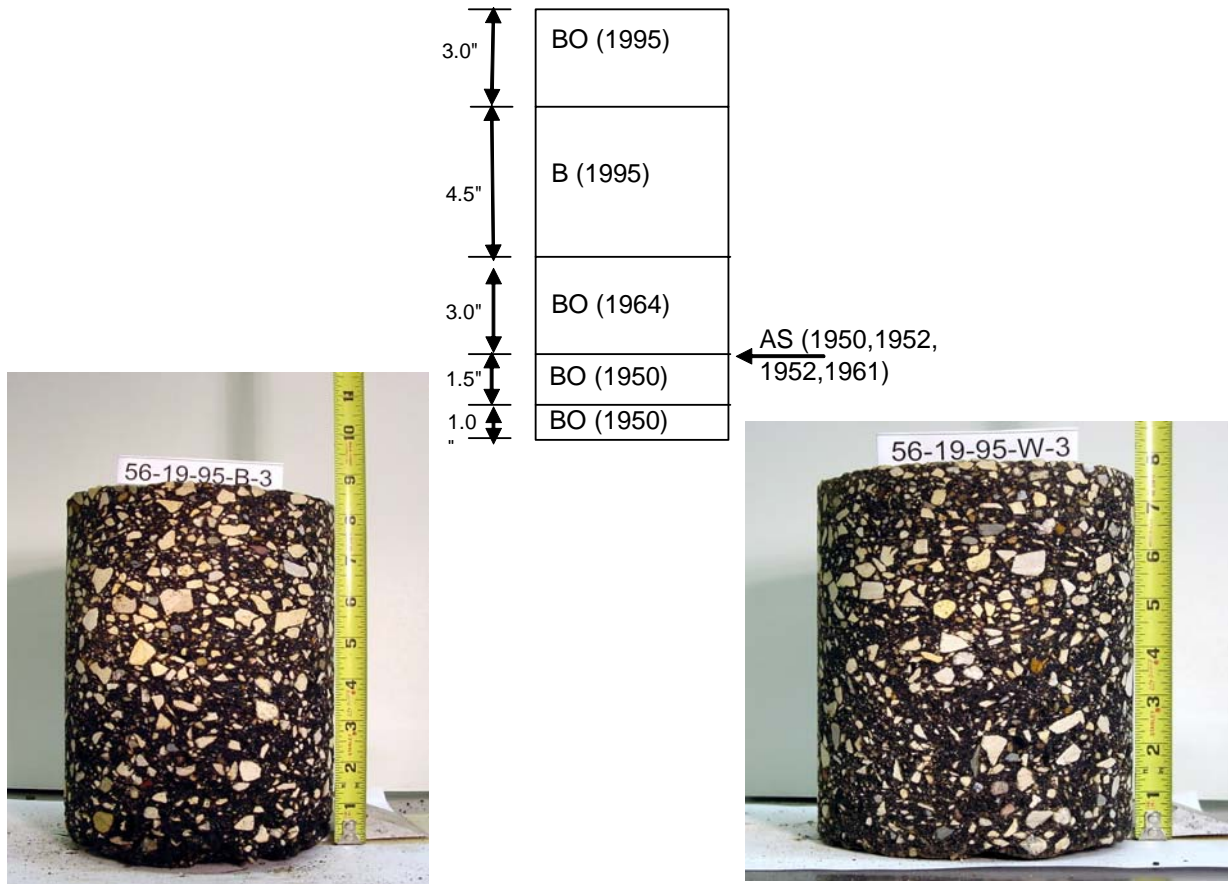
Figure A.9. Specimens from section 19, TH 56

A-9

Work Item	Material ID	Date	Depth(in)	Width(ft)	Mode
Agg. Sealcoat	F2	7/15/1989	NA	NA	In place
Bituminous overlay	31	7/1/1988	1.5	24	In place
Bituminous overlay	31	9/10/1971	2.5	24	In place
Agg. Sealcoat	F1	7/21/1964	NA	NA	In place
Agg. Sealcoat	F4	8/12/1957	NA	NA	In place
Bituminous layer	31	8/10/1955	2	24	New
Cement treated base	**	8/10/1955	6	32	New
Agg. Base	**	7/10/1953	1.5	32	New
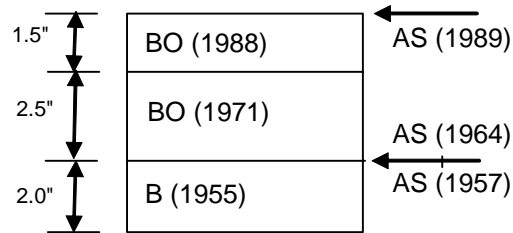
Figure A.10. Specimens from sections 2, 3, 6 and 8, TH 251

Figure A.11. Specimens from sections 3, 6 and 8, TH 251

APPENDIX B

Aging/Optimization Study
2002 Construction Work Update
and early results

Goal

The goal of this study is to determine the cost effectiveness of three pavement preventive maintenance (PPM) treatments on hot mix asphalt (HMA) pavements. This study will also help to determine the proper time for placement of the PPM treatments to maximize the life of HMA roadways.

Research

Three methods of treating the hot mix asphalt pavements will be studied:

1. Seal coats on hot mix asphalt pavements,
2. Seal coats and rejuvenators on hot mix asphalt shoulders, and
3. Fog seals on hot mix asphalt shoulders.

The approach is to divide a section of roadway or shoulder into one-mile segments. The first segment would be treated in year one of the study. The following year, the next segment would be treated with a similar seal coat / fog seal. Seal coats will be applied at the design application rate for cover stone with the binder adjusted for the current condition of the pavement / shoulder. A segment will be left untreated as a control section.

Evaluation

Evaluations will use a combination of some of the following methods:

- PSR (ride data)
- SR (surface ratings)
- Coring
- Friction numbers
- Panel review

The rate of decay for the various segments will determine which segments returned the most value for the total cost expended.

Cooperation

This research project is a cooperative effort of the following Mn/DOT offices:

- OM&RR: Jerry Geib, co-principal investigator.
- District 6: Wes Smith, co-principal investigator.
- Maintenance Operations: Sue Lodahl, And M.O.R.E. funding.
- Koch Materials: Tom Wood (previously of the OM&RR, and co-PI).

Although many more people have assisted in making this project successful, the people listed above are the coordinators for their respective offices.

Seal coats on hot mix asphalt pavements

Table B.1. Treatments on TH 56.

Reference Post R.P.	Year applied	Treatment	Age of road when treated
9-10	NA	Control, constructed in 1999.	NA
14-15	2000	Seal coat:	1 year
15-16	2000	Seal coat:	5 years
13-14	2001	Seal coat:	2 years
16-17	2001	Seal coat:	6 years
12-13	2002	Seal coat:	3 years
17-18	2002	Seal coat:	7 years
11-12	2003	planned seal coat	will be 4 years
18-19	2003	planned seal coat	will be 8 years

2000 Construction

TH 56 is a two-lane rural highway with ADT of 2000. This 24-mile segment located between I-90 and Leroy, MN was constructed in two parts. The section between reference posts (r.p.) 2 and 15 was constructed in 1999 and the section from 15 to 26 was constructed in 1995. Because of the age difference of the two sections, it was decided to construct two different segments each year. The first sections were constructed according to the original work plan starting at r.p. 14 to 15 for the one-year-old section. The additional section was constructed starting at r.p. 15 to 16.

The method of construction used on both of these segments was seal coating using CRS-2P and a New Ulm Quartzite 3/8-inch chip. The application rate of the cover stone was 16 pounds per square yard. The binder application rate for the one-year-old section was 0.32 gallons per square yard. The binder application rate for the five-year-old section was 0.35 gallons per square yard. The additional binder required on the five-year-old-section was due to aging and oxidation that had already occurred. It cost approximately $422.00 more to seal coat the five-year-old section.

Figure B.1. Applying a Seal Coat to a 1 year old section of TH 56, at R.P. 14 (to 15).

Seal coats and rejuvenators on hot mix asphalt shoulders

I-35 was used to study seal coats and rejuvenators on hot mix asphalt shoulders, I-35 is a rural interstate highway with an ADT of 17,500.

Table B.2. Treatments on I-35 NB, on the 8' 6" wide, right hand shoulder.

Reference Post R.P.	Year applied	Treatment	Age of shoulder when treated
14-15	NA	Control: shoulder was placed in 1998.	NA
15-16	2000	Seal coat: 17# FA-3, 0.34 gal/sy CRP-2P.	2 years
16-17	2001	Seal coat: Taconite tailings, CRS-1P.	3 years
17-18	2002	Rejuvenator: Reclamite.	4 years
18-19	2003	TBD.	

R.P. 15-16, Constructed in 2000.

A seal coat, using a approximately 17 lbs./sy. of ⅜" New Ulm Quartzite chip and 0.34 gallons per square yard of CRS-2P emulsion was placed on the northbound right shoulder from reference post 15 to 16. The construction methods used were same as the proper methods for seal coating a highway. Reviews of the section showed almost complete losses of cover aggregate due to snowplow damage. It appears that the difference in the slope that the mainline was paved at, versus the shoulder allowed the snowplows to attack the chips very aggressively.

4/4/2001 10:47am

Figure B.2. Almost 100% loss of the seal coat aggregate after the first winter.

Figure B.3. Close up of shoulder seal coat I-35

Figure B.4. Shoulder seal coat I-35, R.P. 15-16

Based on physical appearance, the seal coat can be considered to be a complete failure. However, the seal coat was placed to protect the shoulder. The emulsion is providing excellent protection to the shoulder.

R.P. 16-17, Constructed on Sept. 4, 2001.

Due to the aggregate lost on R.P. 15-16, a smaller aggregate was used in 2001. A seal coat with taconite tailings and CRS-1P was constructed. The taconite tailings are all passing the # 4 sieve,

which provided a very smooth surface. Construction began with 0.18gal/sy of emulsion and 8.5lbs/sy. of tailings. Excessive roller pick and 'waves' of the aggregate required less emulsion and more rock. Due to the small size of the tailings, this material cannot be placed at a design rate from the seal coat design program. The emulsion was cut back to 0.14gal/sy. and the aggregate increased to 12 lbs./sy. Based on rolling, pick up and curing time, starting rates of 0.10 gal./sy. and 15 lbs./sy was recommended.

Figure B.5. Shoulder seal coat I-35, R.P. 16-17

Fog seals on hot mix asphalt shoulders

All treatments are on I-90 WB, on the 8' wide, right hand shoulder. I-90 is a rural interstate highway with an ADT of 10,800.

Table B.3. Treatments on I-35 NB, on the 8' 6" wide, right hand shoulder.

Reference Post R.P.	Year applied	Treatment	Age of shoulder when treated
176-175	NA	Control, shoulder was placed in 1999.	NA
175-174	2000	Fog seal	1years
	2001	No, new treatments applied.	

The shoulders had been replaced in 1999. This section (r.p.175-174 westbound only) was fog sealed with a CSS-1 diluted, to produce a final product of one part water to three parts

emulsion. The application rate was 0.12 gallons per square yard. Even though the shoulder was only one year old there were numerous pop outs present.

Figure B.6. I-90 Shoulder Starting Condition.
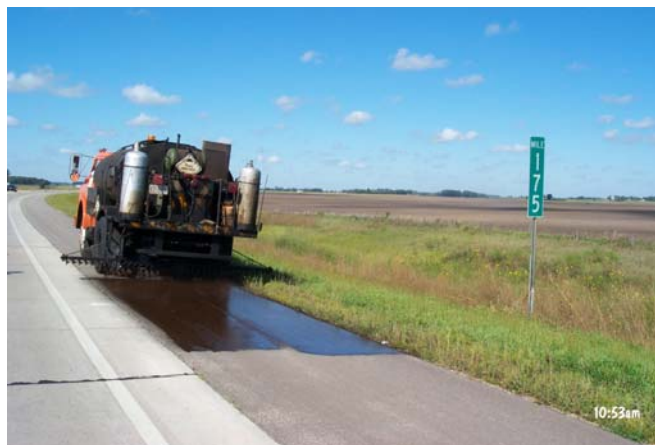
Figure B.7. Starting to apply fog seal

Figure B.8. Emulsion starting to break.

Figure B.9. Fog seal after one winter I-90.

Figure B.10. Close up of fog seal on I-90 after one winter.

Costs

The following are the costs for each segment constructed. The costs for labor and equipment were tracked using MN/DOT's Operations Management System (OMS). The labor and equipment cost includes all overhead charges. The cost of placement of the segments appears very high compared to a routine project. This high cost is because of locations of the test segments the crew was only able to mobilize to the job site and construct the segment/segments and re-mobilize for the next job. The total labor and equipment cost for the day were charged against the segment/segments constructed on that date.

TH 56 Pavement Seal Coat

Table B.4. Segment 1 (r.p. 14 to 15 one-year-old segment)

Binder	Aggregate	Labor	Equipment	Total
$4263.00	$1102.00	$4568.00	$4559.00	$14492.00

Table B.5. Segment 2 (r.p. 15 to 16 five-year-old segment)

Binder	Aggregate	Labor	Equipment	Total
$4685.00	$1102.00	$4568.00	$4559.00	$14914.00

The above prices include re-paint the all pavement markings.

Table B.6. I-35 Shoulder Seal Coat

Binder	Aggregate	Labor	Equipment	Total
$2011.00	$458.00	$1430.00	$1402.00	$5301.00

Table B.7. I-90 Shoulder Fog Seal

Binder	Labor	Equipment	Total
$350.00	$627.00	$121.00	$1097.00

Annual Evaluations

A panel of seven Mn/DOT employees consisting of four from District 6 and three from the Office of Materials and Road Research reviewed all the different segments of the Aging /Optimization Study on April 12, 2001. The following were the different criteria that each segment including the control sections was rated on: Oxidation, Lose of Aggregate (Seal Coats), Pop outs in asphalt, Ride, Appearance, Crack severity, Performance of the PPM Treatment. If a category does not apply a NA was place in that box. The rating scale was from zero to five with five being perfect. The totals of all the raters was add up and an average taken. The following tables show the averages for each category for each segment. In addition to the panel review Mn/DOT's Pavement Management Unit reviews the segments of TH 56 every other year. The PMS uses a combination of ride and pavement distress to determine Pavement Quality Index (PQI). The PMS rating will be included.

TH 56 Pavement Seal Coat

Table B.8. Control Segment r.p. 9 to 10
Panel Review

Year Rated	Oxidation	Lose of Agg.	Pop outs	Ride	Appearance	Cracks	Performance of Tr.
2001	3.78	NA	3.05	4.78	`4.57	3.75	NA

PMS Ratings

Year	PSR	SR	PQI
1999	3.4	3.5	3.4
1997	3.2	2.6	2.9
1995	3.4	3.3	3.3

Table B.9. Segment # 1 Seal Coat r.p. 14 to 15, paved in 1999.
Panel Review

Year Rated	Oxidation	Lose of Agg.	Pop outs	Ride	Appearance	Cracks	Performance of Tr.
2001	NA	1.98	NA	4.37	2.07	3.75	2.2

PMS Ratings

Year	PSR	SR	PQI
1999	3.6	4.0	3.8
1997	2.6	2.6	2.6
1995	2.7	3.0	2.8

Table B.10. Segment # 2 Seal Coat r.p. 15 to 16, paved in 1995.
Panel Review

Year Rated	Oxidation	Lose of Agg.	Pop outs	Ride	Appearance	Cracks	Performance of Tr.
2001	NA	1.8	NA	3.88	1.62	1.25	1.8

PMS Rating

Year	PSR	SR	PQI
1999	3.8	3.9	3.8
1997	3.9	3.9	3.9
1993	2.3	2.8	2.5

Table B.11. Control Segment r.p. 21 to 22, paved in 1995.

Panel Review

Year Rated	Oxidation	Lose of Agg.	Pop outs	Ride	Appearance	Cracks	Performance of Tr.
2001	2.67	NA	3.64	3.57	3.41	3.75	NA

PMS Rating

Year	PSR	SR	PQI
1999	3.9	4.0	3.9
1997	4.0	4.0	4.0
1993	2.6	2.6	2.6

I-35 Shoulder Seal Coat

Table B.12. Control Section r.p. 14 to 15

Year Rated	Oxidation	Lose of Agg.	Pop outs	Ride	Appearance	Cracks	Performance of Treatment
2001	3.36	NA	3.21	4.75	3.67	4.5	NA

Table B.13. Seal Coat r.p. 15 to 16

Year Rated	Oxidation	Lose of Agg.	Pop outs	Ride	Appearance	Cracks	Performance of Treatment
2001	4.8	0.57	NA	5	3.5	5	0.43

I-90 Shoulder Fog Seal

Table B.14. Control Section r.p. 176+ to 175

Year Rated	Oxidation	Lose of Agg.	Pop outs	Ride	Appearance	Cracks	Performance of Treatment
2001	2.66	NA	2.83	4.75	3.08	4.83	NA

Table B.15. Fog Seal r.p. 175 to 174

Year Rated	Oxidation	Lose of Agg.	Pop outs	Ride	Appearance	Cracks	Performance of Treatment
2001	4.32	NA	3.25	4.75	2.87	4.83	3.4

APPENDIX C

Photos of the TH 56 sections taken in August 2007

Figure C.1. TH 56 control section (built in 1999), mile 10 to 11.
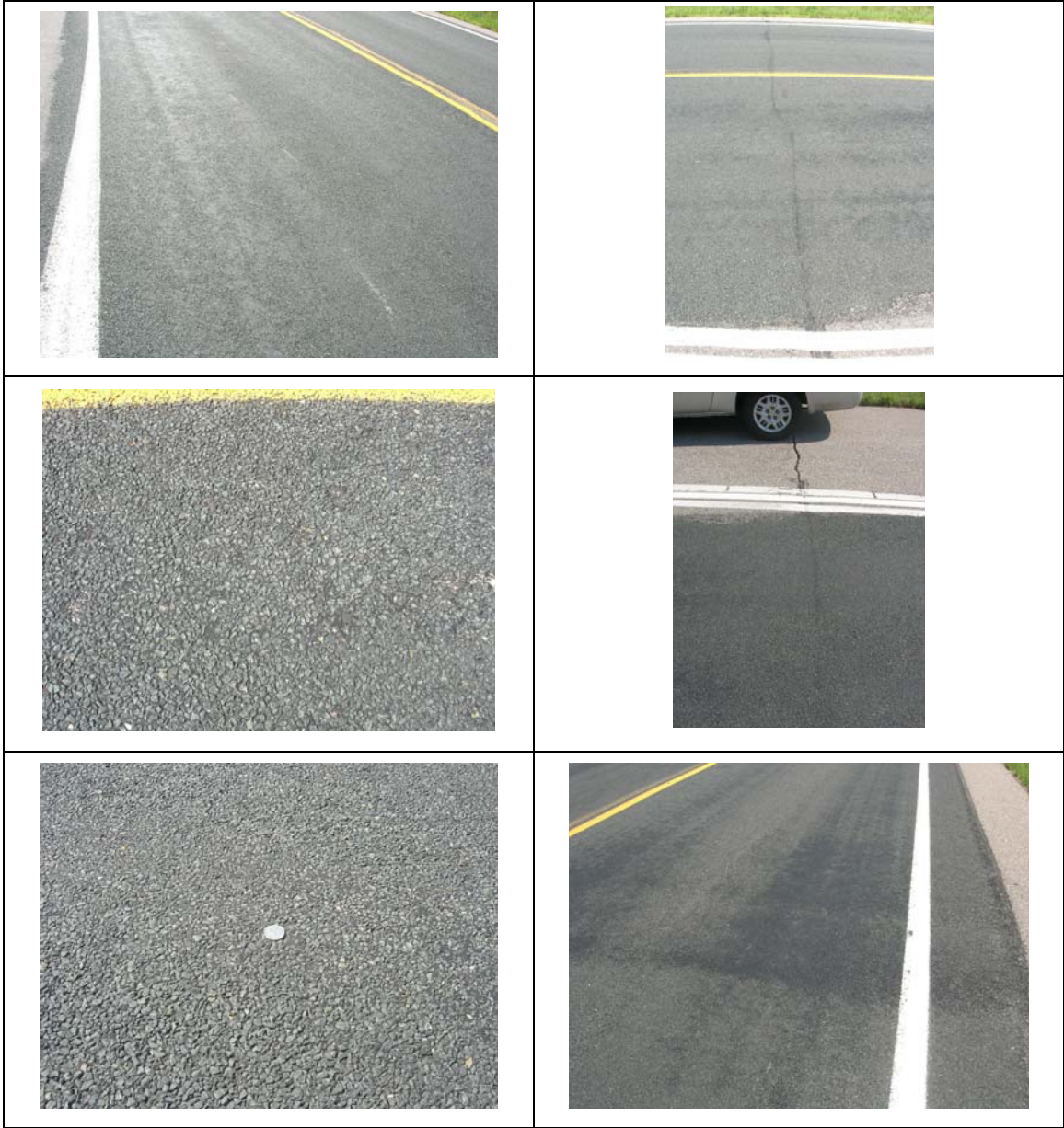
Figure C.2. TH 56 section with surface treatment applied in 2003 (built in 1999), mile 11 to 12.

Mile post 12

Mile post 14

Figure C.3. TH 56 sections with surface treatment applied in 2002 and 2001 (built in 1999), mile 12 to 13 and 13 to 14, respectively.

(Note change in aggregate at mile post 14 from Dresser trap rock to New Ulm quartzite)
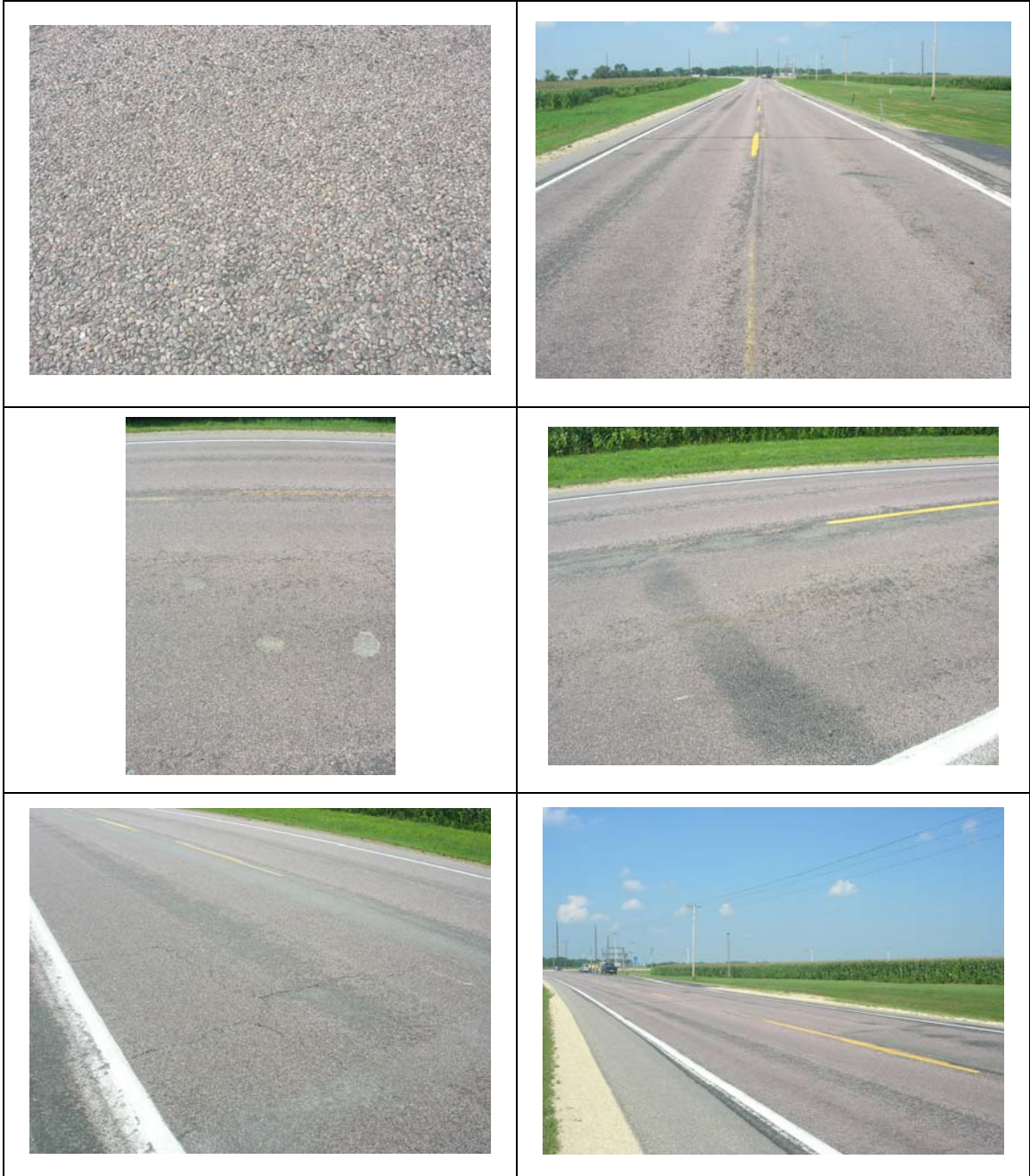
Figure C.4. TH 56 sections with surface treatment applied in 2000 (built in 1999), mile 14 to 15

Mile post 16

Figure C.5. TH 56 sections with surface treatment applied in 2000 (built in 1995), mile 15 to 16

(Note change in aggregate at mile post 16 from New Ulm quartzite to Dresser trap rock)

← 2001 2002 →

Mile post 18

Figure C.6. TH 56 sections with surface treatment applied in 2001 and 2002 (built in 1995), mile 16 to 17 and 17 to 18, respectively
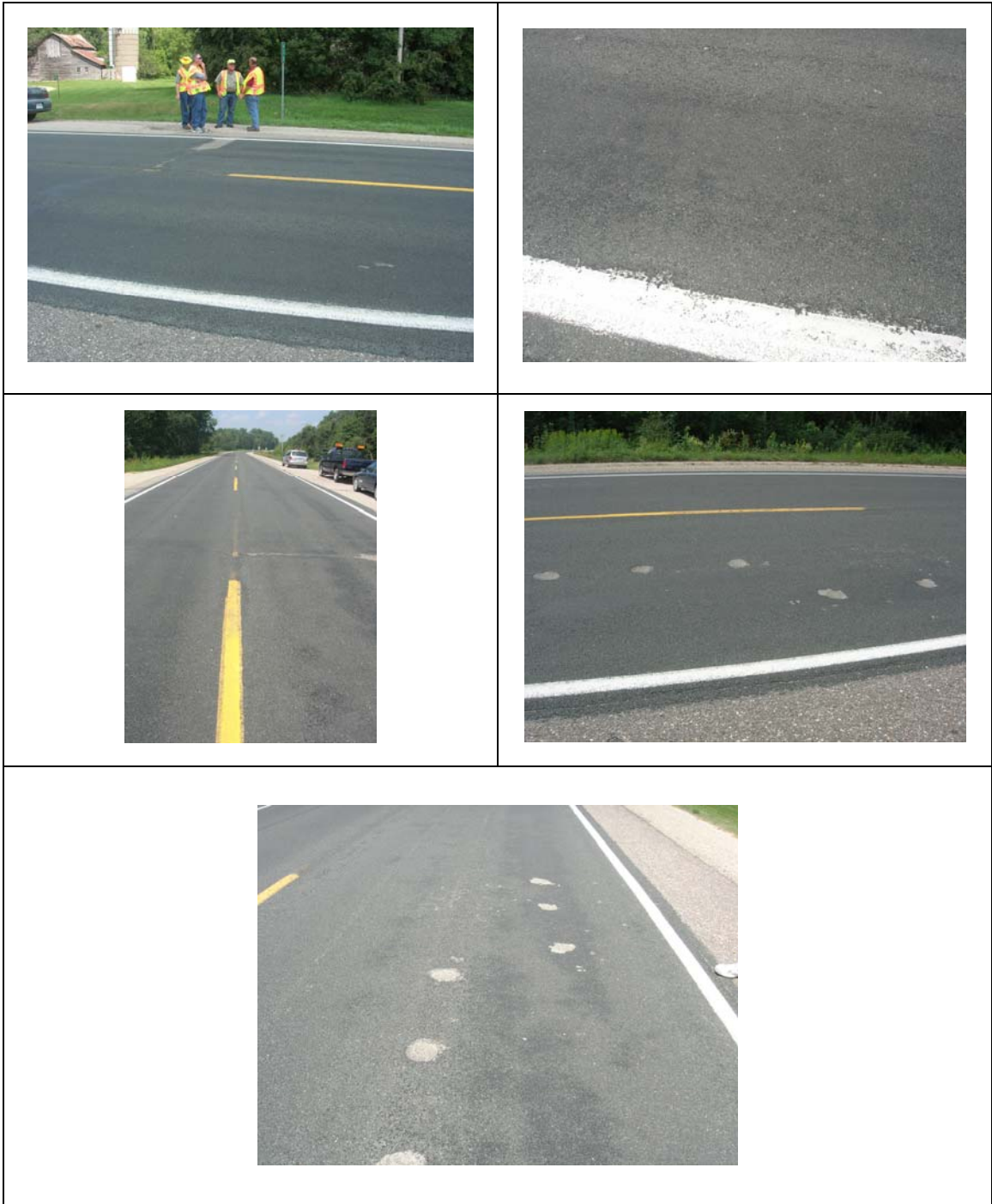
Figure C.7. TH 56 sections with surface treatment applied in 2003 (built in 1995), mile 18 to 19

APPENDIX D

Data Analysis Additional Plots

Wheel path

Between wheel paths
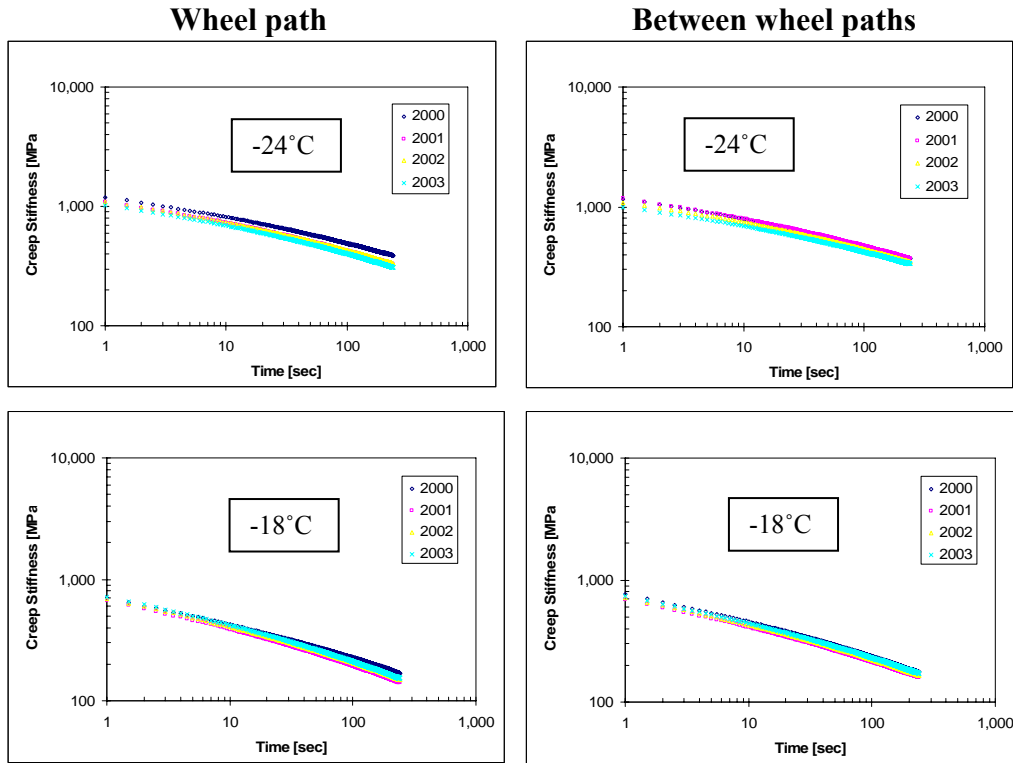
Figure D.1. Creep stiffness vs. time for lower layer TH 56 1995 sections

Wheel path

Between wheel paths
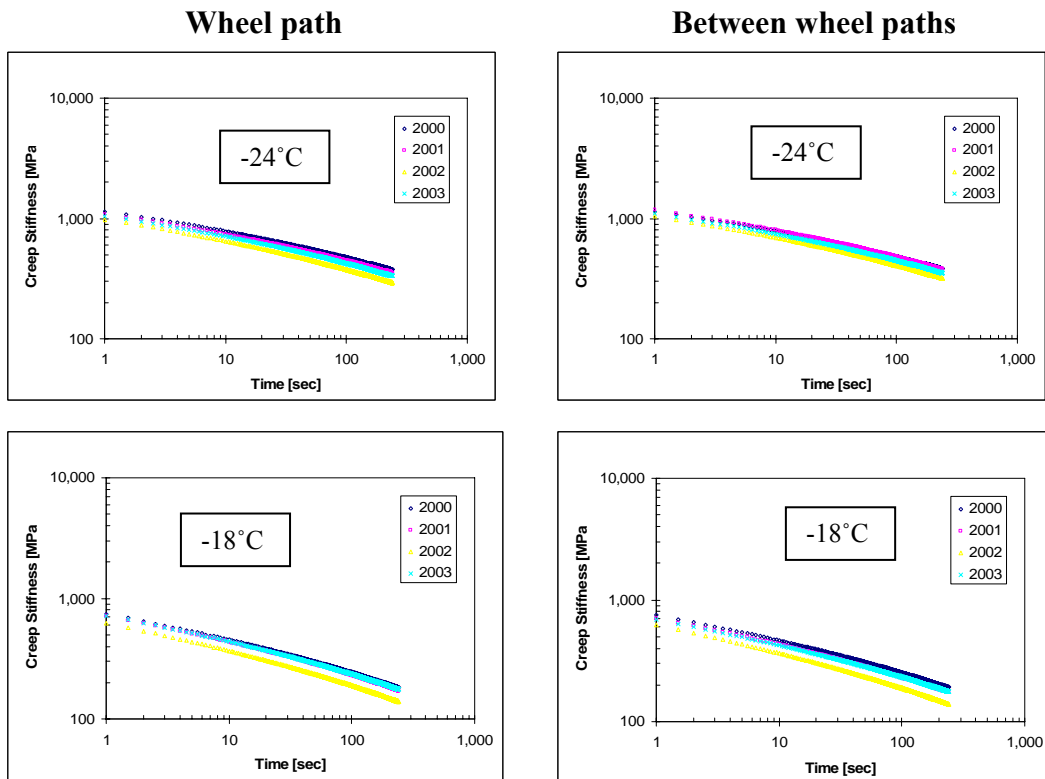
Figure D.2. Creep stiffness vs. time for upper layer TH 56 1995 sections

Wheel path

Between wheel paths
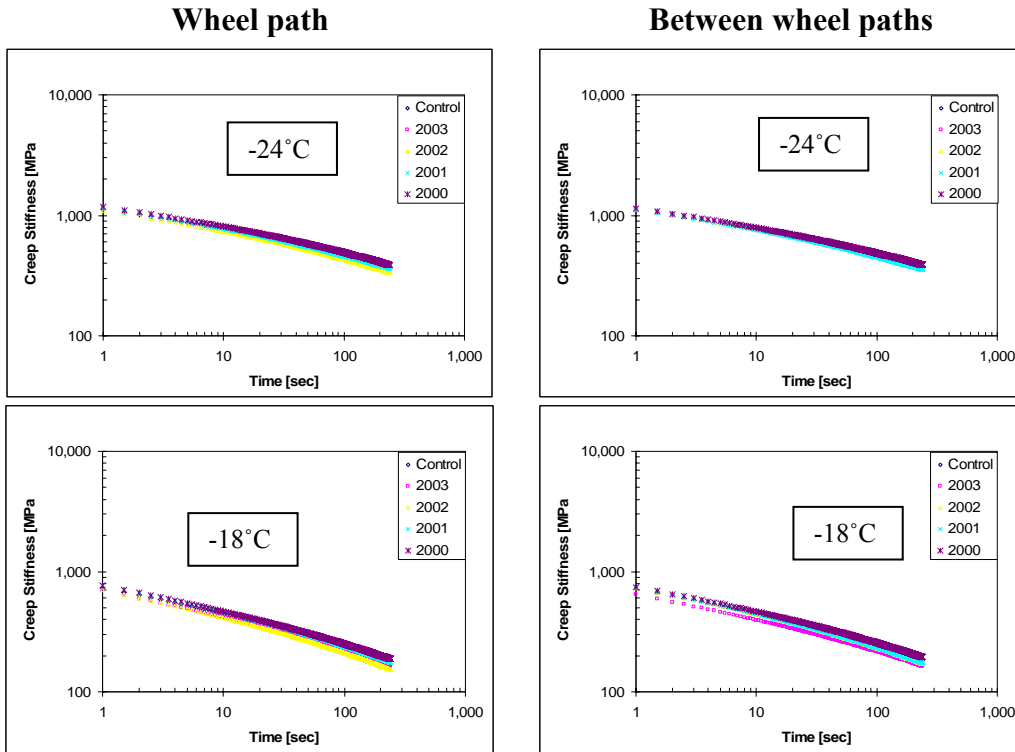
Figure D.3. Creep stiffness vs. time for lower layer TH 56 1999 sections

Wheel path

Between wheel paths
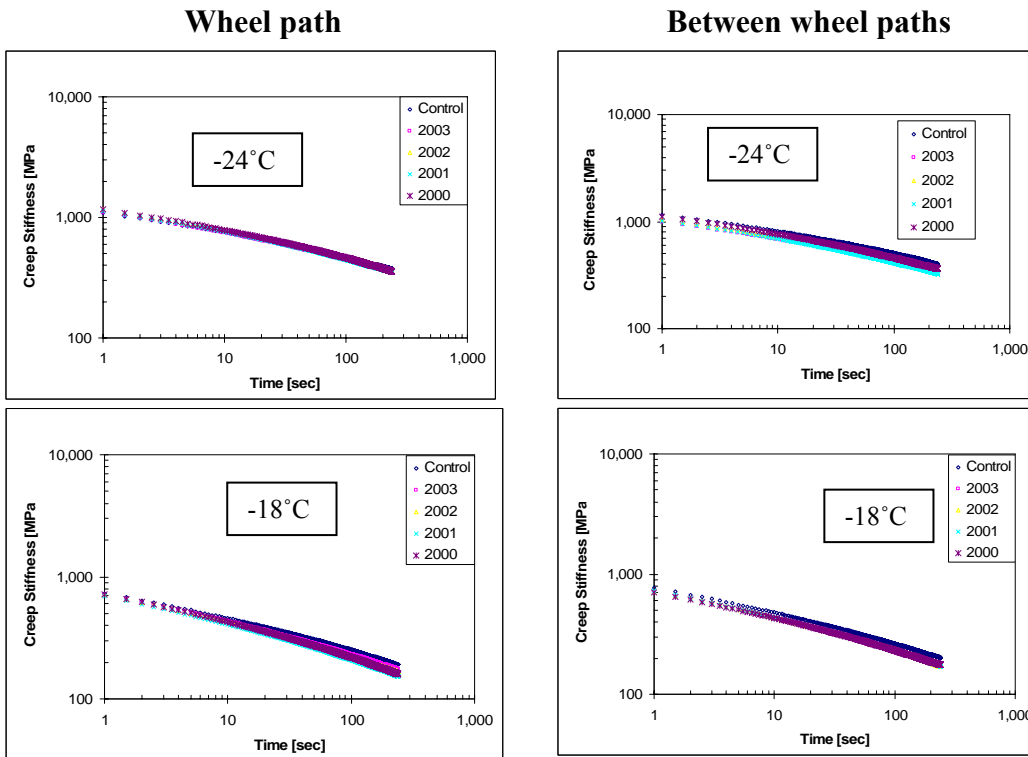
Figure D.4. Creep stiffness vs. time for upper layer TH 56 1999 sections

Wheel path

Between wheel paths
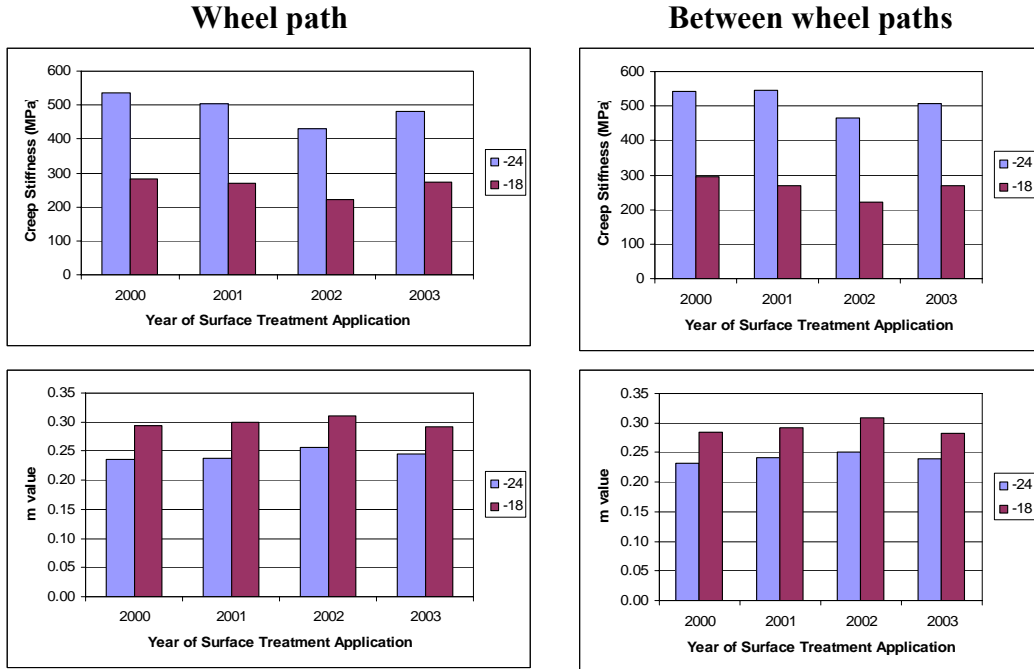
Figure D.5. Stiffness and m at 60 sec. for upper layer, TH 56 1995 sections

Wheel path

Between wheel paths
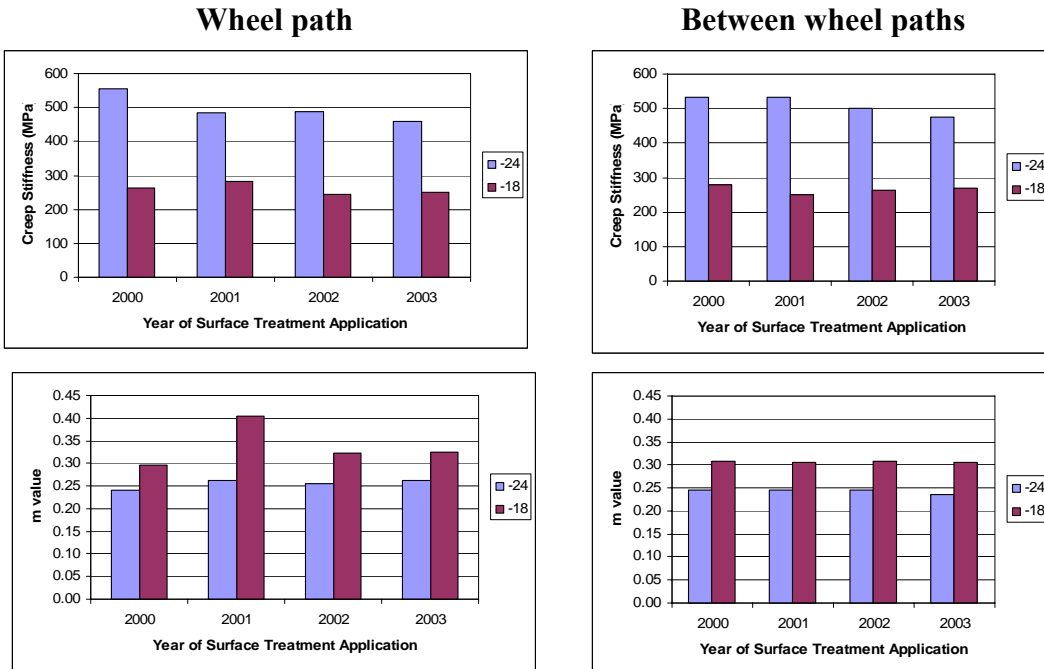
Figure D.6. Stiffness and m at 60 sec. for lower layer, TH 56 1995 sections

Wheel path

Between wheel paths
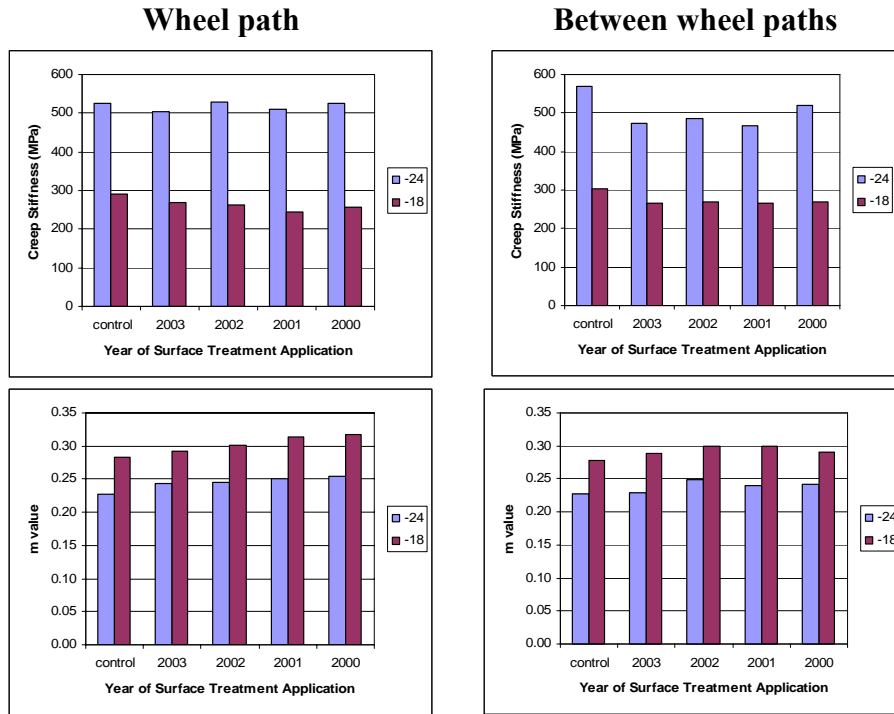
Figure D.7. Stiffness and m at 60 sec. for upper layer, TH 56 1999 sections

Wheel path

Between wheel paths
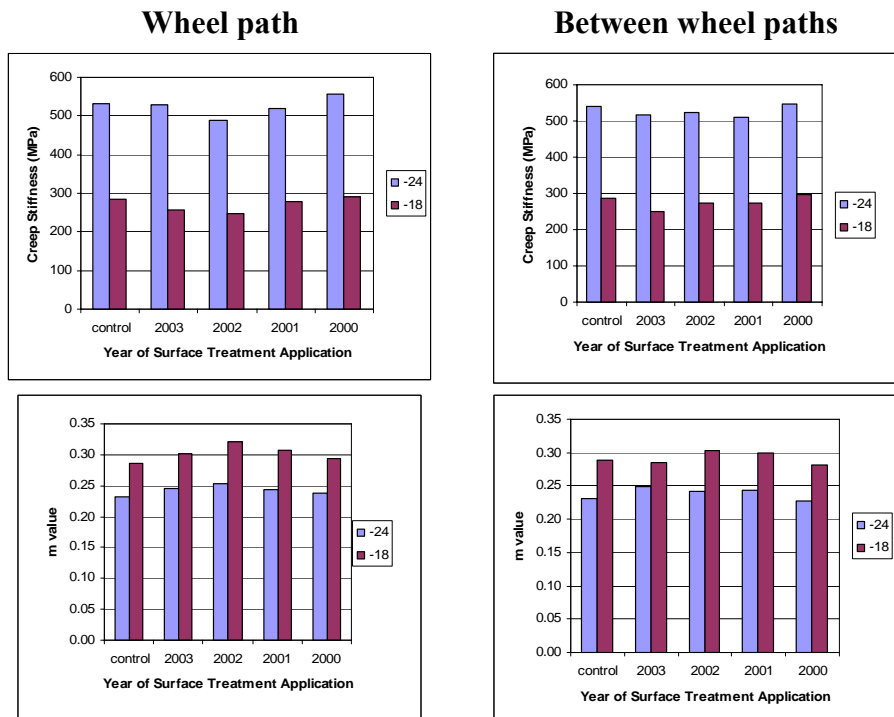
Figure D.8. Stiffness and m at 60 sec. for lower layer, TH 56 1999 sections

Wheel path   **Between wheel paths**
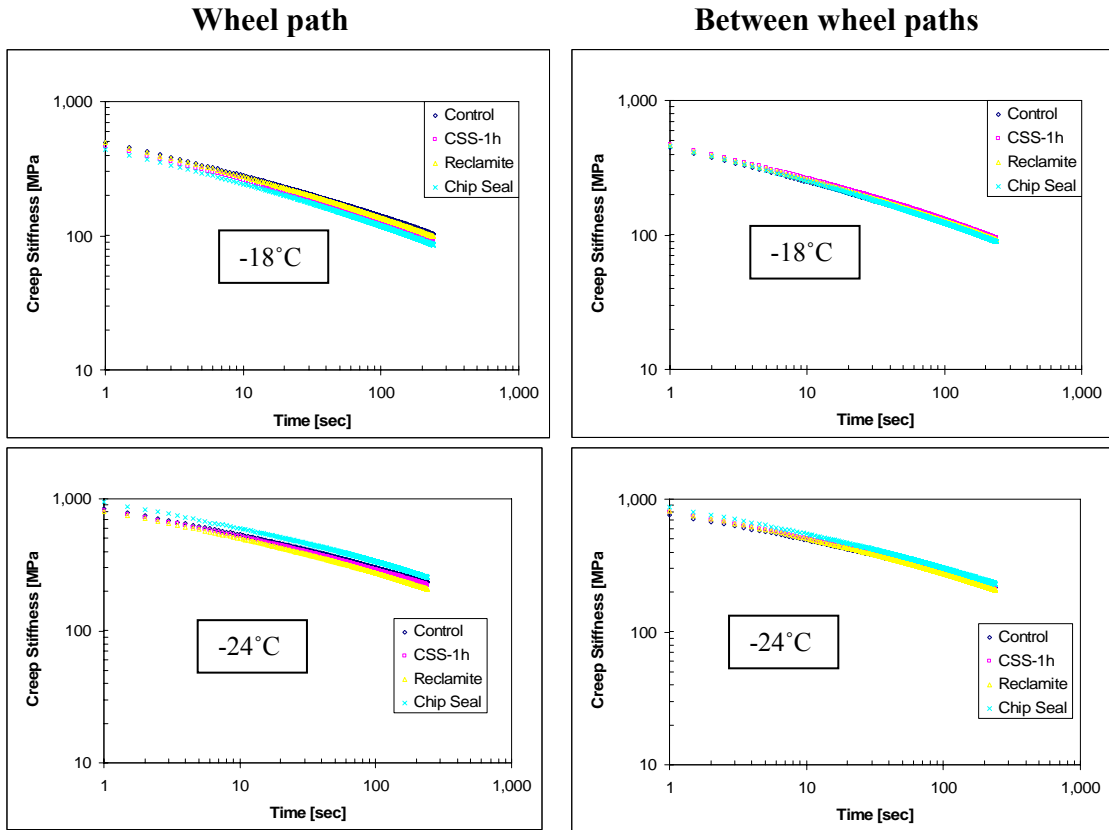
Figure D.9. Creep stiffness vs. time, TH 251 sections

Wheel path   **Between wheel paths**
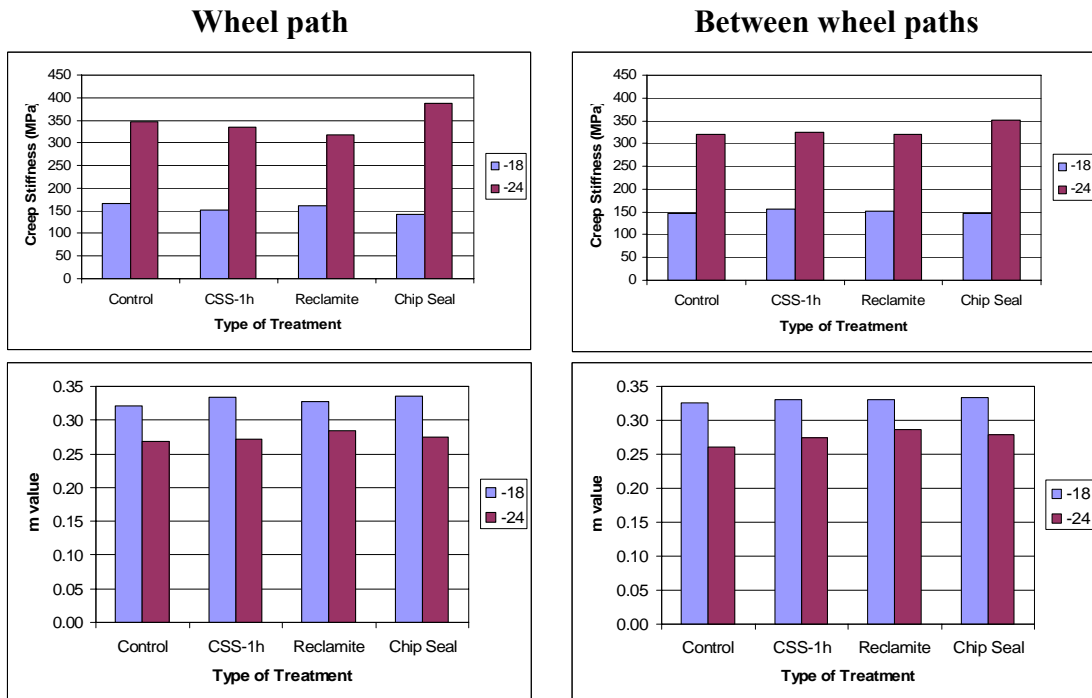
Figure D.10. Stiffness and m at 60 sec. for TH 251 samples
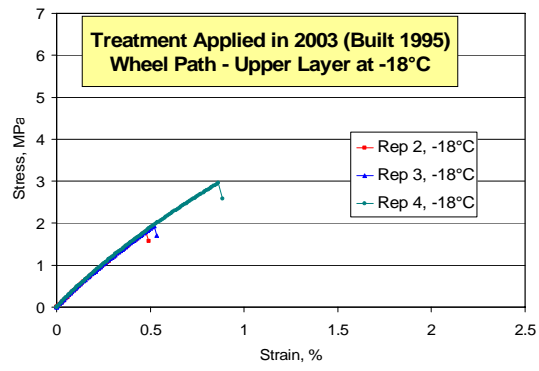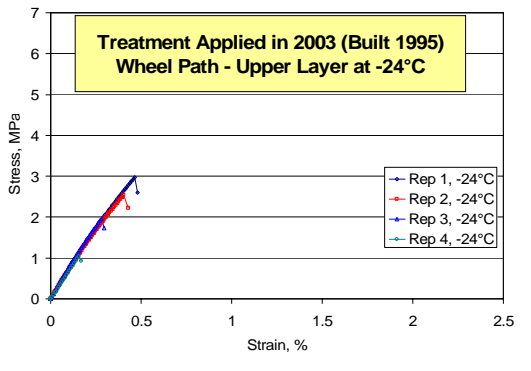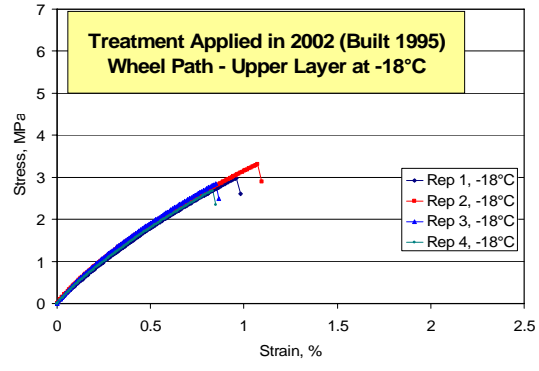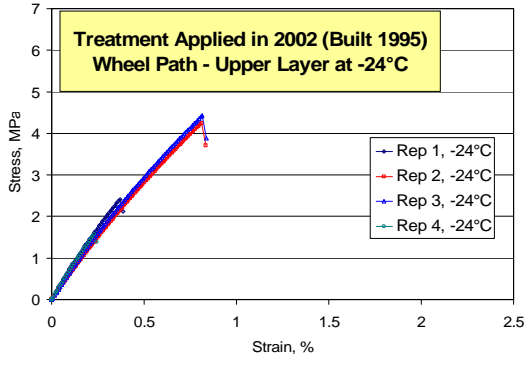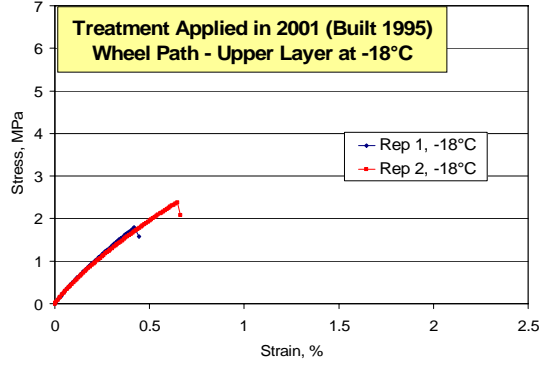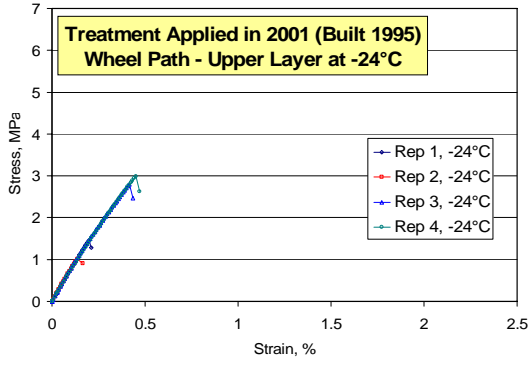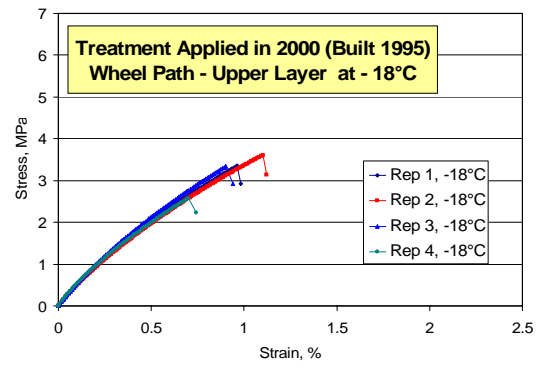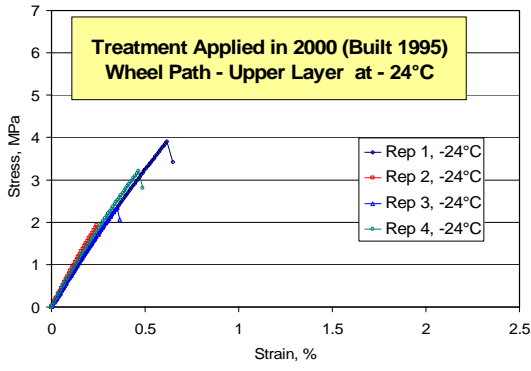
Figure D.11. DTT stress vs. strain curves for wheel path, upper layer, TH 56 1995 sections
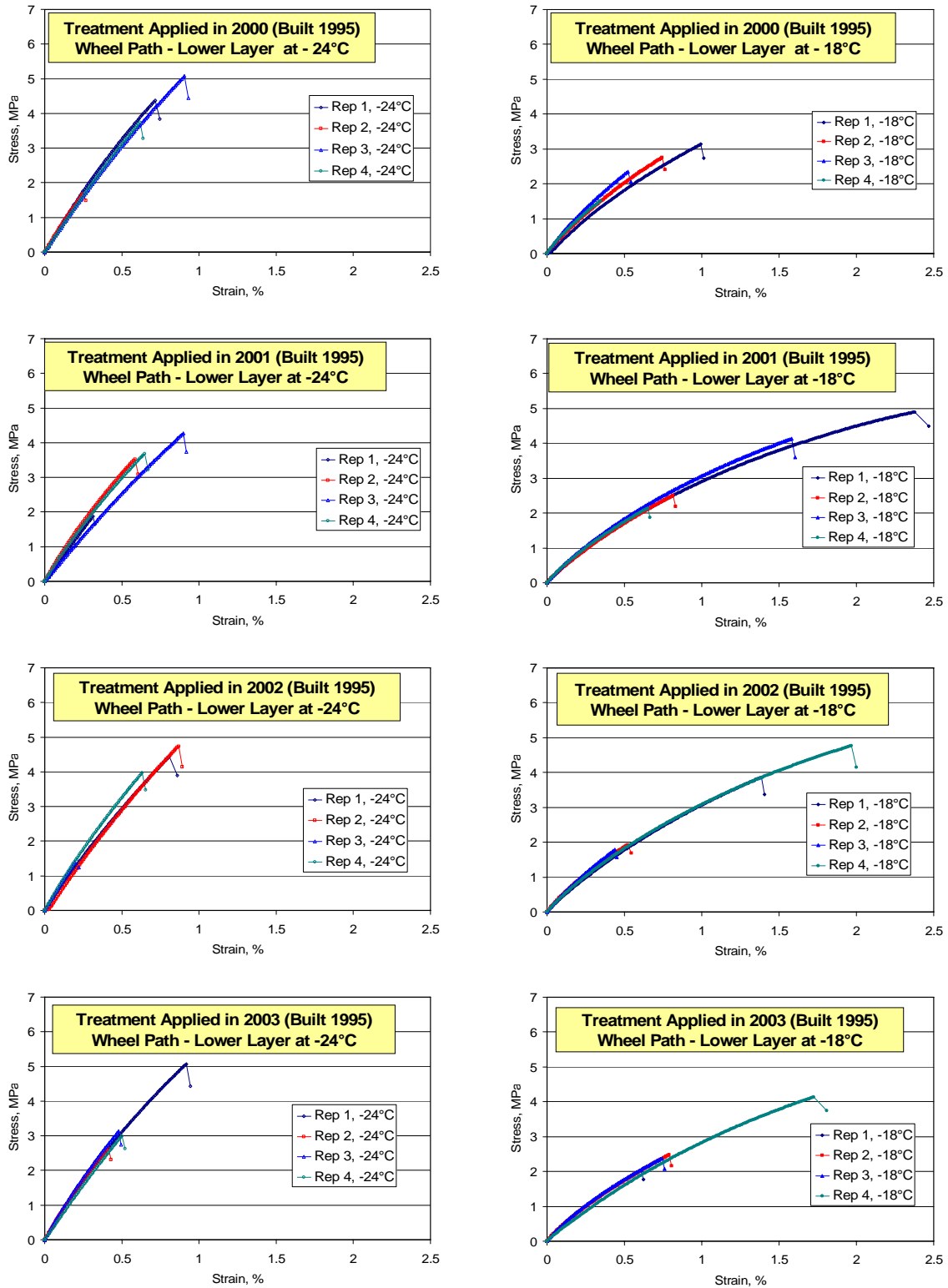
Figure D.12. DTT stress vs. strain curves for wheel path, lower layer, TH 56 1995 sections
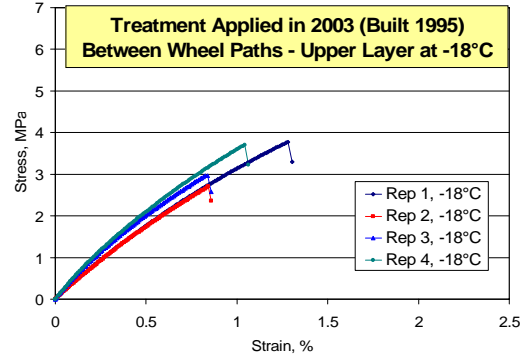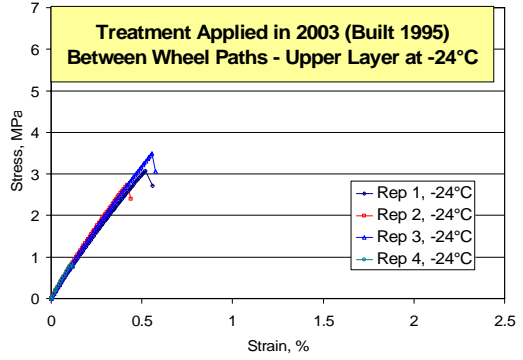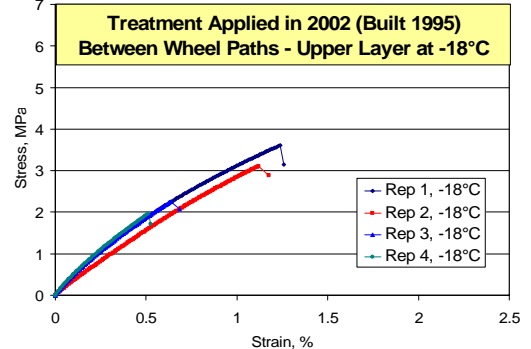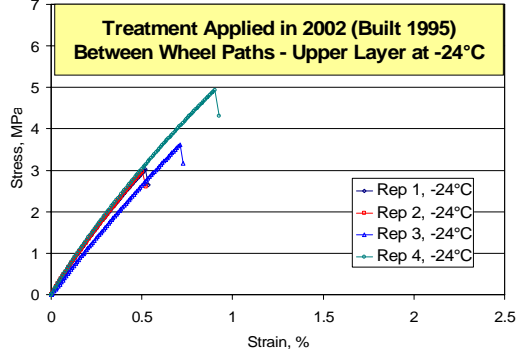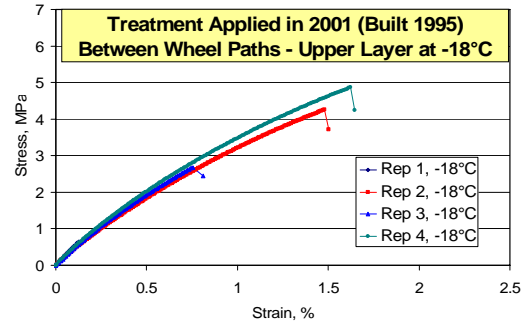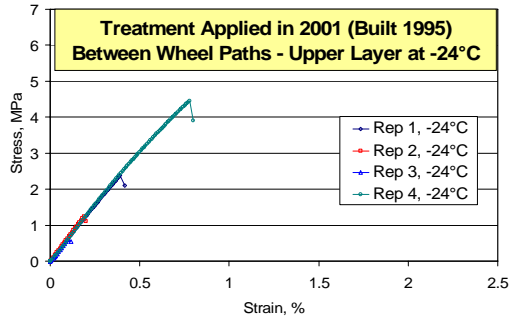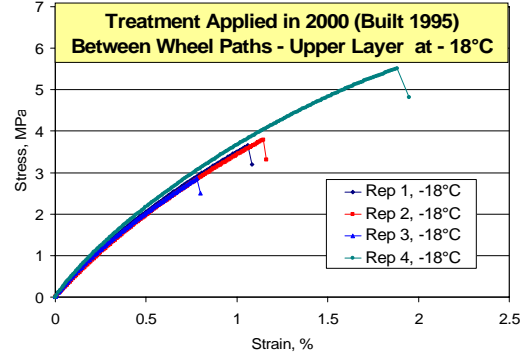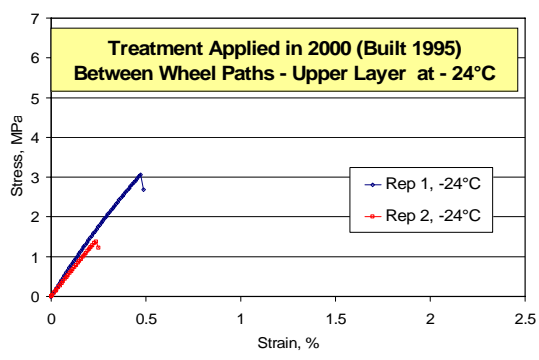
Figure D.13. DTT stress vs. strain curves for between wheel paths, upper layer,   TH 56 1995 sections
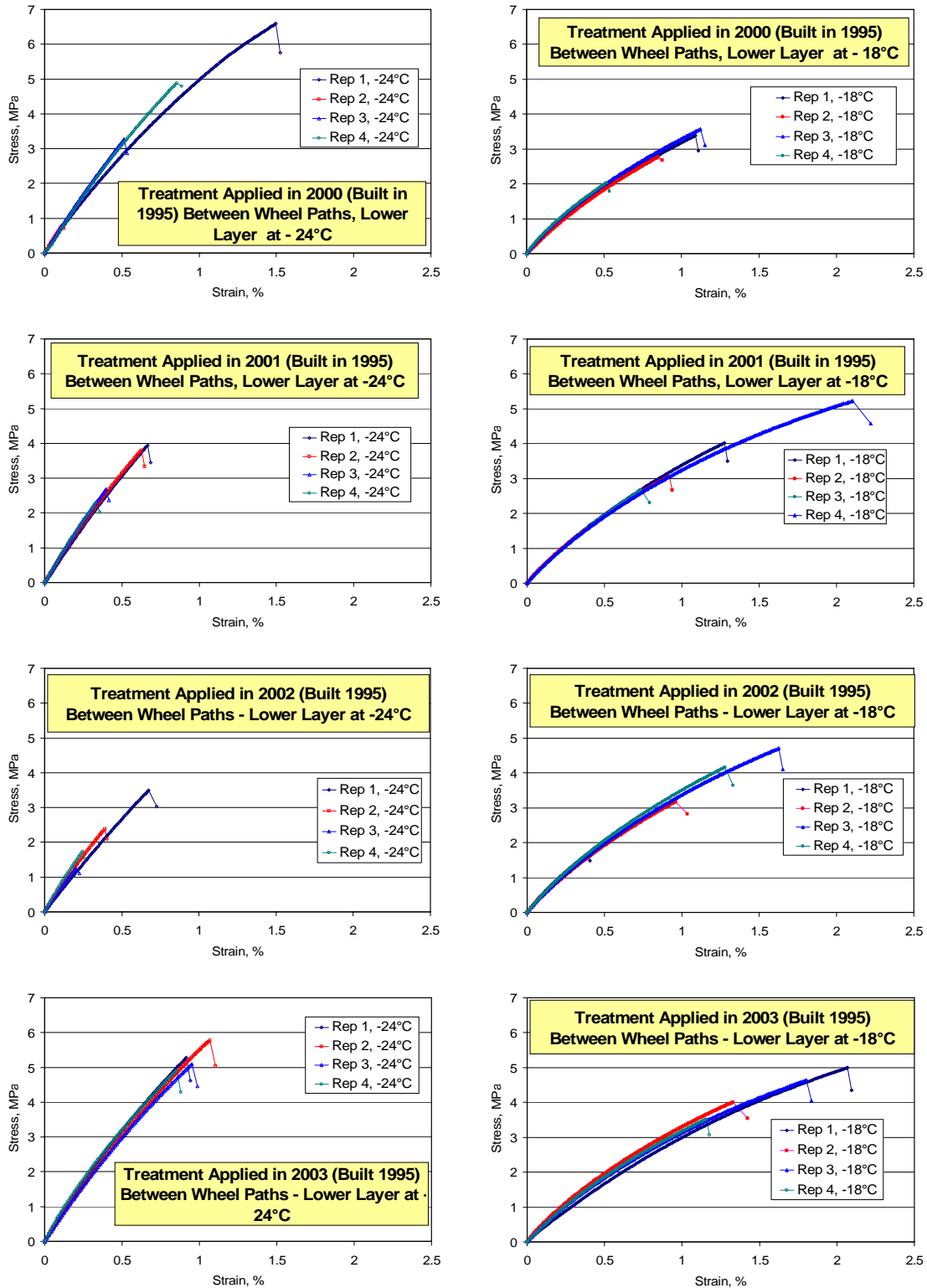
Figure D.14. DTT stress vs. strain curves for between wheel paths, lower layer, TH 56 1995 sections
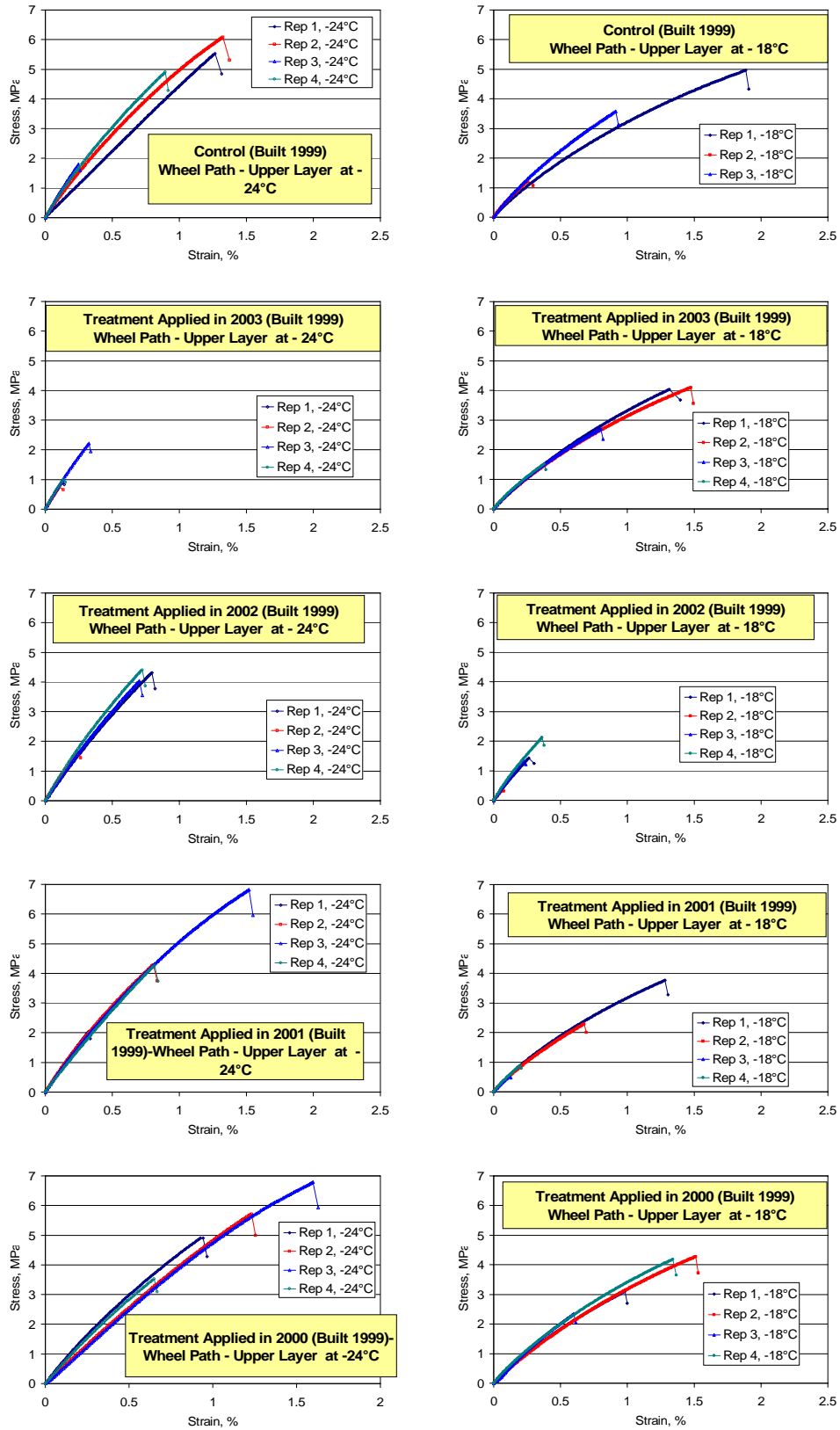
Figure D.15. DTT curves for wheel path, upper layer, TH 56 1999 sections
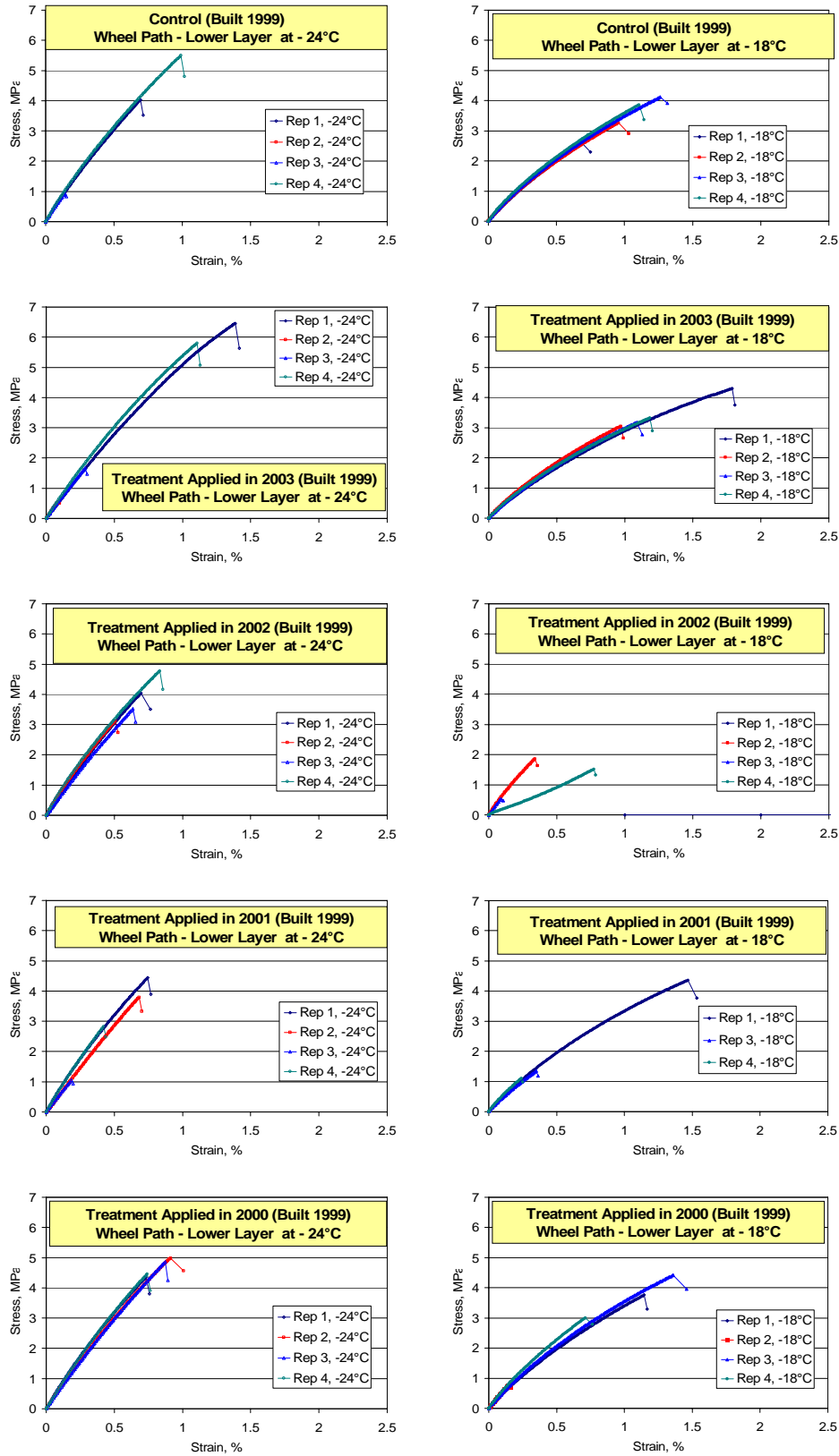
Figure D.16. DTT curves for wheel path, lower layer, TH 56 1999 sections
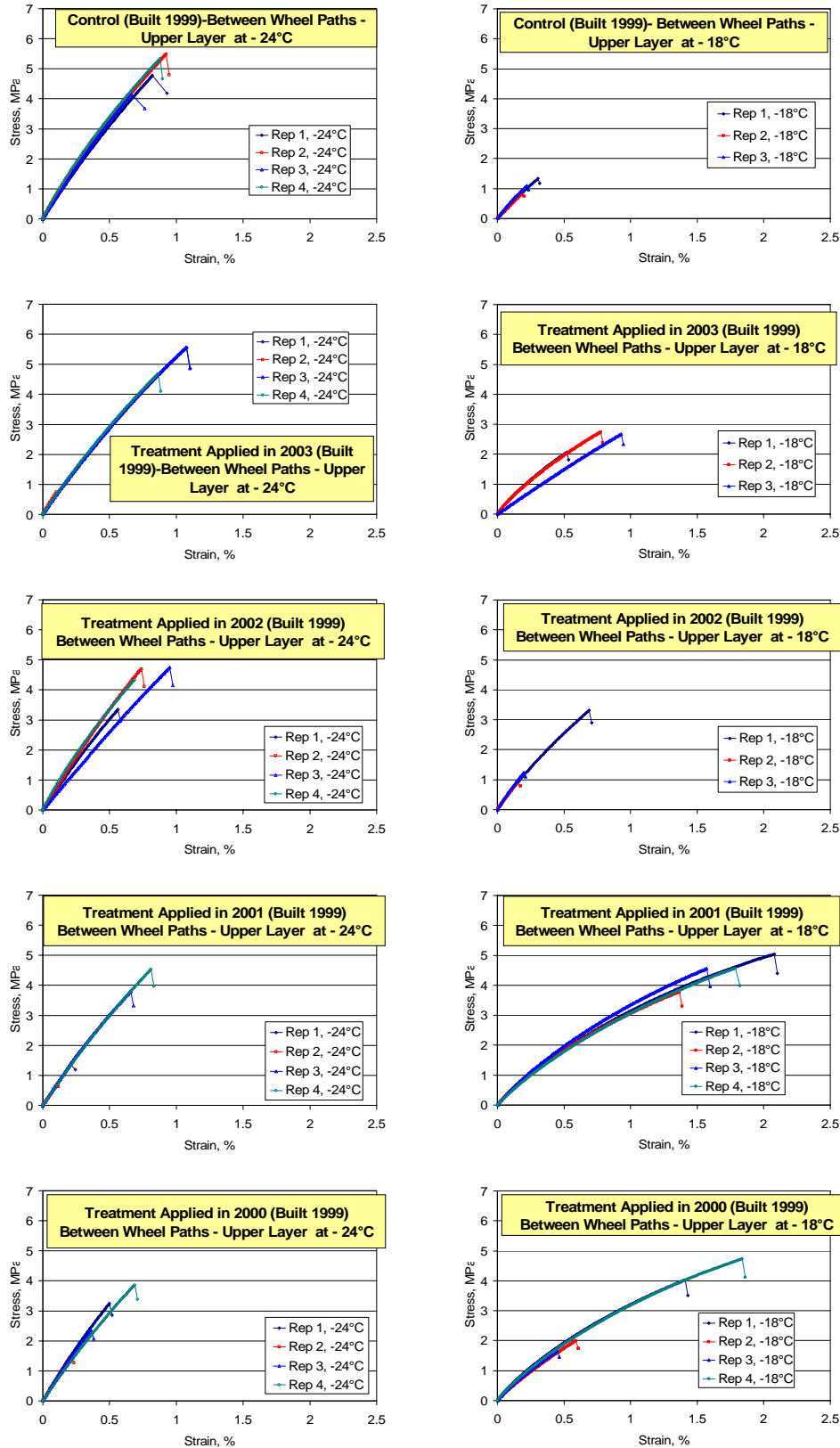
Figure D.17. DTT curves for between wheel paths, upper layer, TH 56 1999 sections
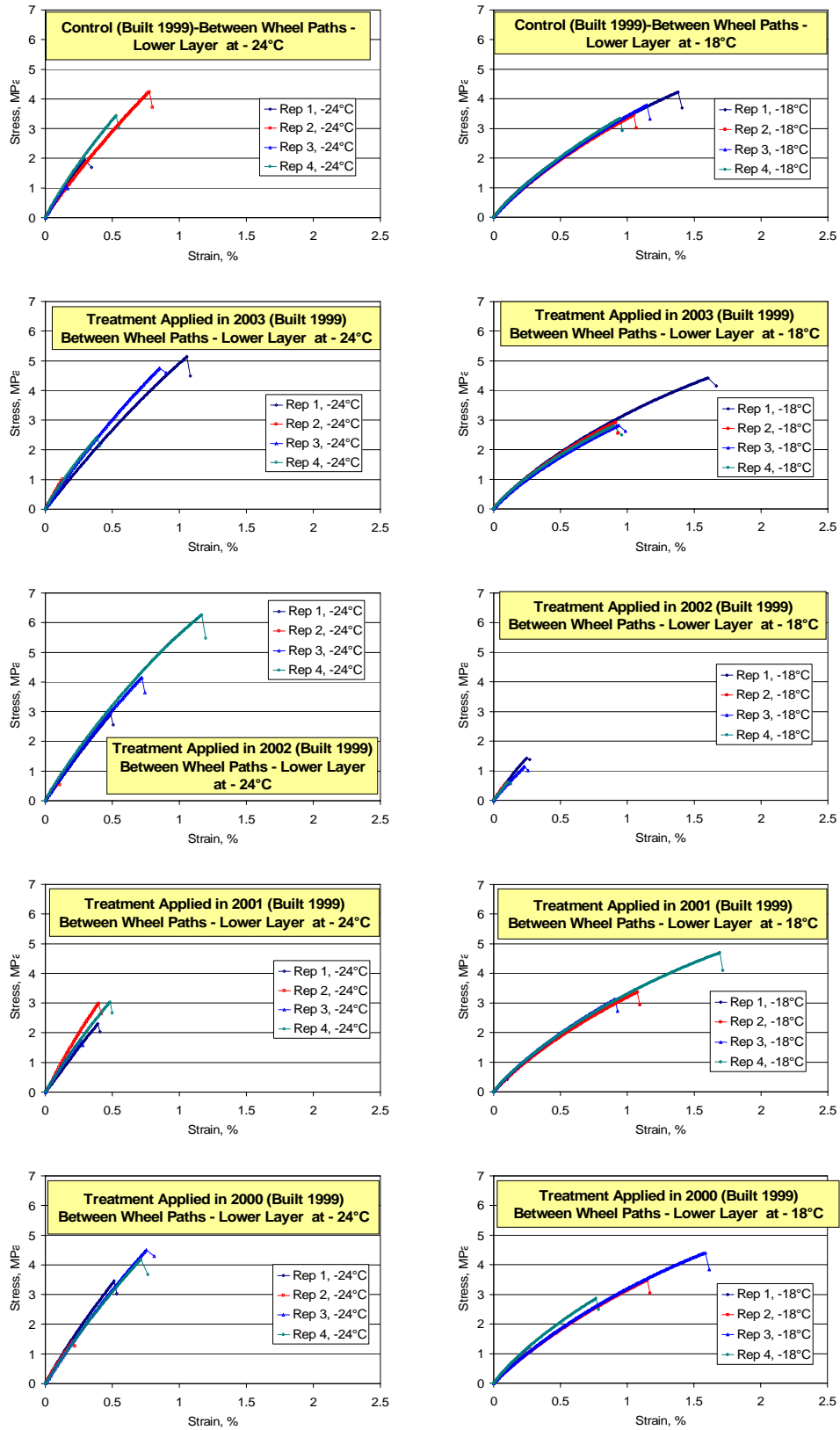
Figure D.18. DTT curves for between wheel paths, lower layer, TH 56 1999 sections

Wheel path

Between wheel paths
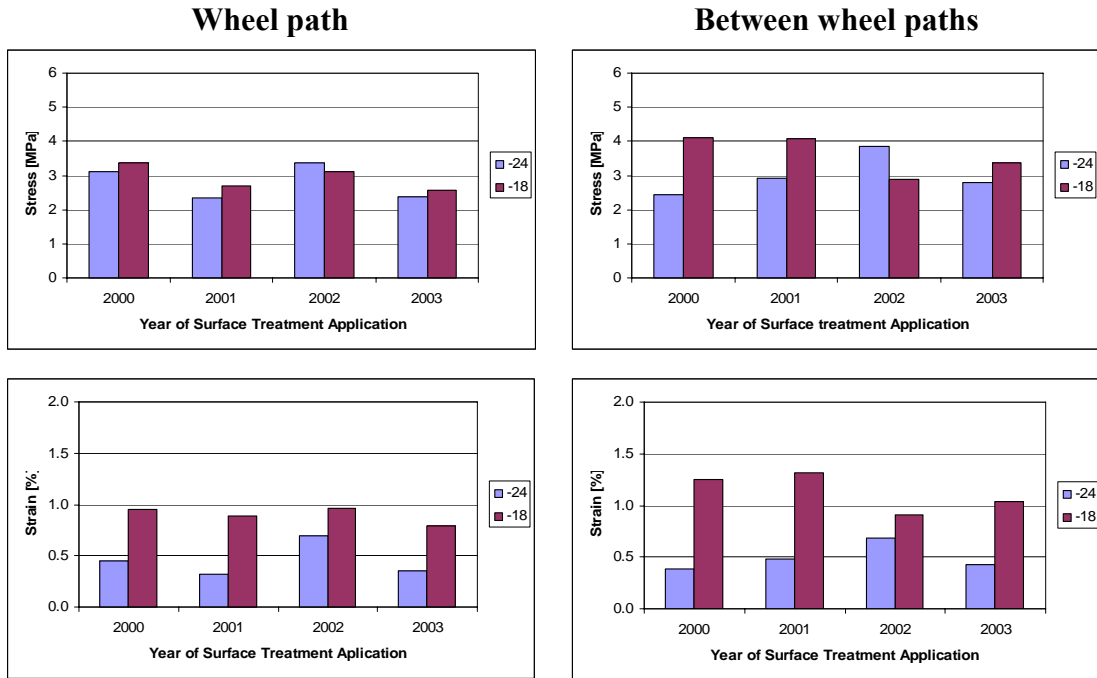
Figure D.19. Stress and strain at failure from DTT for upper layer, TH 56 1995 sections

Wheel path

Between wheel paths
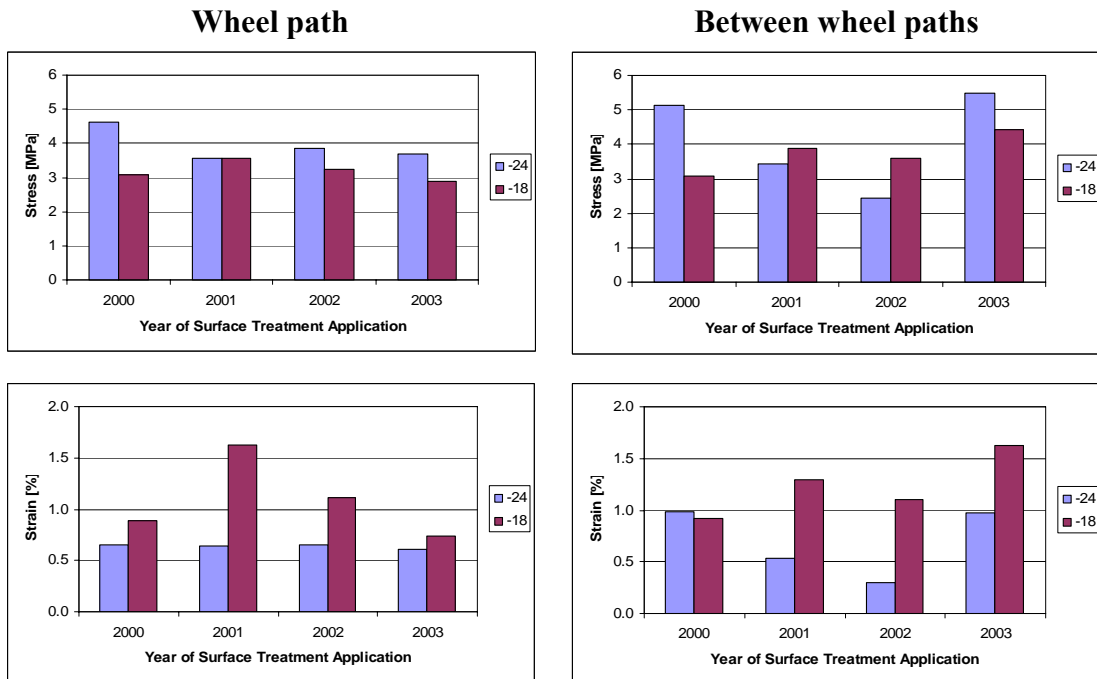
Figure D.20. Stress and strain at failure from DTT for lower layer, TH 56 1995 sections

D-14
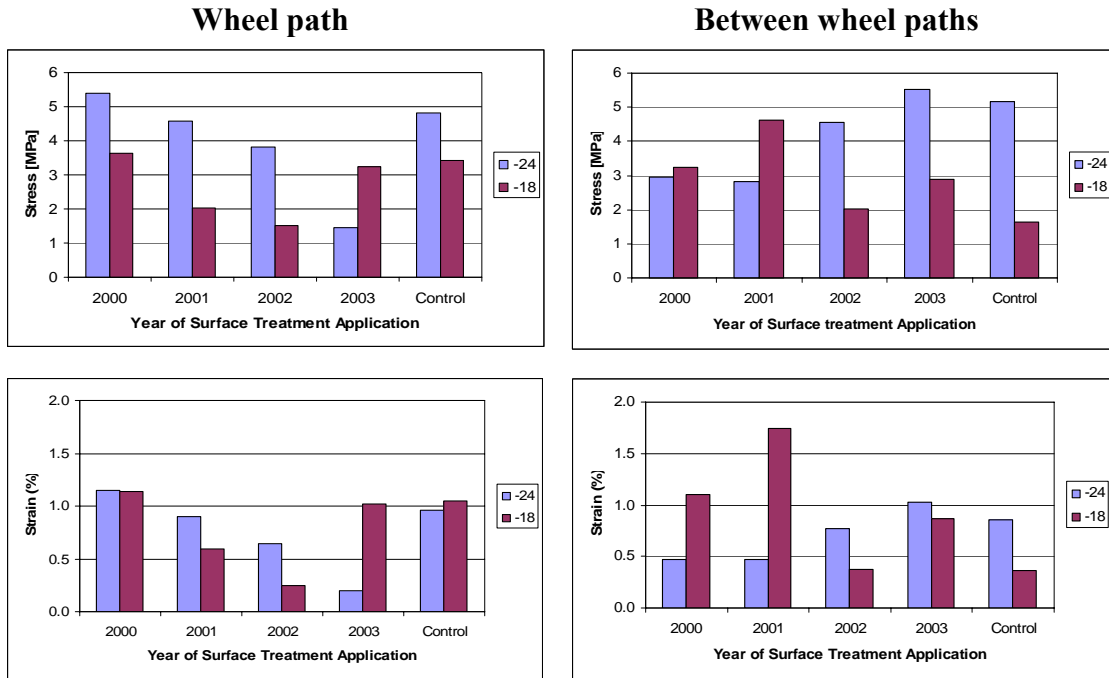
Figure D.21. Stress and strain at failure from DTT for upper layer, TH 56 1999 sections
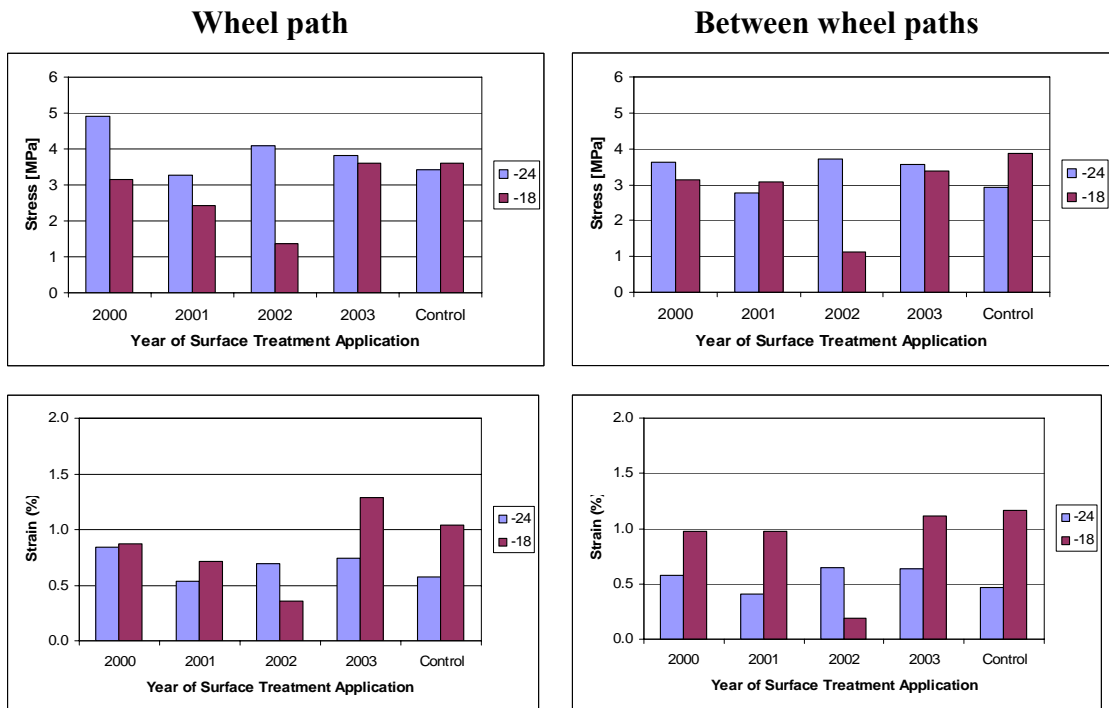
Figure D.22. Stress and strain at failure from DTT for lower layer, TH 56 1999 sections
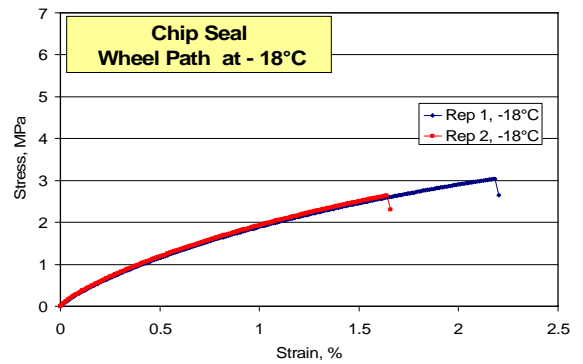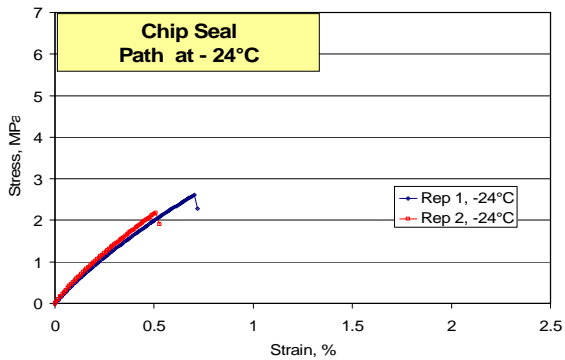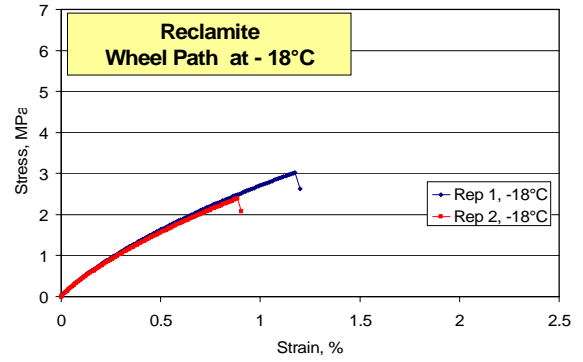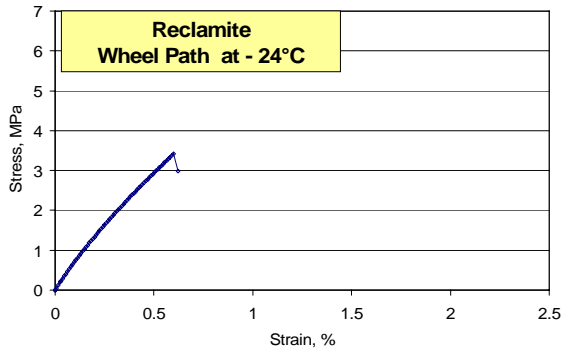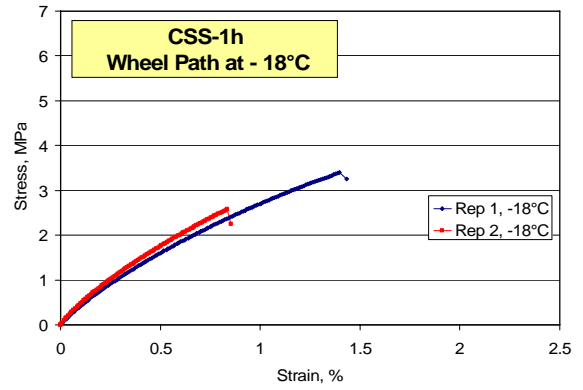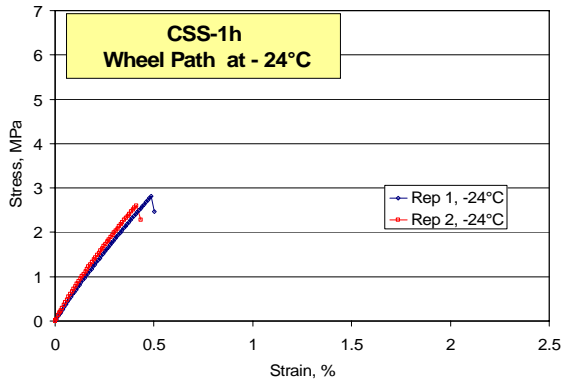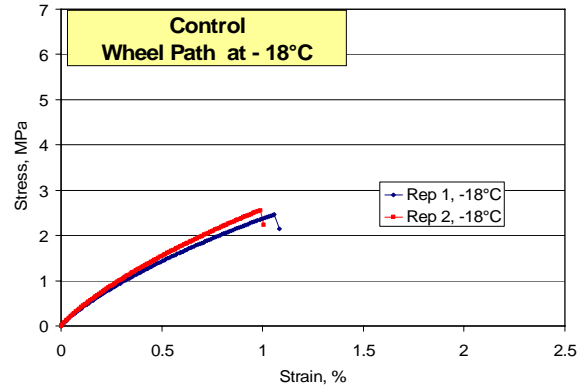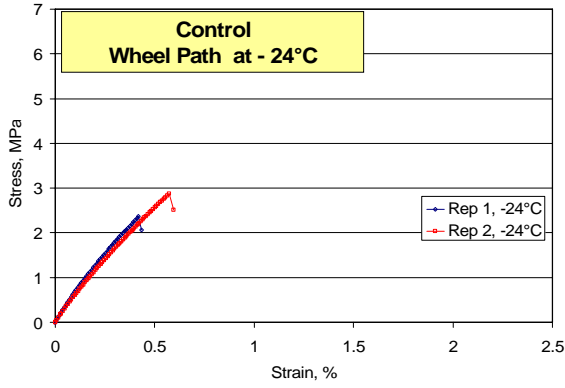
Figure D.23. DTT stress vs. strain curves for wheel path, TH 251
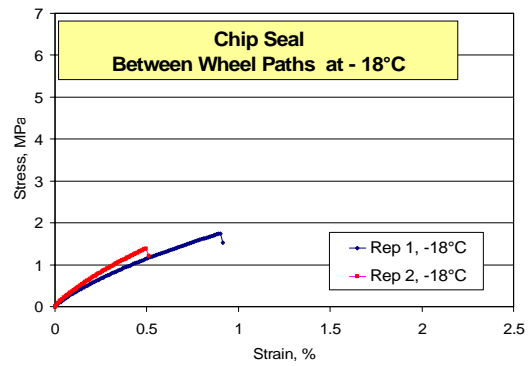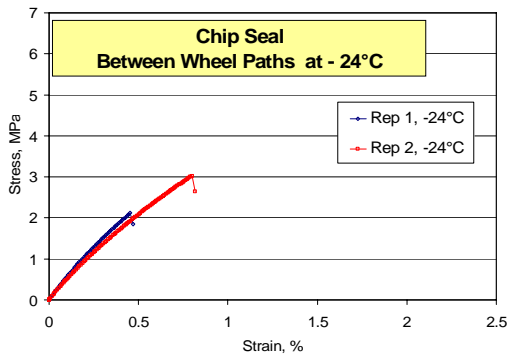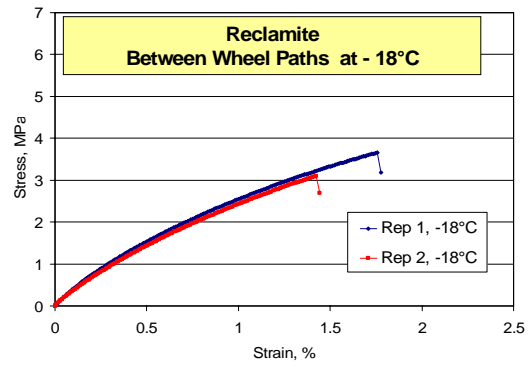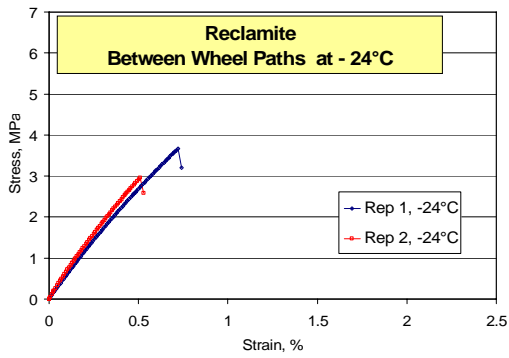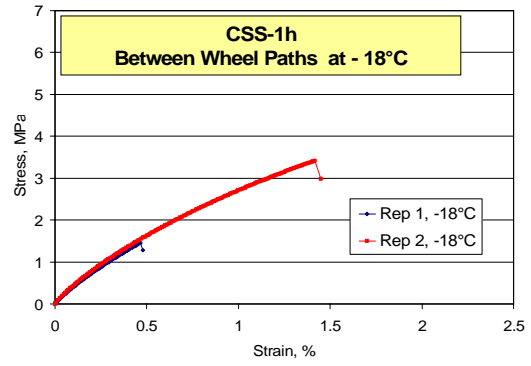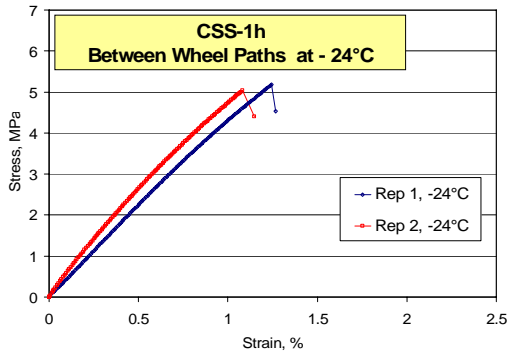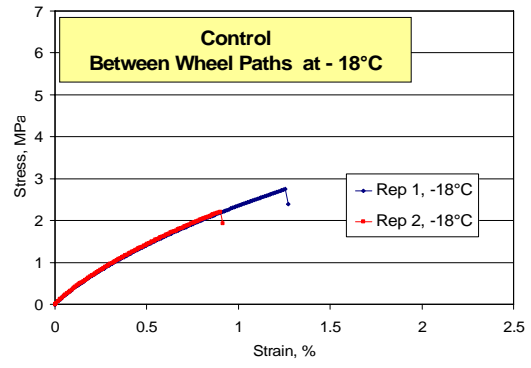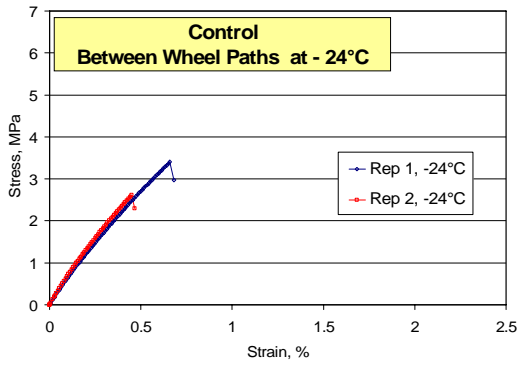
**Figure D.24. DTT stress vs. strain curves for between wheel paths, TH 251**

Wheel path

Between wheel paths
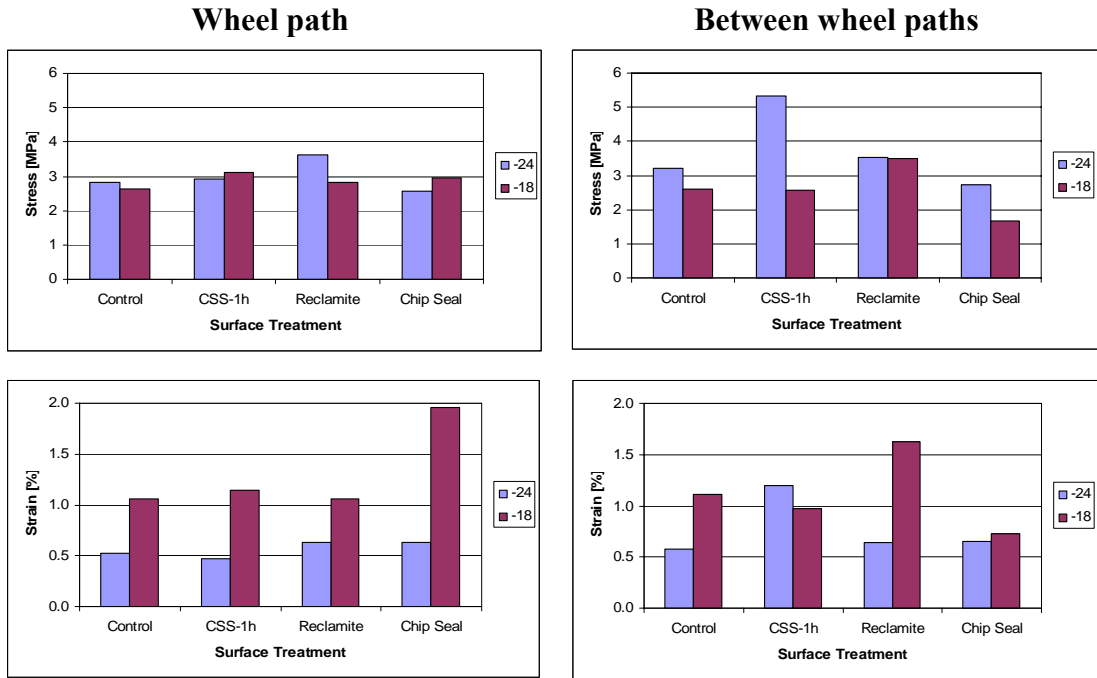
Figure D.25. Stress and strain at failure from DTT, TH 251
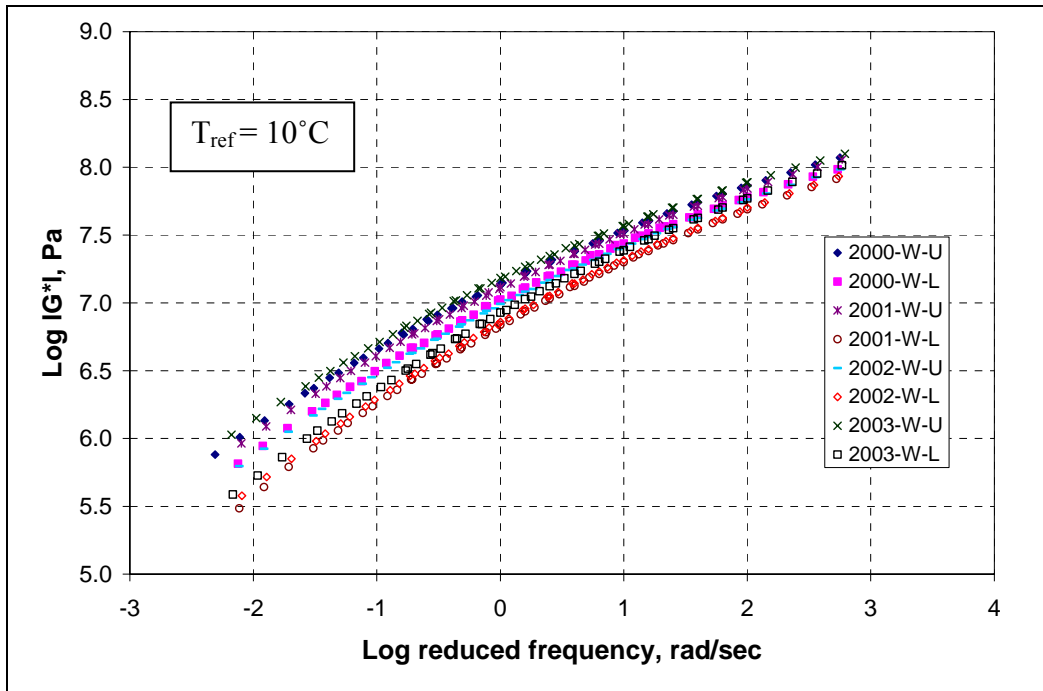
**Figure D.26. Complex modulus master curves for wheel path samples, TH 56 1995 sections**
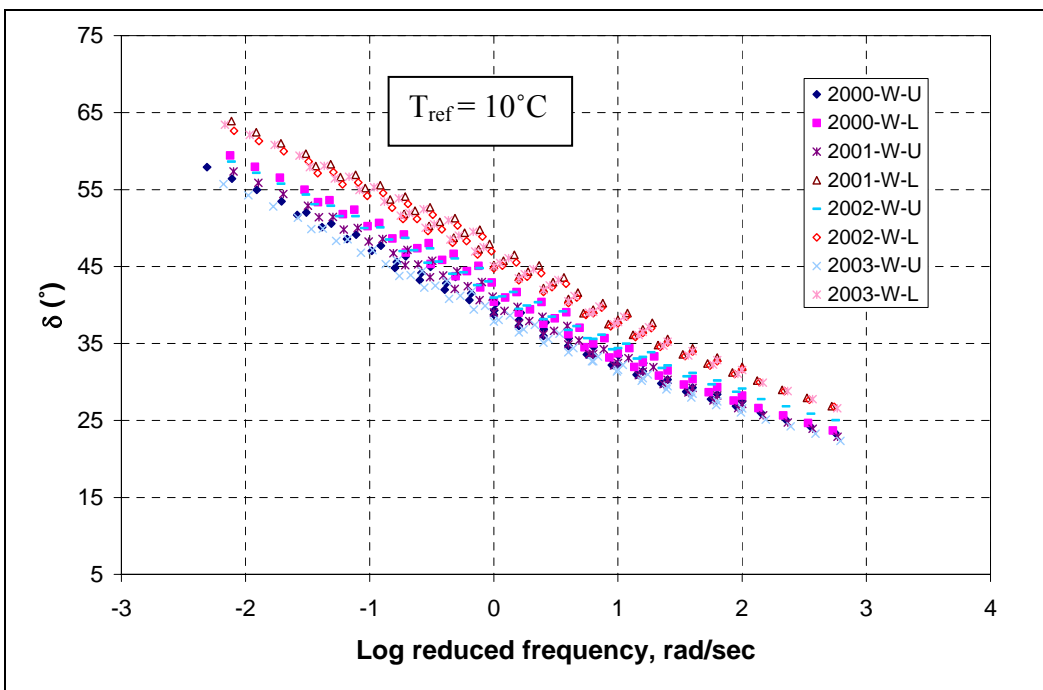
Figure D.27. Phase angle master curves for wheel path samples, TH 56 1995 sections
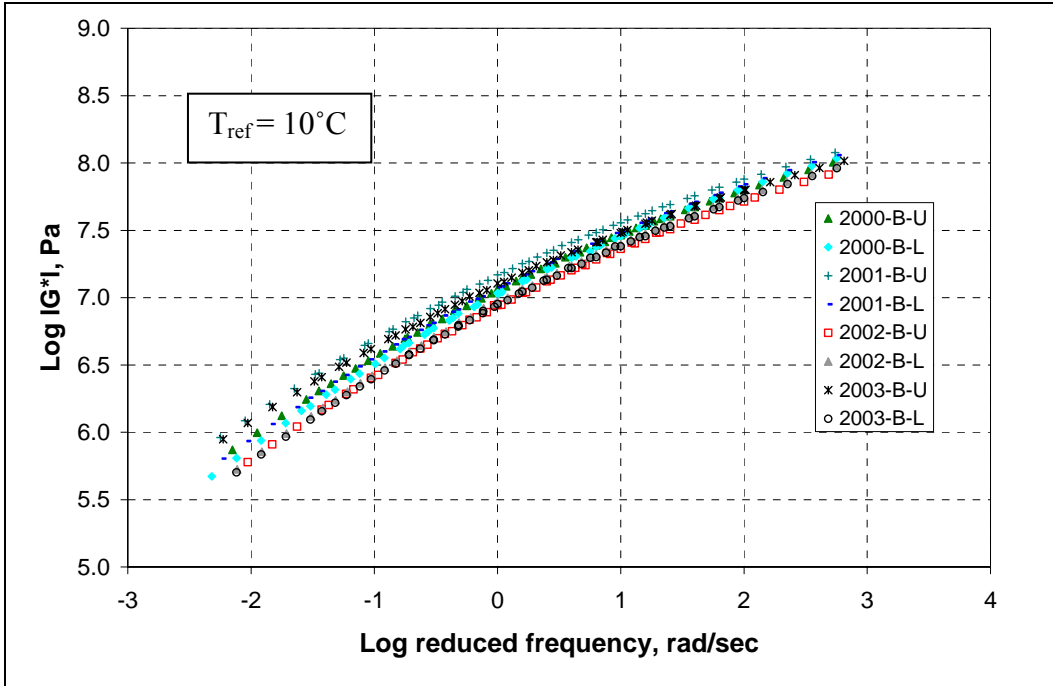
Figure D.28. Complex modulus master curves for between wheel paths samples, TH 56 1995 sections
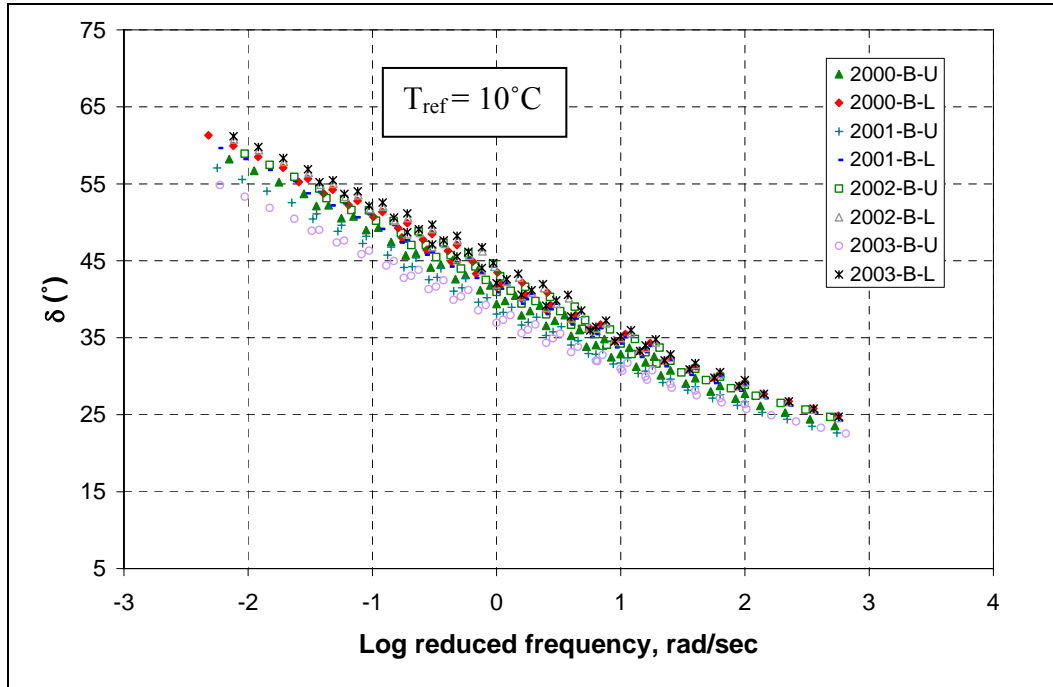

Figure D.29. Phase angle master curves for between wheel paths samples, TH 56 1995 sections
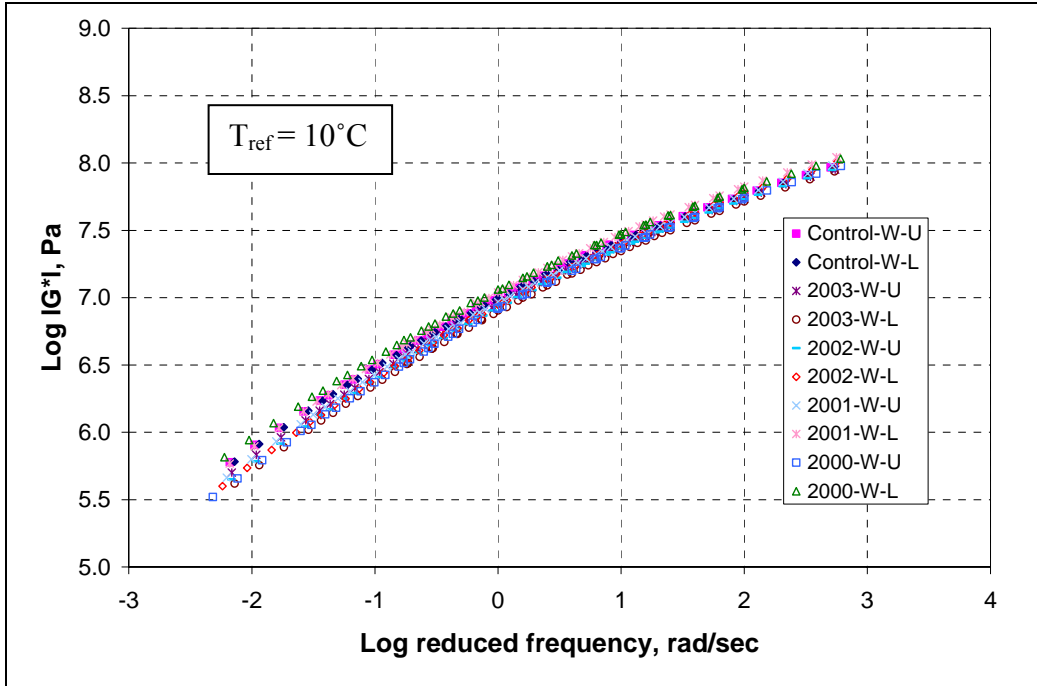
Figure D.30. Complex modulus master curves for wheel path samples, TH 56 1999 sections
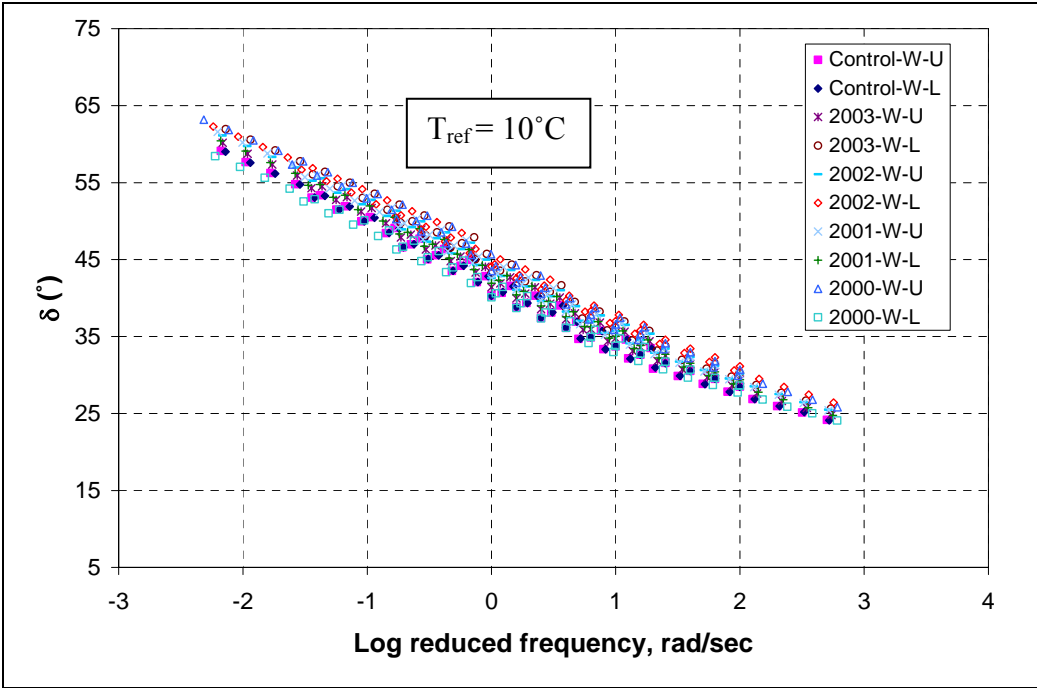

**Figure D.31. Phase angle master curves for wheel path samples, TH 56 1999 sections**
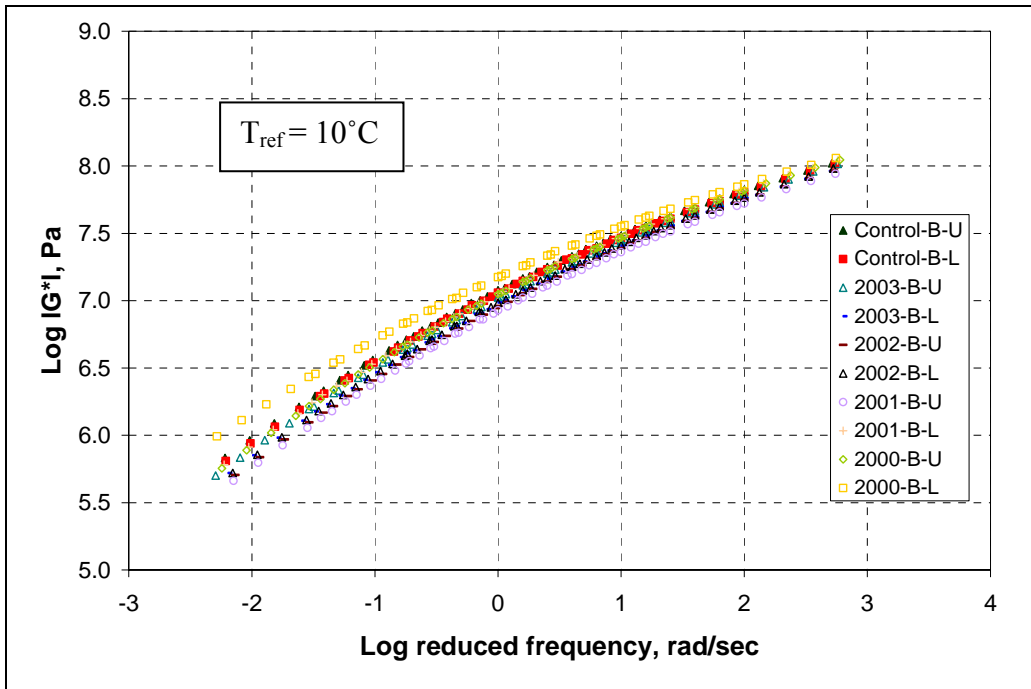
Figure D.32. Complex modulus master curves for between wheel paths samples, TH 56 1999 sections
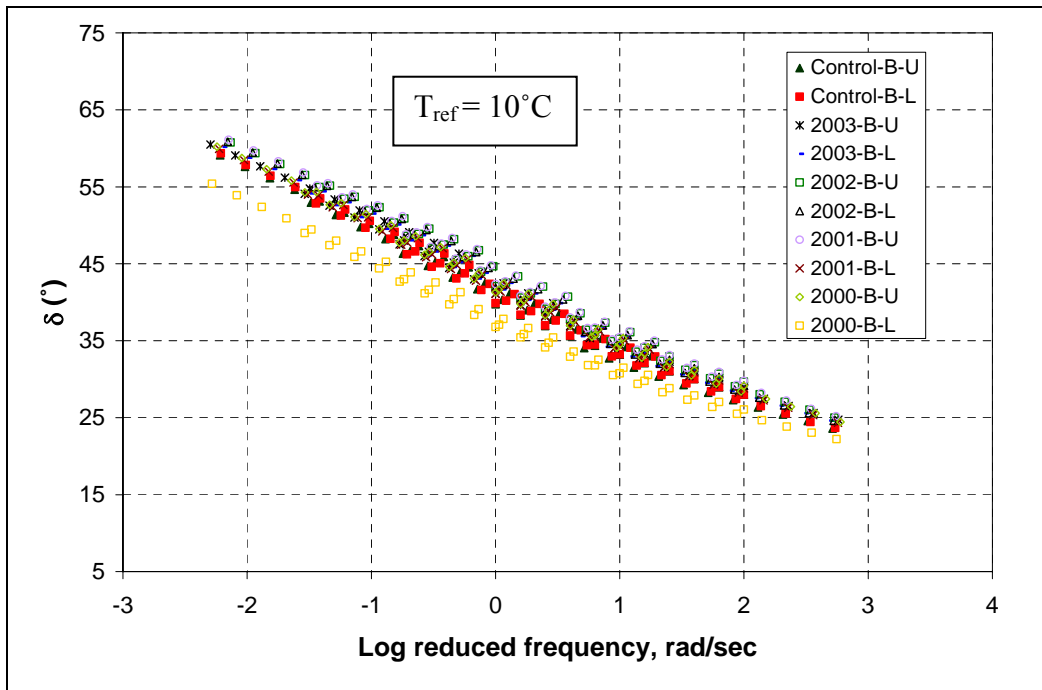
Figure D.33. Phase angle master curves for between wheel paths samples, TH 56 1999 sections

Wheel path

Between wheel paths
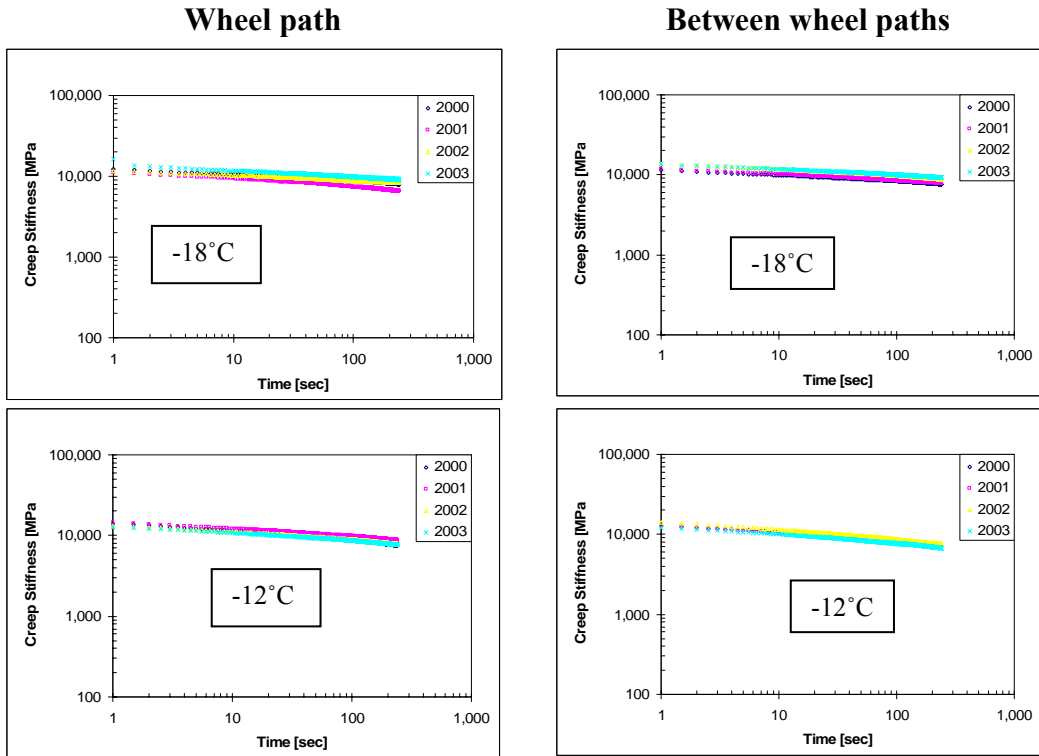
Figure D.34. Mixture creep stiffness vs. time for upper layer, TH 56 1995 sections

Wheel path

Between wheel paths
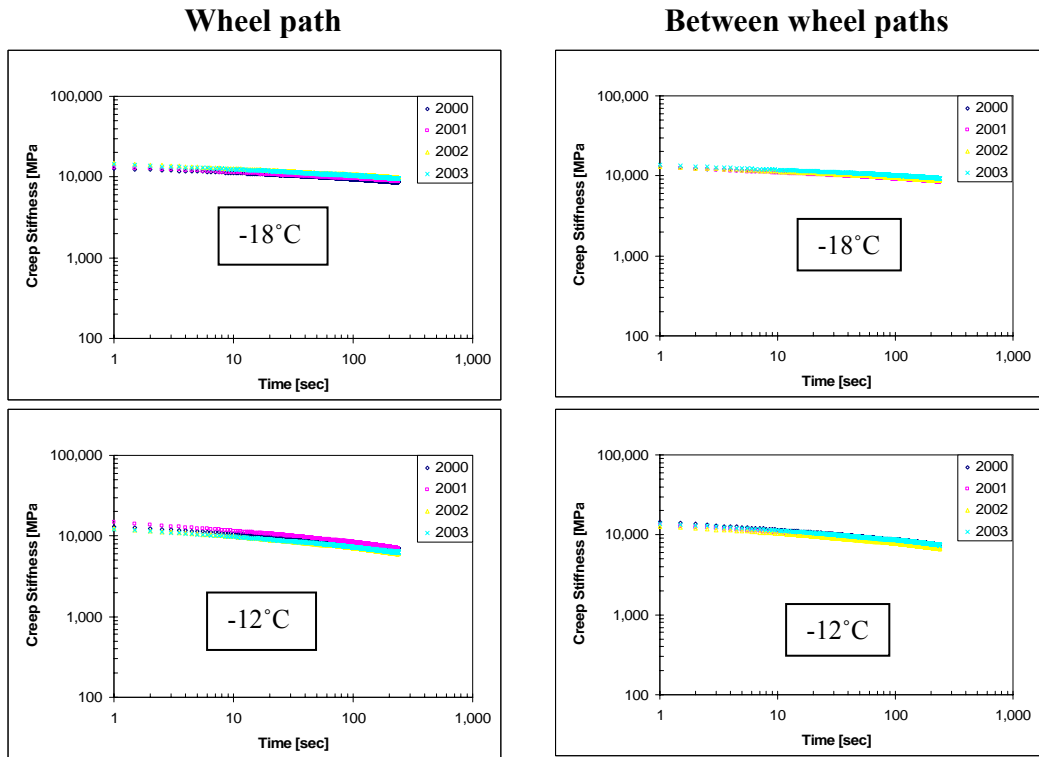
Figure D.35. Mixture creep stiffness vs. time for lower layer, TH 56 1995 sections

Upper layer
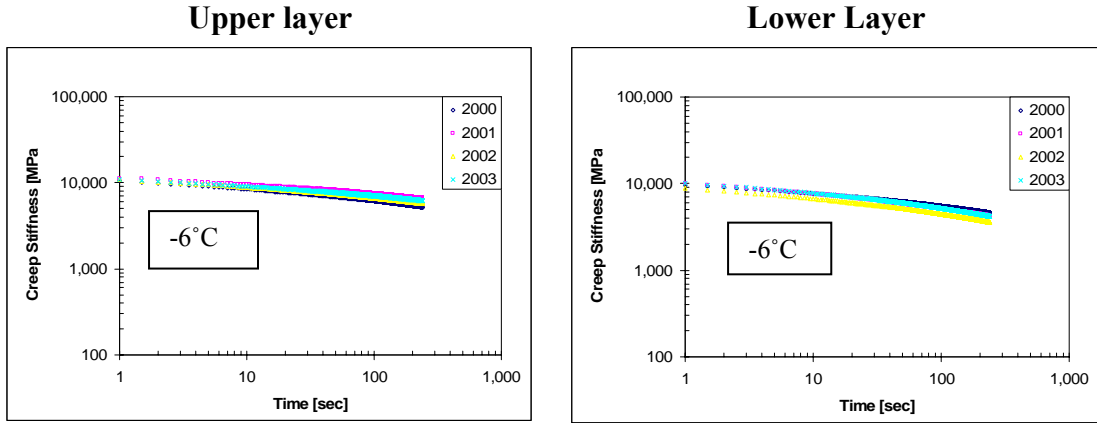
Lower Layer

Figure D.36. Mixture creep stiffness vs. time for samples located in wheel path, TH 56 1995 sections

Wheel path

Between wheel paths
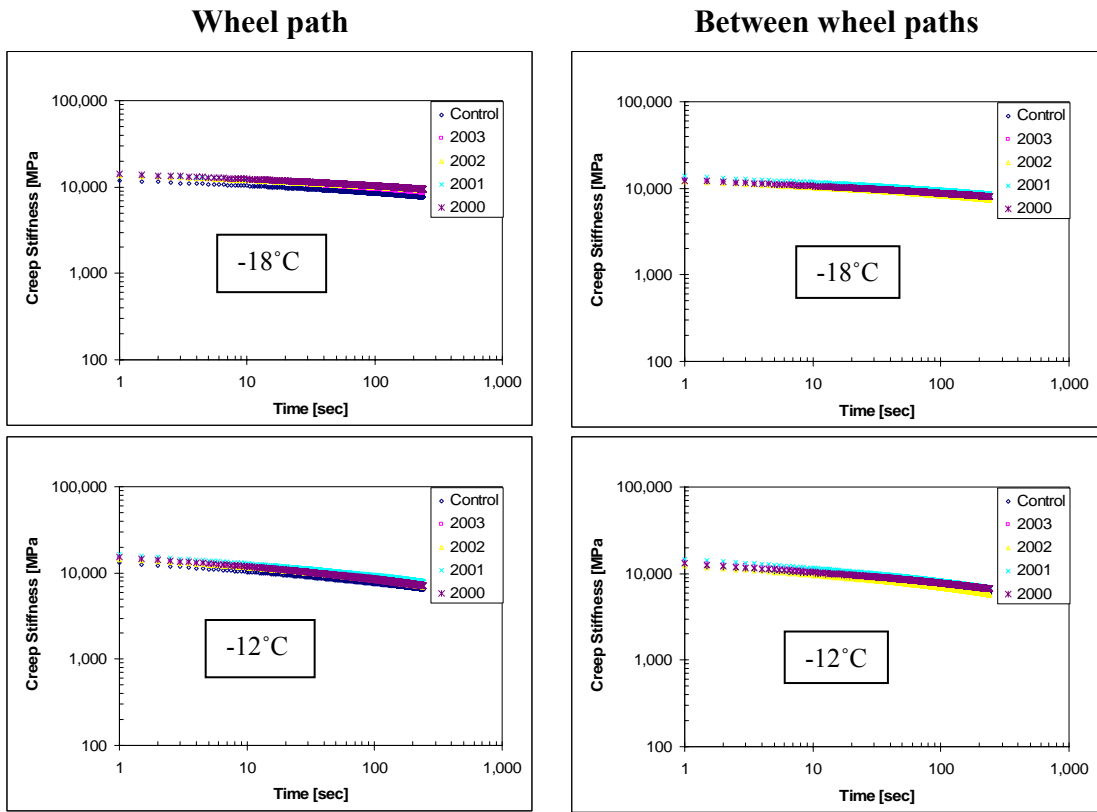
Figure D.37. Mixture creep stiffness vs. time for upper layer, TH 56 1999 sections

Wheel path | **Between wheel paths**
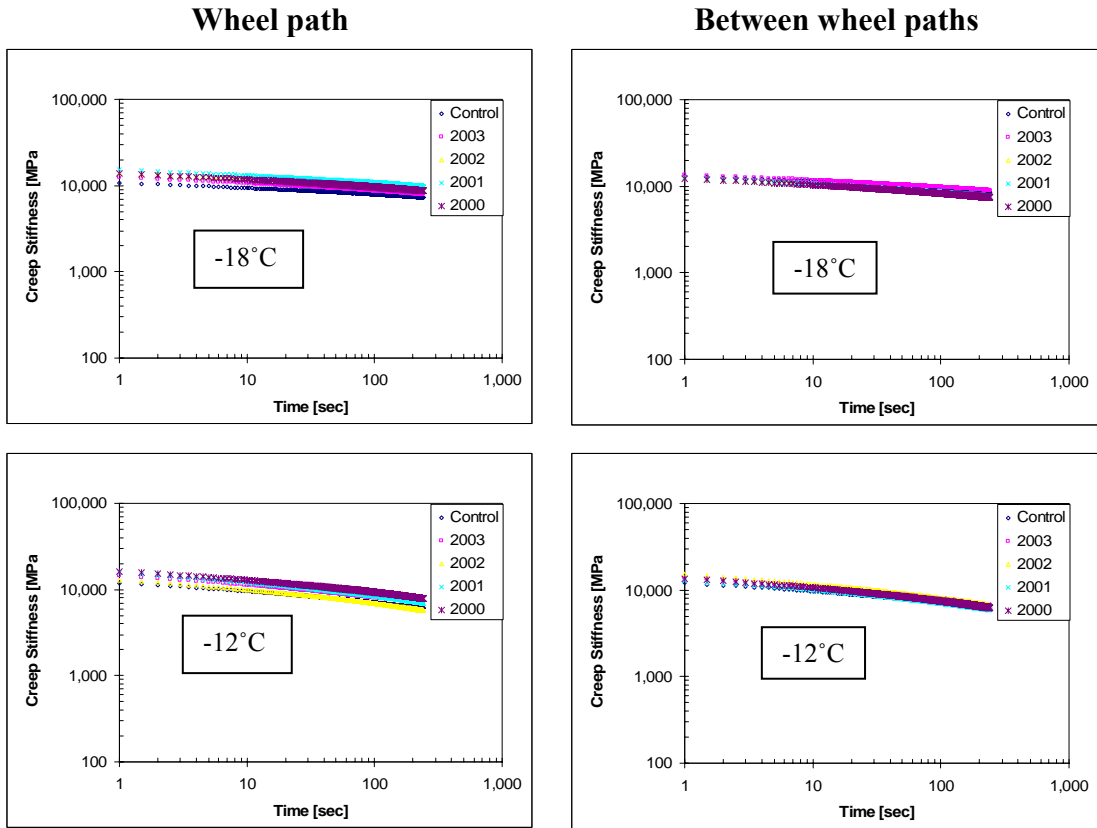
Figure D.38. Mixture creep stiffness vs. time for lower layer, TH 56 1999 sections

Upper layer | **Lower Layer**
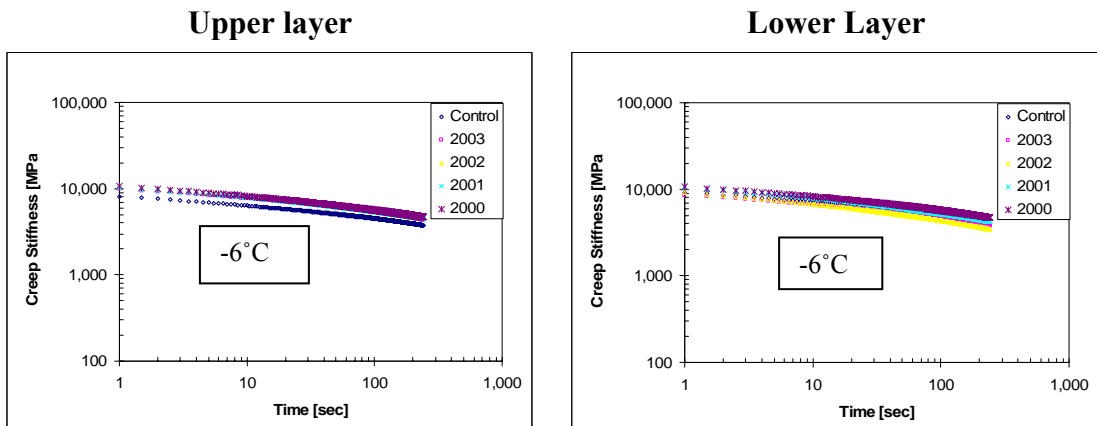

Figure D.39. Mixture creep stiffness vs. time for samples located in wheel path, TH 56 1999 sections
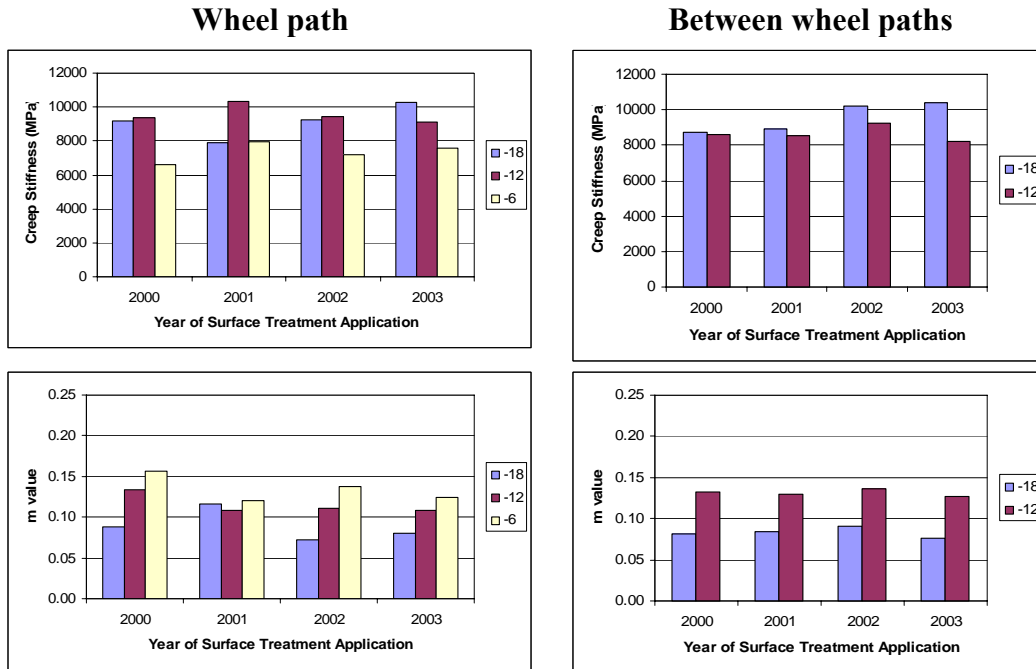
Figure D.40. Stiffness of the mixture and m at 60 sec. for upper layer, TH 56 1995 sections
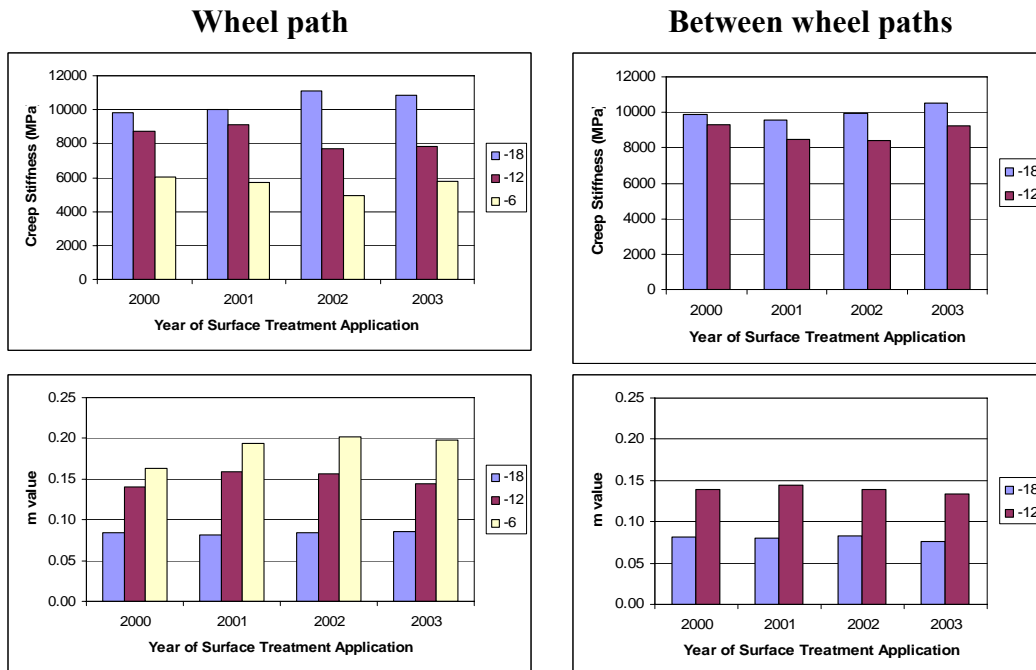
Figure D.41. Stiffness of the mixture and m at 60 sec. for lower layer, TH 56 1995 sections

Wheel path

Between wheel paths
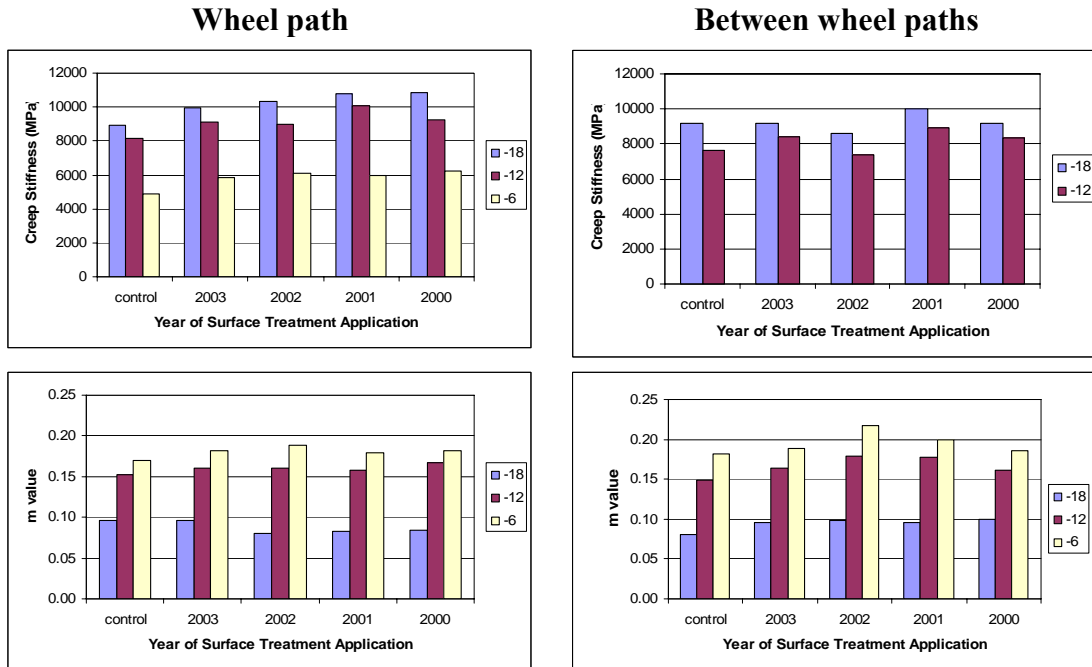
Figure D.42. Stiffness of the mixture and m at 60 sec. for upper layer, TH 56 1999 sections

Wheel path

Between wheel paths
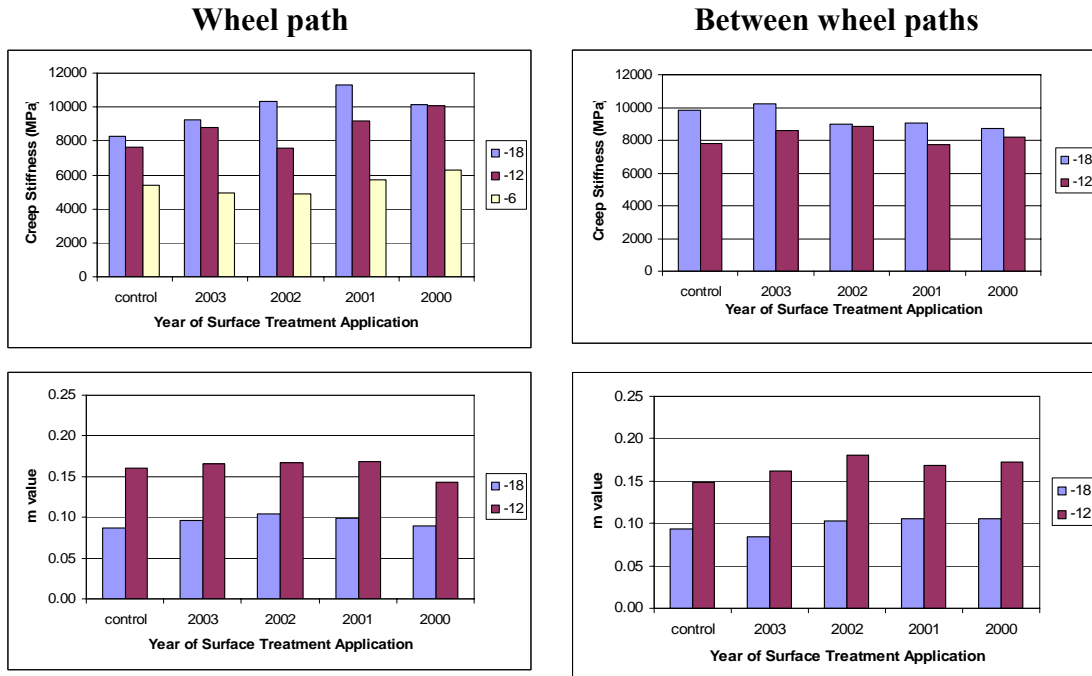
Figure D.43. Stiffness of the mixture and m at 60 sec. for lower layer, TH 56 1999 sections

Wheel path

Between wheel paths
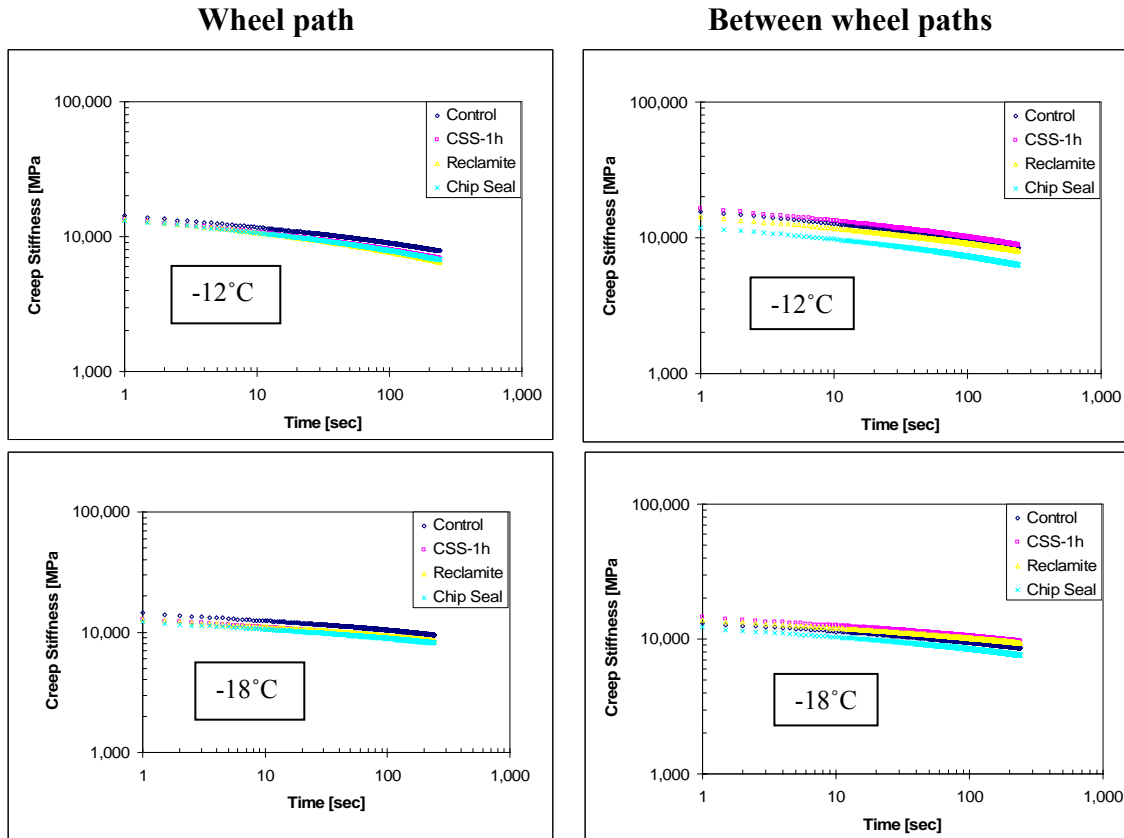
Figure D.44. Mixture creep stiffness vs. time, TH 251 sections

Wheel path

Between wheel paths
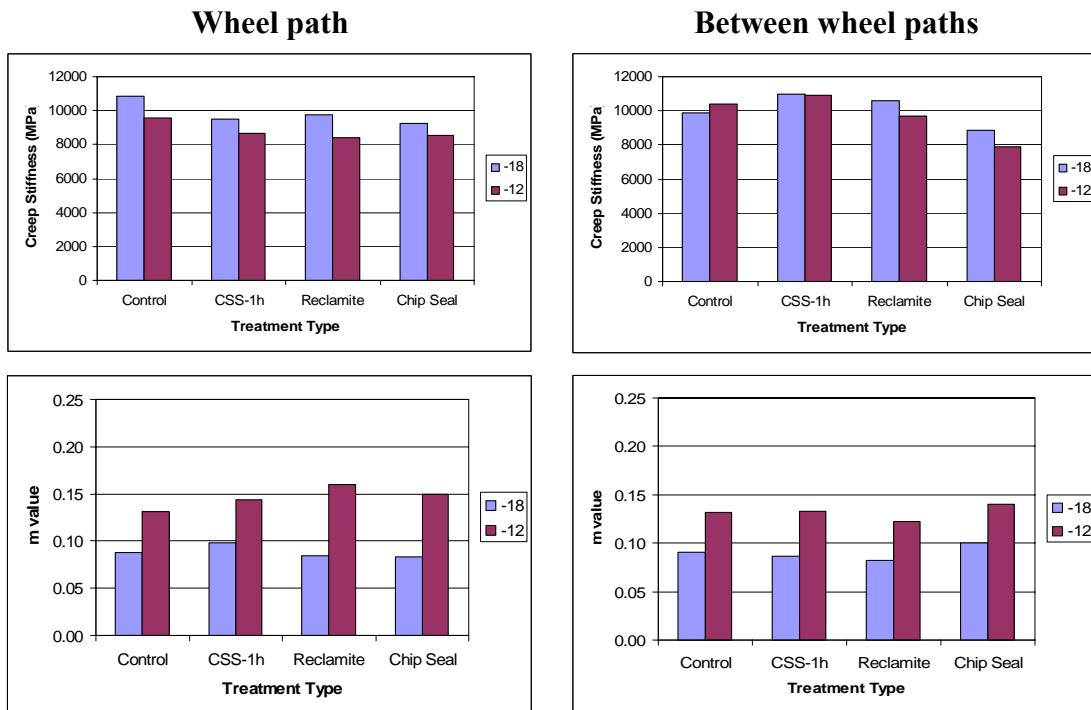
Figure D.45. Stiffness of the mixture and m at 60 sec. for TH 251 sections

Wheel path

Between wheel paths
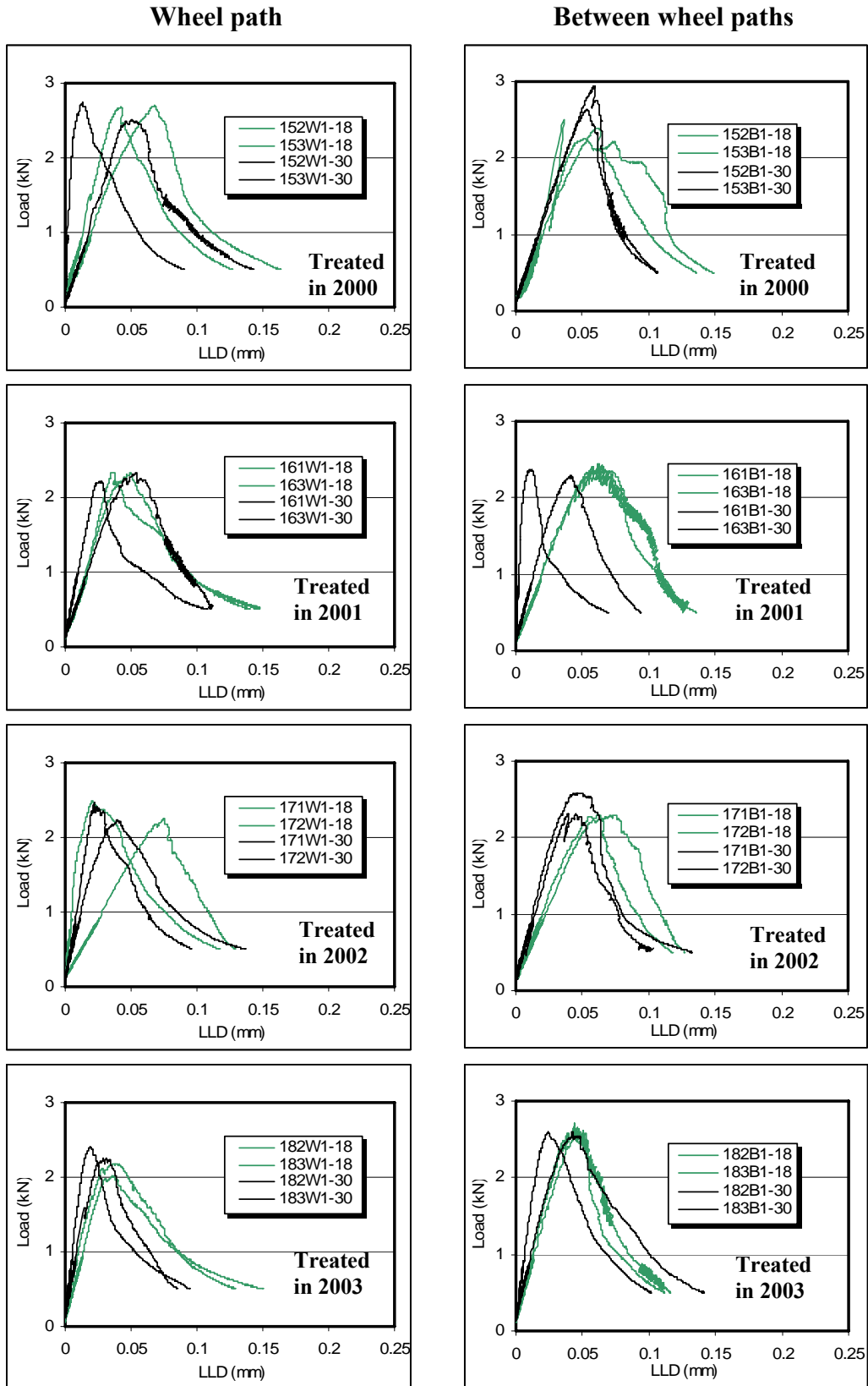
Figure D.46. Load-LLD curves for samples from upper layer, TH 56 1995 sections

Wheel path

Between wheel paths
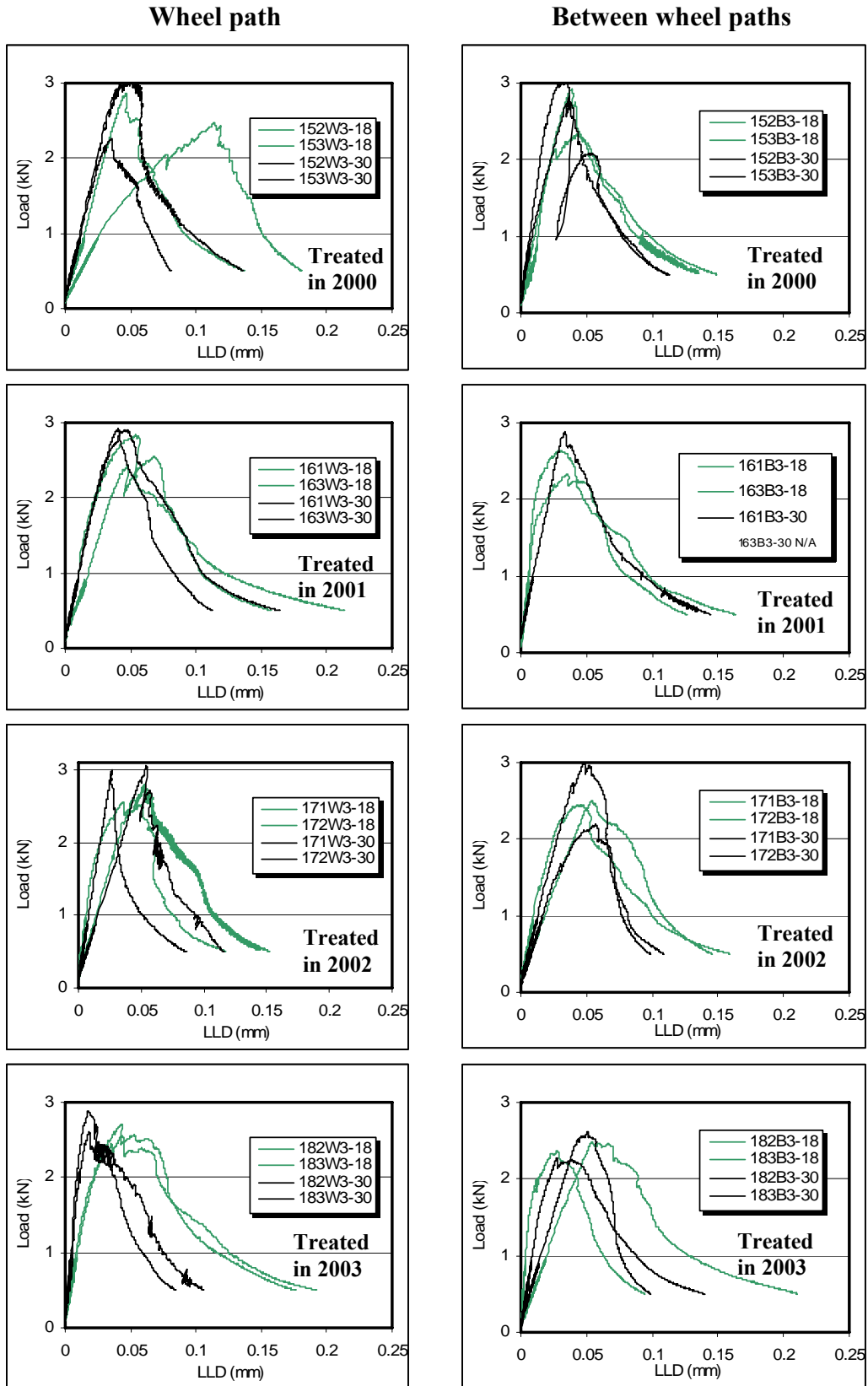
Figure D.47. Load-LLD curves for samples from lower layer, TH 56 1995 sections

Wheel path

Between wheel paths
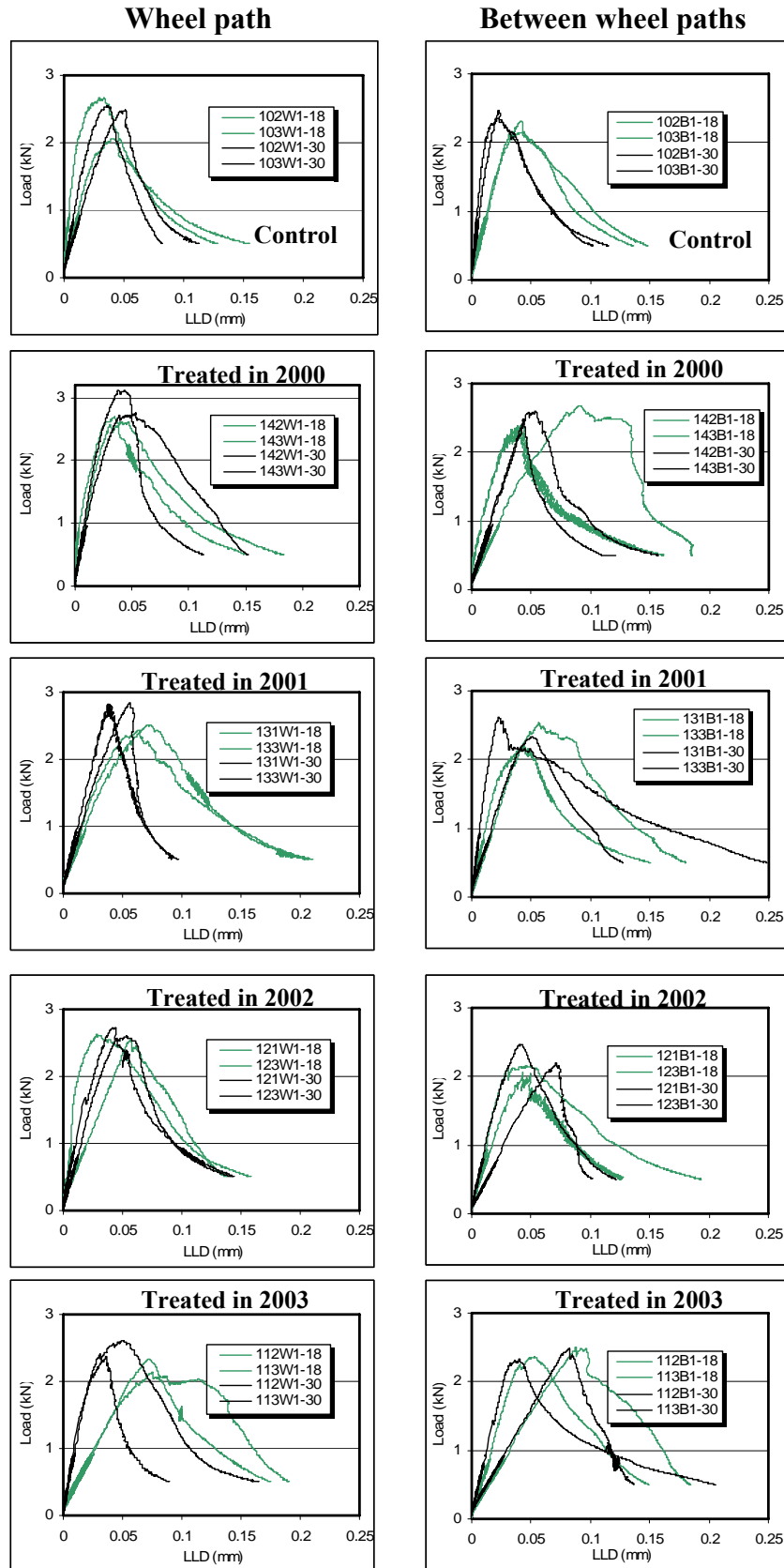
Figure D.48. Load-LLD curves for samples from upper layer, TH 56 1999 sections

Wheel path

Between wheel paths
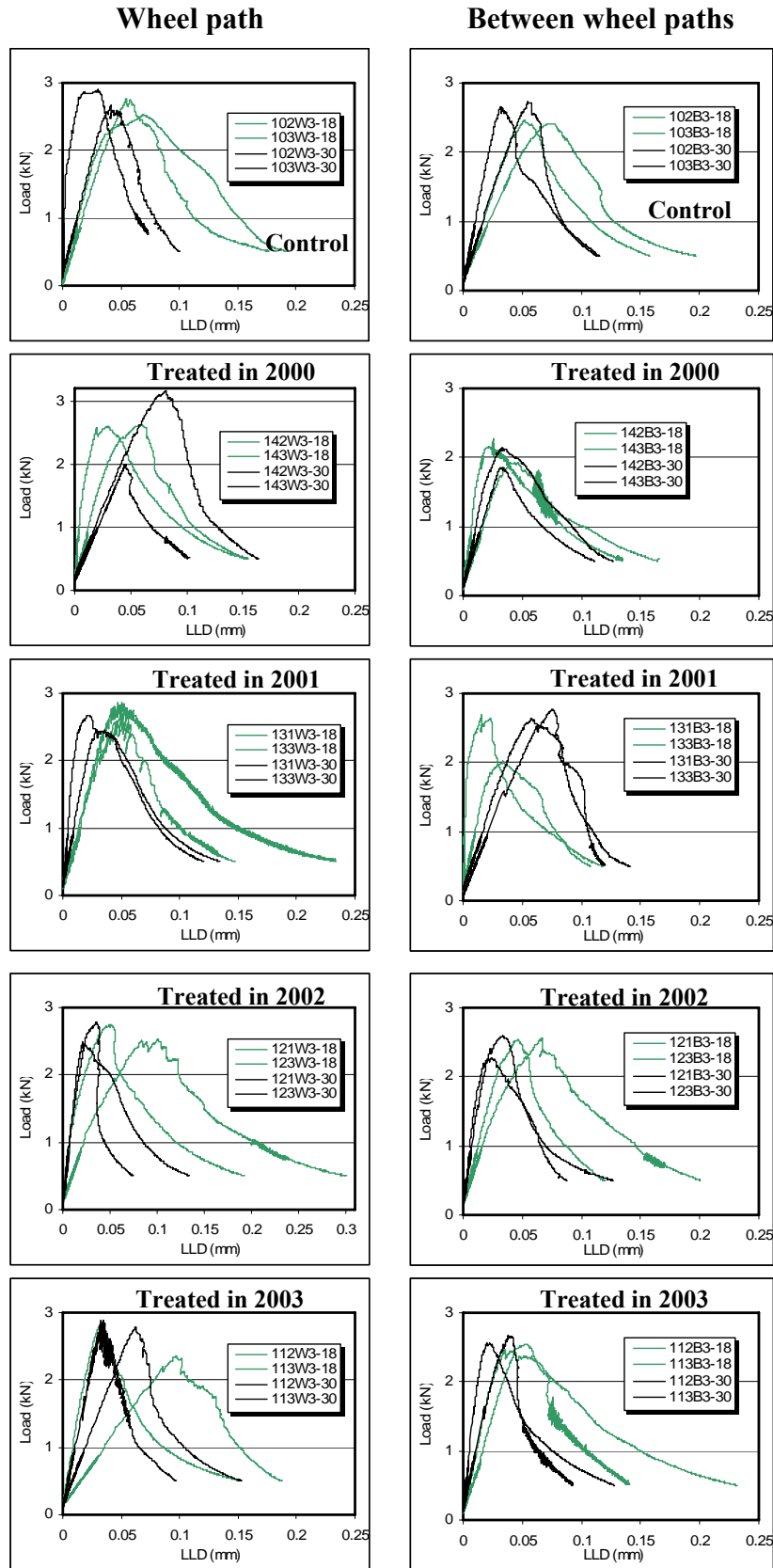
Figure D.49. Load-LLD curves for samples from lower layer, TH 56 1999 sections

Wheel path

Between wheel paths
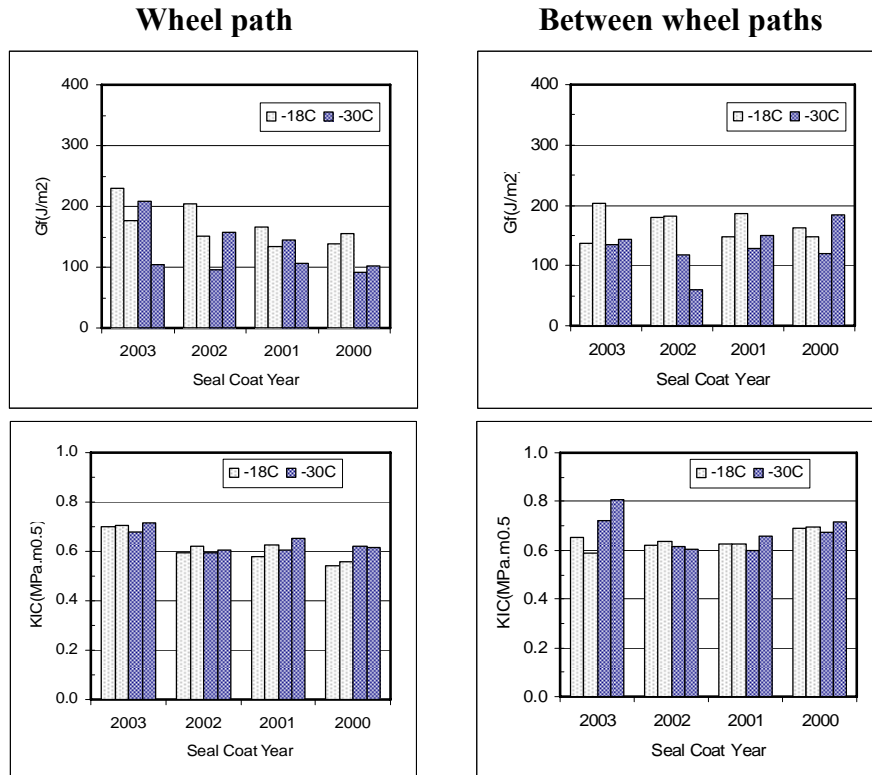
Figure D.50. G_f and K_IC for upper layer, TH 56 1995 sections

Wheel path

Between wheel paths
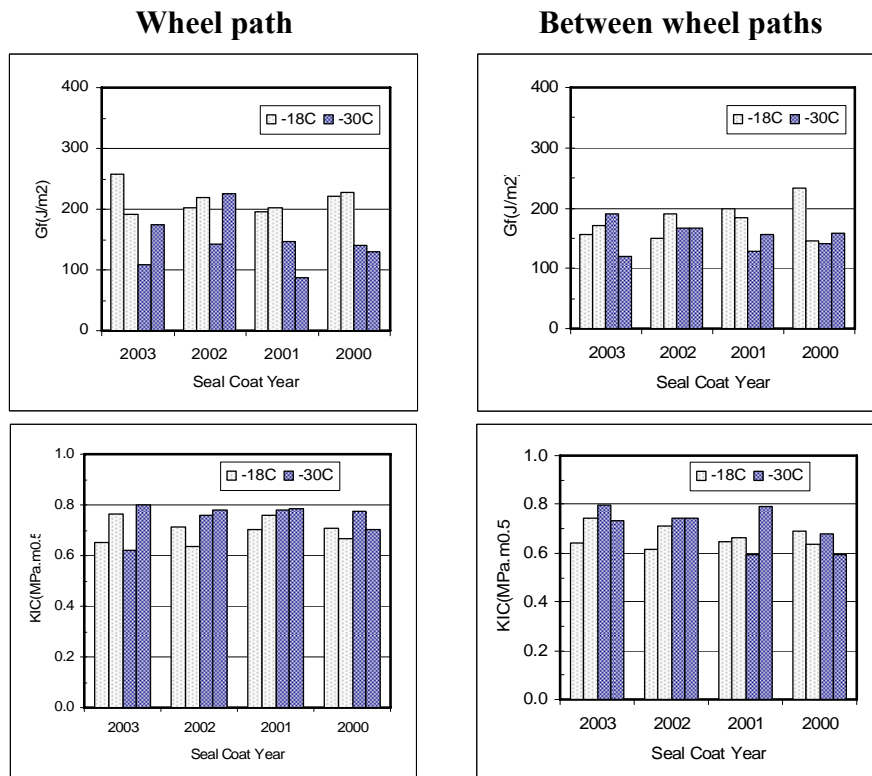
Figure D.51. G_f and K_IC for lower layer, TH 56 1995 sections

Wheel path **Between wheel paths**
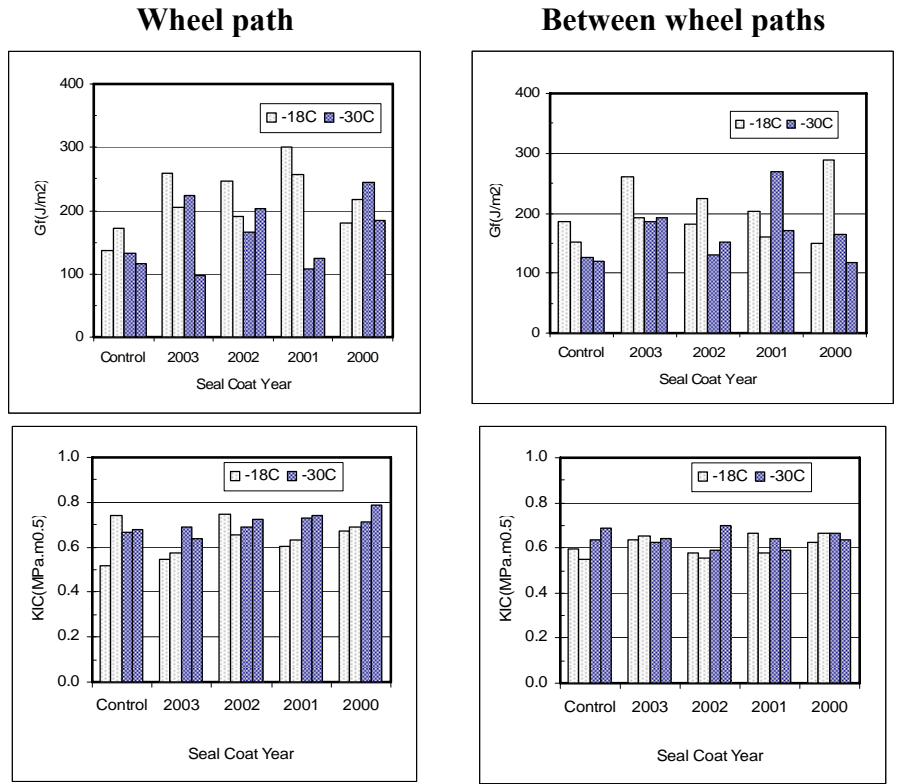
Figure D.52. G_f and K_IC for upper layer, TH 56 1999 sections

Wheel path **Between wheel paths**
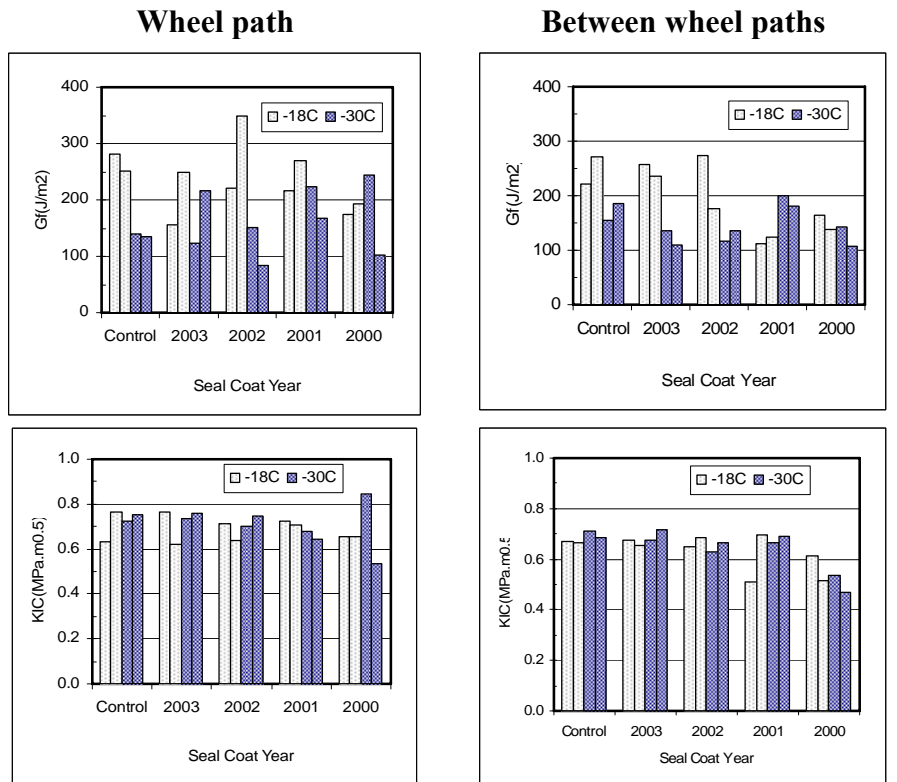
Figure D.53. G_f and K_IC for lower layer, TH 56 1999 sections
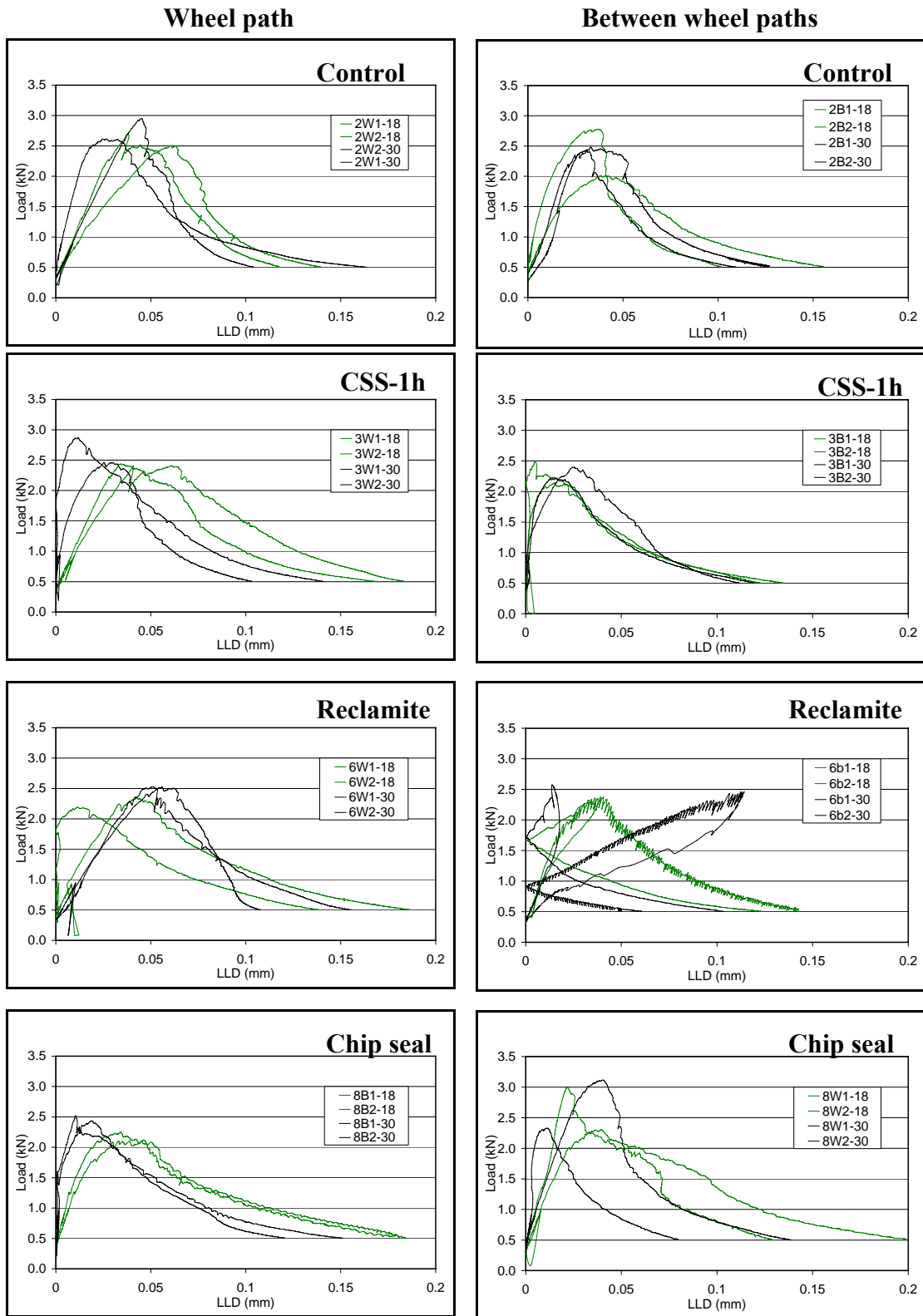
Figure D.54. Load-LLD curves for samples from TH 251 sections

Wheel path

Between wheel paths
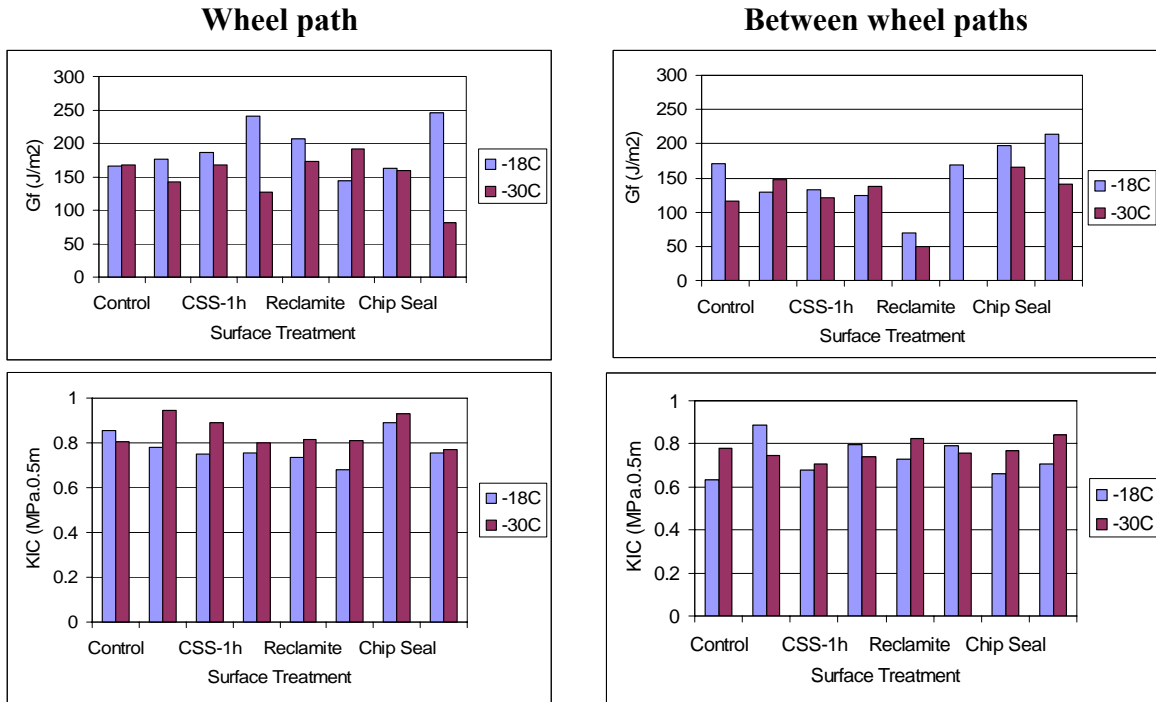
Figure D.55. G_f and K_{IC} for TH 251 samples

APPENDIX E

EXPANDED EXECUTIVE SUMMARY

Finding the optimum time for applying surface treatments is critical in developing a proactive maintenance program as part of a successful pavement management system. Transportation agencies could save significant resources if reactive type of maintenance activities were replaced by proactive activities that could significantly extend the pavements service lives. Due to the complexity and the multitude of factors affecting the pavement deterioration process, most of the guidelines for application of various maintenance treatments are based on empirical observations of the pavement surface condition with time.

This report presents the results of a comprehensive research effort to identify the optimum timing of surface treatment applications by providing a better understanding of the fundamental mechanisms that control the deterioration process of asphalt pavements.

A brief literature search, that included research published as recently as January 2008, was performed. It was found that, similar to earlier research efforts, current guidelines for applying surface treatments are based on empirical macroscopic observations of the pavement surface condition with time, and often times require experienced engineering judgment. In all references it was noted the importance of applying treatments to pavements in relatively good condition.

Some of the most recent studies also address the economic issues involved in the selection process and the timing of the application of treatments. Very recent work performed in Washington State indicated that The Highway Development and Management System (HDM-4) software can be used as an analysis tool for pavement performance predictions, rehabilitation/maintenance programming, funding estimates, budget allocations, policy impact studies, and a wide range of other applications. However, its effectiveness is dependent on the accuracy of its constituent models, which makes data accuracy and proper calibration paramount.

The search also revealed that in the past, Minnesota chip seal surface treatments had very poor performance. A statewide survey concluded that the poor performance of the surface treatments was linked to several factors including the design, programming, and construction of chip seals. Based on studies of chip seal programs around the world, a procedure based on the McLeod designed method, which was modified to increase the resistance of the treatments to snow plows, was implemented. As a result, there have been no reports of failed surface treatments in the last years and, with the addition of polymer modifiers and the use of better quality aggregates, the average service lives of treatments have improved from 5-7 years to 8-10 years.

The search could not find any references relating the suitability for treatment application to the change in mechanical properties of the asphalt materials.

Next, a detailed description of the test sections on Trunk Highway 56 near Austin, MN, and on Trunk Highway 251 near Clarks Grove, MN, respectively, is presented first. Additional information about the cored samples and construction information are included in Appendix A and B. A total of 10 sections were sampled from TH 56 to study the optimum time for the application of the surface treatment and four sections were sampled from TH 251 to investigate the effectiveness of three different types of surface treatments: fog seal (CSS-1h), rejuvenator (Reclamite), and Chip seal (CRS-2p, 3/8" Aggregate).

A thorough dissemination of the data available from different sources for the TH 56 sections revealed that the asphalt mixtures used in the 1995 and 1999 sections, respectively, were different: the 1999 sections were built with a PG 58-28 asphalt binder (mix design MVWE35035B); the 1995 sections used a penetration grade 120/150 asphalt binder (mix design 41WEA50055Y). Also, the TH 56 sections were built with two different types of aggregates: New Ulm Quartzite, and Dresser Trap Rock. In addition, the binder application rate increased

with pavement age, as recommended in the design procedure based on the method developed by McLeod in late 1960's. These additional factors made the interpretation of the test results rather difficult from a statistical point of view.

Six cores were taken from each section of TH 56 and TH 251, respectively: three cores from the wheel path and three cores from between the wheel paths, to determine if the compaction effort from traffic in the wheel path results in differences in the mechanical response from samples coming from these two locations. Note that the initial request of the research team was for 3 times as many cores to increase the number of replicates in the analysis. Test specimens were cut from the TH 56 cores at two different depths, 1 and 3 inches, respectively, to study the influence of aging with depth.

Different types of nontraditional pavement materials characterization methods were investigated next and some were carried out to evaluate the surface condition of pavements, mainly the presence of microcracks and the presence of oxidative aging products in the surface layer of asphalt pavements. For aging, a new method based on X-Ray Photoelectron Spectroscopy (XPS) was briefly described and experimental results were presented. The current method is based on Fourier Transform Infrared (FTIR) spectral analysis performed on samples of asphalt binder extracted from field mixtures. Due to concerns related to the use of chemical solvents in the extraction process that can alter the properties of the binder, there is increased interest to detect aging directly from asphalt mixtures. The limited results indicated that the use of the XPS is not warranted for routine pavement maintenance activities.

For microcracks detection, two methods, the electron microprobe imaging test (SEM) and the fluorescent dyes for inspection of cracking, respectively, were presented. Based on the limited experiments performed, it was concluded that the application of the SEM technology to assess the surface condition of the pavement is difficult due to the localized nature of the test. Specimen preparation can be expensive and time consuming and the specimen tested might not be representative of what is observed in the field. On the other hand, the application of fluorescent dyes may have the potential to reveal the presence of microcracks, not detectable by visual observation or current pavement condition surveying methods, and should be further pursued in field experiments.

A new promising area in remote sensing and detection, the spectral analysis of asphalt pavements to determine aging, was also presented in Chapter 3. Studies performed by several researchers have shown that the principles of imaging spectrometry can be used to estimate the physical structure and chemical composition of the surface of asphalt pavements. Two methods were investigated; ground spectrometry representing ground measurements on the scale of individual materials, and hyperspectral remote sensing from satellite or airplane sensors, on the scale of land cover types. The remote sensing and detection appears to currently lack the level of resolution needed to identify changes in asphalt surface characteristics that would indicate the need for surface treatment application.

Mechanical tests performed on the chemically extracted asphalt binder samples were described next and the test results were tabulated. This included the Bending Beam Rheometer (BBR) that was used to obtain creep stiffness and m-values over 240s loading time at multiple temperatures, Direct Tension Test (DTT) that was used to obtain failure stress and strain and multiple temperatures, and Dynamic Shear Rheometer (DSR) that was used to obtain |G*| and phase angle at different frequencies and temperatures and to generate master curves. The mixture tests were also presented and the results were tabulated. This included the BBR on thin mixture beams to obtain mixture creep stiffness and m-values at multiple temperatures, and the Semi-

Circular Bend Testing (SCB) that was used to obtain fracture toughness and fracture energy at multiple temperatures. In addition, the Fourier Transform Infrared Spectroscopy (FTIR) test performed on the extracted asphalt binders was also described and the carbonyl values were tabulated.

This was followed by extensive statistical analyses of the experimental results based on analysis of variance (ANOVA), correlation matrices, and Tukey honest difference tests. The analyses focused on identifying significant asphalt binder and mixture properties that affect the deterioration process of asphalt pavements that could be used as triggers in an effort to determine the optimum time of surface treatment application. Plots of the experimental data are presented as figures in Appendix D.

The analysis of the results for each of the tests previously described was divided into two groups: TH 56 sections were used to study the optimum time for the application of the surface treatment; TH 251 sections were used to investigate the effectiveness of three different types of surface treatments: fog seal (CSS-1h), rejuvenator (Reclamite), and Chip seal (CRS-2p, 3/8" Aggregate). TH 56 analysis was further divided in two groups according to the construction year: 1995 and 1999. An additional analysis was performed on the combined 1995 and 1999 sections considering the construction year as a factor in the analysis.

The analysis of the extracted binder BBR data indicated that temperature is significant in the prediction of S and m for both 1995 and 1999 sections. Age before treatment is important for the prediction of S but not for m. Based on the p-values, significant differences were observed in m-values with respect to depth for 1995 sections, and location for the 1999 sections. Interactions between the predictors (e.g. age, depth, location, temperature) generated some significance in the ANOVA that was not observed in the correlation matrix. For TH 251 samples, it was found that the m-values in the treated sections are higher than the m-values in the control section. The m-value is an indicator of the relaxation properties of the asphalt binder; higher values of this parameter indicate that the binder relax stresses faster. This result seems to indicate that the application of surface treatments changes the relaxation properties and does not affect stiffness. This finding supports recent discussions in the asphalt chemistry community that aging not only increases the amount of ketones but also changes the aromaticity of binders, which is related to relaxation properties.

For the DTT extracted binder data, a positive and significant correlation is observed between strain at failure and depth for the samples constructed in 1995. As expected, there is a positive correlation between stress and strain at failure and between temperature and strain at failure for the samples constructed in 1995. A negative correlation between the temperature and the stress at failure is observed for the sections constructed in 1999. This negative correlation indicates that when the temperature decreases the stress at failure increases. There are no significant correlations observed between the age before application of the surface treatment and the parameters obtained in the direct tension testing. ANOVA analysis indicated that depth is a significant parameter in the prediction of the stress and strain in the 1995 sections. Temperature is significant for the prediction of strains at failure for sections constructed in 1995 and 1999. As it was observed previously in the correlation matrices, stress at failure depends on the temperature for the samples in sections constructed in 1999 but not in 1995. For the TH 251 samples, no significant differences between the stress and strain at failure of the control section and the sections treated with fog seal (CSS-1h), rejuvenator (Reclamite), and Chip seal (CRS-2p, 3/8" Aggregate) were identified.

The analysis of the DSR results on the extracted asphalt binder samples from TH 56 indicated that for 1995 sections there is a significant positive correlation observed between depth and the phase angle, indicating that as the depth increases, the phase angle increases too. Also, a negative correlation is observed between $|G*|$ and depth, indicating that $|G*|$ decreases with depth. For the 1999 sections, contrary to what it was expected, there is a significant negative correlation between the age before application of the surface treatment and $|G*|$; older binders are expected to have higher stiffness. The increase in the emulsion application rate with the age of the pavement before treatment could be one of the reasons why this correlation is observed. In the ANOVA, depth is significant in the prediction of the phase angle for sections constructed in 1995. Age of the pavement before treatment is significant for the prediction of $|G*|$ but as mentioned before, this significance is most likely due to the effect of changing the application rate of the emulsion and not to aging. For TH 251, it is observed that $|G*|$ is significantly higher for the sections treated with CSS-1h and Reclamite compared to the control section. Location is significant in the prediction of $|G*|$; the negative sign in the estimate of the location coefficient indicates that the moduli of the samples coming from between the wheel paths are lower than the moduli of samples from the wheel path.

The analysis of the FTIR data for the TH 56 extracted binder samples indicated that the normalized carbonyl peak area has a positive correlation with age before treatment meaning that as age before treatment increases carbonyl content increases. The correlation between carbonyl area and depth is significant and negative. Thus, the asphalt binder in the top of the AC layer aged more than the binder in the bottom. ANOVA indicates that all parameters are significant in the prediction of the carbonyl content. The p-value for location is 0.047, close to be not significant; interactions between the location and the other variables generate some significance that is not observed in the correlation matrix. For the TH 251, two trends were clearly observed: carbonyl content reduces with depth and the samples from the chip seal section have the least amount of carbonyl while the samples from the CSS-1h seal coat section have the largest amount of carbonyl. For the surface samples, asphalt binders located between the wheel paths oxidized more than the binders located in the wheel path. It also appears that the chip seal sections had the lowest oxidation.

For asphalt mixtures samples, both mechanical tests as well as volumetric analysis were performed. For the TH 56 1995 sections it is observed that the air voids in the specimens from the upper layer are slightly higher than the specimens from the lower layer. For the 1999 sections the opposite is observed. It is also noticed that the sections treated earlier have less air voids than the sections treated later, which is more noticeable for the specimens located in the wheel path. The previous figures indicate that the air voids for the specimens taken from the wheel path had lower air voids than from between the wheel paths. For TH 251, the samples located in the wheel path have less air void content than the samples between the wheel paths. It is also notice that the samples treated with chip seal have slighter higher air void content than the other specimens.

The analysis of the BBR results on thin asphalt mixture samples indicates a high positive correlation factor between location and voids meaning that the samples located between the wheel paths have higher void content compared to samples in the wheel path. In ANOVA, the depth is significant for the prediction of the m-value for 1995 samples. In the previous analysis no correlation was observed between these two variables. Interactions between the predictors generate some significance in the ANOVA that is not observed in the correlation matrix. For TH 251, it is observed that at -18°C the mixture treated with the chip seal shows slightly lower creep

stiffness with respect to time compared to the other mixtures. It is also noticed that at -12°C the mixtures treated with Reclamite and chip seal have the lowest creep stiffness. The control section samples located in the wheel path have the highest mixture stiffness at both temperatures. On the other hand, the mixtures treated with chip seal have the lowest stiffness and the highest m-values. It is also observed that for the samples located between the wheel paths, the highest stiffness corresponds to the mixture treated with CSS-1h. From ANOVA, the parameters that are important in the prediction of the mixture stiffness are location, voids and temperature. Also from the negative coefficient estimate of the Reclamite treatment it is observed that the samples treated with Reclamite have significantly lower stiffness compared to the control section samples. Although the estimated coefficients from the other two treatments are also negative, they are not significant for the linear model proposed. The only parameters significant in the prediction of the m-value of the mixture are temperature and location. The location coefficient estimate for the prediction of Smix is not consistent to what it is expected. The positive sign indicates that the samples located in between the wheel paths have higher stiffness than the samples located in the wheel path.

The analysis of the SCB fracture test results for TH 56 shows a significant positive correlation of fracture toughness and fracture energy with depth, indicating that both fracture parameters increase when the depth increases. Voids content and age before treatment have a negative correlation, when the age of the pavement increases then the void content is reduced. Temperature has a strong effect on both fracture parameters. For the fracture energy and fracture toughness, the correlation is positive and negative, respectively. When the temperature increases the fracture toughness decreases and the fracture energy increases. A negative correlation, close to be significant, between the age before treatment and the fracture toughness (in italic and underline) is also observed. This result may indicate that the toughness of the mixture is reduced when the age of the pavement before treatment increases. There is a positive correlation for the void content with location and depth meaning that as the depth increases the void content increases and that higher void content are found in samples located in between the wheel paths. A negative correlation is observed for the fracture toughness with the location and the void content, indicating that samples located in the wheel path have higher fracture toughness than samples in between the wheel paths. Also, increasing the void content reduces the fracture toughness of the sample. In the ANOVA, it is observed that temperature is significant in the prediction of Gf and KIC for both 1995 and 1999 sections. Also, depth is significant for the prediction of both fracture parameters for 1995 samples. For TH 251, at -18°C, the highest fracture toughness from between the wheel paths is obtained from the control section. On the other hand, the highest fracture toughness from the wheel path is observed in the section treated with chip seal. The highest fracture energy for both locations at -18°C is observed in the section treated with chip seal. Also, it is observed that in between the wheel paths and at -30°C the section treated with chip seal shows the largest fracture energy and fracture toughness. The control and Reclamite sections have the highest fracture toughness and fracture energy in the wheel path and at 30°C, respectively. In ANOVA it is observed that temperature is significant in the prediction of Gf and KIC while void content and location are significant for the prediction of fracture energy only. No significant differences are observed between the fracture energy and fracture toughness of the control section and the sections with surface treatments.

For the TH 56 sections an additional ANOVA was performed on the BBR extracted binder and thin mixture beams to include the effects of the design parameters of the seal coat and the emulsion application rate. This ANOVA considers the construction year as a factor in the

model. The factors and interactions of factors, significant at the 5% significance level were further investigated by using a Tukey Honest significant difference multiple comparisons test. The binder analysis indicated that the upper layer of cell 17 had significantly lower creep stiffness values than other cells; however, the statistical analysis of the m-value did not show cell 17 as being significantly different than other cells. The pavement age when treated is not significant in the m-value analysis. In the mixture analysis, m-value was found much more sensitive to both the pavement construction year and the depth below the pavement surface, as well as the interaction between the two, than was the creep stiffness. The 1999 sections had significantly higher relaxation rates than the 1995 sections, and the effect of depth on the m-value, although not as pronounced as the construction year, was significant in the statistical analysis. The analysis also indicated that the lower layer consistently had a higher m-value than the upper layer, meaning that the m-value appears to be a good indicator of aging in asphalt pavements. The path was also identified as a significant factor in the statistical analysis; the creep stiffness was higher in the wheel path than between the wheel paths. This behavior could be explained by the increased compaction in the wheel paths induced by vehicle loading.

Although the analyses did not identify a clear "winner", they led to a number of important conclusions that clearly indicate the potential use of some of these test methods in improving the timing of surface treatment application and the type of treatment. For the TH 56 sections binder data, the FTIR appeared to be the most sensitive to the age of the material and had a significant positive correlation with pavement age. The DSR, BBR, and DT data analyses were less significant and many times led to contradictory results; note, however, that the emulsion application rate was also adjusted with the age of the pavement, and these results appear to indicate that this is a good practice. The mixture BBR analyses seemed to agree the most with common knowledge. For example, the 1995 pavement had higher creep stiffness, and a lower relaxation rate than the 1999 sections, indicating that older pavements are stiffer and have a lower relaxation rate than newer pavements. The depth below the pavement surface was found to have a very significant effect on the m-value; the relaxation rate of the lower layer was higher than the upper layer, which also agrees with the current knowledge about aging. However, the analyses also indicated that the 1995 and 1999 sections were different, due to either the use of different asphalt mix designs and possibly binders, or to different construction practice.

An attempt to identify the best window of time for the surface treatment application was done based on the average fracture properties for each section in TH 56. It appears that there is a window of time between 4 and 6 years were the fracture toughness is higher. However, note that the difference between the maximum and minimum fracture toughness at both temperatures may not be significant. Based on the limited number of tests performed, it also appears that the surface treatment that prevents aging the best is the chip seal. Samples from the section treated with chip seal show the highest fracture energy, the lowest stiffness of the mixture and the binder and the highest m-value of the binder. Additionally, the binders extracted from the section treated with chip seal show one of the highest strains at failure.

The last part contains a substantial analysis of measured pavement temperature data from MnROAD and simulations of pavement temperature using a one-dimensional finite difference heat transfer model. Several methods to extract pavement thermal diffusivity from pavement temperature measurements at two or more depths are also described in this chapter. The analysis clearly indicated that surface temperature gradients can be up to 5°C/cm, which suggest that aging is more significant in the very top few centimeters of the pavement. In addition, the temperature rate of change at the surface can be as high as 40°C/hour during rain events when

the pavement surface is hot, which may lead to microcracks formation. It was also found that the daytime maximum pavement temperature greatly exceeds maximum air temperature, with surface temperatures of up to 63°C (145°F) in mid-summer, 5°C above the upper limit of the asphalt binder performance grade (PG) commonly used in Minnesota.

The pavement temperature model developed at St. Anthony Falls laboratory (SAFL) seems suitable to model pavement and subgrade temperatures at RWIS sites and therefore, can provide a tool to check the consistency of the pavement temperature data measured at RWIS sites by predicting expected pavement temperature time series from the measured climate data at the RWIS sites with the model calibrated against the much more detailed data from the MnROAD site. Substantial differences between predicted and measured pavement temperatures at an individual RWIS would be indicative of a need for quality control of the instrumentation, while widespread differences could indicate regional differences in pavement responses to weather.

At the end of the report, the most important conclusions and recommendations for future research are presented. The mechanical tests performed on asphalt binders and mixtures samples in this study can be used to detect changes in properties related to performance. In particular, the BBR test on thin mixture beams appears to be a promising tool in evaluating the properties of thin layers of mixture within the constructed asphalt layers. The method to detect microcracks using a fluorescent penetrant should be further investigated using more powerful UV lamps and surfactants that allow the fluorescent solution to better penetrate into microcracks.   The pavement temperature analysis can be expanded to determine moisture content in the pavements and subgrade from temperature signals during freeze-thaw cycles. When pavement temperatures cross the freezing point, measured temperature signals in the pavement and subgrade are delayed by latent heat of freezing or thawing. By including latent heat of freezing in the heat conduction equation during freeze/thaw cycles one can arrive at moisture estimates from measured temperature time series in spring and fall. The freeze/thaw/moisture model can be combined with measured temperature and moisture time series to characterize the time and length scales over which freeze-thaw cycles occur, from seasonal freezing of the soil to depths of meters to daily freeze thaw cycles in the upper few centimeters of the pavement.